National Library of Canada
Acquisitions and Bibliographic Services Branch
395 Wellington Street
Ottawa, Ontario
K1A 0N4

Bibliothèque nationale du Canada
Direction des acquisitions et des services bibliographiques
395, rue Wellington
Ottawa (Ontario)
K1A 0N4

Your file Votre référence

Our file Notre référence

NOTICE

The quality of this microform is heavily dependent upon the quality of the original thesis submitted for microfilming. Every effort has been made to ensure the highest quality of reproduction possible.

If pages are missing, contact the university which granted the degree.

Some pages may have indistinct print especially if the original pages were typed with a poor typewriter ribbon or if the university sent us an inferior photocopy.

AVIS

La qualité de cette microforme dépend grandement de la qualité de la thèse soumise au microfilmage. Nous avons tout fait pour assurer une qualité supérieure de reproduction.

S'il manque des pages, veuillez communiquer avec l'université qui a conféré le grade.

La qualité d'impression de certaines pages peut laisser à désirer, surtout si les pages originales ont été dactylographiées à l'aide d'un ruban usé ou si l'université nous a fait parvenir une photocopie de qualité inférieure.

Canada

Sea Ice Behaviour in Creep/Fracture Regime: An Experimental and Theoretical Study

Caizhao Zhan, B.Sc., M.Sc.

A Thesis
Submitted to School of Graduate Studies
under the supervision of
Drs. Erman Evgin and Nirmal K. Sinha

in partial fulfillment of
the requirements for the degree of
Doctor of Philosophy
in Civil Engineering

The Doctor of Philosophy Program in Civil Engineering is a joint program between Carleton University and the University of Ottawa, which is administered by the Ottawa-Carleton Institute for Civil Engineering

ISBN 0-315-83851-5

UNIVERSITÉ D'OTTAWA
UNIVERSITY OF OTTAWA

ACKNOWLEDGEMENT

The author would like to express his sincere thanks to his thesis supervisors, Drs. Erman Evgin and Nirmal K. Sinha, for their guidance, encouragement, and patience for the past four years. The financial support was provided from various sources. These include the Operating Grant of Dr. Evgin, NSERC supported joint project in which Dr. Timco was the principal investigator, and the NSERC grant of Dr. Sinha.

The National Research Council of Canada allowed the use of laboratory facilities and test equipment for both laboratory and field tests. Special thanks are extended to R. Jerome for his technical assistance in laboratory and field tests.

Logistic support for the field project at Resolute, N.W.T. was provided by the Polar Continental Shelf Project (PCSP), Energy, Mines and Resources. The field work would have been impossible without the assistance of Claude Brunet, Station Manager of PCSP in Resolute. Mr. Andrew Clarke from the weather station in Resolute is thanked for providing ice growth data in Resolute Bay and valuable information leading to an ideal test site. The guidance and help offered by Drs. M.E. Shokr from Atmospheric Environment Service, Environment Canada, and N.K. Sinha during the field work are greatly appreciated.

The recommendations offered by the members of the advisory committee, Drs. M. Cheung from Civil Engineering Department, G.W. Timco and O.J. Svec from National Research Council of Canada, NRCC, are greatly acknowledged.

Most importantly, I would like to express my thanks to my parents for their encouragement, support and understanding throughout my education, and especially to my wife, Xiaoming, for her support and understanding.

In memory of my uncles

ABSTRACT

An experimental and theoretical study of sea ice behaviour is the subject of the research described in this thesis. The thesis has three parts. The first part presents the experimental results. Both laboratory and field tests were carried out. The laboratory tests were conducted at NRCC laboratory in Ottawa. In the laboratory, constant load experiments were performed on columnar-grained natural first year sea ice sampled in 1991 from Resolute Passage N.W.T. off Barrow strait/Lancaster Sound. Axial and lateral strains were measured, and acoustic emission data were recorded. Creep tests were carried out at -10^0C, -20^0C, and -30^0C. These creep tests are considered to be the first of its kind. Field tests were conducted at Resolute Bay in 1992. Two types of investigations were carried out in the field: (1) microstructural study of first year columnar grained sea ice as a function of depth, (2) borehole indentation tests on first year columnar grained sea ice with various boundary conditions.

Sea ice is composed of grains with substructures consisting of subgrains, brine, air bubbles and solid salts depending upon temperature. Microstructural information provided the basis for developing a relationship between growth rate, salinity, and brine layer spacing. The borehole indentation tests were used to determine the effect of confinement and anisotropy on the rate dependence of strength and deformation of columnar grained sea ice.

The microstructure of columnar-grained sea ice is rather complex because of the presence of the second (brine) and third (solid salt crystals) phases. It was, therefore, decided to examine first the rheological response of fresh water columnar grained ice.

A three dimensional constitutive model for the ductile behaviour of fresh water columnar grained ice was developed. The constitutive model is capable of describing the inherent anisotropy caused by the fabric, the grain size effect, the crack evolution, the effect of crack on viscous strain, and the deformation of the cracks. The model is used to predict the dependence of strength on the angle between the mean c-axis (axis of symmetry) and loading direction for oriented columnar-grained ice (classified as S3) and the anisotropic response of transversely isotropic columnar-grained (S2) ice. Comparisons of model predictions with experimental

results for S2 ice on rate dependence of strength, grain size effect on time dependence of strains are provided.

The model for fresh water ice was subsequently extended to sea ice to account for the effect of brine pockets on its mechanical behaviour. This constitutive model for sea ice is based on an assumed geometric pattern for the distribution of brine pockets in a single grain of sea ice. An initial defect tensor for a single grain of sea ice is defined based on the geometric pattern neglecting, for simplicity, the subgrain structures. Subsequently, the initial defect tensor for polycrystalline ice is obtained from the initial defect tensor for a single grain of sea ice and the probability distribution of c-axis. The effect of the initial defect on the response of sea ice to different types of loading is expressed by introducing two additional tensors. One of these tensor is called the influence tensor for deviatoric stresses, and the other one is the influence tensor for hydrostatic stresses. The constitutive equations for columnar grained sea ice are the same as those for fresh water columnar grained ice, except that an effective stress tensor is used in the sea ice constitutive equations to replace the stress tensor in the model for fresh water ice. Comparisons between model predictions and laboratory test results under both uniaxial and multiaxial loading conditions are provided.

In the last part, Sinha's creep model, because of its simplicity, was generalized into 3-D and implemented into a finite element program. Comparisons between the finite element results and the analytical solutions of various cases were made, in order to verify the correctness of the model implementation into the finite element program. The finite element program was used to analyse the borehole indentation test results from the field study at Resolute. Some of the observation in the field tests were explained by the finite element analyses.

Contents

List of Figures

List of Tables

Chapter 1

Introduction

1.1 Statement of problem

In cold regions, the increasing industrial activities have increased the demand for the solutions of ice engineering problems. One of the problems is the use of ice structures to serve mankind. Another problem is that ice can be the cause of external load to structures. Whether to ensure the safety of ice structures or to determine the magnitude of ice forces on structures, it is necessary to understand the mechanical behaviour of ice and to formulate mathematically its behaviour. Subsequently, the ice model should be implemented into a computer program to solve engineering problems.

One of the difficulties in modelling the ice behaviour is the inherent and induced anisotropy. Most of the ice encountered on the lakes, rivers, and oceans are columnar-grained. Fresh water columnar grained ice often exhibits transverse isotropy with c-axis (optic axis) of the grain randomly orientated in the horizontal plane (or the plane normal to the length of the columns). Sea ice, especially landfast ice, shows c-axis orientated parallel to the water current (Weeks and Gow, 1978; and Nakawa and Sinha, 1984). Columnar grained ice exhibits high anisotropy. A columnar-grained ice sample loaded uniaxially normal to the length of the columns of grains shows negligible strain in the direction of the columns compared to the axial strain and the other lateral strain (Wang, 1981; Sinha, 1989a; Sinha, et. al, 1992). Also, a sample loaded uniaxially in the direction parallel to the columns exhibits much higher strength than a sample loaded in the

direction normal to the columns (Peyton, 1966; Michel, 1978a; Wang, 1981; Sinha, 1983b, 1984a; Timco and Frederking, 1982, 1986; Frederking and Timco, 1984). It is therefore essential to bring the anisotropic behaviour of the columnar grained ice into the constitutive model.

Many constitutive equations have been developed. However, very few constitutive equations can be used to model the anisotropic behaviour of columnar grained ice. The conventional equivalent stress method was used to model the anisotropy (Ting and Sunder, 1985; Sunder and Wu, 1989; and Pulkkinen, 1989). The problem with this method is that with different fabric, different material parameters are needed. In the case of a polycrystalline anisotropic material without any symmetry axis or plane, the equivalent stress method as it was defined is not applicable. Sjolind (1987) employed a fourth order tensor to represent the anisotropy, which requires up to 81 material constants. The fourth order tensor is different for each type of ice with different fabric.

Up to now, there is no constitutive model which can predict both the strength as a function of the angle between the c-axis and loading direction and the magnitude of anisotropic deformation for orientated columnar grained ice. In addition, there is no ice model which can be used to predict the difference between the vertical and horizontal strength of columnar grained ice.

One important difference between fresh water ice and sea ice is that sea ice has a cellular substructure consisting of almost evenly spaced subgrains or ice platelets. Along the subgrain boundaries, brine inclusions are present in the form of liquid and solid depending on temperature. It is the brine layer spacing or the size of the subgrains and the shape of the brine pockets that are used to characterize the substructures of sea ice. The substructures of sea ice significantly influence its mechanical behaviour. It is therefore essential to account for the substructures of sea ice in the constitutive model.

A geometric model was proposed by Assur (1958) for brine ice relationship. Based on the geometric model, a relationship was established between strength and brine volume. However, this relationship can only be used for columnar grained ice subjected to uniaxial load in the horizontal plane.

Compared to fresh water ice, very few constitutive models were developed for sea ice due to its complexity. Ting and Sunder (1985) developed a constitutive

model for sea ice. However, no consideration was given to the substructures of sea ice.

Both laboratory and field tests along with detailed information on the test conditions and the material are the basic means to understand the mechanical behaviour of a material. Constant stress laboratory tests with measurement of all strains and combined with microstructural study are essential to understand the rheological behaviour of sea ice. Although there are many experimental investigations on the strength of sea ice, no useful constant load creep test data are available on sea ice. Field tests usually involve large samples with nonuniform stress state and temperature distribution. Therefore, a field test with measurements of load and displacement combined with microstructure study can be used to make a comprehensive validation of the constitutive model.

To solve a complicated engineering problem, the constitutive model must be implemented into a finite element or boundary element program. The implementation must be verified with analytical solutions, if they are available, under both uniform and nonuniform stress states.

1.2 Research objectives

The main objectives of this research are:

1. to perform creep tests on natural sea ice,
2. to develop a constitutive model for sea ice,
3. to develop a 3-D finite element program which includes a constitutive model for ice,
4. to determine the in-situ creep/fracture characteristics of sea ice.

The sea ice model is able to take into account the anisotropy due to fabric, the effects of microcracks on deformation, and the opening and sliding of microcracks. The effects of brine inclusions, temperature, and grain size on sea ice behaviour are considered. The model is used to predict both the strength dependence on the angle between the mean c-axis and loading direction and the magnitude of

the anisotropic deformation of orientated columnar grained ice. In addition, the anisotropic behaviour of columnar-grained S2 ice is predicted.

Sinha's model is generalized into 3-D and implemented into a 3-D finite element program. The numerical implementation is verified with a number of analytical solutions. The 3-D finite element program is used to analyse field borehole indentation test results.

1.3 Scope of research

To achieve the research objectives, the following work is proposed for the thesis:

1. Carry out constant load tests on first year natural columnar grained sea ice at different temperatures and stress levels with the measurements of strains and acoustic emissions.

2. Study material damage using acoustic emission technology and the double microtoming technique.

3. Carry out field borehole indentation tests at different loading rate and boundary conditions.

4. Study the microstructure of the sea ice using double microtoming technique.

5. Develop a constitutive model for fresh water columnar grained ice to take into account the inherent anisotropy due to fabric, the effects of microcracks on deformation, and the sliding and opening of microcracks, and validate the constitutive model by comparing model predictions with available experimental data.

6. Extend the constitutive model for fresh water columnar grained ice to sea ice by introducing the influence tensors for deviatoric and hydrostatic stresses based on the microstructures of sea ice, and validate the sea ice model by comparing the model predictions with the test results.

7. Generalize Sinha's creep model with cracking to three dimensional, and implement the generalized model to a three dimensional finite element program.

8. Verify the model implementation into the finite element program by comparing the finite element results with analytical solutions for different cases under both uniform and nonuniform stress states.

9. Analyze the borehole indentation test data with the three dimensional finite element program.

Chapter 2

Laboratory constant load test on first year sea ice

2.1 Introduction

The majority of mechanical tests on sea ice were performed to determine the flexural strength or strength under uniaxial compression or tension. A number of studies were also carried out under multiaxial compression. A rather exhaustive list of publication up to 1983 and a compilation of available data can be found in Lainey and Tinawi (1984). Creep studies on sea ice, however, were limited to the bending of beams or plates. Tabata (1958), for example, came to the conclusion that sea ice was a linear viscoelastic material. Vaudrey and Katona (1975) also came to the same conclusion and used linear viscoelasticity in developing their finite element program (VISICE) for analyzing the bearing capacity problem of sea ice covers. For a certain class of short term engineering problems, ice can be treated as a linear viscoelastic material (Sinha, 1978a; Gold and Sinha, 1981) which provides justification for the assumption used by Tabata (1958), Vaudrey and Katona (1975), Vinogradov and Masterson (1989).

Plate bending information is essential to the bearing capacity of ice covers. Beam and plate bending experiments are simple to perform but the results are difficult to analyse for nonlinear rate sensitive material like sea ice. The nonlinearity of sea ice has been well demonstrated in a large number of compressive

strength tests (Wang 1979; Frederking and Timco, 1983; Sinha, 1984a, 1986; Chen and Lee, 1986; Richter-Menge, 1991). Surprisingly, there is very few experimental data on uniaxial or multiaxial creep of sea ice. Li et al. (1991) conducted uniaxial creep test on columnar grained sea ice at temperature between -1.5^0C to -5^0C. However, due to the extremely high temperature, they used, brine drained out and material changed its properties during the creep test. No useful uniaxial creep data on sea ice, vital for understanding the rheological behaviour of a material, are available in the open literature.

2.2 Present experimental study

Experiments were carried out on natural first year oriented columnar grained sea ice from Resolute Passage off Barrow Strait. Uniaxial constant load experiments were performed at three temperatures in conjunction with the measurements of lateral strains and acoustic emissions. The load was applied normal to the length of the columns of grains, i.e. horizontal loading. The details are given below. As a sign convention, compressive stresses are assumed positive in the thesis.

2.2.1 Ice characteristics

A uniform flat sheet of first year sea ice covered Resolute passage in May, 1991 during SIMS-1991 (Sea Ice Monitoring Sites) experiments. Microstructures of this ice were studied in the field (Shokr and Sinha, 1992). Except for the top 10 cm, ice was predominantly columnar grained with an average salinity of 5 parts per thousand. Large blocks were obtained from one of the stations where in situ borehole indentation tests were conducted. The blocks were recovered from a depth 0.5 to 1 meter (avoiding the top layer) using a chain saw when the air temperature were about 263 K (-10^0C). The blocks were brought to the base camp within an hour of excavation and stored in a cold room maintained at 253 K (-20^0C). A few days later they were shipped to Ottawa in heavily insulated boxes with air spaces inside the boxes filled with cold snow. Air transportation took about 8 hours. In Ottawa, the blocks were stored in a deep freezer at a temperature about 248 K for three months. The tests were carried out in September, 1991. A few

days before the tests, the large blocks were taken out from the deep freezer. They were marked and cut into smaller blocks in the cold room at 253 K. The smaller blocks were then stored in the individual plastic bags inside the freezer. These small blocks were taken out of the freezer , one at a time, as required. They were taken to the cold room and allowed to reach the cold room temperature before they were machined using milling machine and a lathe.

2.2.2 Sample preparation and test method

Constant load tests were carried out at 263 K, 253 K and 243 K on prismatic samples with final dimensions of about 50 mm × 100 mm × 250 mm, their long dimension parallel to the surface of the ice cover and therefore normal to the length of the columnar grains. A milling machine was used to prepare the major surfaces. The end surfaces were prepared with a lathe. The specimen end surface were given a final polish by hand with a fine grade sand paper, placed on a flat granite block. All cutter markers were removed, making certain that the surfaces were flat and at right angles to the long axis of the prisms. The specimens were prepared one or two days before the test at the experimental temperature. However, the sample tested at 243 K were made at 253 K because of the technical problem with the milling machine at that low temperature. The samples were then stored in the individual plastic bags until they were tested.

Small pieces of ice were used to make thin sections by double microtoming technique (Sinha, 1977). Examples of horizontal and vertical thin sections are shown in Fig. 2.1. Broken piece of ice were taken outside the cold room in sealed glass jars for melting and determining the salinity of the stored ice. The data were used for the comparison purposes with those determined from the freshly sampled ice. Similar results were obtained.

A commercial, closed-loop, servo-hydraulic system (1.0 MN frame and 250 KN actuator capacity, MTS) was used. The machine is situated inside the cold room near an observation window; the controls, pump, and the recording system were kept outside. Compressive load was applied to the 50 mm × 100 mm faces of the specimen. The loading train consisted of two-152 mm diameter, polished stainless steel compression platens (one at the top and one at the bottom of the specimen),

a spherical seat, and a load cell. The lower platen was attached to the actuator and the upper platen reacted against the load frame through the spherical seat and the load cell. To avoid any heat from the hydraulic fluid in the actuator system reaching the specimen, the lower platen was specially designed with a circulation system connected to a constant temperature bath kept inside the cold room.

The load was applied to the specimen within a fraction of second and then maintained constant until it was removed rapidly at the desired time. Axial and lateral strains were measured using MTS extensometers attached directly to the specimen surfaces (Fig. 2.2) using special seats and following a technique described by Sinha (1986). The strains were continuously measured during the entire loading/unloading period. The recovery of strains after unloading were recorded for a sufficiently long time until no changes could be detected within the error of measurements. The relative displacement between the top and the bottom platens was also recorded using the built-in actuator displacement gauge. Load cell output and the displacement output from all gauges were recorded separately, as a function of time, on strip chart recorders and a digital data logging system outside the cold room. The strip chart recordings provided a convenient method of monitoring the progress of a test. The relative displacement provided a measure of the average axial strain along the entire length of the test specimen during the loading phase, however, the built-in gauge could not provide any strain recovery curve after unloading. Fig. 2.3 shows a comparison of axial strains measured at the sample sides and the strain at the sample ends. For all the tests performed, the differences between the two sets of measurements were small. The differences between the two measurements indicated that the sample deformations were uniform, and bending in the sample, if any, were negligible.

An acoustic emission sensor was attached to the specimen and the microcracking activities were recorded using an AET-5000 system kept outside the cold room. Ice temperature was measured using a thermistor probe before and after each test.

2.3 Test results

Seventeen constant load tests were carried out. The details of the test results are presented below.

2.3.1 Time dependence of strains

A typical example of the time dependence of the axial strain, lateral strains and volumetric strain at 263 K is given in Fig. 2.4. Very similar to fresh water polycrystalline ice, sea ice also shows the three creep stage; primary, transitory and tertiary. The creep rate decreases with time until reaching a minimum value, and then increases with further deformation.

The deformation is highly anisotropic, which is primarily two dimensional. The strain along the columns, ϵ_3, was very small. However, the lateral strain ϵ_2 was significantly larger than the axial strain ϵ_1 during the tertiary stage. This observation is in agreement with previous constant displacement rate tests of Wang (1981) and constant stress/strain rate tests of Sinha (1989c) on sea ice, and constant load creep tests of Sinha (1989a) on fresh water ice. These observations are the indications of the fact that the microcracks formed during the deformation and that the geometry of the cracks were essentially two dimensional. Visual observations indicated the formation of the long and narrow cracks tending to be parallel to the long grain boundaries of the columnar grains.

The recovery curve after unloading shows small but measurable amount of delayed elastic strain. The delayed volumetric strain, associated with delayed elastic strain, is almost zero. The magnitude of the axial recovery strain at the time of unloading in the tertiary creep range (1.0 to 2.5% strain) is between 10 to 25 times higher than the axial elastic strain. The delayed elastic strain also shows significant anisotropy, the delayed elastic strain along the length of the columns of grains is much smaller than that in the other two directions. This anisotropy in terms of delayed elasticity, for non-cracking and negligible permanent strain was reported by Sinha (1989c). Similar observation was also made by Duval and Kalifa (1991) for oriented glacial ice.

The measurement of the lateral strains allows estimation of the volumetric strain as long as the deformation is not far from uniform; that is, for small strains. The volumetric strain is calculated as the sum of the three strains. A measurement of the volumetric strain provides the indications of the failure mechanism such as volume dilation.

Figure 2.5 to Fig. 2.12 show the time dependence of axial, lateral, and volu-

metric strains at different temperatures and stresses.

2.3.2 Stress dependence of strain and strain rate

The time dependence of axial strain at different stress levels at 263 K is given in Fig. 2.13. The results show that with the increase of the stress level, the time required to reach a given strain decreases. Fig. 2.14 shows the time dependence of axial strain rate at different stress levels at 263 K. The increase in stress increases the strain rate at a given time. The black square marker represents the time to the minimum strain rate for each stress. A straight line can be used to represent the time dependence of the minimum strain rate as illustrated by the broken line in Fig. 2.14. Similar test results for laboratory-made fresh water granular ice were presented by Mellor and Cole (1983).

Figures 2.15 and 2.16 show the time dependence of axial strain and axial strain rate at different stress levels respectively at 253 K. Figs. 2.17 and 2.18 show similar results at 243 K.

2.3.3 Temperature dependence of strain and strain rate

The time dependence of axial strain, volumetric strain, and axial strain rate at different temperatures for tests under a constant stress of 1.5 MPa are shown in Figs. 2.19, 2.20 and 2.21. It can be seen that in Figs. 2.19 and 2.20 that the time required to reach a given strain decreases significantly with the increase in temperature. The strain rate increases with the increase of temperature at a given time (Fig. 2.21). The black square marker represents the time to minimum strain rate for each temperature. The straight dash line in the Fig. 2.21 is a good representation of the time dependence of the minimum strain rate. Similar results are shown in Figs. 2.22, 2.23 and 2.24 at a stress level of 2.5 MPa.

The time dependence of axial strain and axial strain rate for stress 0.7 MPa at different temperatures are presented in Figs. 2.25 and 2.26, respectively. The increase in temperature decreases the time to a given strain (Fig. 2.25) and increases the strain rate at a given time (Fig. 2.26). Similar test results at other stress levels are presented in Figs. 2.27 and 2.28 for 1.0 MPa, and Figs. 2.29 and 2.30 for 2.0 MPa.

2.4 Analysis of test data

The basic information for the seventeen constant load creep tests are listed in Table 2.1 for stress, temperature, minimum strain rate, $\dot{\epsilon}_m$, time to minimum strain rate, t_m, and strain at minimum strain rate, ϵ_m.

Table 2.1 Information for constant load tests

Test no.	Stress MPa	Temp. ^0C	$\dot{\epsilon_m}$ $10^{-5}s^{-1}$	t_m s	ϵ_m
Test 1	0.67	-10.0	0.053	20430.0	0.0153
Test 2	0.82	-10.0	0.17	2320.0	0.0054
Test 3	0.99	-9.8	0.73	902.0	0.00844
Test 4	1.23	-10.0	1.50	172.0	0.00328
Test 5	1.48	-10.0	2.30	133.3	0.00376
Test 6	1.97	-10.1	7.25	16.0	0.00140
Test 7	2.47	-10.0	9.20	7.5	0.00054
Test 8	0.66	-19.5	0.018	25420.0	0.00665
Test 9	0.98	-19.6	0.275	1250.0	0.00428
Test 10	1.47	-19.7	0.8	303.0	0.0031
Test 11	2.02	-19.8	2.70	22.0	0.0009
Test 12	2.48	-20.0	3.47	12.33	0.00071
Test 13	0.71	-29.8	0.0019	121800.0	0.00364
Test 14	1.01	-29.6	0.0147	2335.0	0.00487
Test 15	1.47	-29.5	0.30	739.3	0.00263
Test 16	1.99	-29.6	1.0	35.0	0.00073
Test 17	2.47	-30.0	1.2	25.0	0.00062

2.4.1 Stress dependence of minimum strain rate

Minimum strain rate indicates the onset of failure because its occurrence signifies the onset of accelerating creep induced by the significant structural damage (Sinha, 1989a). Fig. 2.31 shows that there is a one to one correspondence as pointed out by Sinha et al. (1992) between the dependence of minimum strain rate on stress,

observed during the present creep tests at 263 K, and the dependence of maximum stress on strain rate in constant strain rate tests reported by Sinha (1984a) and Chen and Lee (1986) for similar first year columnar-grained sea ice. The same conclusion for columnar grained fresh water ice was drawn by Sinha (1981b), and for isotropic fresh water granular ice was reached by (Mellor and Cole, 1982, 1983, and Cole, 1983). The solid line in Fig. 2.31 represents the relationship, between maximum stress and the imposed strain rate, proposed by Sinha (1984a).

$$\sigma_f = 45\dot{\epsilon}^{0.32} \tag{2.1}$$

where σ_f is the maximum stress in MPa; $\dot{\epsilon}$ is the average strain rate up to the maximum stress.

It must be mentioned that Sinha's (1984a) tests were carried out in the field (Mould Bay, Prince Patrick Island, Canada) on freshly sampled sea ice, and the specimens were similar in size to the sample used in the present creep tests. The strain rate in Eq. 2.1 represents the average value up to the peak stress and was obtained using the gauges mounted on the specimens. Chen and Lee (1986), however, conducted their tests on in situ, full thickness ice blocks with dimensions of about $2.0m \times 3.05m \times 6.1m$ under closed loop controlled tests. These large scale tests were carried out in the landfast ice, north of Alaska.

Figure 2.32 shows the stress dependence of minimum strain rate at 253 K. With the increase of stress, the minimum strain rate increases. Similar result is presented in Fig. 2.33 for a temperature 243 K.

2.4.2 Stress dependence of time to minimum strain rate

The stress dependence of time t_m is shown in Fig. 2.34 for temperature 263 K. With the increase of stress, the time to minimum strain rate decreases. The stress dependence of t_m can be represented by the following equation.

$$t_m = 1014(\frac{\sigma}{\sigma_1})^{-5.84} \tag{2.2}$$

where $\sigma_1 = 1.0MPa$ is a reference stress; the time t_m is in seconds.

Figures 2.35 and 2.36 present the stress dependence of t_m at temperatures 253 and 243 K, respectively. Similarly, the relationships between t_m and stress can be given by the following equations at temperature 253 and 243 K, respectively.

$$\begin{aligned} t_m &= 1834(\frac{\sigma}{\sigma_1})^{-5.74} \\ t_m &= 13000(\frac{\sigma}{\sigma_1})^{-7.47} \end{aligned} \tag{2.3}$$

The powers in Eqs. 2.2 and 2.3 are much higher than the power about 2.48 obtained by Sinha (1984a) for columnar grained sea ice in constant displacement rate tests.

The stress and temperature dependence of t_m is presented in Fig. 2.37. The decrease in temperature tends to increase the time to minimum strain rate or failure.

2.4.3 Stress dependence of strain at minimum strain rate

The stress dependence of strain at minimum strain rate is shown in Fig. 2.38 at a temperature 263 K. This figure shows that strains at minimum strain rate decrease with increase in stress. Similar results are also obtained at temperature 253 K and 243 K, respectively, and shown in Figs. 2.39 and 2.40. This decreasing ductility with the increase of stress or rate of loading was noticed by Sinha (1983b) for first year columnar grained sea ice loaded normal to the length of the columns of grains under constant strain rate tests. However, this observation is in contrary to the stress dependence of strain at failure in constant displacement rate test reported by Sinha (1984a) for first year columnar grained sea ice loaded normal to the long axis of grains. The constant load test on granular ice by Mellor and Cole (1982, 1983) shows negligible stress dependence of the strain at minimum strain rate, although the strain is scattered between 0.6 to 1.2 %. Fig. 2.41 presents the comparison of the rate dependence of strain at failure between present creep study for columnar grained sea ice and the constant displacement rate test results of Sinha (1982) on fresh water columnar-grained ice. The figure shows that the

columnar-grained sea ice is more ductile than the fresh water columnar-grained ice.

Although the stress dependence of strain at minimum strain rate is significant, the strain at minimum strain rate has little dependence on temperature as can be seen in Fig. 2.42.

2.4.4 Recovery strain

The recovery strain is defined as the axial strain recovered after unloading, which includes elastic and delayed elastic strains. Fig. 2.43 presents the time dependence of the recovery strains at 263 K at different stress levels. In general, all of these curves show that the recovery strain increases with the increase of time and approaches a constant value at infinite time. The difference among these curves is that the magnitude of the recovery strain is higher for higher stress.

If the delayed elastic strain has the same time dependence under different stress levels and is linearly dependent on stress, it would be expected that the normalized recovery strain, defined as the recovery strain multiplied by a stress ratio $\frac{\sigma_1}{\sigma}$, will be the same at different stress levels. Fig. 2.44 presents the time dependence of the normalized recovery strain at temperature 263 K. Although the results are scattered in this figure, the stress dependence of the normalized recovery strain is very small, if any.

Similar results on the time dependence of recovery strain and the normalized recovery strain are presented in Figs. 2.45 and 2.46 respectively at temperature 253 K, and in Figs. 2.47 and 2.48 respectively at temperature 243 K.

The time dependence of recovery strain for stress 0.7 MPa at different temperatures is shown in Fig. 2.49. This figure shows that the recovery strain increases with the increase of time and approaches a constant value. In general, the rate to reach the constant value increases with the increase of temperature. Similar results are obtained at stress level 1.0, 1.5, 2.0 and 2.5 MPa as shown in Figs. 2.50, 2.51, 2.52 and 2.53, accordingly.

The total recovery strain was obtained, when the change in strain is almost zero after unloading for a long time. The stress dependence of the total recovery strain is plotted in Fig. 2.54. With the increase of stress, the total recovery strain

increases. While, the temperature has a negligible effect on the stress dependence of the total recovery strain.

If the Young's modulus for sea ice is assumed as 9.0 GPa (Sinha, 1989b), the ratio between the total recovery strain ϵ_r the elastic strain ϵ_e can be obtained. Fig. 2.55 presents the stress dependence of the ratio $\frac{\epsilon_r}{\epsilon_e}$ at different temperatures. This figure shows that the total recovery strain is about 10 to 25 times higher than the elastic strain depending upon the stress level.

The total recovery strains developed during the creep tests are related to the loading histories. If the recovery time after unloading is long enough, when no change in delayed elasticity can be detected, the measured total recovery strain gives a measure of the delayed elastic strain developed during loading. Since the loading times were not the same, consideration should be given not only to the stress but also to the loading history. The loading time dependence of $\frac{\epsilon_r}{\epsilon_e}$ is presented in Fig. 2.56. It is clearly shown that the ratio $\frac{\epsilon_r}{\epsilon_e}$ increases with the loading time. The three solid lines represent the theoretical prediction of the time dependence of $\frac{\epsilon_r}{\epsilon_e}$ with Sinha's model (1979a) (see Eq. 6.1 in Chapter 6) for a grain size 0.4 mm and at temperatures 263, 253, and 243 K. In general, Sinha's model gives a better prediction at longer time (lower stress) than that at a shorter time (higher stress). This larger difference between model prediction and the test data at higher stress could be due to enhancement of delayed elastic strain by crack activities.

2.4.5 Determination of apparent activation energy

The stress and temperature dependence of minimum creep rate for polycrystalline materials at elevated temperature, in general, can be given by

$$\dot{\epsilon}_m \propto exp(-\frac{Q}{RT})(\frac{\sigma}{\sigma_1})^n \tag{2.4}$$

where σ_1 is a reference stress; n is the stress exponent; Q is the apparent creep activation energy; R is the universal gas constant; T is temperature.

If the minimum strain rates at two different temperature T_1 and T_2 for a given stress are known, the apparent activation energy can be obtained from Eq. 2.3 as

$$Q = \frac{RT_1T_2}{T_1 - T_2} ln(\frac{\dot{\epsilon}_{m1}}{\dot{\epsilon}_{m2}}) \tag{2.5}$$

where $\dot{\epsilon}_{m1}$ and $\dot{\epsilon}_{m2}$ are minimum strain rate at temperature T_1 and T_2, respectively.

The apparent activation energy for minimum creep rate determined from the present test results in the temperature range 263 K and 253 K, and 253 K and 243 K are presented in Fig. 2.57 in terms of the applied stress; the lines are drawn to show a general trend in the two data sets. For temperatures between 263 K and 253 K, the apparent activation energy has a negligible dependence on stress in the range studied (0.7 to 2.5 MPa). At low temperatures between 253 K and 243 K, however, the apparent activation energy decreases rapidly with the increase of stress level at low stresses and approaches a constant value at stress levels higher than about 1.5 MPa. Note that the two lines crosses each other; the apparent activation energy at higher temperature is higher than that at lower temperature with stress level higher than about 1.5 MPa. A theoretical prediction of the apparent activation energy for the first crack given by Sinha (1984b) shows similar stress and temperature dependence of apparent activation energy.

It should be mentioned that the apparent activation energy obtained here are similar to the values reported for fresh water columnar-grained ice reported by Ramseier (1972) and Gold (1972b). This similarity of the apparent activation energy between the columnar grained fresh water ice and columnar-grained sea ice shows that the presence of brine in sea ice does not significantly affect the apparent activation energy.

2.4.6 Effective modulus and strain ratio

In viscoelastic analysis, the time dependence of the effective modulus and Poisson's ratio are the very basic material properties. The effective modulus for a uniaxial constant stress test is defined as the ratio between stress and the axial strain. The strain ratio is defined as the ratio between lateral strains and axial strain.

The time dependence of the effective modulus at 263 K at different stress levels is presented in Fig. 2.58. Overall, the effective modulus decreases with the increase

of time. However, the time dependence of the effective modulus becomes more pronounced at higher stress level. This clearly shows that sea ice as a material can not be treated as a linear viscoelastic material. Similar results at temperature 253 and 243 K are presented in Figs. 2.59 and 2.60, respectively.

The time dependence of strain ratios is presented in Fig. 2.61 for stress 2.0 MPa and temperature 253 K. The upper line represents the strain ratio $\frac{\epsilon_3}{\epsilon_1}$. The lower curve represents $\frac{\epsilon_3}{\epsilon_1}$. It shows that the strain ratio $\frac{\epsilon_3}{\epsilon_1}$ increases with time, while the strain ratio $\frac{\epsilon_3}{\epsilon_1}$ decreases with time. Columnar-grained sea ice, therefore, is highly anisotropic; the deformation is essentially two dimensional as discussed earlier in Section 2.3.1. Similar result for stress 2.0 MPa and at temperature 263 K and 243 K are presented in Figs. 2.62 and 2.63, respectively.

2.4.7 Cracking activities

The acoustic emission data were recorded using AET-5000. The time dependence of the event number for stress 1.0 MPa at temperature 263 K is presented in Fig. 2.64. The rate of event number is shown in Fig. 2.65. In general, the acoustic emission rate decreases with the increase of time. Similar results are shown in Figs. 2.66 and 2.67 for stress 0.7 MPa and temperature 263 K. Figs. 2.68 and 2.69 show the time dependence of event number and rate of the events for stress 2.0 MPa and temperature 263 K. These figures show that an increase in stress level increases the cracking activity.

The microstructure studies of ice after the creep tests were carried out by making thin sections. The orientation of the cracks is shown in Fig. 2.70 for a tested ice sample at a stress 2.5 MPa and temperature 253 K. This figure shows that the majority of cracks are parallel to the loading axis. Similar conclusion was made by Gold (1972) and Sinha (1982) on fresh water columnar grained S2 ice.

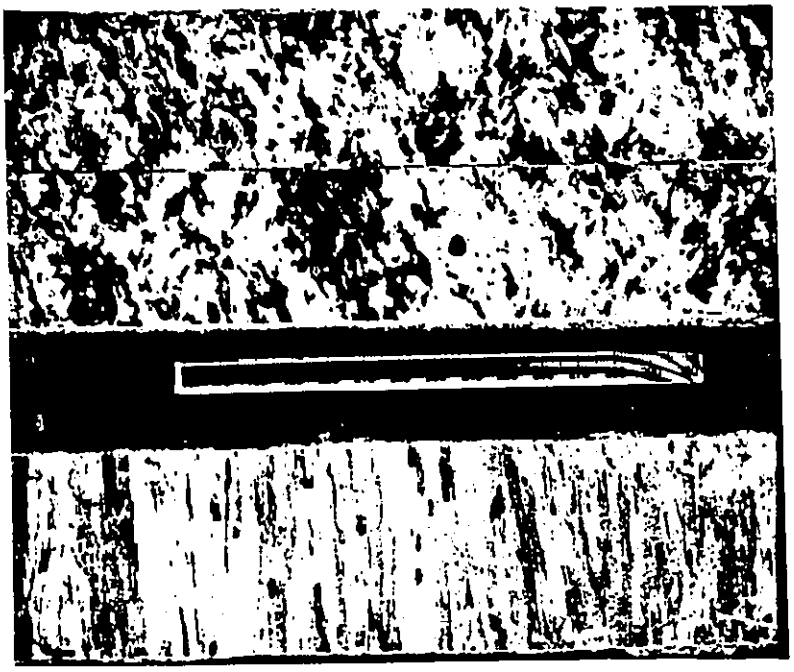

Figure 2.1 Horizontal and vertical thin sections for FY columnar grained sea ice

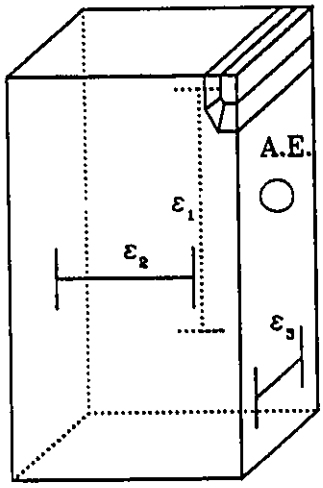

Figure 2.2 Locations of MTS strain guages and acoustic emission detector

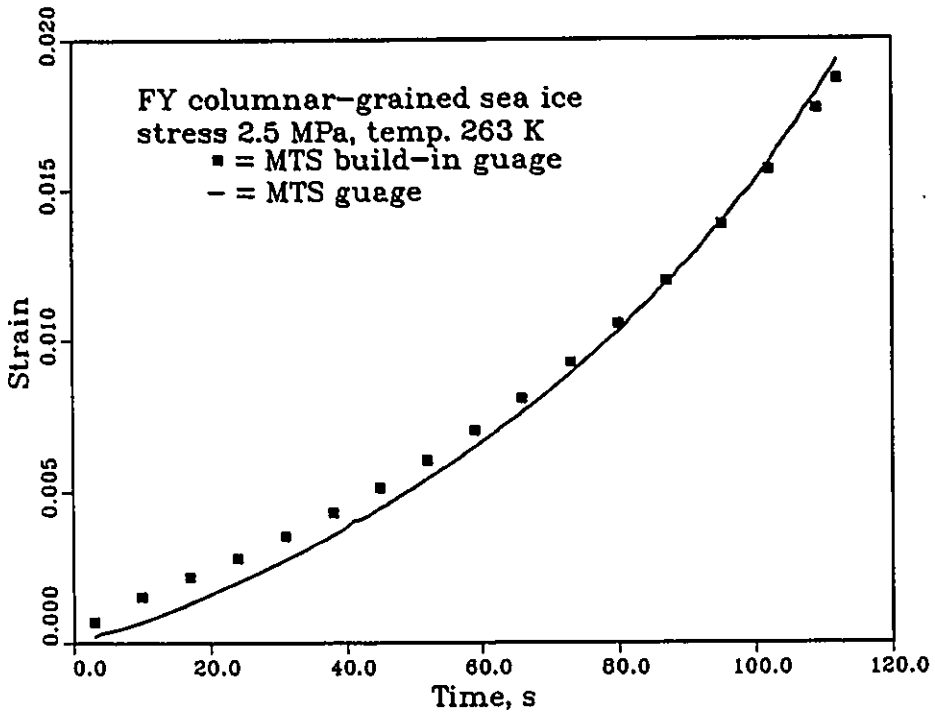

Figure 2.3 Comparisons of strain measurements between MTS build–in guage and MTS strain gauge attched to ice sample

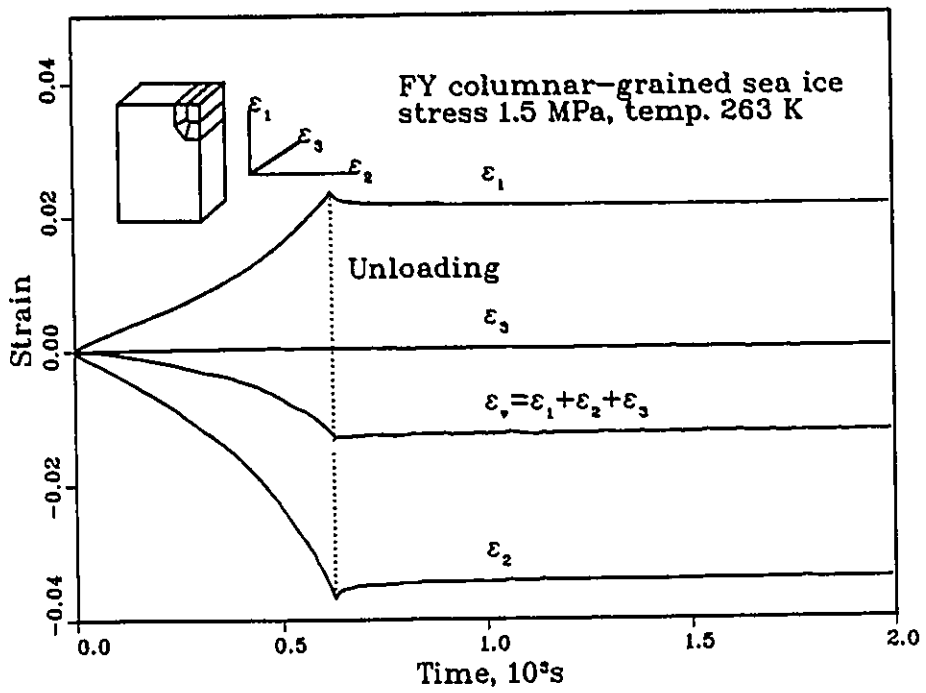

Figure 2.4 Time dependence of strains for FY columnar grained sea ice loaded normal to long columns

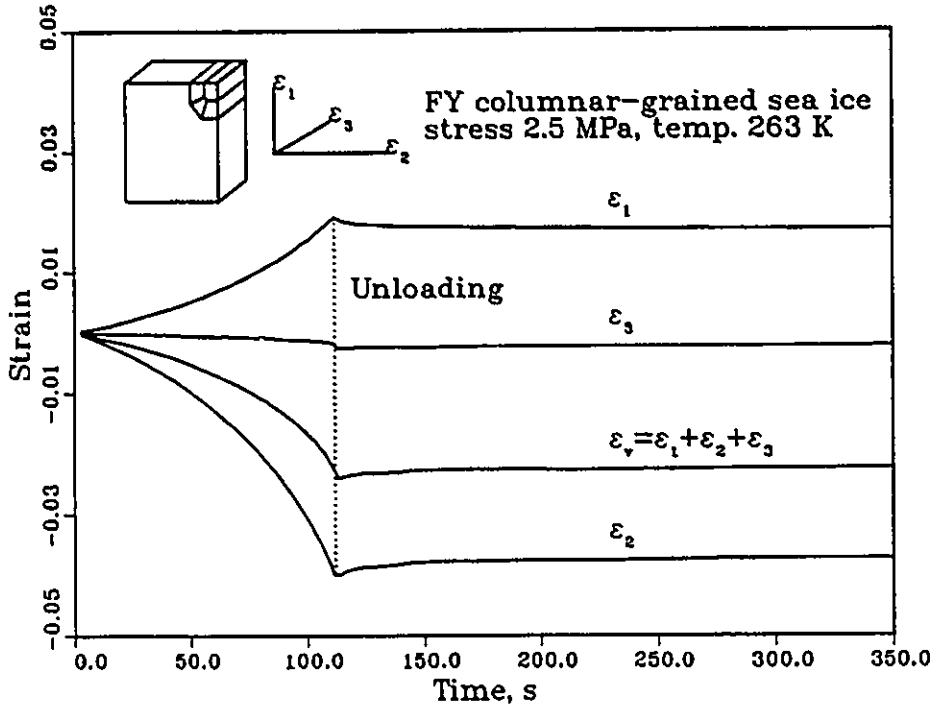

Figure 2.5 Time dependence of strains for FY columnar grained sea ice loaded normal to long columns

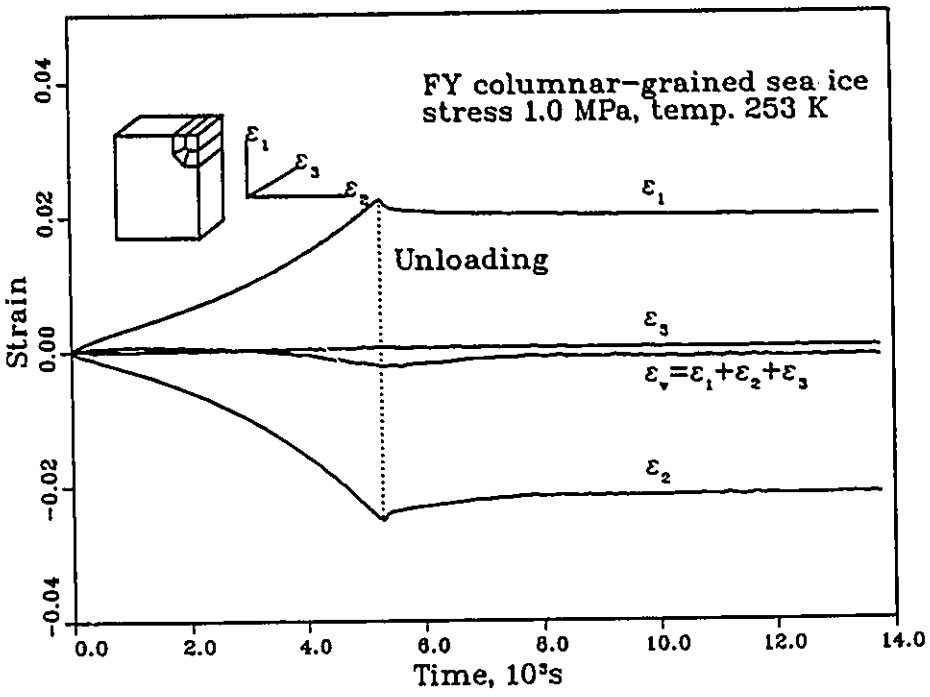

Figure 2.6 Time dependence of strains for FY columnar grained sea ice loaded normal to long columns

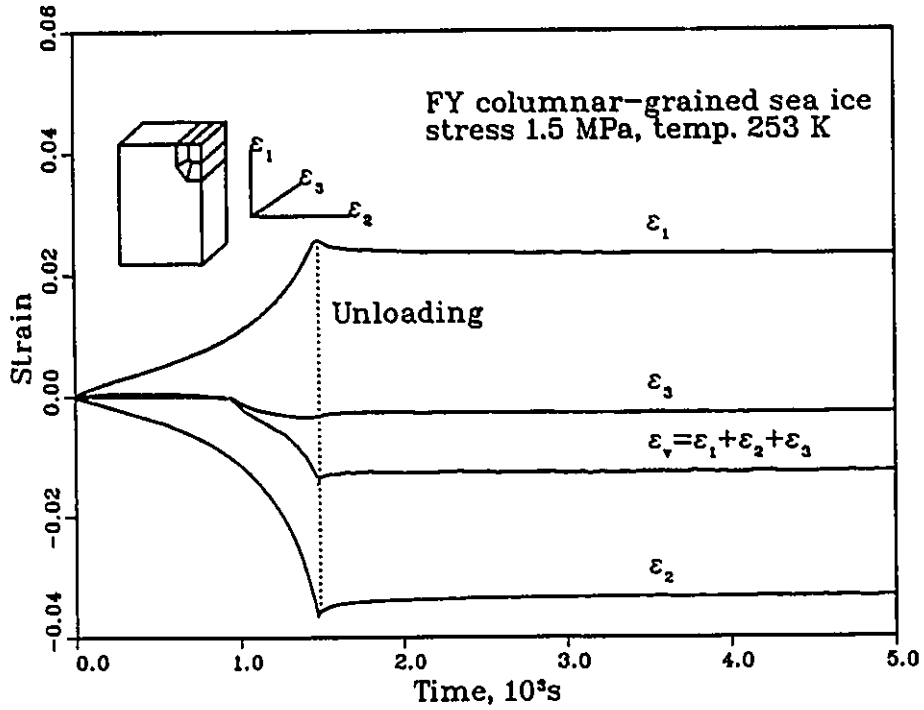

Figure 2.7 Time dependence of strains for FY columnar grained sea ice loaded normal to long columns

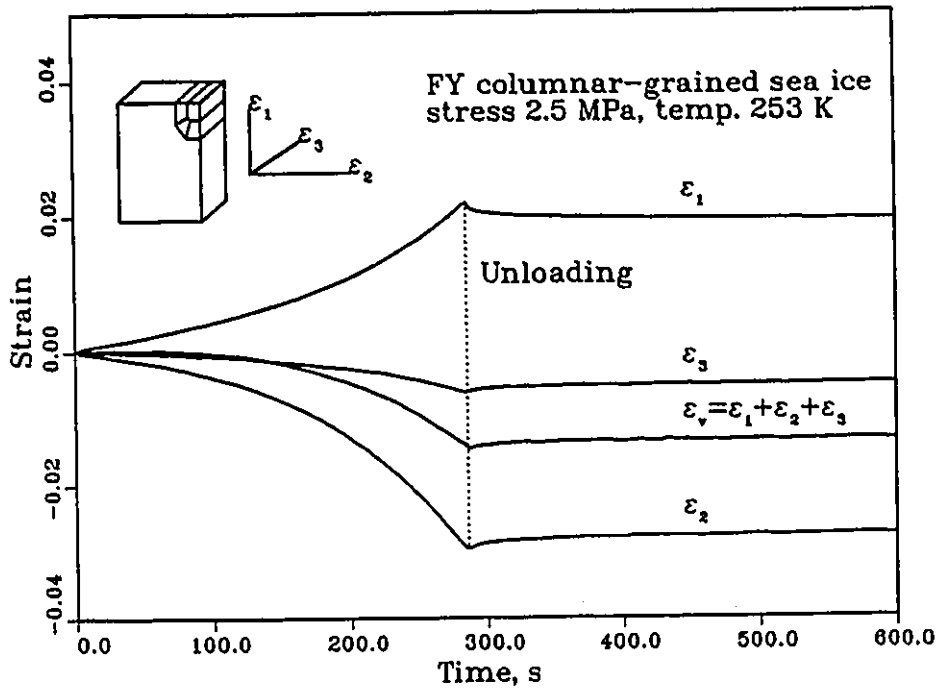

Figure 2.8 Time dependence of strains for FY columnar grained sea ice loaded normal to long columns

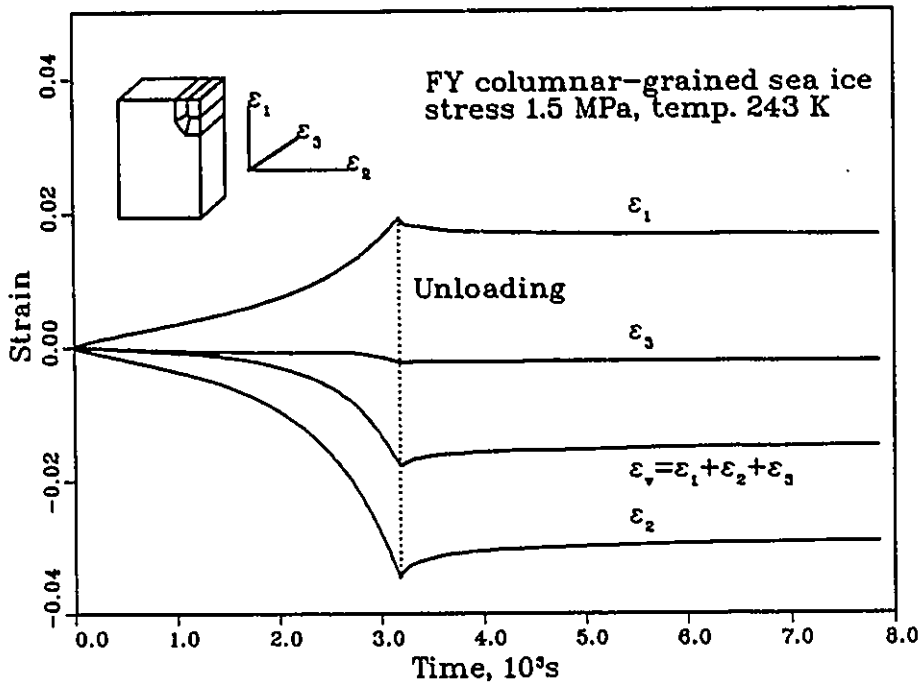

Figure 2.9 Time dependence of strains for FY columnar grained sea ice loaded normal to long columns

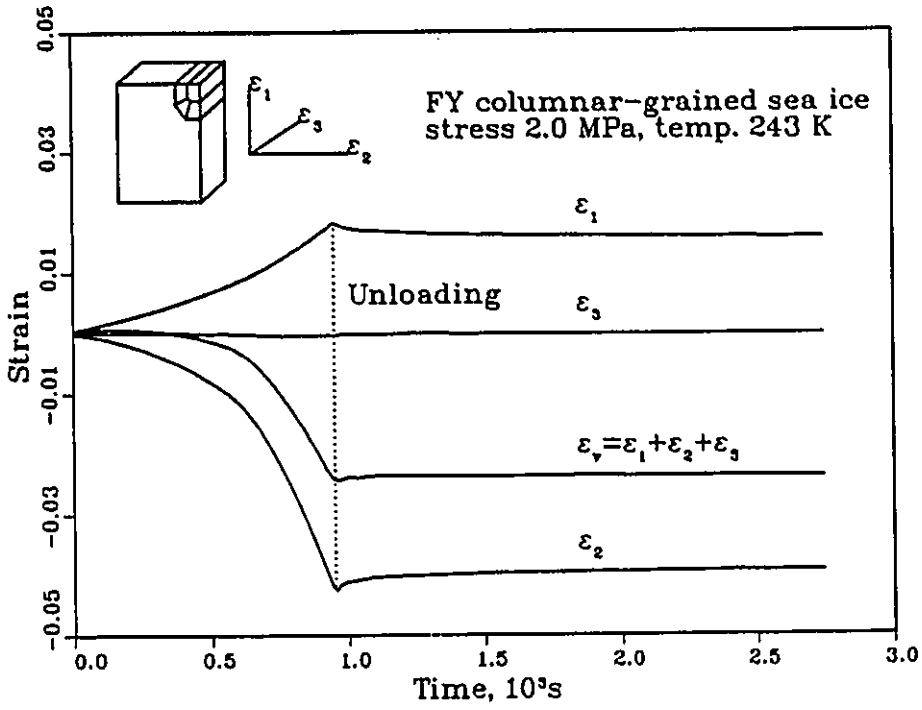

Figure 2.10 Time dependence of strains for FY columnar grained sea ice loaded normal to long columns

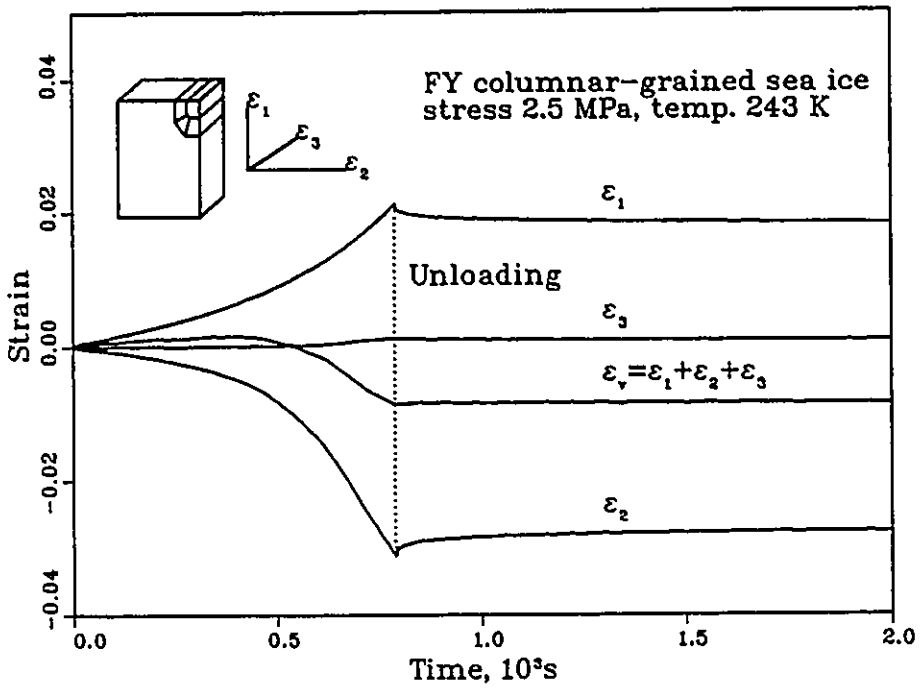

Figure 2.11 Time dependence of strains for FY columnar grained sea ice loaded normal to long columns

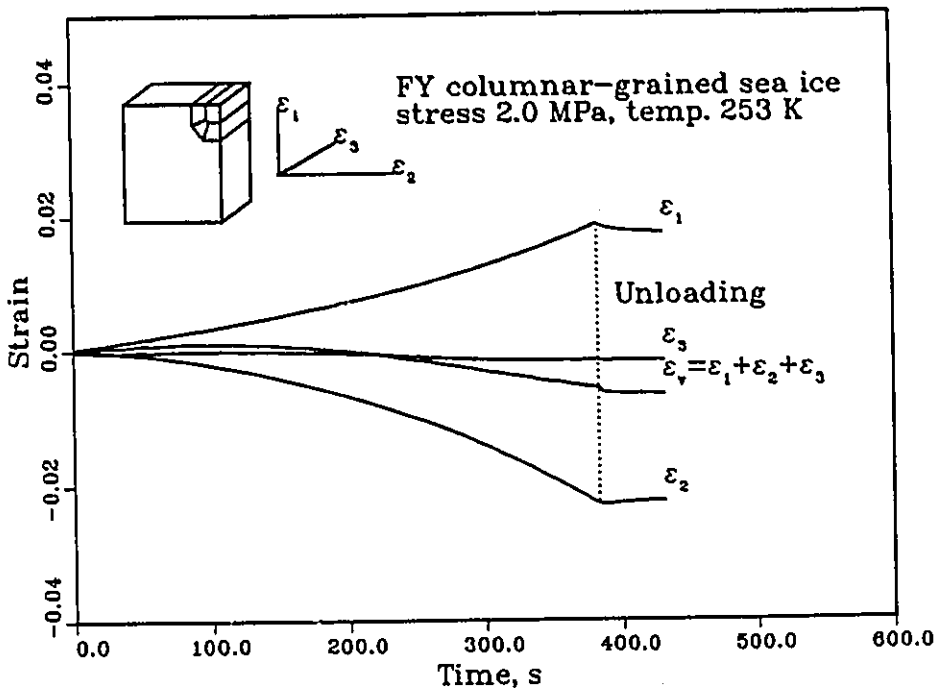

Figure 2.12 Time dependence of strains for FY columnar grained sea ice loaded normal to long columns

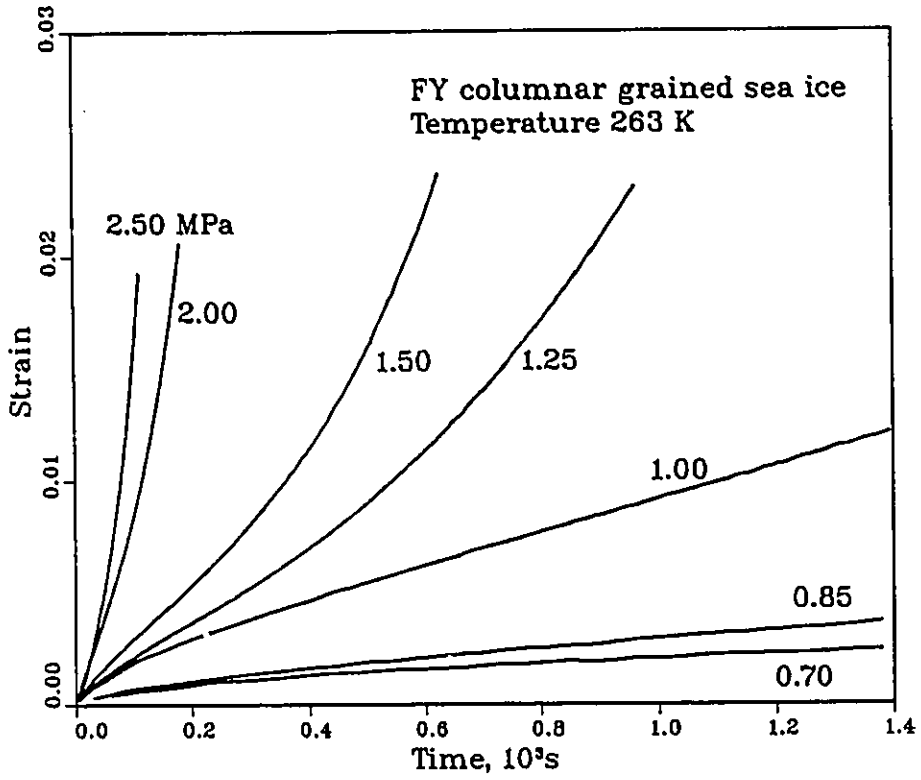

Figure 2.13 Time dependence of axial strains for FY columnar-grained sea ice under constant load applied normal to columns

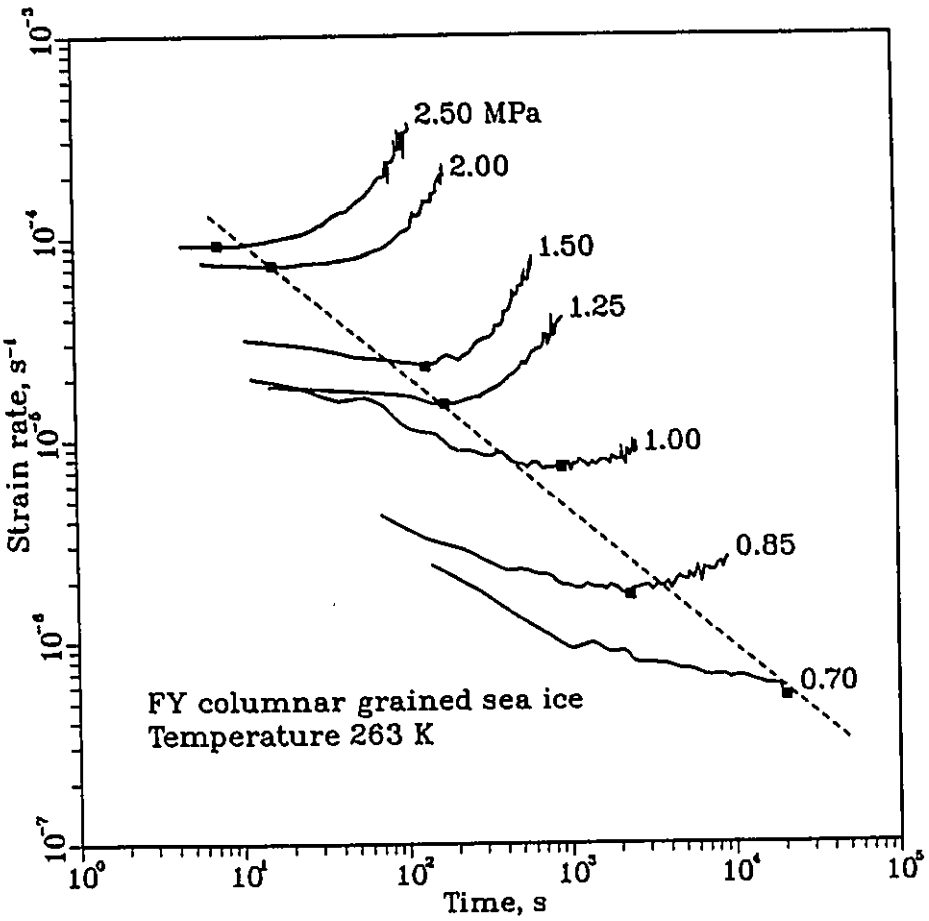

Figure 2.14 Time dependence of axial strain rate for FY columnar–grained sea ice under constant load applied normal to columns

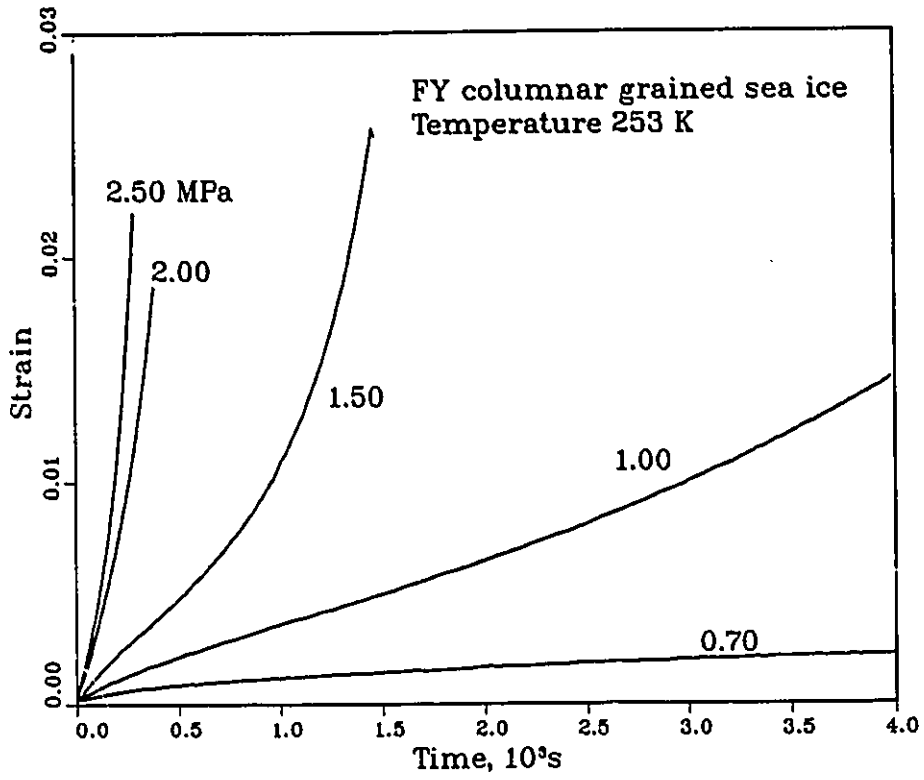

Figure 2.15 Time dependence of axial strain for FY columnar-grained sea ice under constant load applied normal to columns

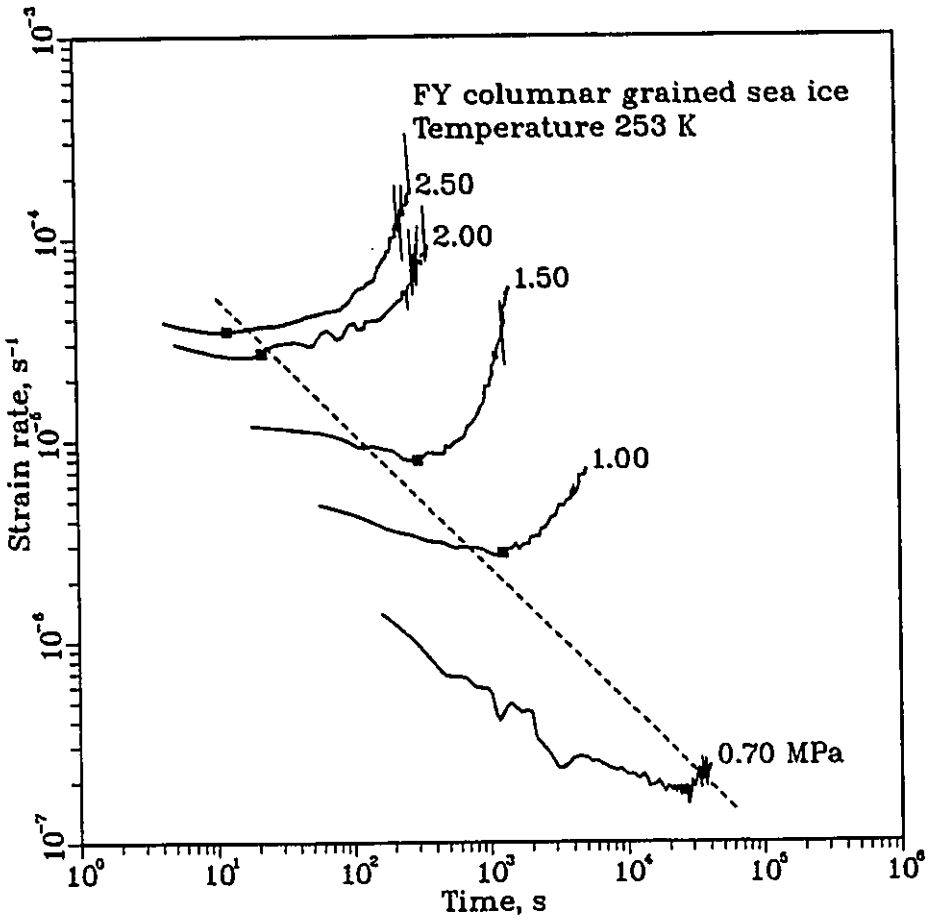

Figure 2.16 Time dependence of axial strain rate for FY columnar–grained sea ice under constant load applied normal to columns

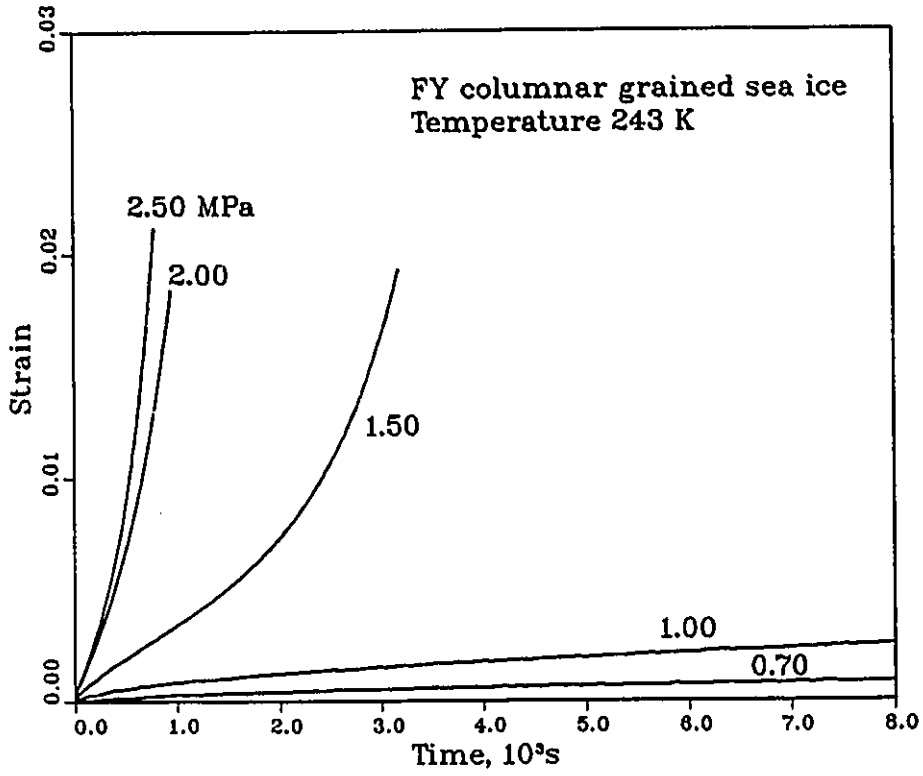

Figure 2.17 Time dependence of axial strain for FY columnar–grained sea ice under constant load applied normal to columns

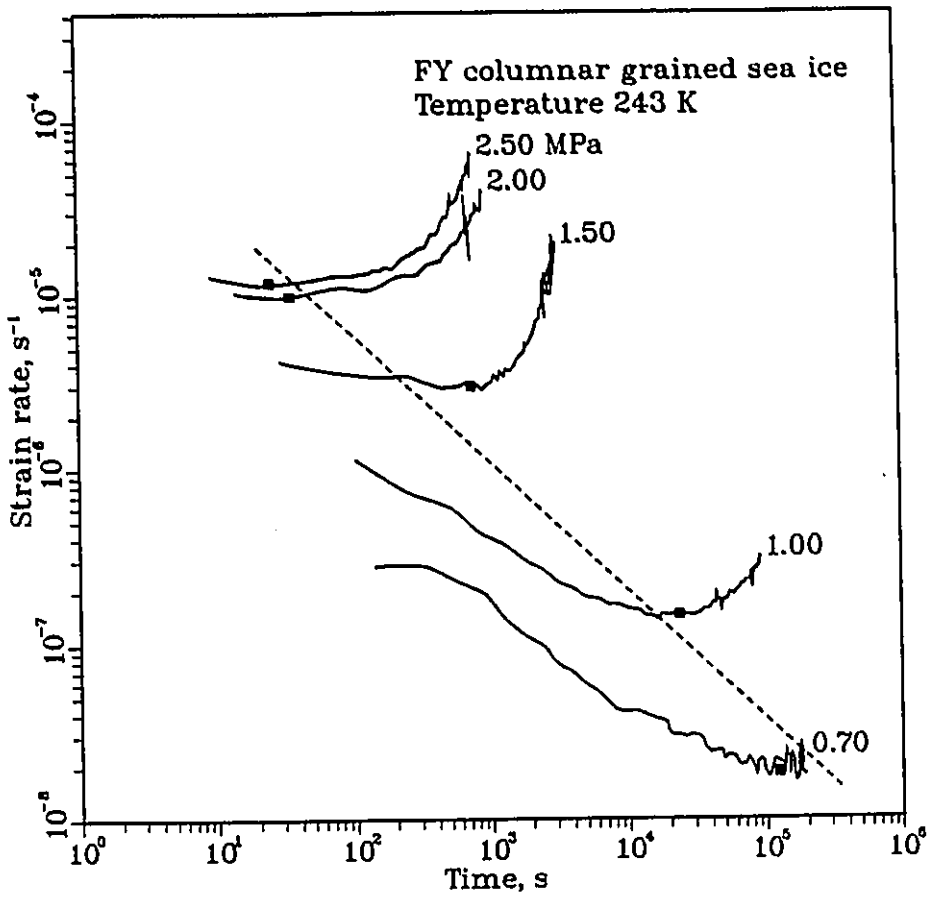

Figure 2.18 Time dependence of axial strain rate for FY columnar–grained sea ice under constant load applied normal to columns at different stress levels and at temperature 243 k

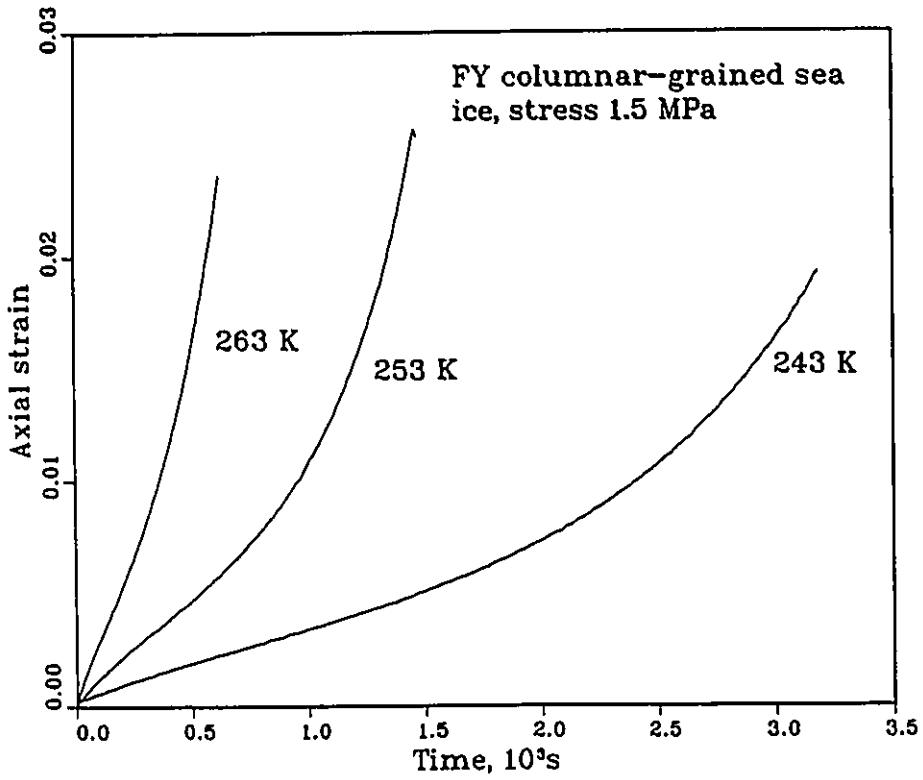

Figure 2.19 Time dependence of axial strains at different temperatures in constant load test at stress level 1.5 MPa

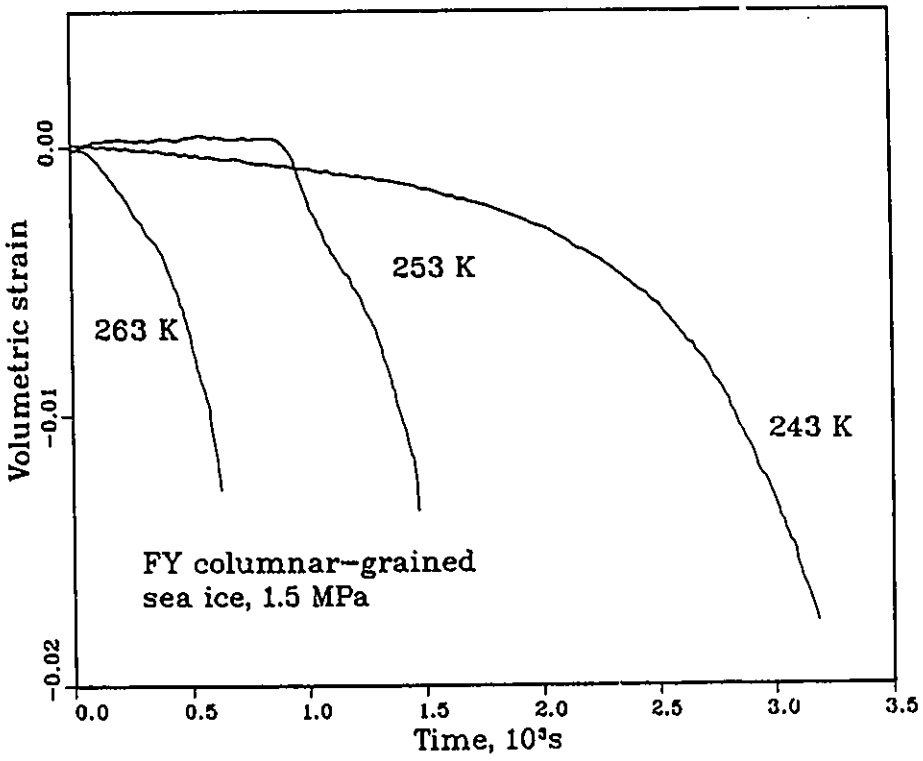

Figure 2.20 Time dependence of volumetric strains at different temperatures in constant load test at stress level 1.5 MPa

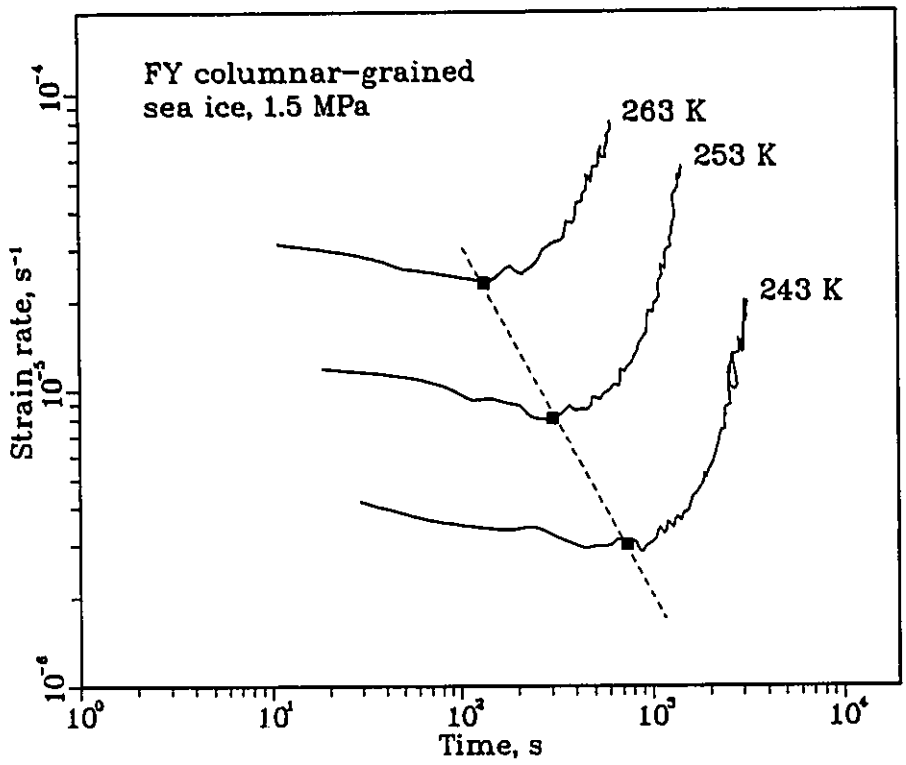

Figure 2.21 Time dependence of axial strain rate at different temperatures in constant load test at stress level 1.5 MPa

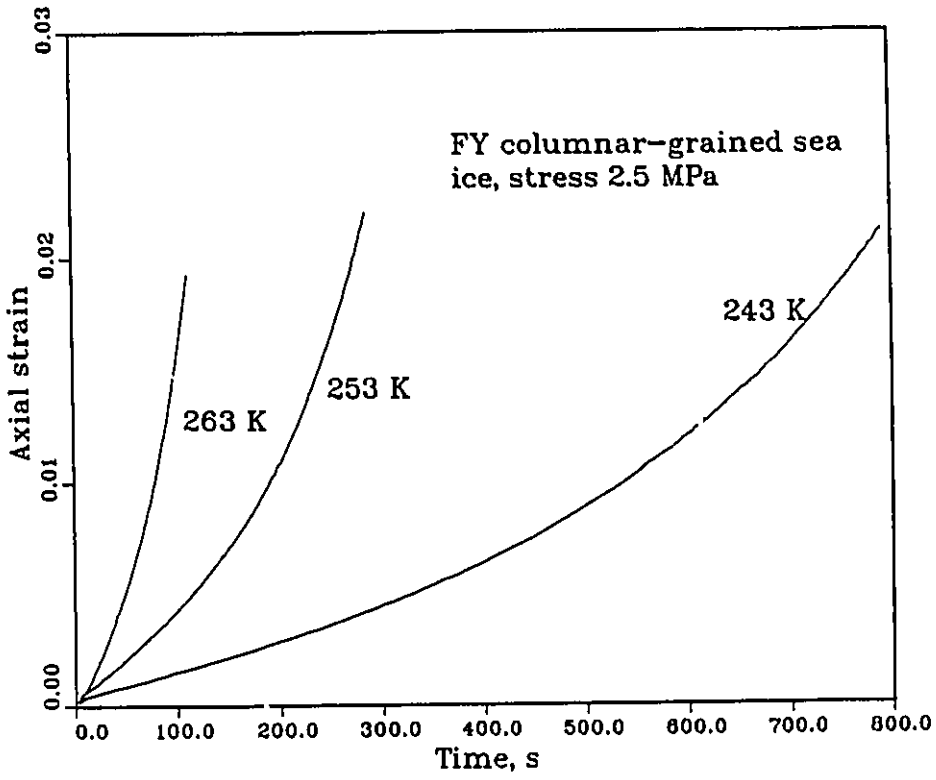

Figure 2.22 Time dependence of axial strains at different temperatures in constant load test at stress level 2.5 MPa

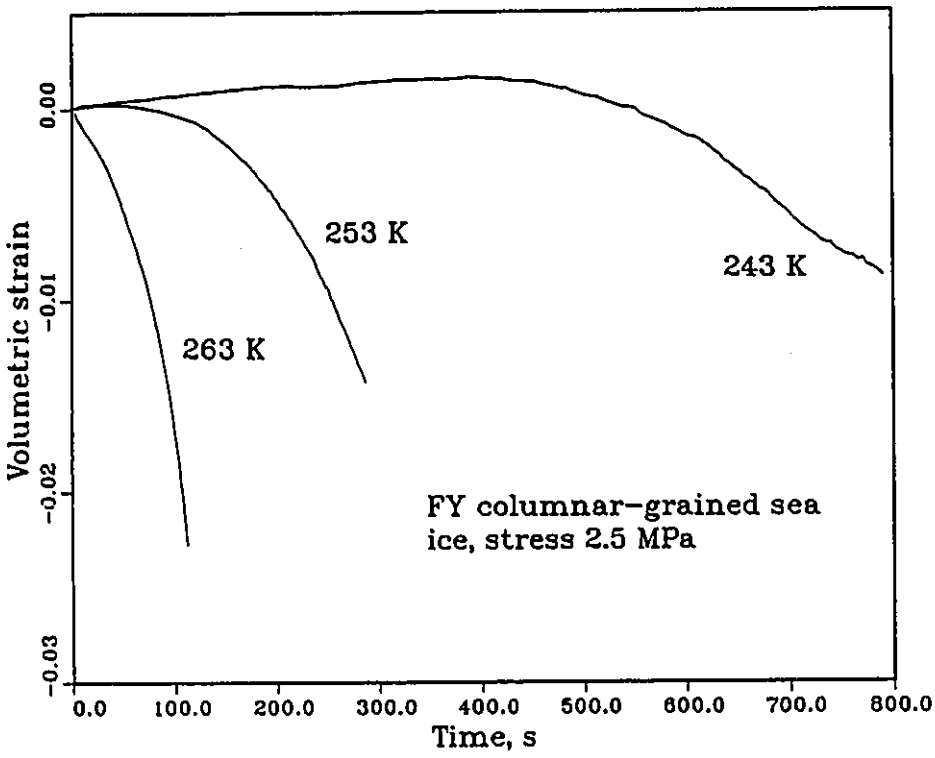

Figure 2.23 Time dependence of volumetric strains at different temperatures in constant load test at stress level 2.5 MPa

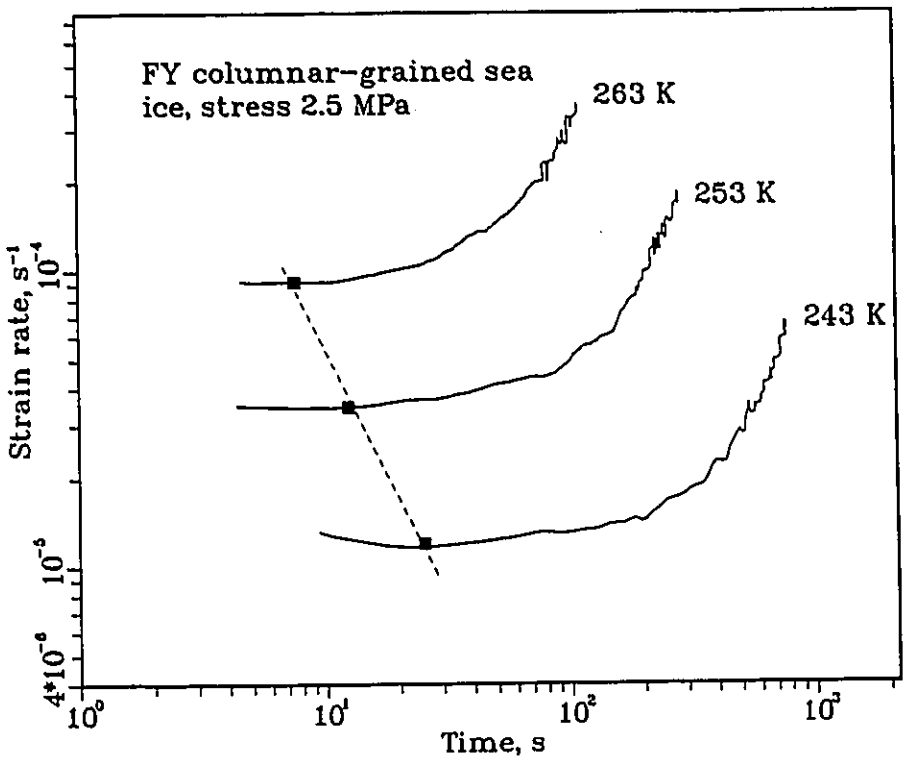

Figure 2.24 Time dependence of axial strain rate at different temperatures in constant load test at stress level 2.5 MPa

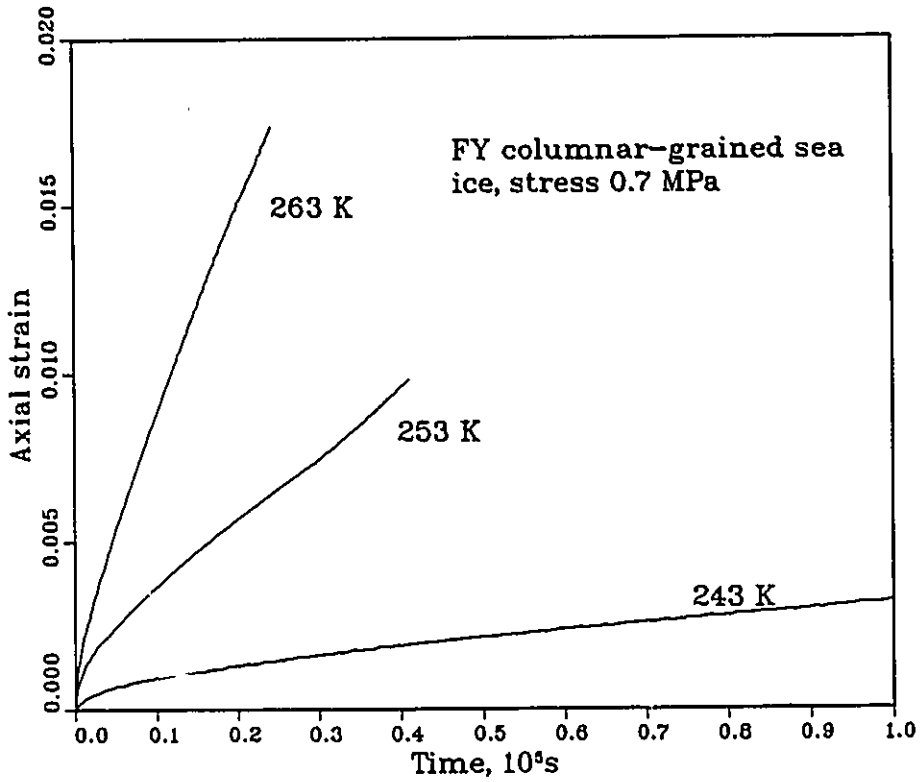

Figure 2.25 Time dependence of axial strains at different temperatures in constant load test at stress level 0.7 MPa

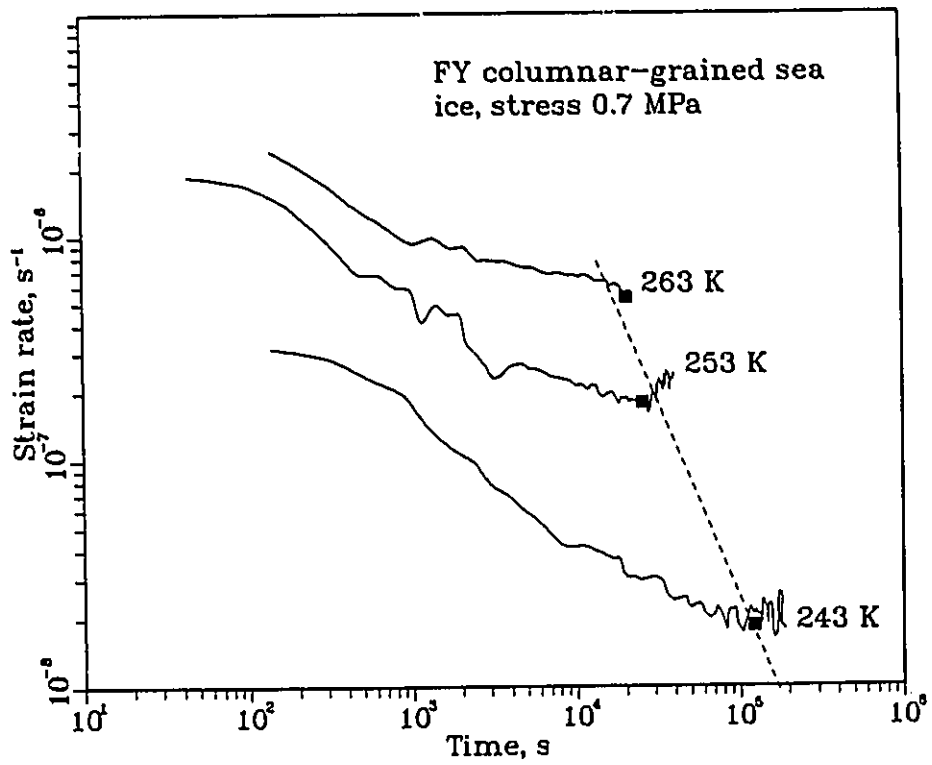

Figure 2.26 Time dependence of axial strain rate at different temperatures in constant load test at stress level 0.7 MPa

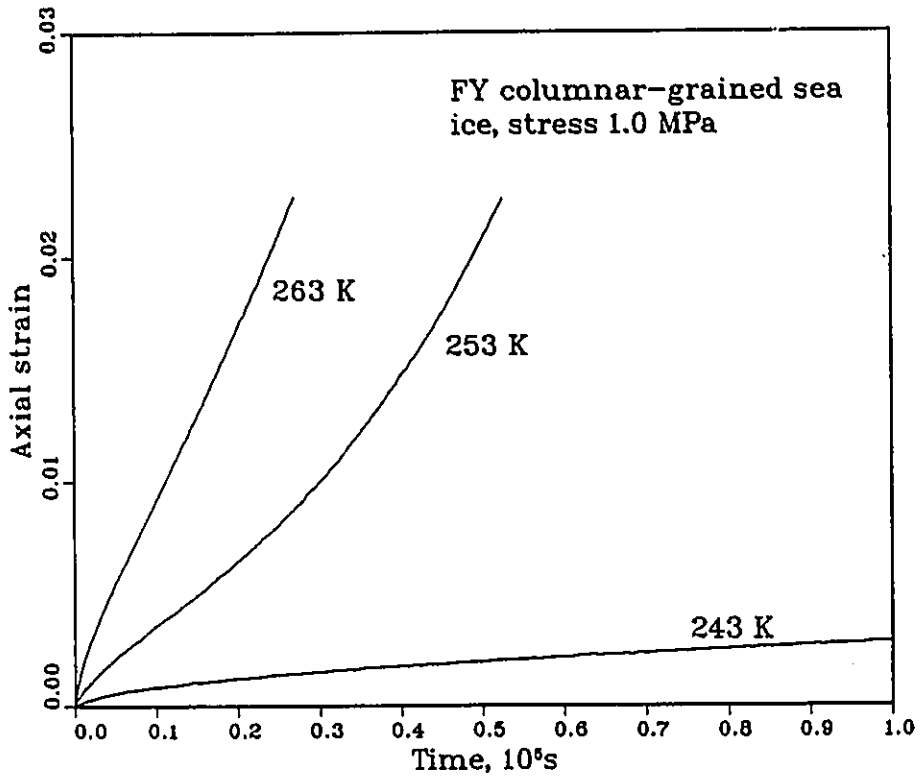

Figure 2.27 Time dependence of axial strains at different temperatures in constant load test at stress level 1.0 MPa

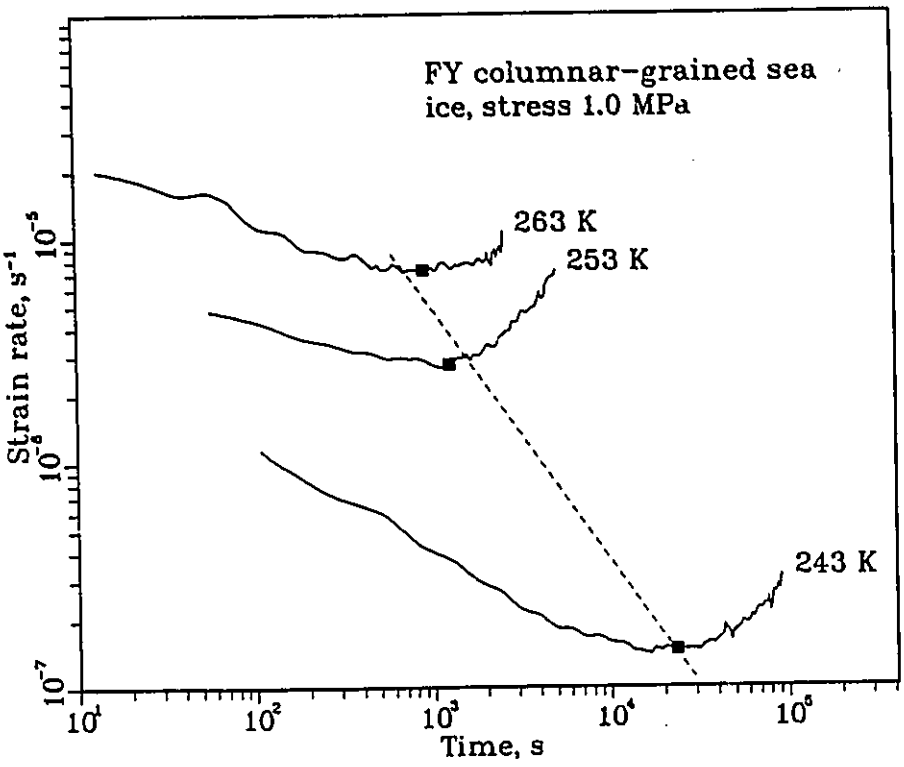

Figure 2.28 Time dependence of axial strain rate at different temperatures in constant load test at stress level 1.0 MPa

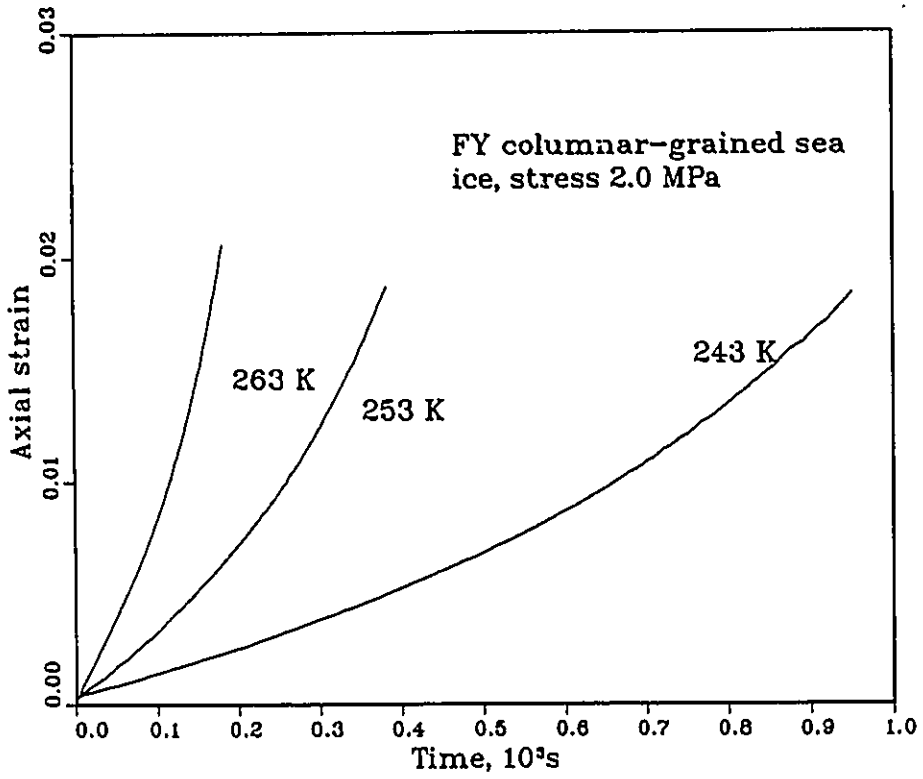

Figure 2.29 Time dependence of axial strains at different temperatures in constant load test at stress level 2.0 MPa

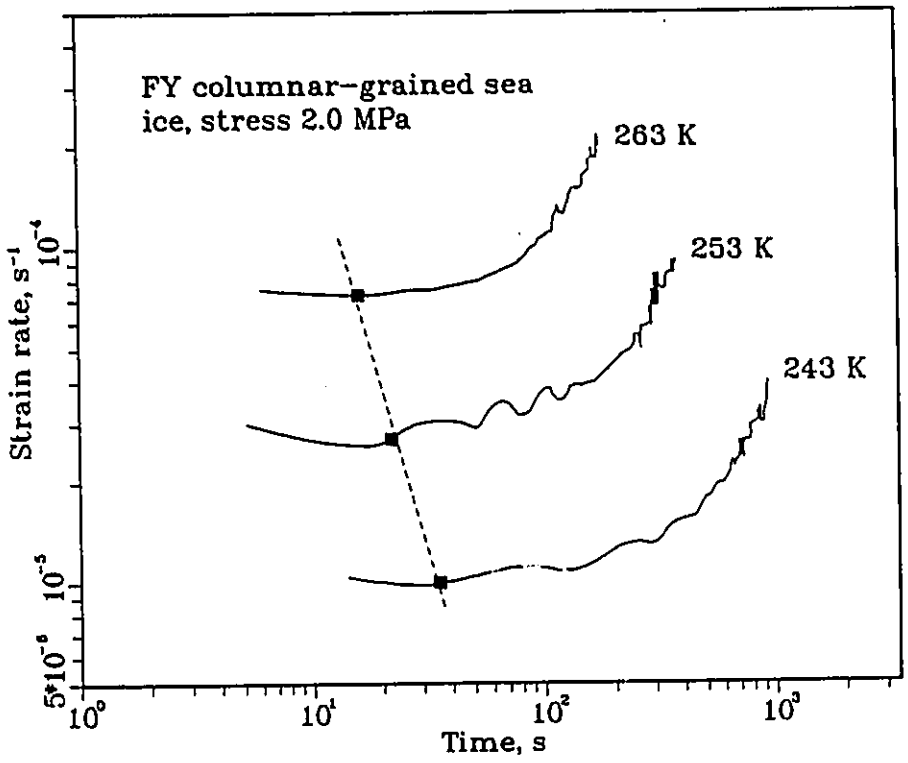

Figure 2.30 Time dependence of axial strain rate at different temperatures in constant load test at stress level 2.0 MPa

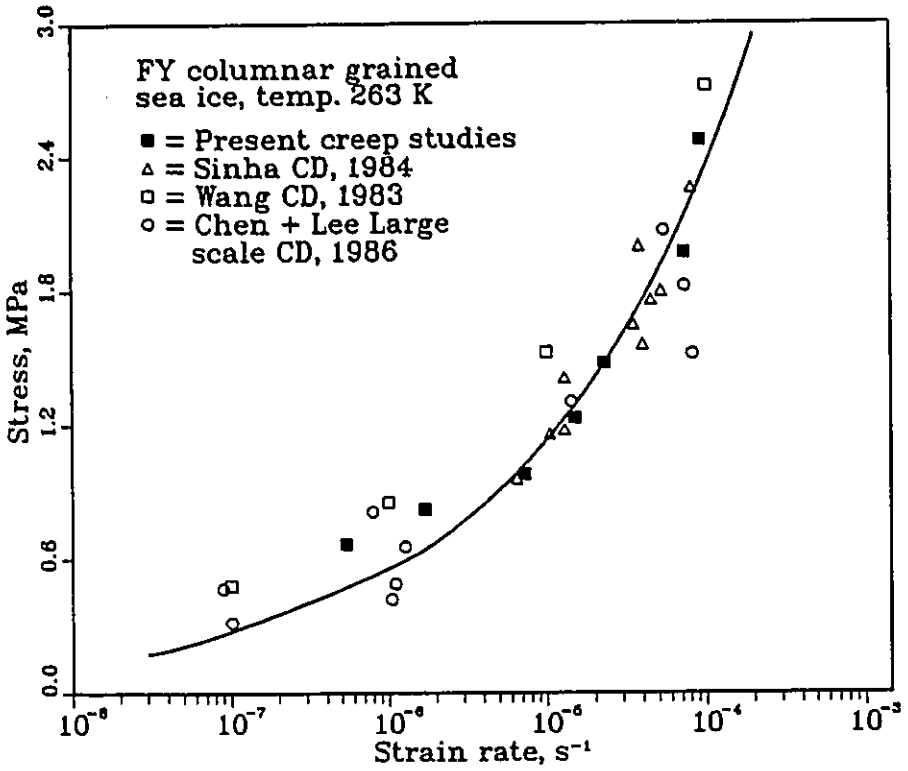

Figure 2.31 Interdependence between minimun strain rate and stress in CS test and maximun stress and strain rate in CD test

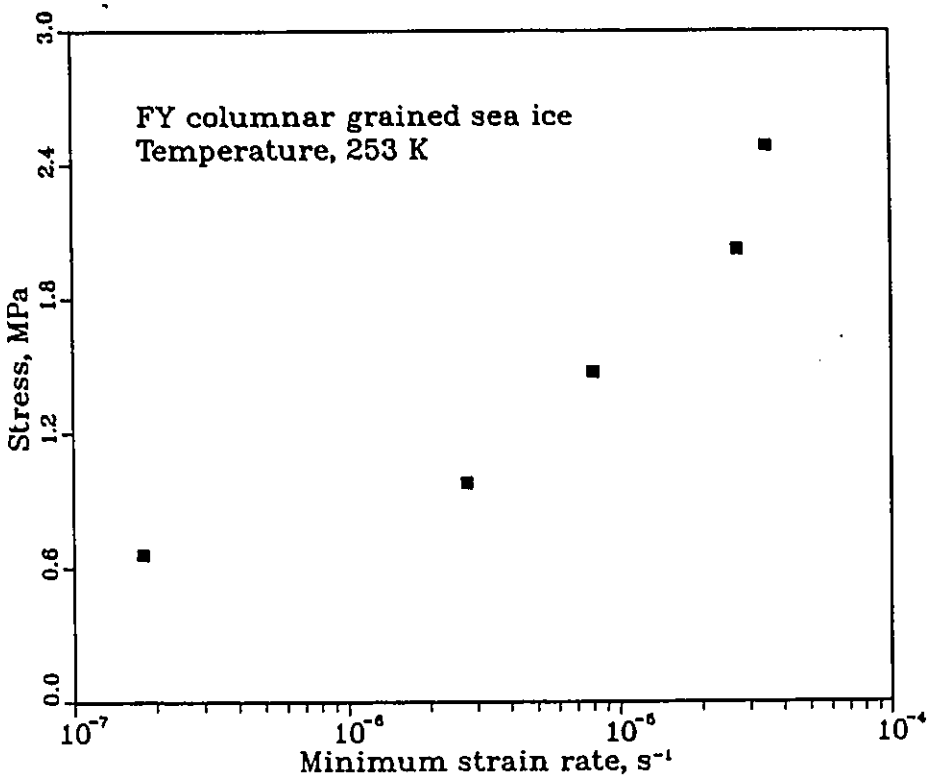

Figure 2.32 Stress dependence of minimum strain rate in constant load test for FY columnar grained sea ice at 253 K

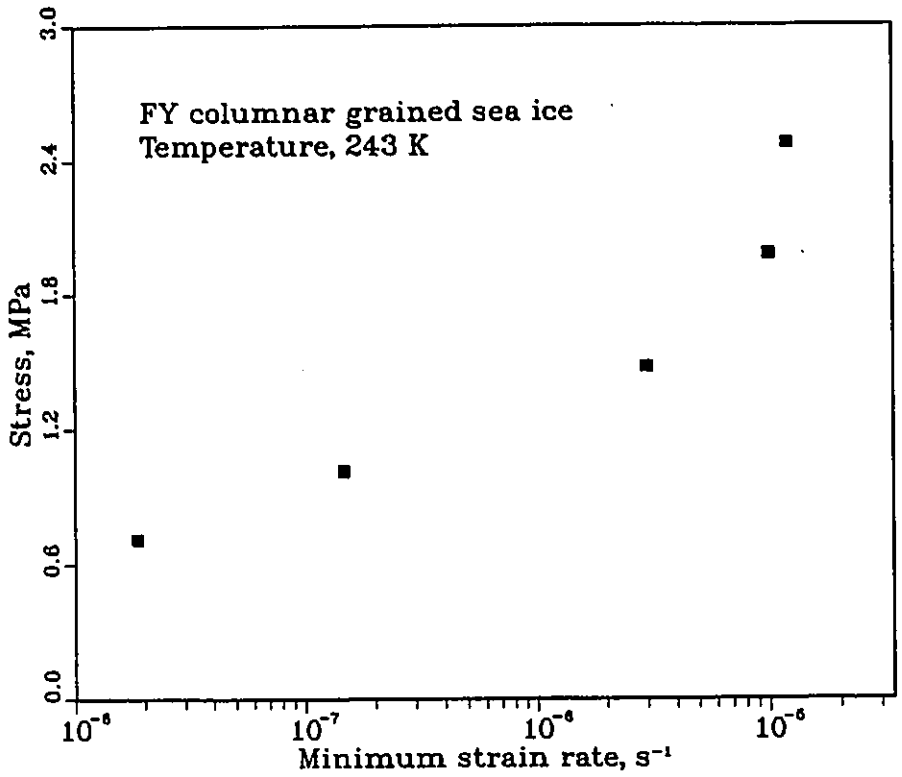

Figure 2.33 Stress dependence of minimum strain rate in constant load test for FY columnar grained sea ice at 243 K

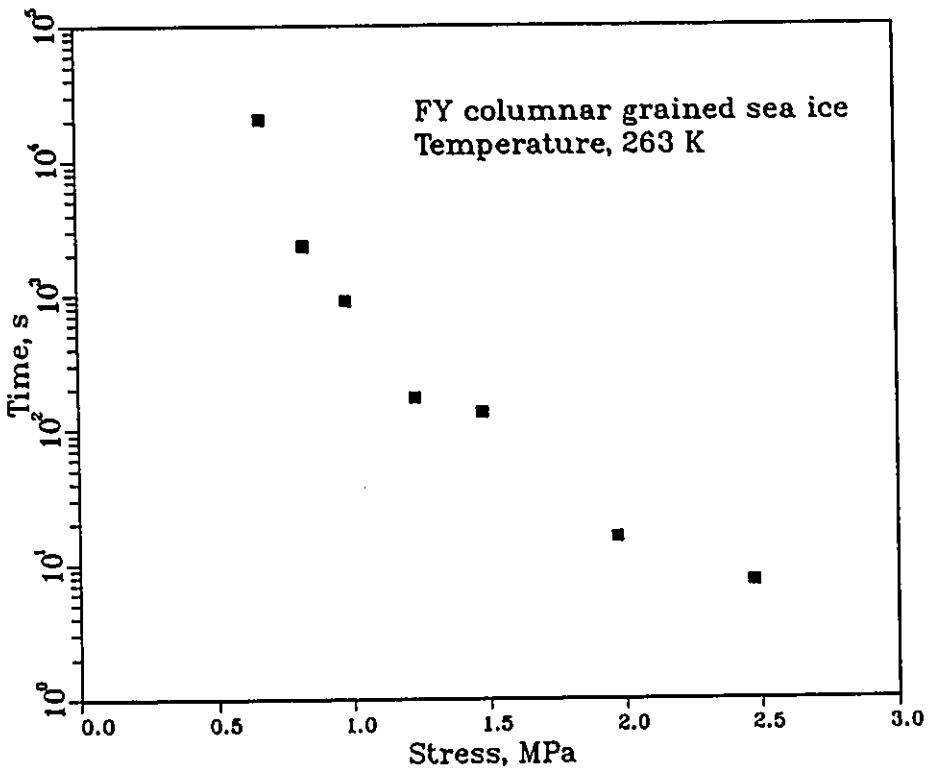

Figure 2.34 Stress dependence of time to minimum strain rate in constant load test for FY columnar grained sea ice at 263 K

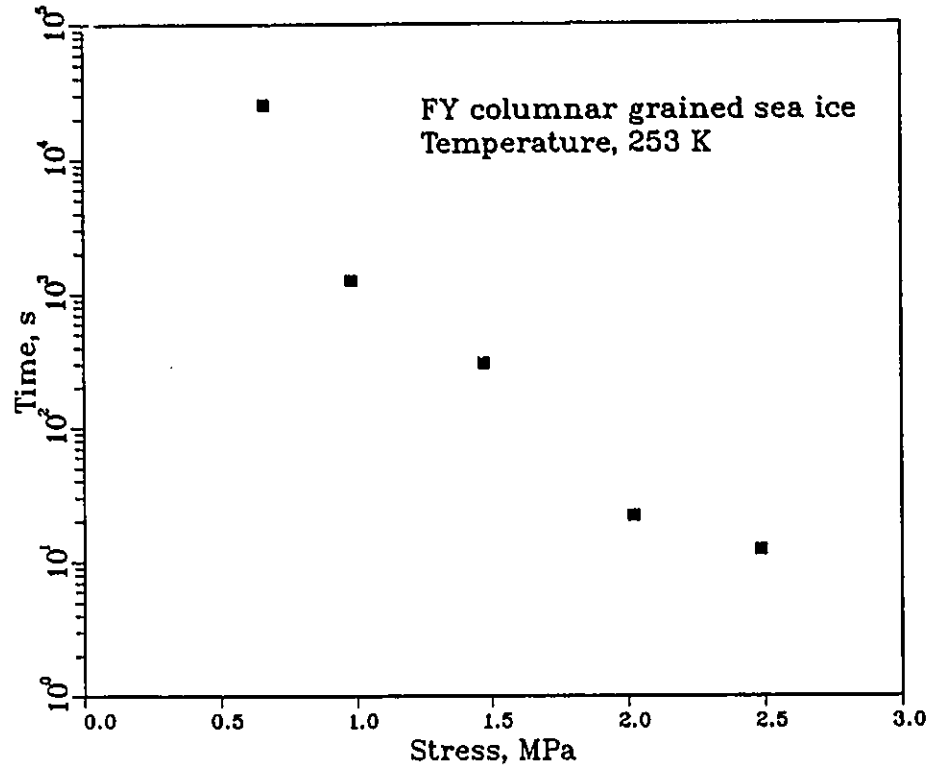

Figure 2.35 Stress dependence of time to minimum strain rate in constant load test for FY columnar grained sea ice at 253 K

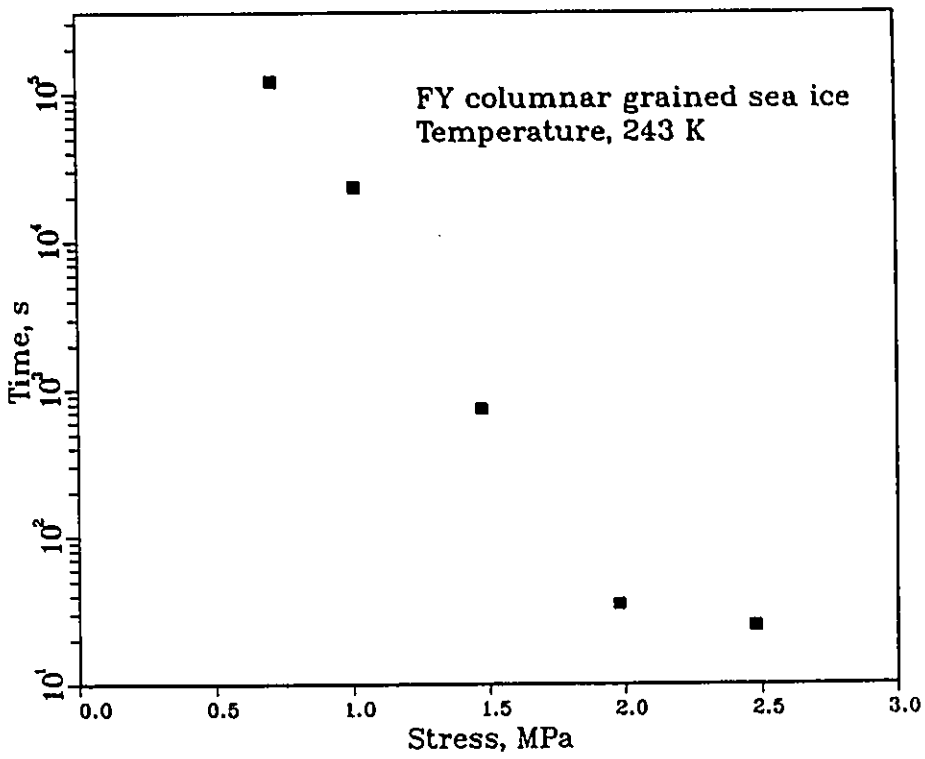

Figure 2.36 Stress dependence of time to minimum strain rate in constant load test for FY columnar grained sea ice at 243 K

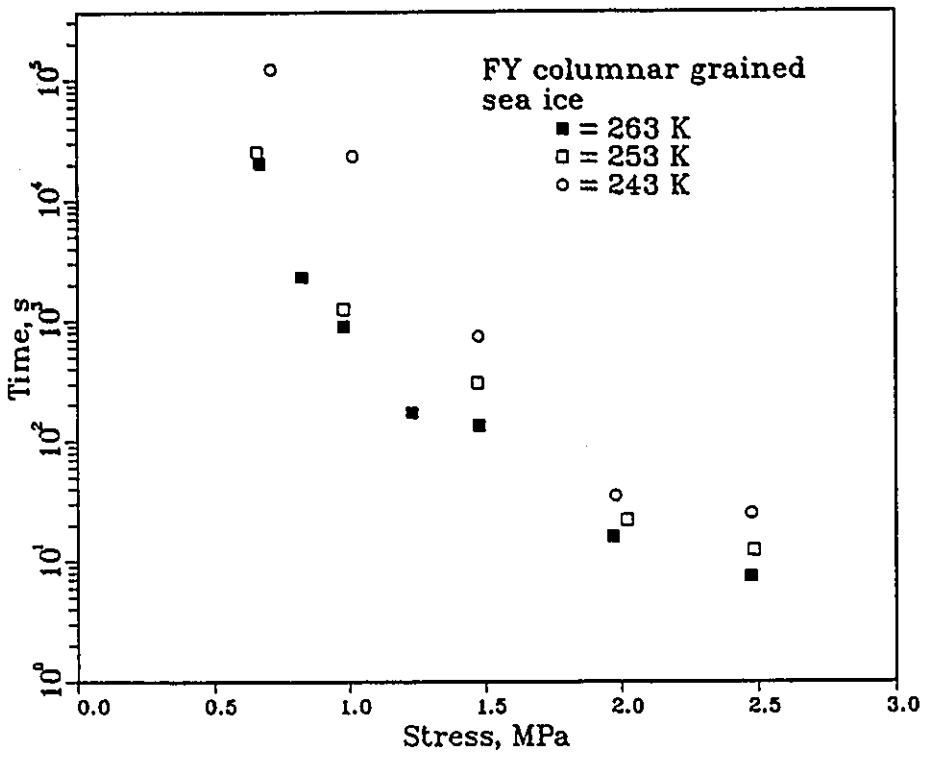

Figure 2.37 Comparison of stress dependence of time to minimum strain rate for FY columnar grained sea ice at different temperatures

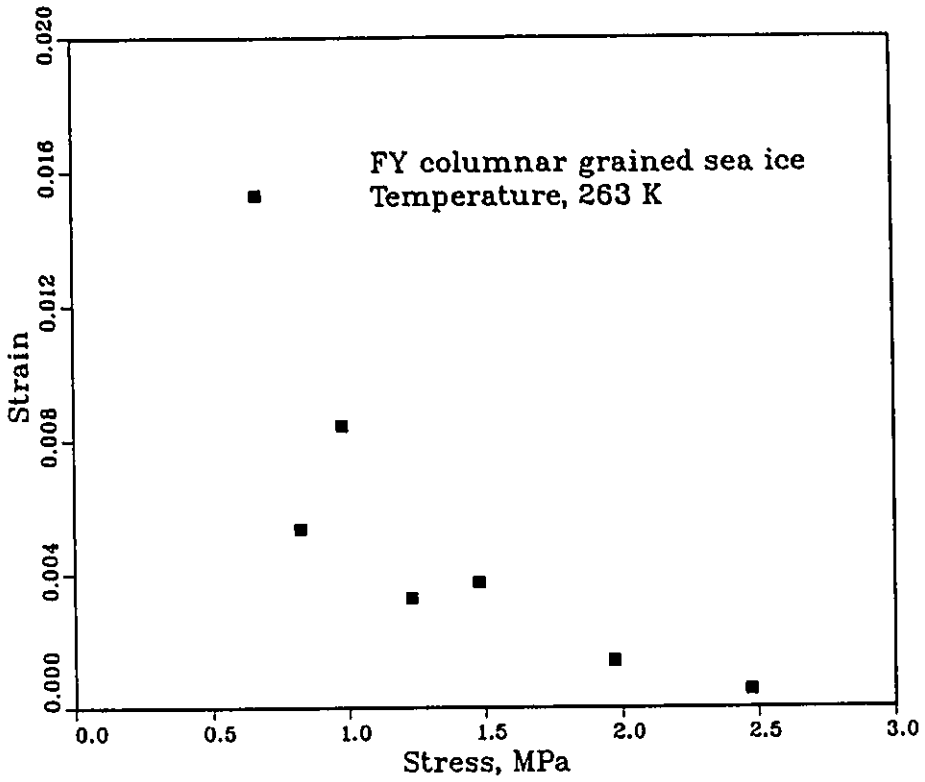

Figure 2.38 Stress dependence of strain to minimum strain rate in constant load test for FY columnar grained sea ice at 263 K

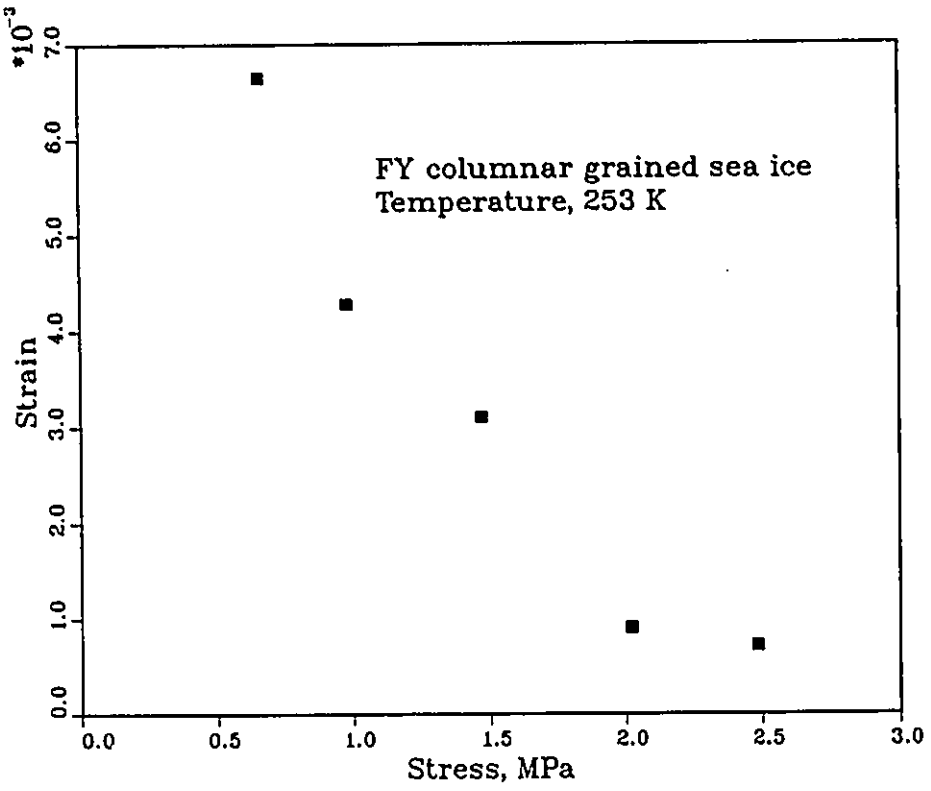

Figure 2.39 Stress dependence of strain to minimum strain rate in constant load test for FY columnar grained sea ice at 253 K

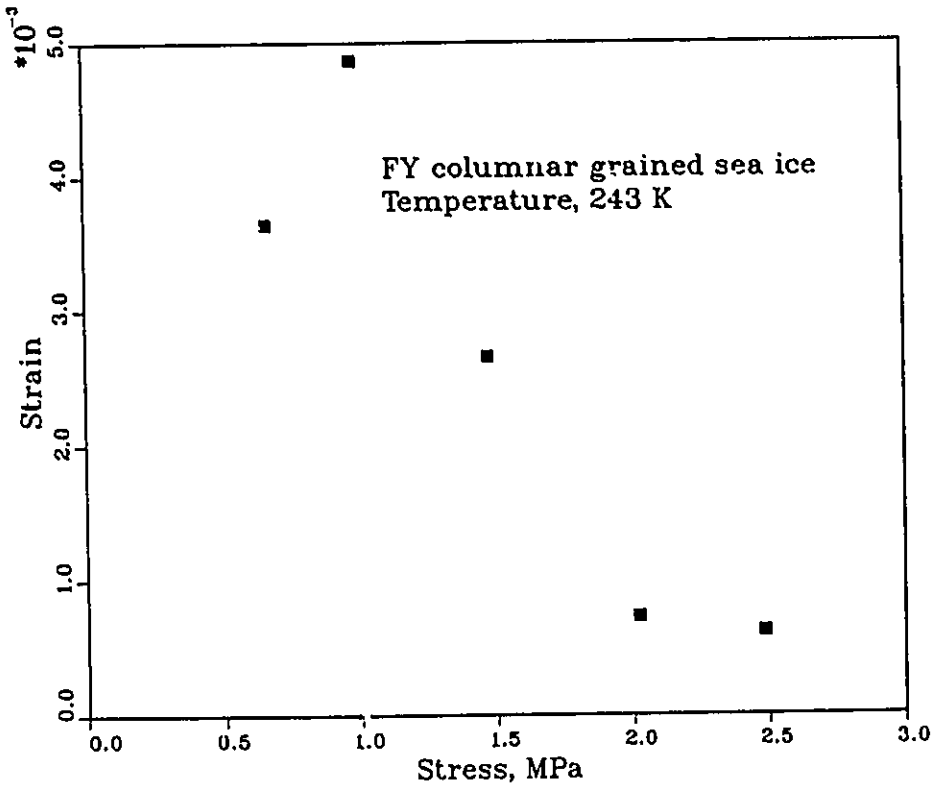

Figure 2.40 Stress dependence of strain to minimum strain rate in constant load test for FY columnar grained sea ice at 243 K

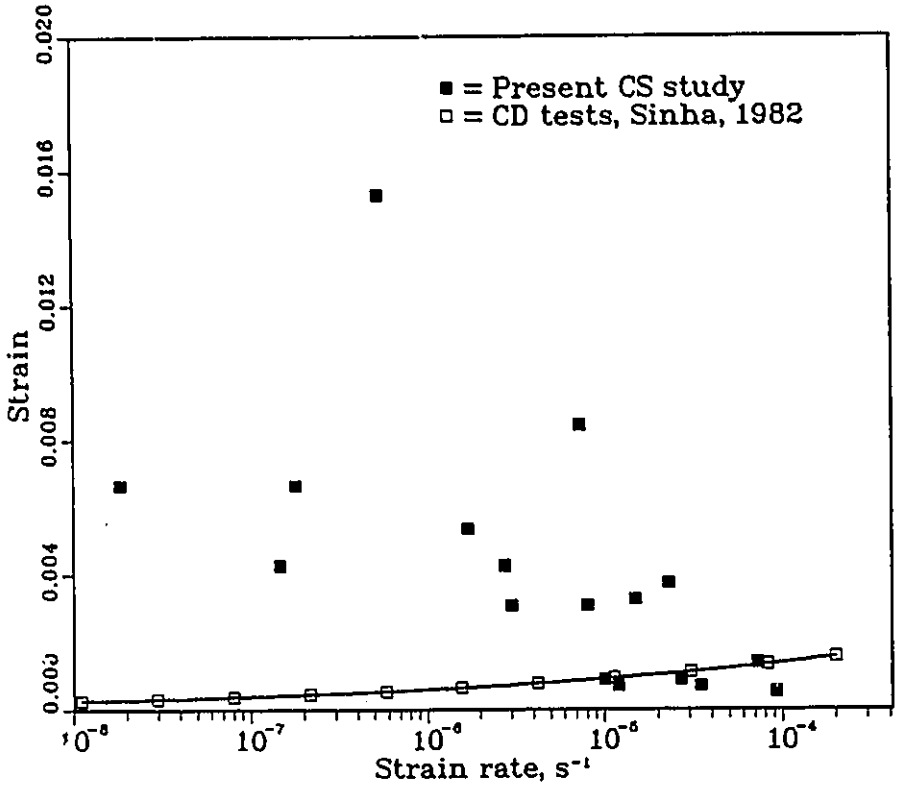

Figure 2.41 Comparison of rate dependence of strain at failure between S3b ice in CS tests and S2 ice in CD tests

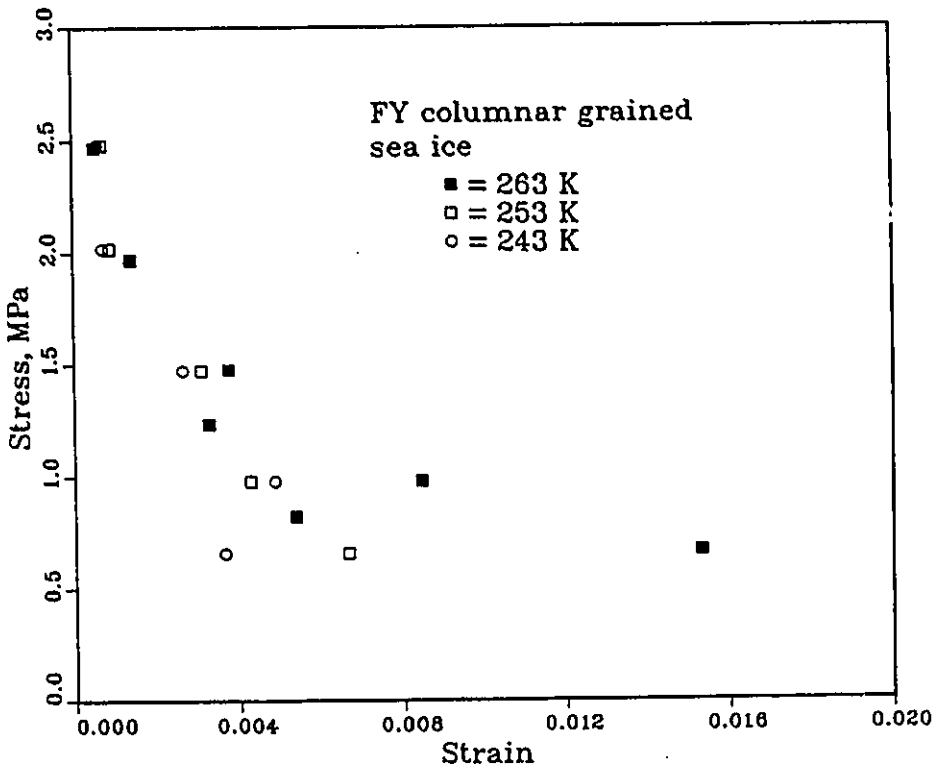

Figure 2.42 Stress and temperature dependence of strain at minimum strain rate for FY columnar grained sea ice

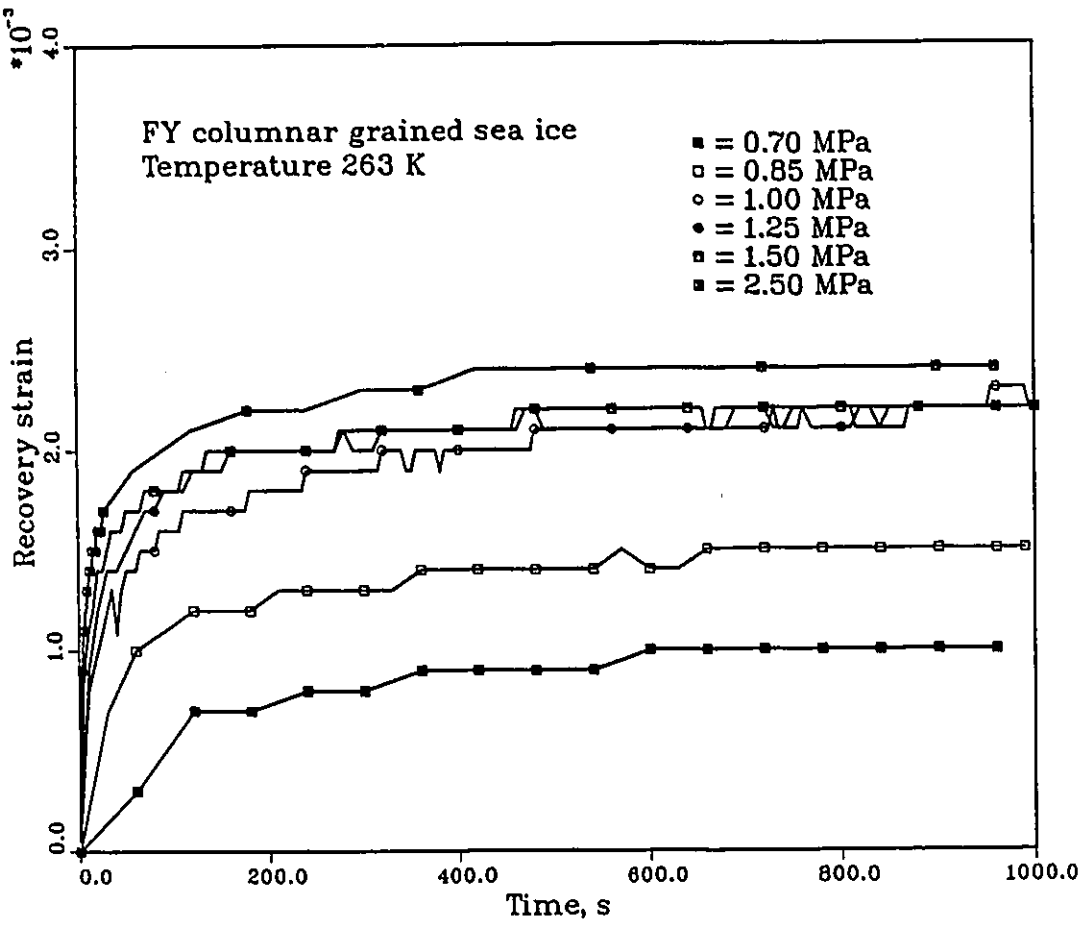

Figure 2.43 Time dependence of recovery strain at different stress levels for FY columnar grained sea ice in constant load test at temperature 263 K

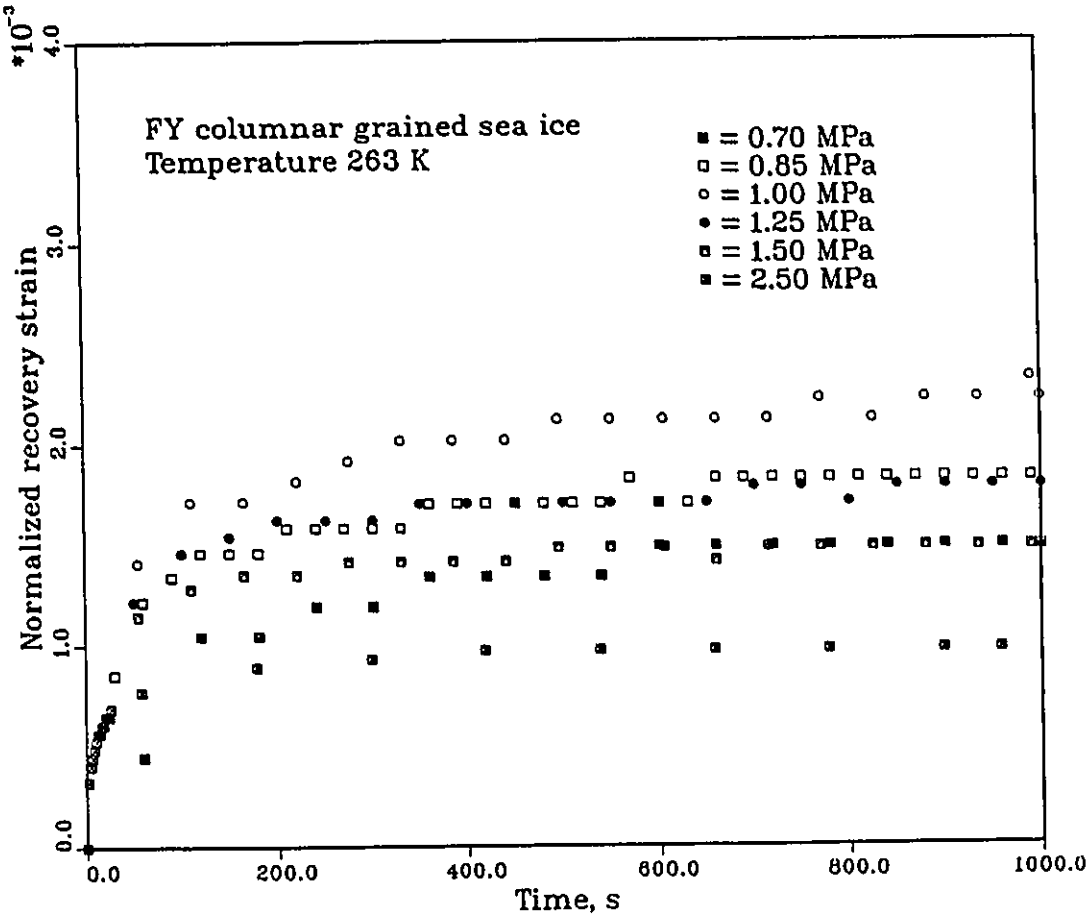

Figure 2.44 Time dependence of normalized recovery strain at different stress levels for FY columnar grained sea ice in constant load test at temperature 263 K

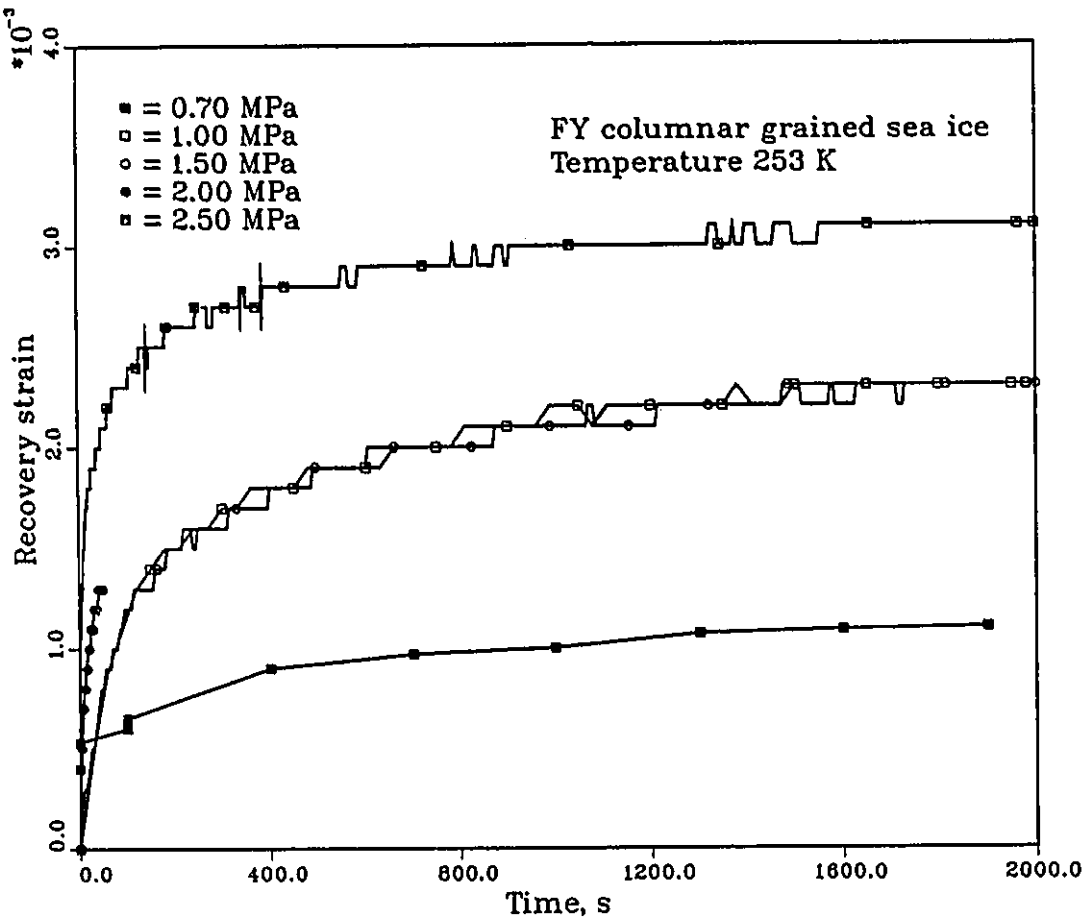

Figure 2.45 Time dependence of recovery strain at different stress levels for FY columnar grained sea ice in constant load test at temperature 253 K

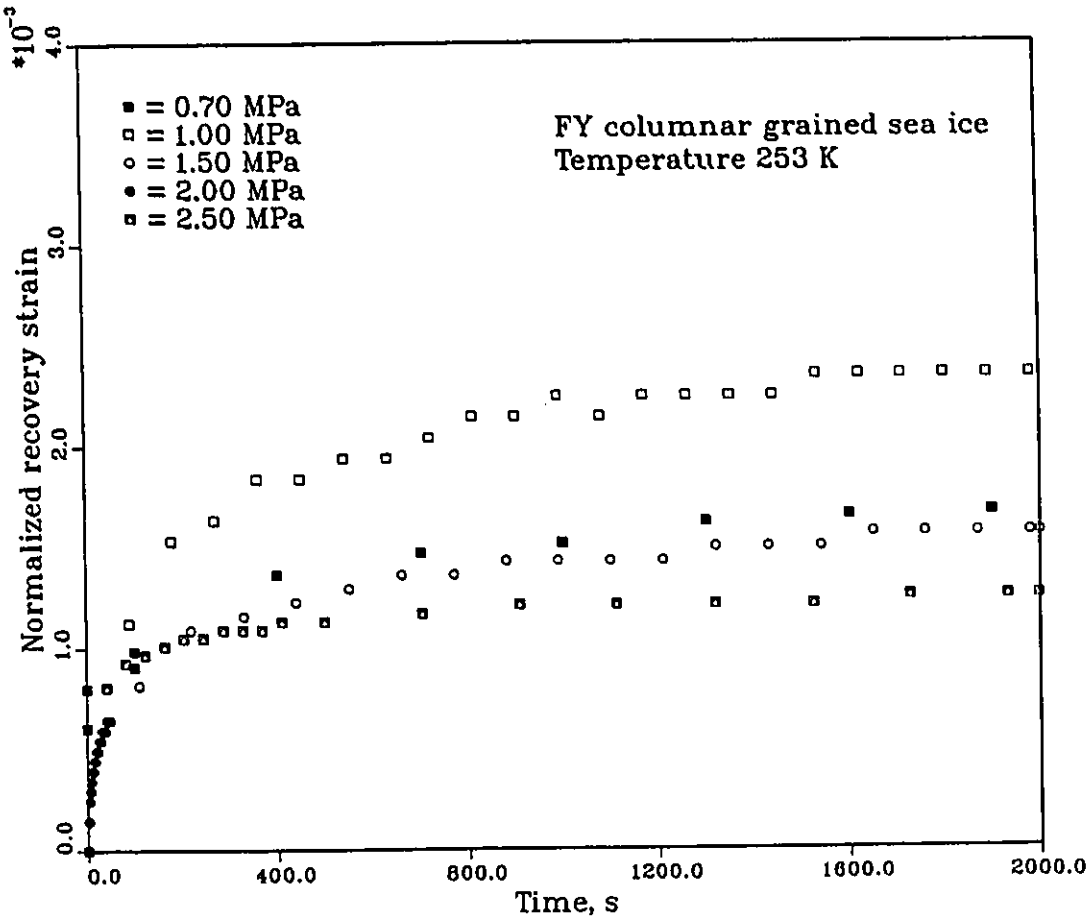

Figure 2.46 Time dependence of normalized recovery strain at different stress levels for FY columnar grained sea ice in constant load test at temperature 253 K

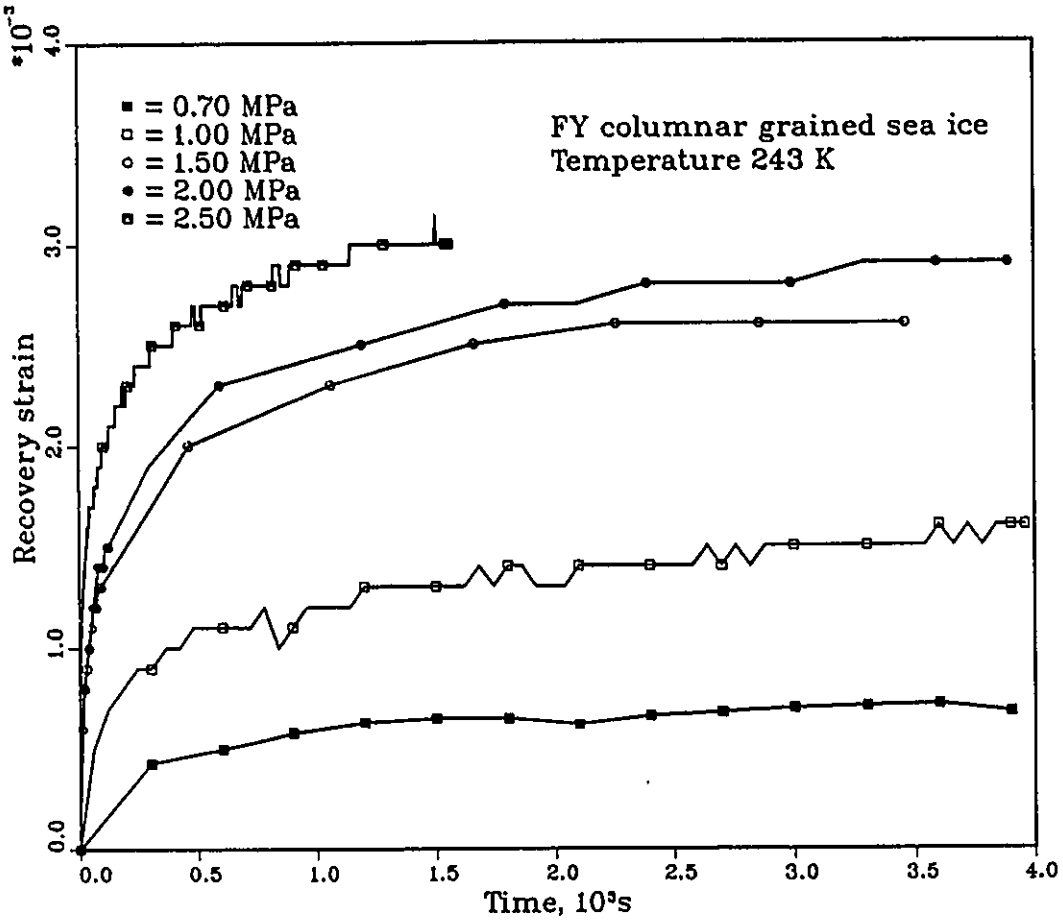

Figure 2.47 Time dependence of recovery strain at different stress levels for FY columnar grained sea ice in constant load test at temperature 243 K

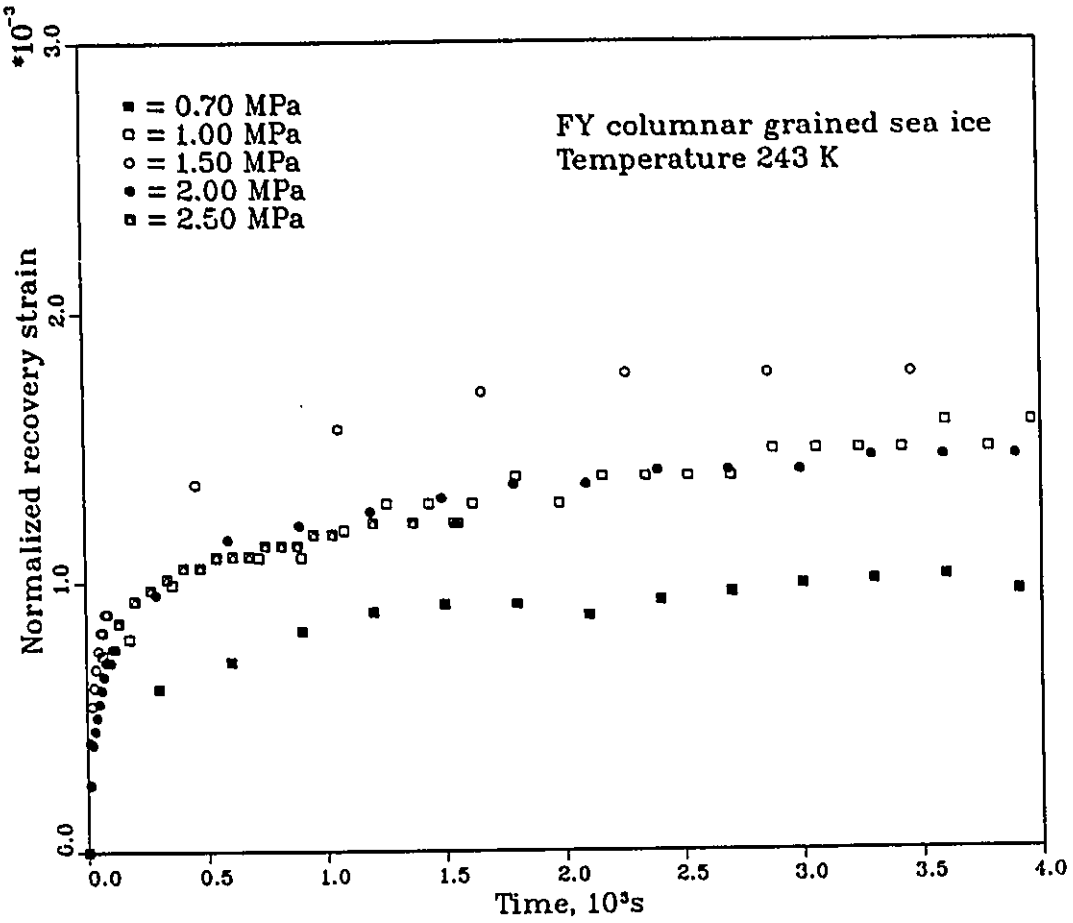

Figure 2.48 Time dependence of normalized recovery strain at different stress levels for FY columnar grained sea ice in constant load test at temperature 243 K

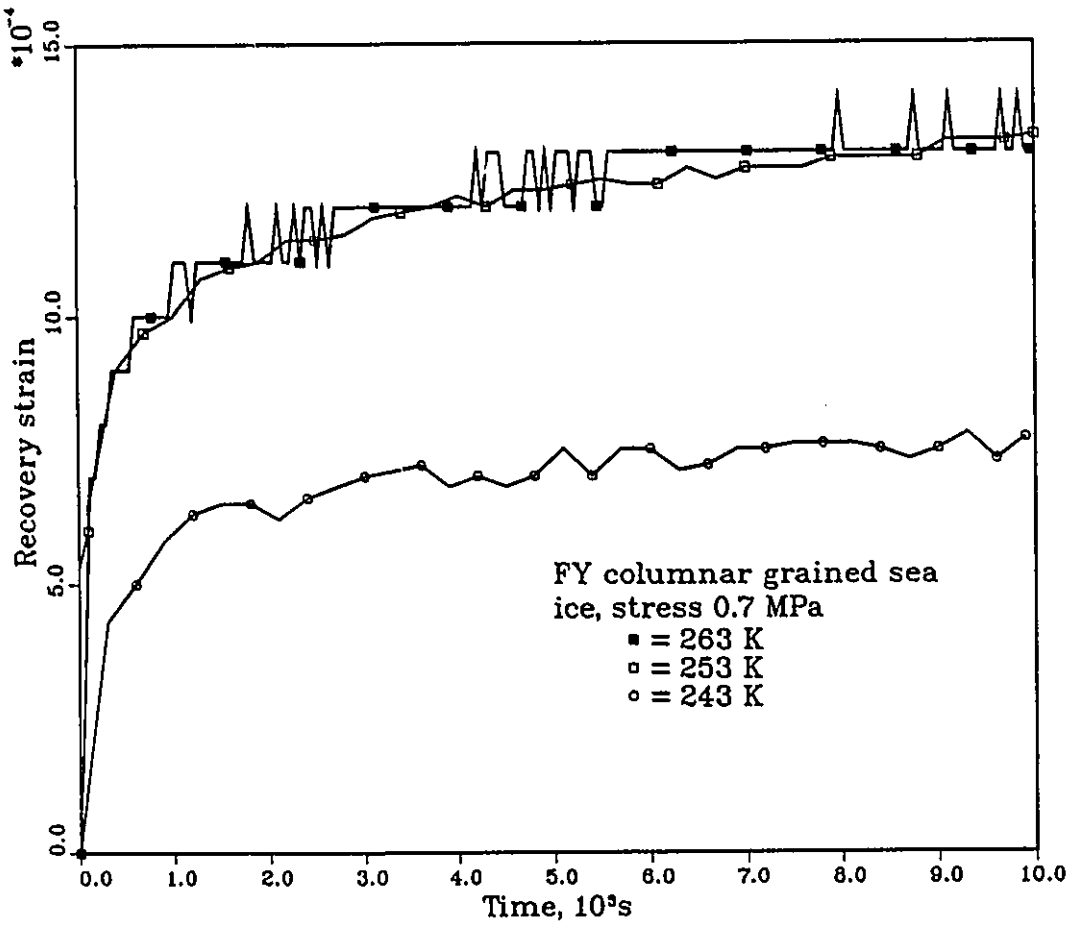

Figure 2.49 Time dependence of recovery strain at different temperatures for FY columnar grained sea ice in constant load test at stress level 0.7 MPa

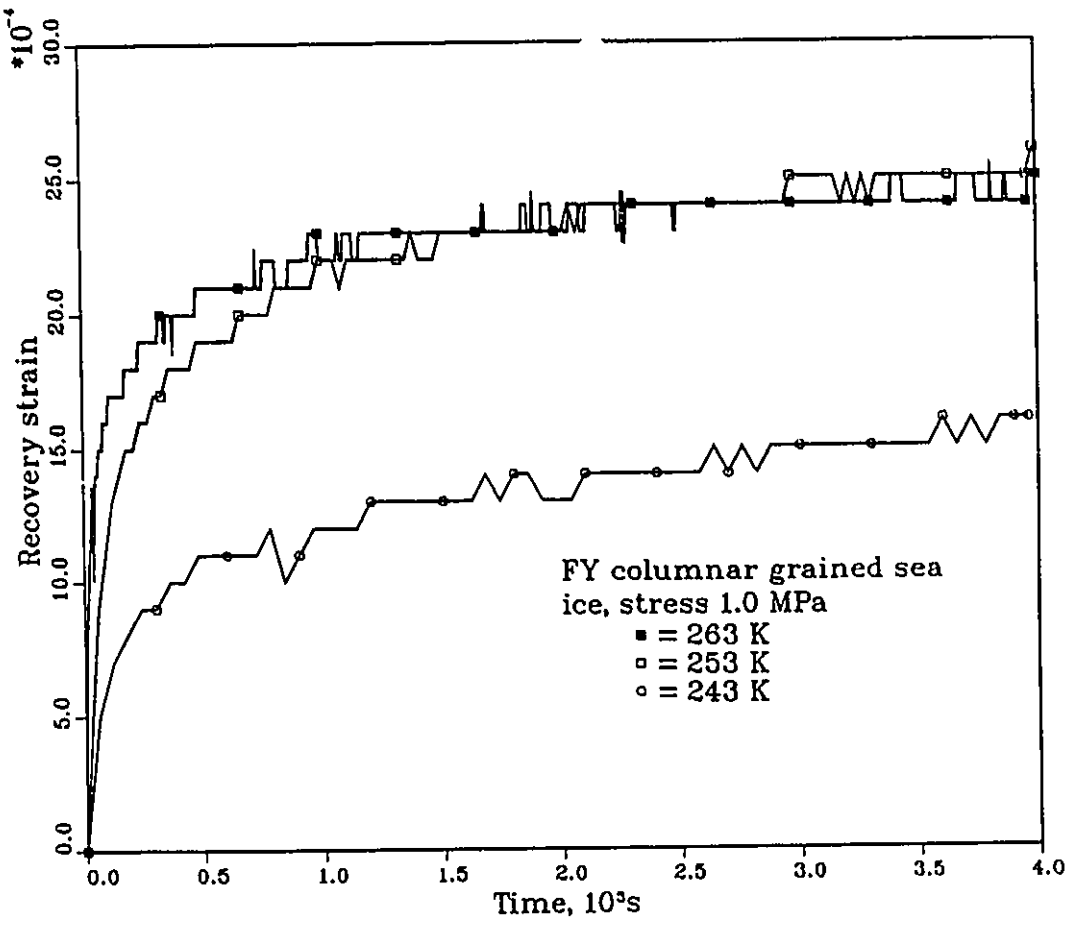

Figure 2.50 Time dependence of recovery strain at different temperatures for FY columnar grained sea ice in constant load test at stress level 1.0 MPa

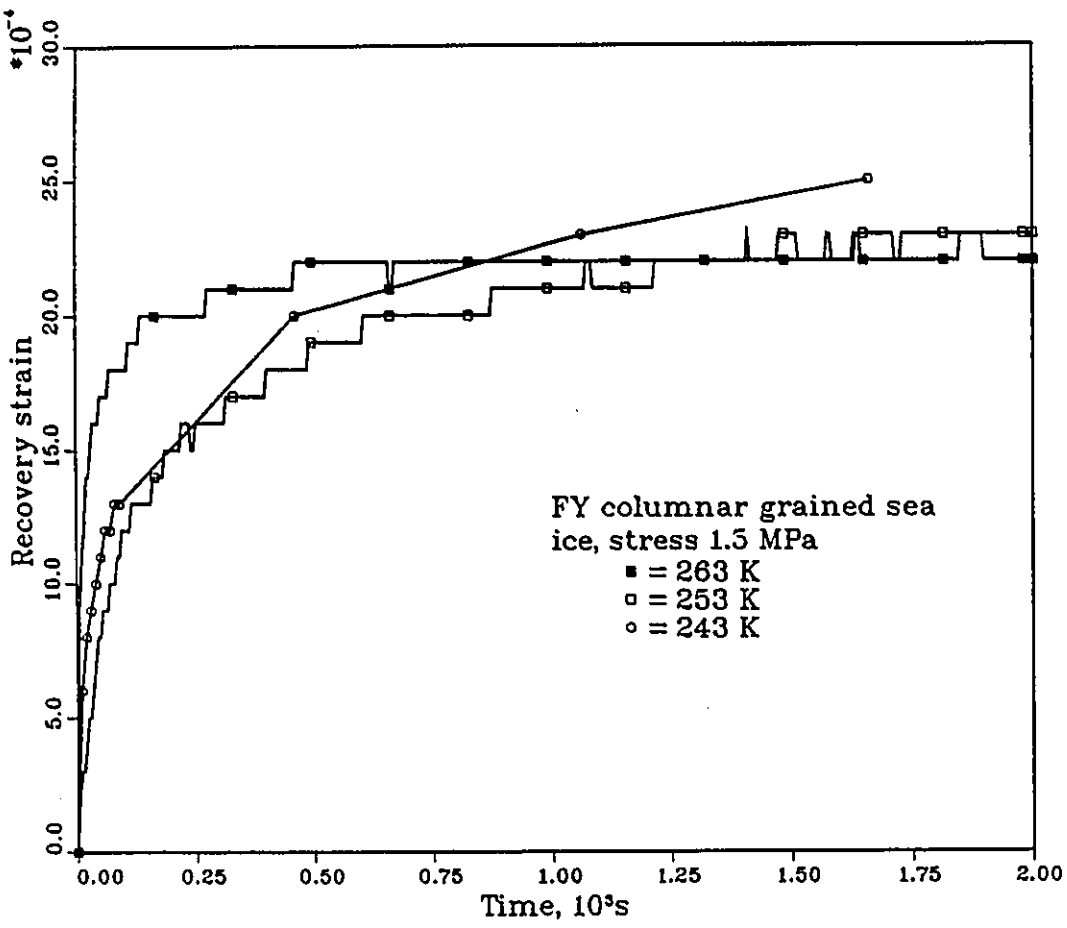

Figure 2.51 Time dependence of recovery strain at different temperatures for FY columnar grained sea ice in constant load test at stress level 1.5 MPa

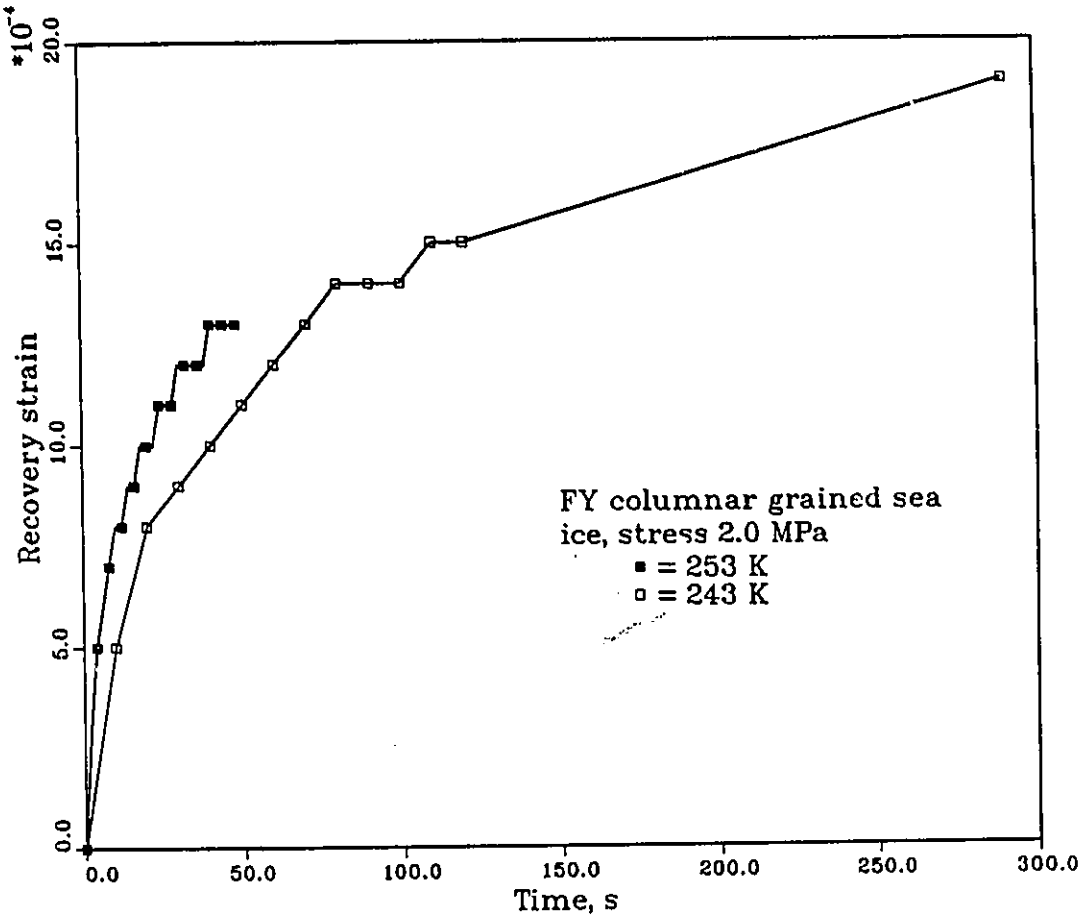

Figure 2.52 Time dependence of recovery strain at different temperatures for FY columnar grained sea ice in constant load test at stress level 2.0 MPa

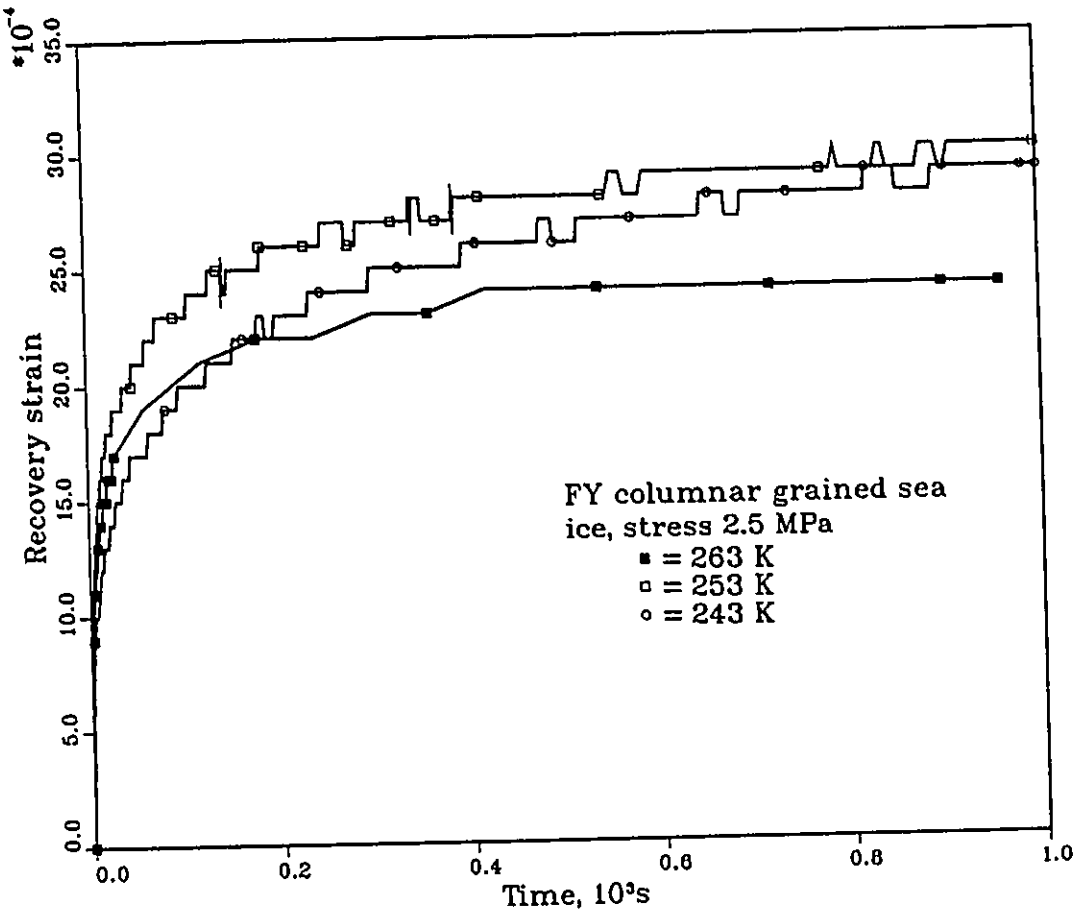

Figure 2.53 Time dependence of recovery strain at different temperatures for FY columnar grained sea ice in constant load test at stress level 2.5 MPa

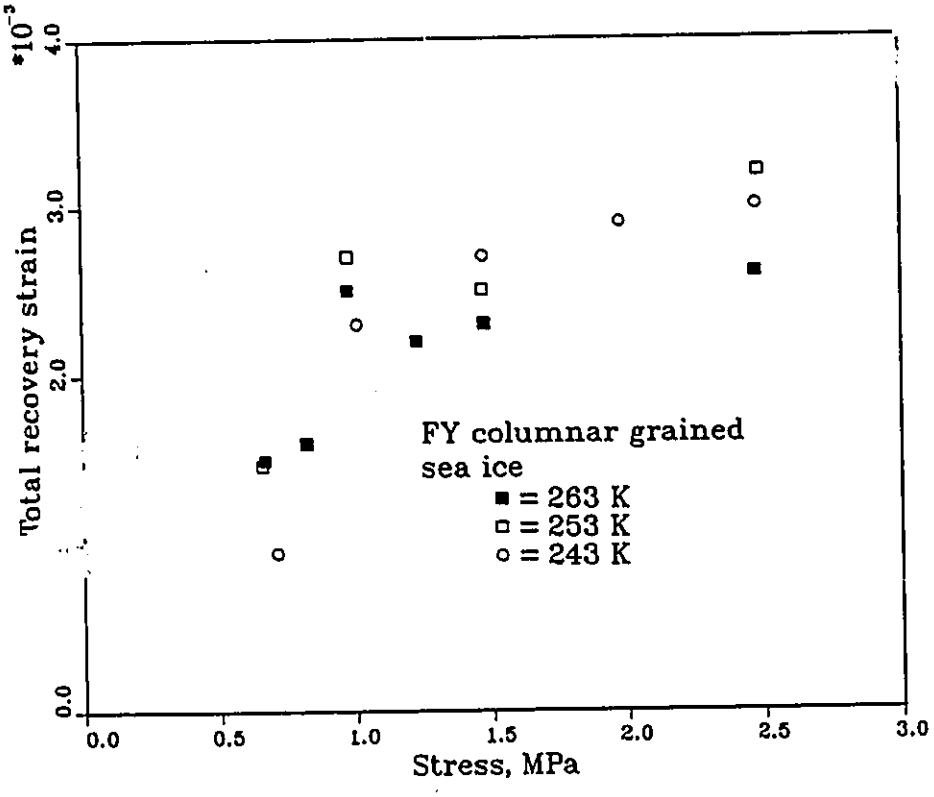

Figure 2.54 Stress dependence of total recovery strain for FY columnar grained sea ice under constant load

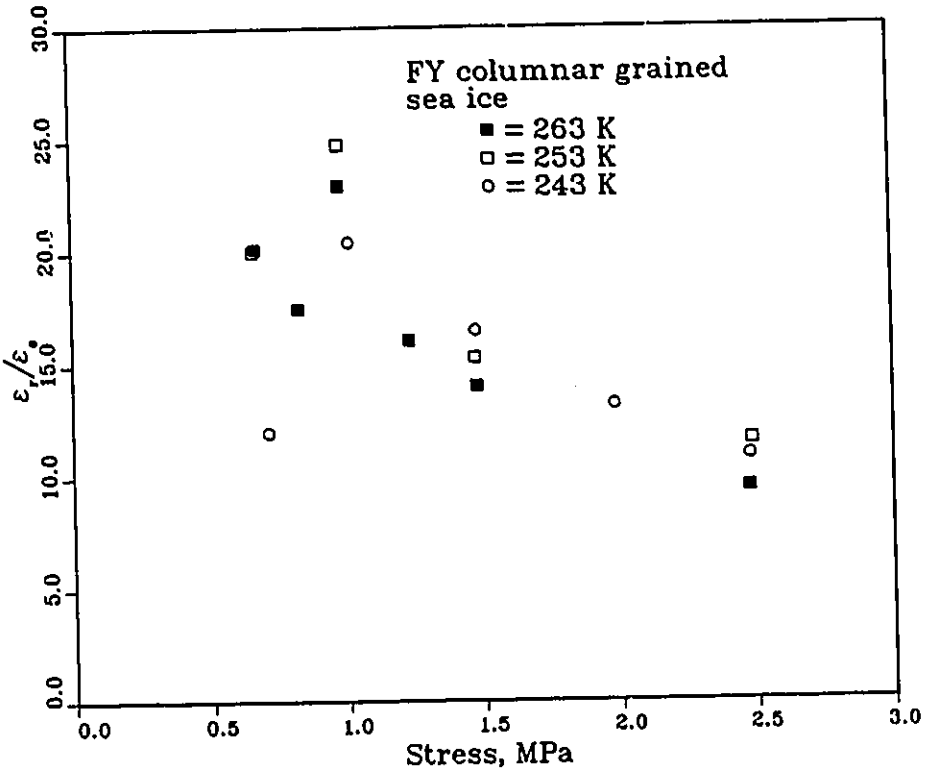

Figure 2.55 Stress dependence of strain ratio between total recovery strain and elastic strain

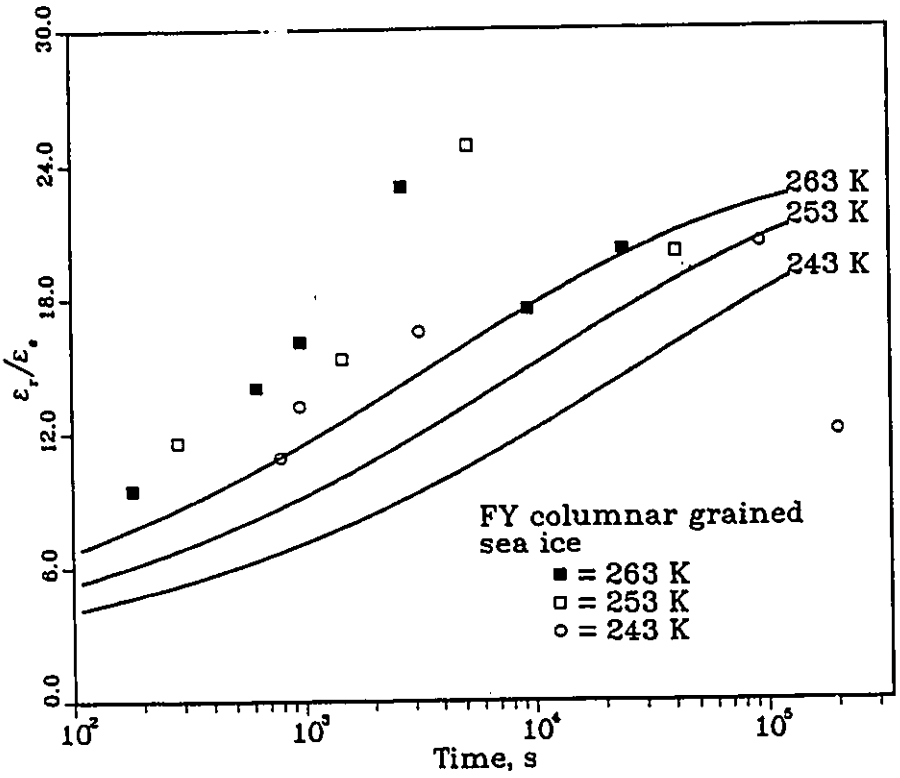

Figure 2.56 Time dependence of strain ratio between total recovery strain and elastic strain

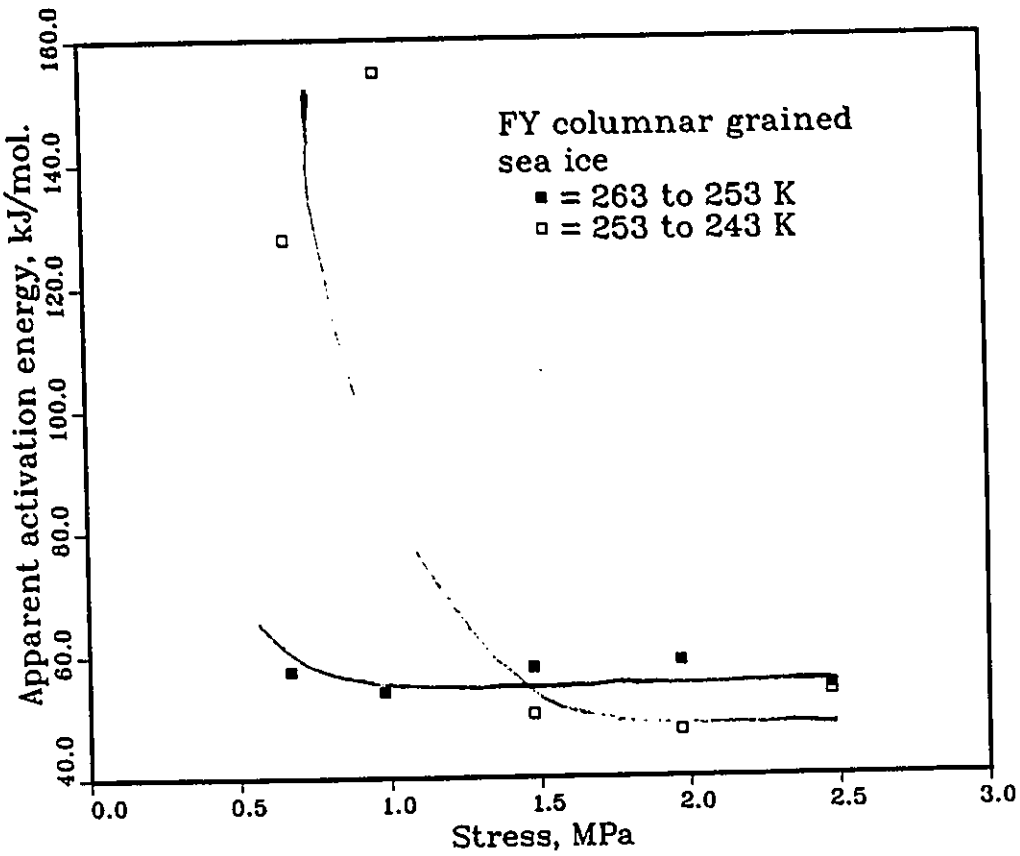

Figure 2.57 Stress dependence of apparent activation energy for minimum creep rate obtained from constant load tests

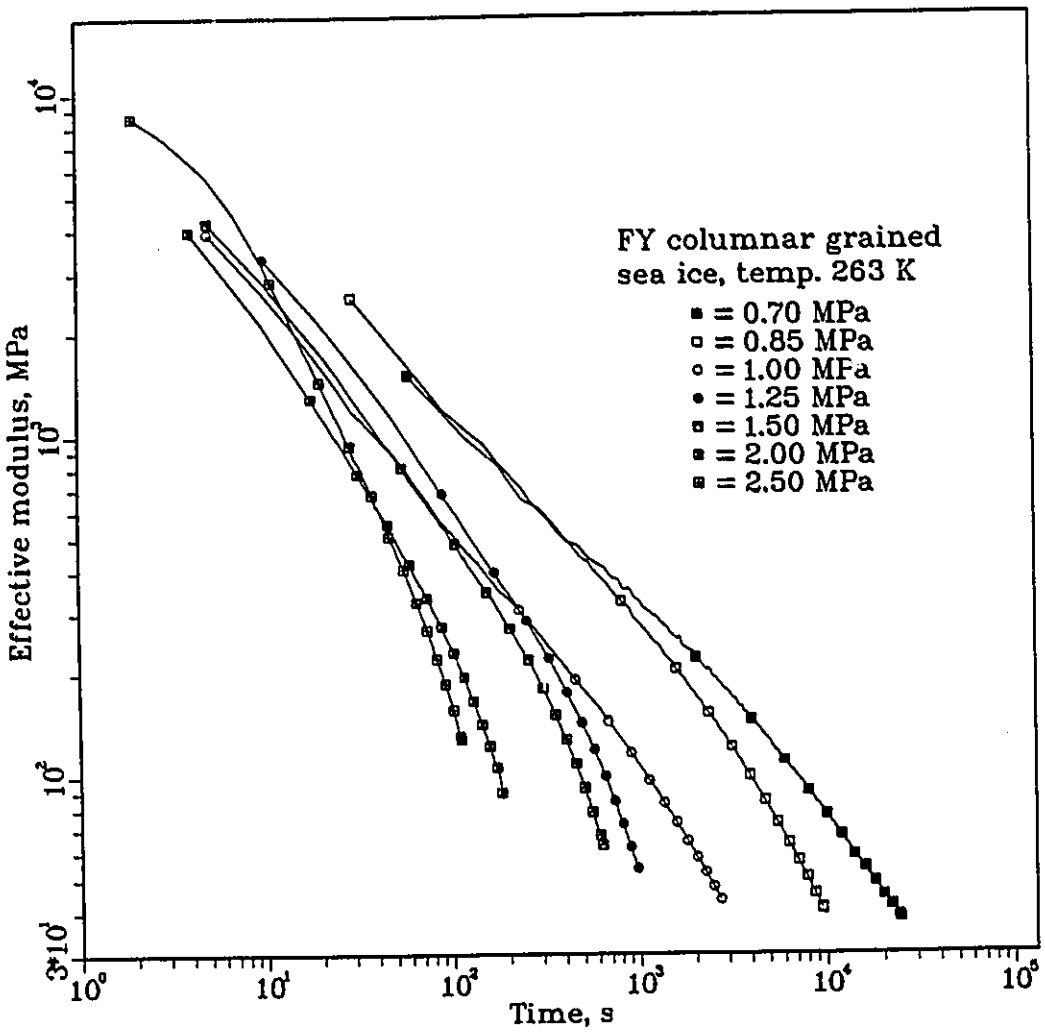

Figure 2.58 Time dependence of effective modulus for FY columnar grained sea ice at different stress levels in CS test at temperature 263 K

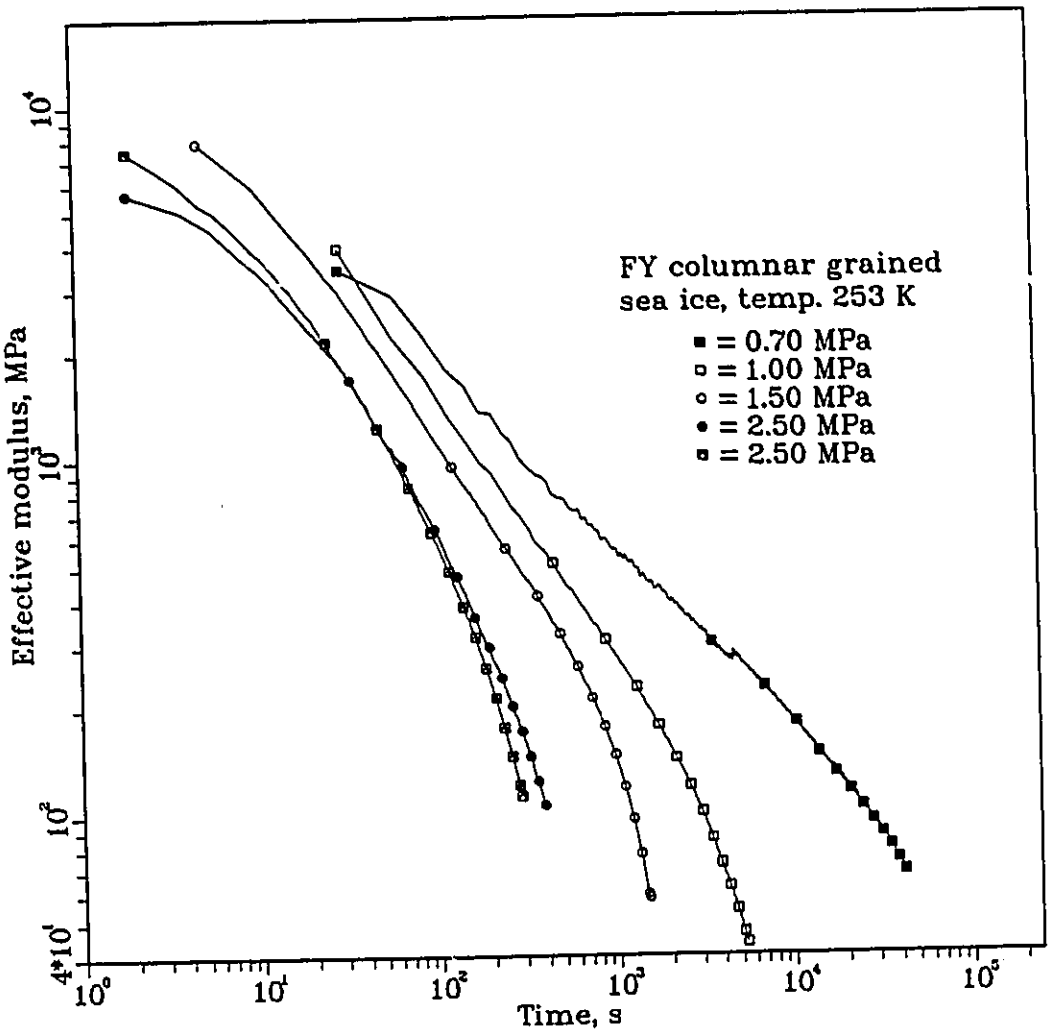

Figure 2.59 Time dependence of effective modulus for FY columnar grained sea ice at different stress levels in CS test at temperature 253 K

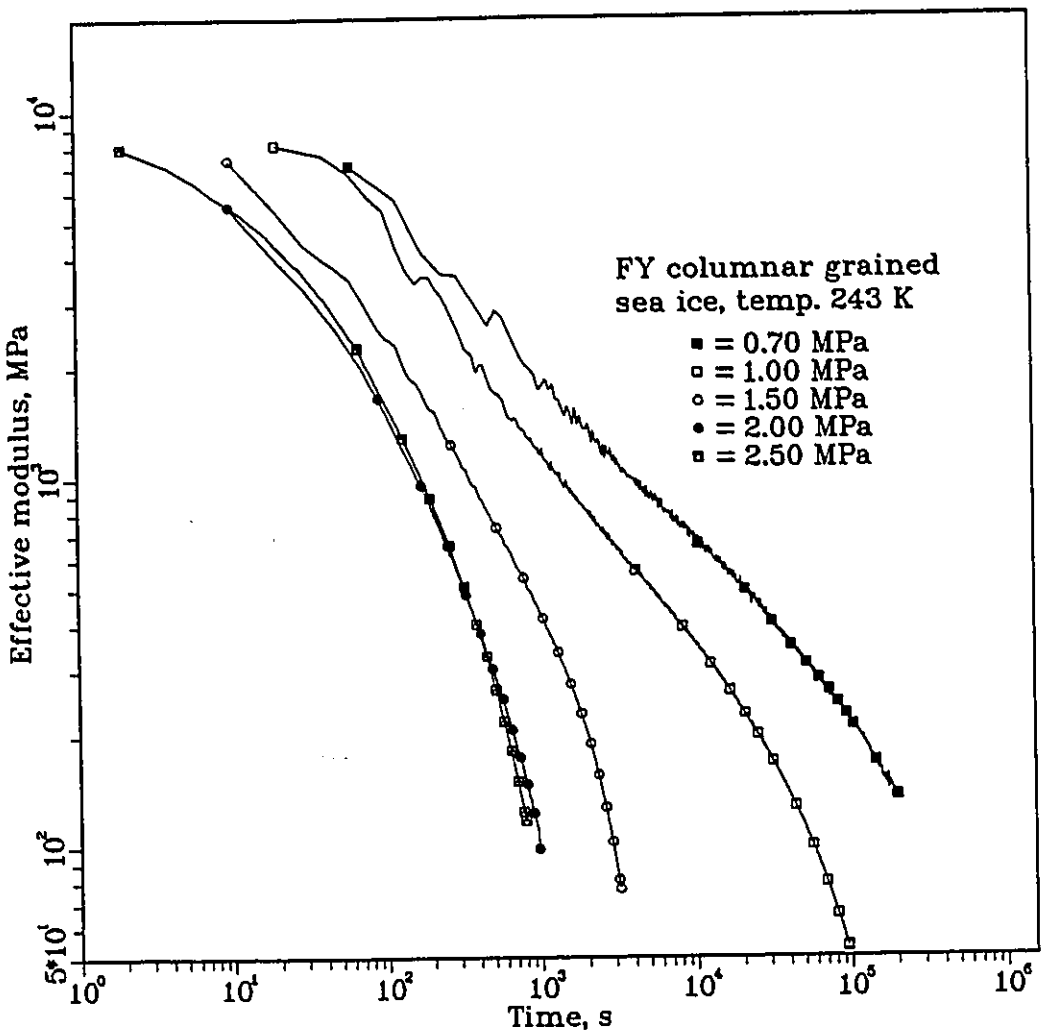

Figure 2.60 Time dependence of apparent mudulus for FY columnar grained sea ice at different stress levels in CS test at temperature 243 K

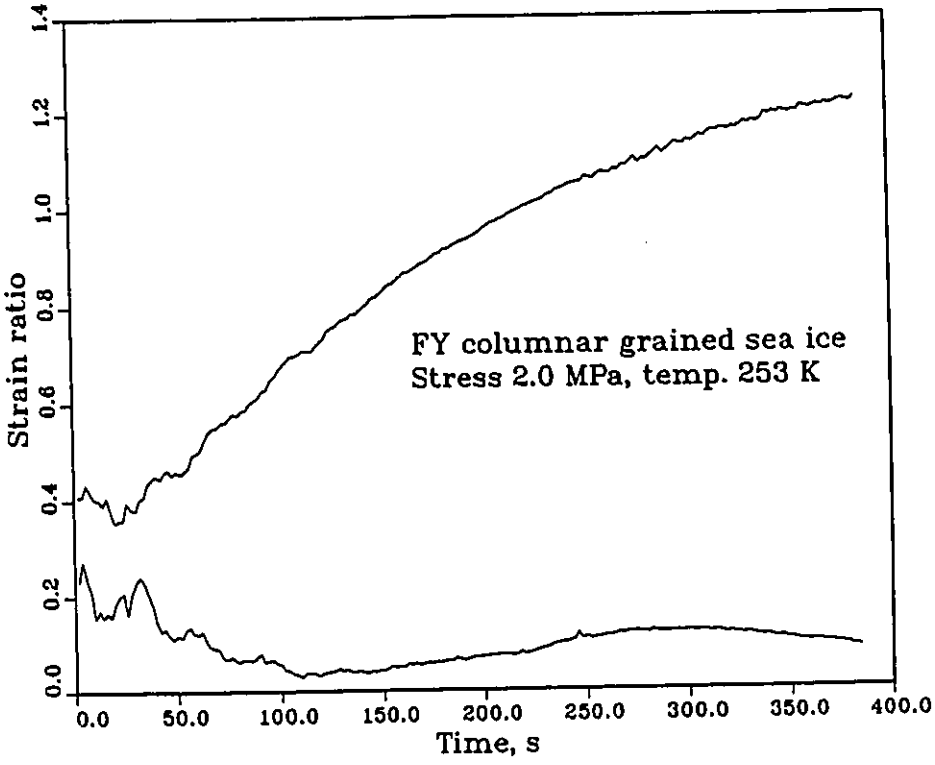

Figure 2.61 Time dependence of strain ratios for FY columnar grained sea ice in constant load test

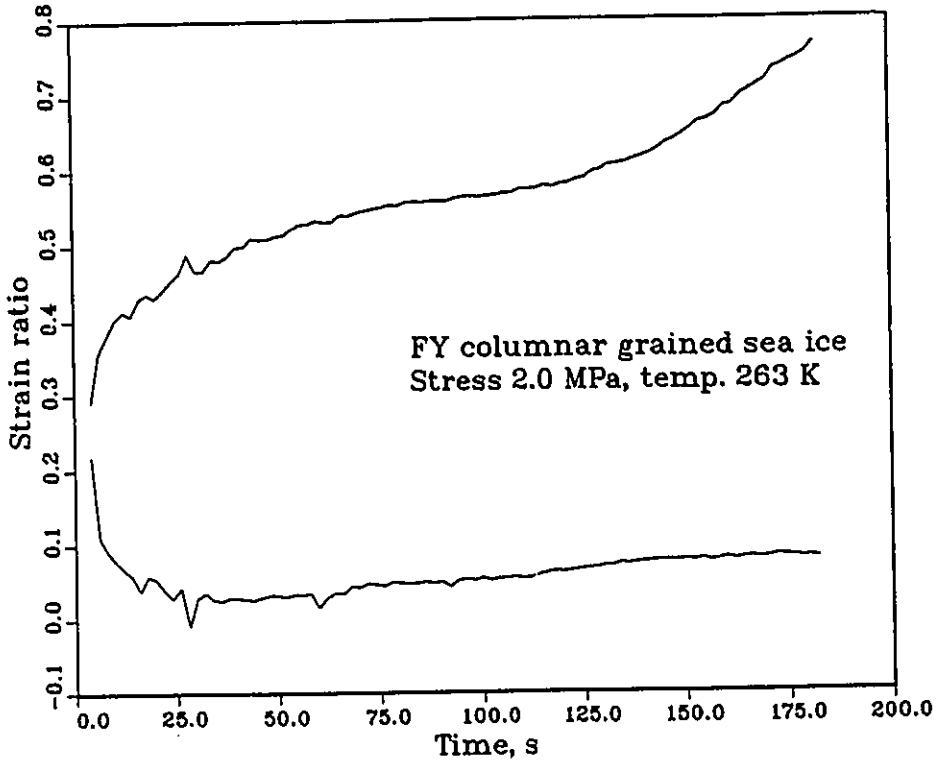

Figure 2.62 Time dependence of strain ratios for FY columnar grained sea ice in constant load test

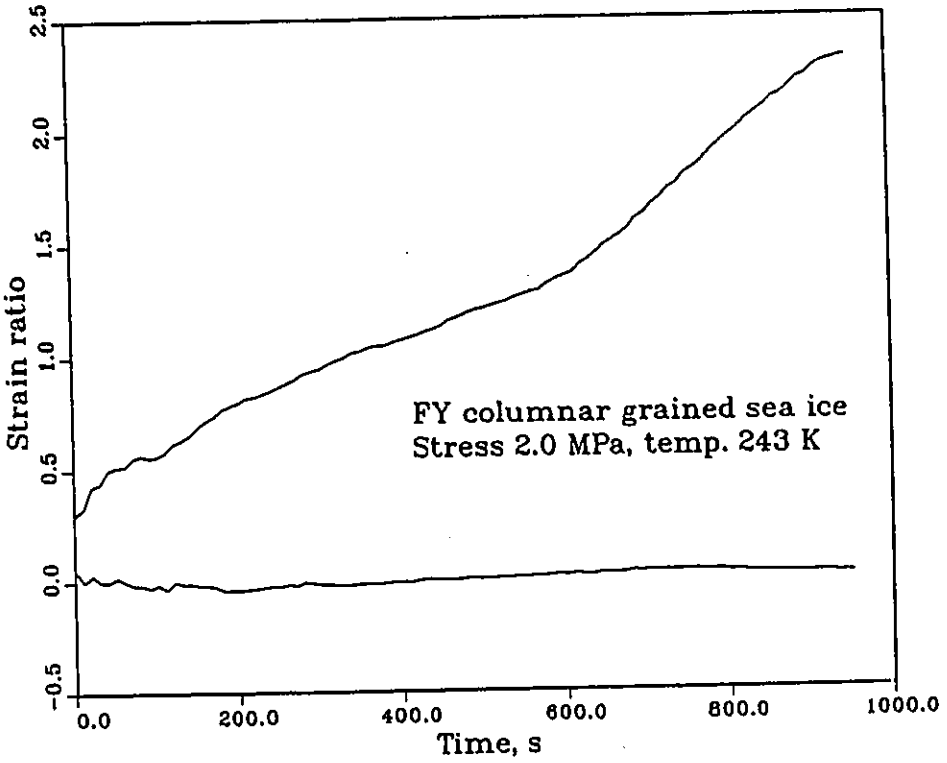

Figure 2.63 Time dependence of strain ratios for FY columnar grained sea ice in constant load test

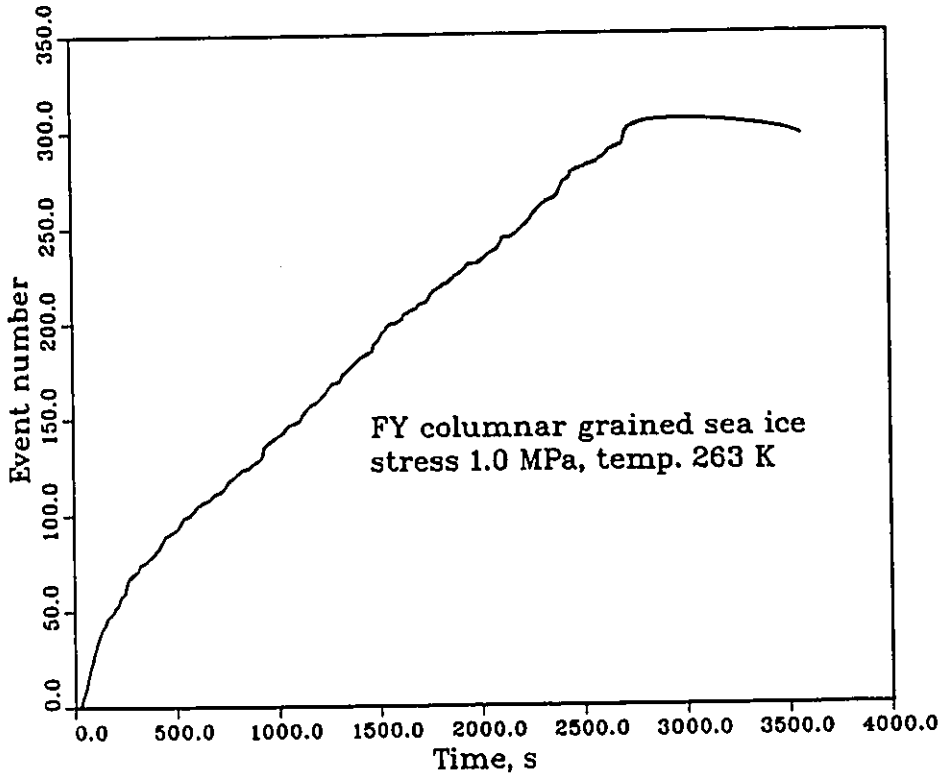

Figure 2.64 Time dependence of acoustic emission number for FY columnar grained sea ice in constant load test

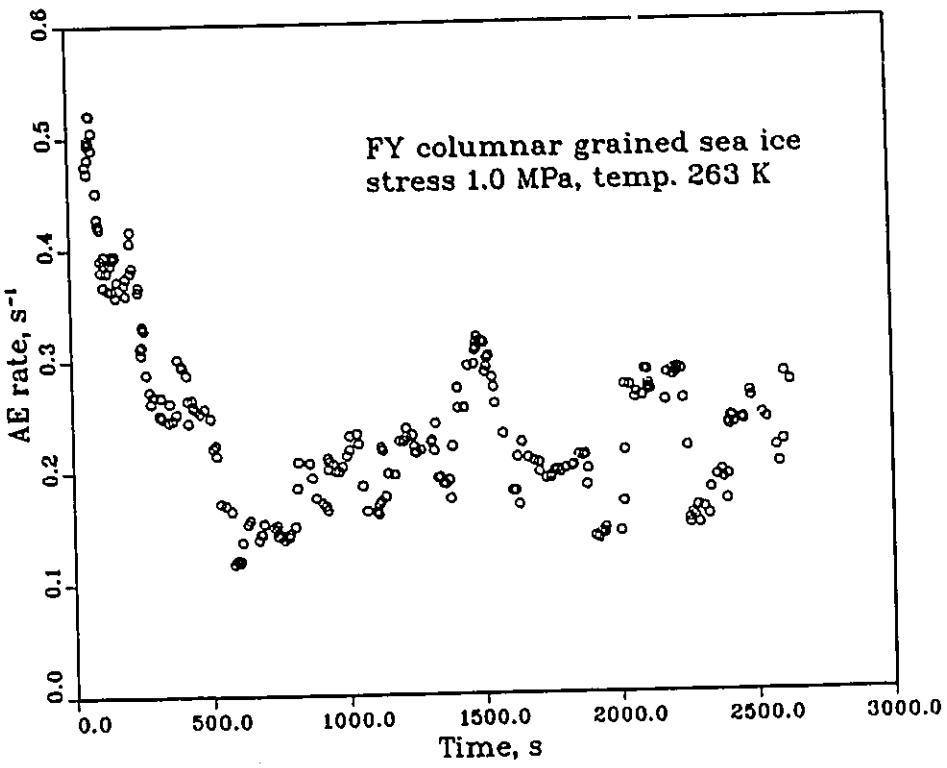

Figure 2.65 Time dependence of AE rate for FY columnar grained sea ice in constant load test

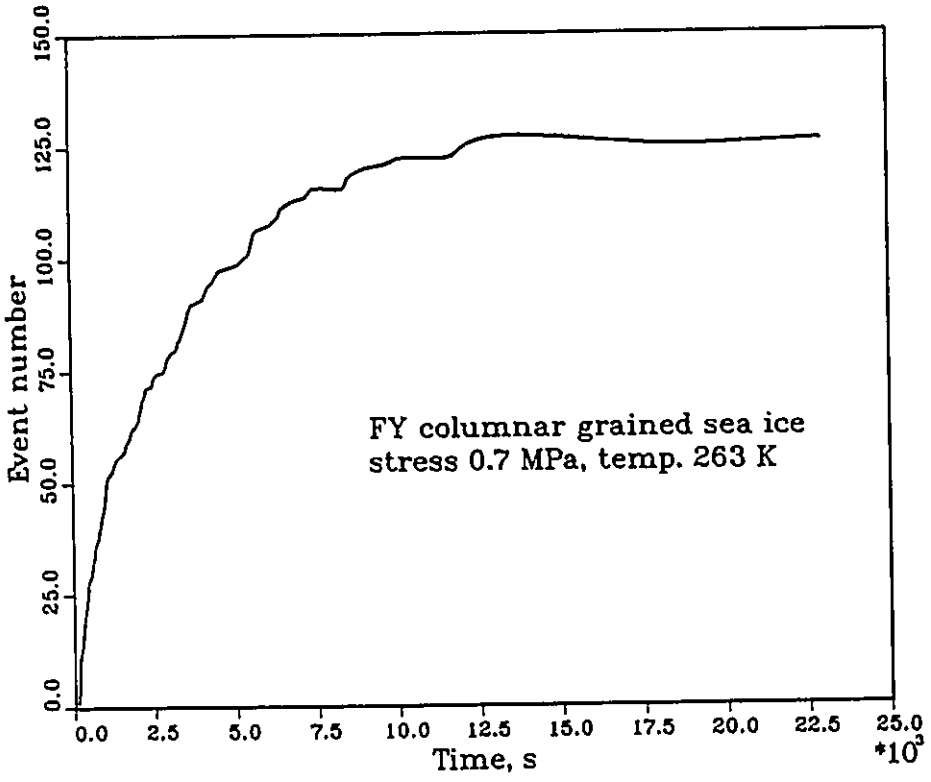

Figure 2.66 Time dependence of acoustic emission number for FY columnar grained sea ice in constant load test

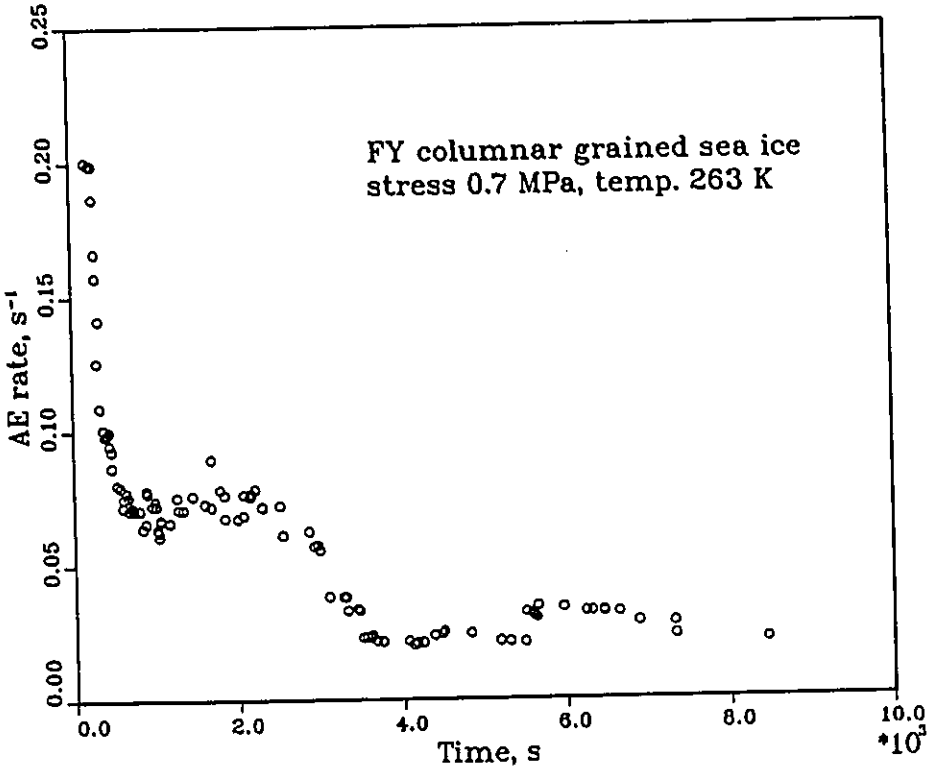

Figure 2.67 Time dependence of AE rate for FY columnar grained sea ice in constant load test

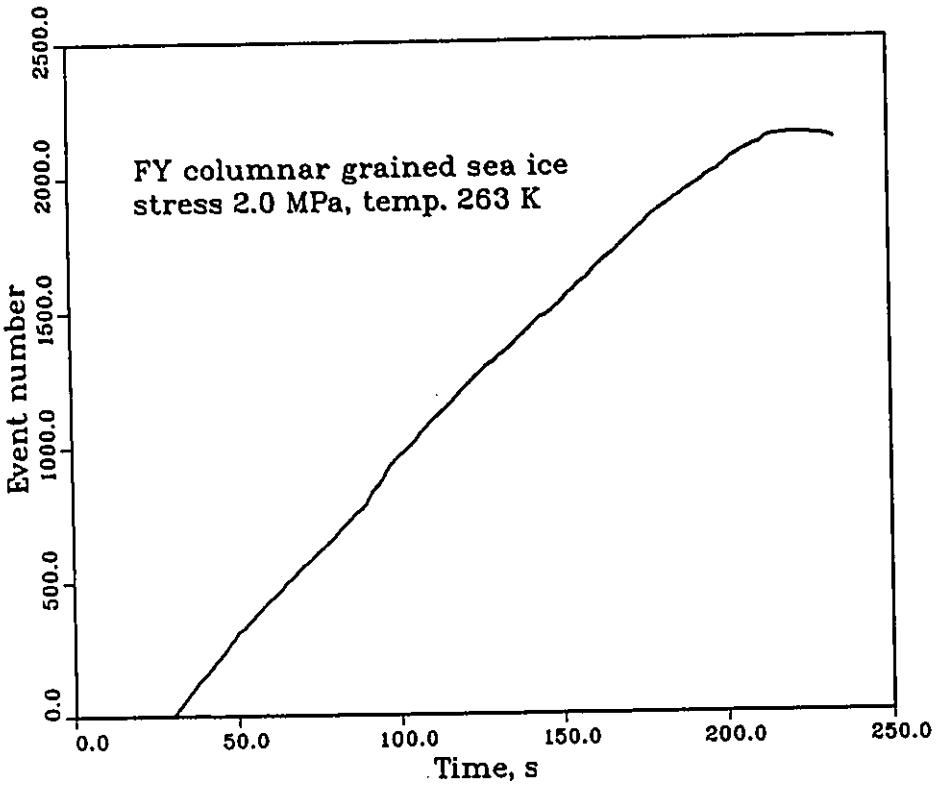

Figure 2.68 Time dependence of acoustic emission number for FY columnar grained sea ice in constant load test

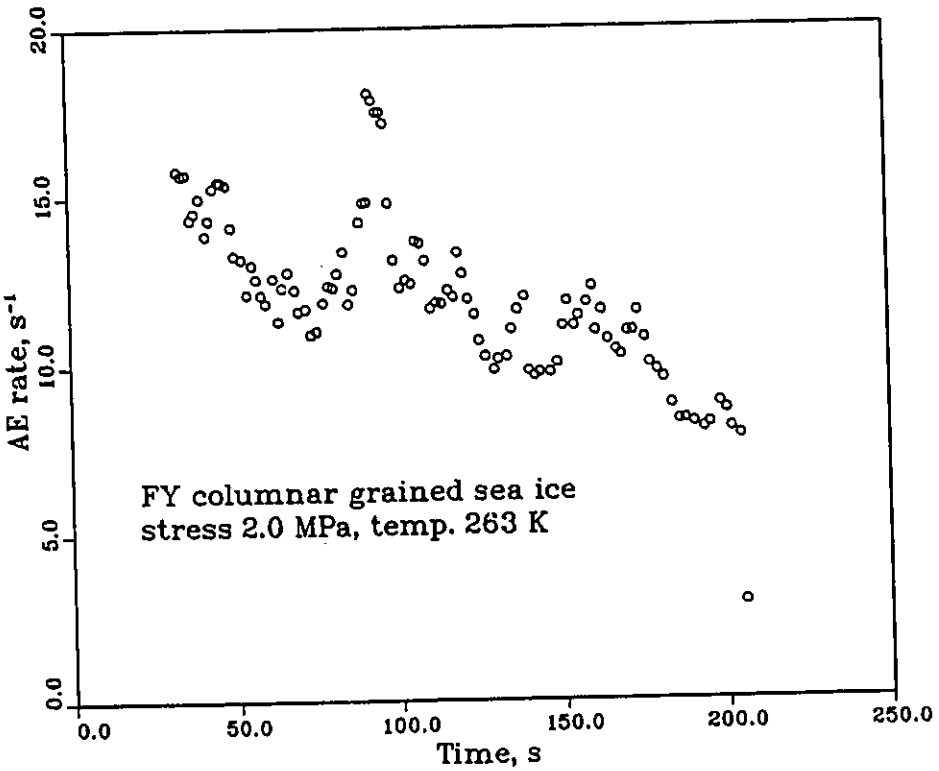

Figure 2.69 Time dependence of AE rate for FY columnar grained sea ice in constant load test

Figure 2.70 Crack orientation of tested ice sample at stress 2.5MPa temperature 253 K

Chapter 3

Field test on first year sea ice

3.1 Introduction

Field tests were carried out in Resolute ($74^0 42'N, 94^0 50'W$), N.W.T., Canada in May, 1992 during SIMS-1992 (Sea Ice Monitoring Sites) experiments. Two studies were carried out. One was the microstructure studies of first year sea ice. The other one was borehole indentation test.

Microstructural study was carried out to determine the relationship between growth rate, salinity, and brine layer spacing of first year sea ice as a function of depth. The borehole indentation test was carried out with the NRCC borehole indentor for two loading configurations. One was the conventional test in which a circular hole was made, and the pressure was applied to the wall of the hole at a given depth by two curved plates to match the curvature of the wall (Sinha, 1990b, and 1991b). The pressure and displacement were measured as a function of time. The other one was called H test in which ice was cut as an H in the horizontal plane to reduce the confinement, and a hole was made in the center of the H. The main objectives of doing the H test were to investigate the effects of confinement and anisotropy on the rate dependence of strength, and deformation of the oriented columnar grained sea ice. The initial plan was to do H test with different dimensions for H and loading rates. Due to the difficulty in cutting ice in the field, only the loading rate effect was investigated.

3.2 Growth history of the ice sheet

Canada has four weather stations in the High Arctic: Alert, Eureka, Resolute, and Mould Bay. The weather stations are operated by the Atmospheric Environment Services of Canada. The growth histories of sea ice in Resolute Bay, adjacent to the Inuit village, are recorded by the Resolute weather station as part of their routine. The growth of the ice and snow thicknesses at the test site was measured every week by the staff from the weather station. Based on the information obtained from the weather station in Resolute, a field test site 300 meters off the shore in Resolute Bay was chosen.

The mean daily air temperature for 1991-1992 season in Resolute is shown in Fig. 3.1. The freeze up data for the bay was September 28, 1991. The measured ice and snow thicknesses in the bay during the winter of 1991-1992 are plotted in Fig. 3.2. The solid straight line is a good representation of the increase in snow thickness with time. Snow densities and snow thickness were also measured at a land site in Resolute by the weather station. The measured snow density and snow thickness at the land site is shown in Fig. 3.3.

The ice cover in the bay was found to be very flat except near the shore line. Microstructure studies, to be discussed in Section 3.3 in details, showed that the ice in the bay was oriented columnar grained sea ice except for the top 2 cm.

A simple model for estimating the growth of first year sea ice in the High Arctic was proposed by Sinha and Nakawo (1981). Based on the model, the growth of ice, dh, at any time is given by

$$dh = \frac{k_i K_s}{L\rho} \frac{T_m - T_a}{k_i h_s + k_s h_i} dt \tag{3.1}$$

where k_i and k_s are the thermal conductivity of ice and snow; L is the latent heat of fusion; ρ is the density of sea ice; h_i and h_s are the thickness of ice and snow, respectively; T_m is the freezing point of sea ice; T_a is the ambient air temperature; and t is the time.

If the mean air temperature in Eq. 3.1 is given in terms of days, the growth rate, dh_N, between (N-1)th day and Nth day is given by

$$
\begin{aligned}
dh_i^N &= \frac{k_i k_s}{L\rho}\frac{T_m - T_a}{k_i h_s^\theta + k_s h_i^\theta} \\
h_s^\theta &= h_s^{N-1} + \theta dh_s^N \\
h_i^\theta &= h_i^{N-1} + \theta dh_i^N
\end{aligned} \tag{3.2}
$$

where θ is a parameter between zero and one, in the calculation θ is given as 0.5; h_s^{N-1} and h_i^{N-1} are snow and ice thickness at the end of the (N-1)th day after freezing up, respectively; dh_s^N and dh_i^N are the increase of snow and ice thickness during the Nth day.

Rearrangement of Eq. 3.2 gives

$$
k_s 0(dh_i^N)^2 + (k_i h_s^\theta + k_s h_i^{N-1})dh_i^N = \frac{k_i k_s}{L\rho}(T_m - T_a) \tag{3.3}
$$

Based on Eq. 3.3, the ice thickness was calculated daily using the daily mean air temperature and the physical properties of snow and ice shown in Table 3.1. The ice thickness at the freeze up point (September 28, 1991) was assumed to be zero. A linear increase of snow thickness on the surface of ice with time was assumed (Fig. 3.2). The average snow density on the land measured during the same period (Fig. 3.3) was used for the calculation.

Table 3.1 Physical properties of snow and ice

T_m	-1.8 ^0C for sea water with salinity 32 parts per thousand
ρ	0.91 g/cm^3 Field measurement
L	70 cal g^{-1} (Anderson 1960; Schwerdtfeger 1963)
k_i	5×10^{-3} cal $cm^{-1}s^{-1}$ $^0C^{-1}$ for sea ice of about 4 parts per thousand salinity (Schwerdtfeger 1963)
k_s	4.8×10^{-4} cal $cm^{-1}s^{-1}$ $^0C^{-1}$ for snow density 286 kg/m^3 at -20 ^0C to -30 ^0C (Pitman and Zuckerman 1967; Mellor 1977)

Figure 3.4 shows the comparison between the actual measurement of the ice thickness and the prediction from Sinha and Nakawo's model. It is shown that this simple model provides an acceptable estimation of the growth of sea ice.

A comparison of the daily growth rate calculated from the theory and the daily growth rate estimated from the field measurement is made in Fig. 3.5 in terms of ice thickness (top) and time (bottom), respectively.

Since the ice thicknesses were measured once a week and the locations were randomly selected in a general area, the estimated growth rate showed a large scatter. Therefore, a running mean of three points (two weeks) were calculated for the entire period. There are shown in Fig. 3.6. To take into account of the thermal inertia of the ice cover, it was also decided to apply an average method to the theoretical calculations. The solid lines in Fig. 3.6 represent the running mean, over two week period, of the theoretical results.

3.3 Salinity and brine layer spacing

3.3.1 Method of measurement

Two full ice cores about 2 meters were recovered from Resolute Bay with a fiber glass core auger with an inside diameter of about 10 cm, when the air temperature was about -15^0C. The top of each core was marked, before sampling, with respect to a fixed land mark on the shore. Subsequent pieces of the ice cores were matched carefully and marked. They were then transported to the base camp, Polar Continental Shelf Project, in half an hour. The ice cores were stored at -20 ^0C for about 10 hours. Sections for salinity measurement were collected, using a band saw inside a cold room at temperature -15^0C, every 2.5 cm all the way down to about 4 cm above the bottom of the core. Salinity samples were stored in individual sealed containers. They were then taken to a warm room and were melted at room temperature overnight. A salinometer was used to measure the salinity at temperature about 22^0C.

While collecting salinity samples, it was found that this full core was solid ice free from any brine channels. It was then decided to do microstructure studies also on the same core, even though the top 70 cm of the core was already sectioned for salinity measurement. Horizontal thick sections, for microstructural analyses, were made for about 10 cm apart starting 80 cm below the top surface. Thick sections for the top 80 cm were collected from another core which was located

less than 2 meters away from the first full core in the test site. Thin sections were made from thick sections using the double microtoming technique (Sinha, 1977) at a temperature of about -15 ^{0}C. All together 19 horizontal and three vertical thin sections were made. Thin sections were photographed with known magnification, using cross polarized light, scattered light, and combined cross polarized light and scattered light.

The brine layer spacing measurements in the field were done with a microscope soon after the thin sections were made. Later on in Ottawa, a slide projector was used to measure the brine layer spacing from the slides taken with combined cross polarized light and scattered light.

3.3.2 Test results and analyses

One horizontal thin section at a depth of 80 cm and one vertical thin section at depth between 14 cm and 28 cm are presented in Fig. 3.7. This figure shows that the ice is oriented columnar grained. The mean c-axis of the grain was oriented parallel to the shore line, identified from the markings on the core.

The vertical salinity distribution exhibits a "C" type of curve with higher salinity near the top and the bottom surfaces as shown in Fig. 3.8. In the bulk of the ice, the salinity decreases with an increase in ice thickness. This decrease in salinity with depth is related to the decrease in the growth rate of ice. This is in agreement with innumerable previous observations on first year sea ice.

The relationship between the average brine layer spacing and the ice thickness is shown in Fig. 3.9. The two dotted lines represent the brine layer spacing measured in the field and in the laboratory. The figure shows that over all with the increase of ice thickness, the brine layer spacing increases. The average brine layer spacing is about 0.75 mm through the whole ice thickness.

Looking at Figs. 3.8 and 3.9 more closely, the sharp decrease of salinity at depth between 50 and 100 cm (see Fig. 3.8) is accompanied by the sharp increase of brine layer spacing around the same ice depth.

The theoretical growth rate obtained from Sinha and Nakawa's model was used for plotting the average brine layer spacing and salinity versus growth rate. Three reasons are given for the use of the theoretical growth rate. First, the ice thickness

measured in the field represented ice thickness at different locations in a small area, which does not represent growth of ice in one specific position. Therefore, the growth rate from field measurement may give some errors. Secondly, the growth of ice from 0 to 0.6 meters is not available from the field measurement, due to the safety considerations. And thirdly, the growth of ice predicted from Sinha and Nakawo's model gives a very good representation of the growth of ice as shown in Fig. 3.4.

Figure 3.10 shows the dependence of brine layer spacing on the theoretical growth rate. This figure clearly shows that with the increase of the growth rate, the brine layer spacing decreases, which is consistent with previous laboratory investigations by Weeks and Hamilton (1962), and Arctic sea ice studies of Nakawo and Sinha (1984).

The relationship between salinity and growth rate was formulated by Weeks and Lofgren (1967) based on the theoretical consideration of Burton et al. (1953). The proposed relation is given by

$$q = \frac{q_0}{q_0 + (1 - q_0)exp(-\frac{\delta v}{D})} \tag{3.4}$$

where q is the effective solute distribution coefficient defined as solute concentration in the solid divided by the solute concentration in the solution; q_0 is the effective value of q at very low growth rate; D is diffusion coefficient of the solute in the solution; δ is the thickness of diffusion limited boundary layer; v is the growth rate.

Table 3.2 List of $\frac{\delta}{D}$ and q_0 used by different authors

Authors	$\frac{\delta}{D}$, $s.cm^{-1}$	q_0	Type of ice
Weeks and Lofgren, 1967	5090	0.26	N_aCl ice
Cox and Weeks, 1975	7243	0.26	N_aCl ice
Nakawo and Sinha, 1981	42000	0.12	FY sea ice
Present study, 1992	42000	0.0594	FY sea ice

Figure 3.11 shows the dependence of salinity at the time when the sample is

taken on the growth rate. The solid line is obtained with Eq. 3.4 using parameters shown in Table 3.2. In the calculation, $q_0 = 0.0594$ is chosen based on the lowest salinity measured. This figure shows that with the increase of the growth rate, the salinity increases.

The dependence of the brine layer spacing on the salinity is shown in Fig. 3.12. With the increase of salinity, the brine layer spacing decreases.

3.4 Borehole indentation tests

3.4.1 Test method

In-situ borehole indentation tests were carried out in Resolute Bay adjacent to the location where microstructural studies, reported in Section 3.3, were conducted. The borehole indentation test system was loaded on a Komatik and taken to the test site by a snowmobile. All tests were carried out in three consecutive days. The fluctuation of air temperature was small during the test period. Air temperature was measured each day during test. It was around -13^0C to -15^0C. The temperature at snow ice interface was around -11^0C. The ice temperature at about 80 cm below surface was about -8.7^0C. The test was carried out at a depth of about 34 cm below the surface of ice sheet. Therefore, the ice temperature can be estimated as -10^0C. Ice temperature remained constant during the test period.

The test arrangement is shown in Fig. 3.13. After drilling a hole of 15 cm in diameter to about 60 cm with a fiber-glass core auger, the ice sheet was marked for the cutting. The ice sheet was cut with a chain saw to a depth of about 55-60 cm to an H shape in the horizontal plane as shown in Fig. 3.14. The size of the H in the horizontal plane was about 2 m $\times$ 0.92 m. The test was carried out to a depth of about 34 cm with different loading rate. The pressure was applied to the ice hydraulically by pushing plates on the opposite ends of two circular indentors (see Fig. 3.15) with a diameter of 9 cm. The loading rate was controlled by a flow control valve. A pressure transducer in the hydraulical system was calibrated to give the average applied pressure on the plates, and two LVDT type displacement gauges provided data on the relative displacement of the plates into ice. The

pressure and the relative displacement were recorded in both a chart recorder and a digital data logger. Details of the test system was described by Sinha (1990b, 1991b). It takes about half an hour to finish an H test. For a conventional test, only 5 minutes is needed.

3.4.2 Test results and analysis for H test

Ten H tests were carried out with different ACL (angle between the mean c-axis and loading direction) under different loading rate. Details of the test results are given below.

Figure 3.16 shows one of the borehole indentation test result with the mean c-axis parallel to the loading direction. Similar to a uniaxial constant displacement rate test with a soft machine (Sinha, 1981a), the indentation rate increases with time to approaches a constant value (Fig. 3.16a). The stress increases to a maximum value with the increase of the indentation rate. Later on, the stress decreases with the onset of the constant indentation rate. The displacement rate is not constant due to the stiffness of the test system, the displacement rate and the stress rate up to the maximum stress or failure are then calculated as an average value up to the maximum stress (Sinha, 1987).

Figures 3.17 and 3.18 show similar test results as Fig. 3.16 with the mean c-axis 45 degrees and normal to the loading direction, respectively.

The rate dependence of the stress and displacement diagram is shown in Fig. 3.19 with an ACL angle zero degree. All of the curves show that the stress increases to a maximum at about the same displacement, and then decreases. However, the maximum stresses are different for different loading rates. A higher loading rate results in a higher maximum stress.

Similar rate dependence of stress and displacement diagrams are shown in Figs. 3.20 and 3.21 for ACL angle 45 and 90 degrees, respectively.

A comparison of stress and displacement diagram for ACL angle 0 and 90 degrees is shown in Fig. 3.22 with about the same displacement rate. Basically, not much difference can be detected considering the uncertainty of ice properties from place to place.

Figure 3.23 presents the comparison of stress and displacement diagram for

ACL angle 45 and 90 degrees at about the same displacement rate. Similar to Fig. 3.22, not much difference can be detected.

The maximum stresses are of interest from the engineering point of view. Table 3.3 lists some information about the displacement, time, and stress when maximum stress occurred.

Table 3.3 Results of H tests

Test no.	ACL	$\dot{D}$ mm/s	σ_f MPa	D_f mm	t_f s
Test 1	0.0	0.0312	14.35	3.24	103.7
Test 2	0.0	0.1909	23.27	3.34	17.5
Test 3	0.0	0.1382	24.55	4.70	34.0
Test 4	90.0	0.0054	9.69	2.71	499.2
Test 5	90.0	0.1163	24.29	3.81	32.7
Test 6	90.0	0.1816	25.40	3.63	20.0
Test 7	90.0	0.1016	23.36	3.05	30.0
Test 8	90.0	0.0391	18.23	3.12	80.0
Test 9	45.0	0.0768	20.28	3.49	45.5
Test 10	45.0	0.0604	18.70	3.92	65.0

In the Table 3.3, D is the displacement on the surface of ice and borehole indentor; σ is the average stress applied on the surface of the borehole, which is calculated as the load applied divided by the area of the borehole indentor; σ_f is the maximum stress reached in each test; $\dot{D}$ is the average displacement rate to the maximum stress; D_f and t_f are the displacement and time to the maximum stress.

Figure 3.24 shows the rate dependence of the maximum stress for H test with different angles between the mean c-axis and the loading direction. Two correlations (solid lines in Fig. 3.24) are obtained based on the test data, which are given as

$$\begin{aligned} \sigma_f &= 41.2\dot{D}^{0.276} \\ \sigma_f &= 24.5\dot{\sigma}^{0.233} \end{aligned} \tag{3.5}$$

In general, Fig. 3.24 shows that the maximum stress increases with the increase of the loading rate. However, the angle between the mean c-axis and the loading direction has a negligible effect on the maximum stress. Similar conclusion has been drawn for conventional borehole indentation test by Sinha (1987). Two reasons could be used to explain that. First, the test was conducted at a depth of 34 cm, therefore, the order of the c-axis orientation, in terms of the scatter angle of the c-axis, at that point is still high. Based on the model prediction in Chapter 5, when the scatter angle is higher than 45 degrees, the ACL angle has no effect on the maximum stress of the ice. Secondly, the orientations of the principal stress around the borehole indentor, as the FE analyses showed in Chapter 6, are different at different locations. Therefore, an ACL angle of 45 degrees does not mean that the major principal stress is 45 degrees to the mean c-axis. Therefore, a small effect would be expected.

Large scale radial cracks were observed in the H tests. The orientation of the large crack depends on the angle between the mean c-axis and loading direction as shown in Fig. 3.25. In general, all the large cracks are formed in the vertical plane. However, the crack orientation in the horizontal plane is quite different with the different loading directions. When the loading direction is parallel to the mean c-axis, the crack radiates from the center of the indentor and is parallel to the mean c-axis. When the loading direction is 45 degrees to the mean c-axis, the crack tends to orientate again to the mean c-axis direction. However, when the loading direction is normal to the mean c-axis, the cracks formed at the two sides of the borehole indentor, the orientation of the cracks is about 45 degrees to the loading direction. This strong dependence of the crack orientation on the ACL angle is explained in Chapter 6 based on the principal stress distribution around the borehole indentor.

The indentation rate dependence of the time and deformation at failure is presented in Fig. 3.26 for H tests. As shown in Fig. 3.26, a straight line can be used to represent the indentation rate dependence of time at failure. The following relationship between the indentation rate and time at failure is obtained using the least square method.

$$t = 4.44\dot{D}^{-0.908} \tag{3.6}$$

A power of -0.90S is very close to -1.0, which implies that the failure time is almost inversely proportional to the indentation rate. This is further confirmed by the negligible rate dependence of the deformation at failure as shown in Fig. 3.26(b).

3.4.3 Test results and analysis for conventional test

Eighteen conventional tests were carried out with different ACL angle. Details of the test results are presented below.

Figure 3.27 shows the conventional borehole indentation test results with the mean c-axis 45 degrees to the loading direction. It shows that initially the increase of stress is fast while the indentation rate is low. Later on, the indentation rate is high, while the increase of stress is small.

In most of the conventional tests, stress continues to increase after yielding at a constant displacement rate. Yield stress is defined as the stress at the onset of the constant indentation rate as shown in Fig. 3.27. This definition for yield stress corresponds to the failure stress in the case of H test. The stress and displacement rate are then defined as the average values up to the yield point (Sinha, 1987).

Similar test results are obtained for ACL angle 45 and 90 degrees as shown in Figs. 3.28 and 3.29, respectively.

The rate dependence of the stress and displacement diagram is shown in Fig. 3.30 with an ACL angle zero degree. Overall, it shows that the increase of loading rate results in a higher maximum stress.

Similar results are obtained for ACL angle 45 and 90 degrees as shown in Figs. 3.31 and 3.32, respectively.

A comparison of stress and displacement diagram for ACL angle 0 and 90 degrees is shown in Fig. 3.33 with about the same displacement rate. Basically, no difference can be detected considering the variation of other factors.

Figure 3.34 presents the comparison of stress and displacement diagram for ACL angle 45 and 90 degrees at about the same displacement rate. Similar to Fig. 3.33, no difference can be detected.

The yield stresses are of interest from the engineering point of view. Table 3.4 lists the information about the displacement, time, and stress at the point when

the yield stress occurred.

Table 3.4 Results for conventional tests

Test no.	ACL	$\dot{D}$ mm/s	σ_y MPa	D_y mm	t_y s
Test 1	0.0	0.1324	22.18	9.27	70.0
Test 2	0.0	0.1267	24.86	7.35	58.0
Test 3	0.0	0.0377	16.95	4.15	110.0
Test 4	0.0	0.1509	26.34	5.58	37.0
Test 5	0.0	0.0151	11.23	2.64	175.0
Test 6	0.0	0.0323	16.05	5.43	168.0
Test 7	45.0	0.0841	20.23	6.06	72.0
Test 8	45.0	0.1040	21.83	5.41	52.0
Test 9	45.0	0.0989	22.47	5.24	53.0
Test 10	45.0	0.0875	22.69	5.86	67.0
Test 11	45.0	0.0223	13.22	4.01	180.0
Test 12	45.0	0.0078	10.08	2.03	260.0
Test 13	90.0	0.2337	29.33	5.84	25.0
Test 14	90.0	0.0803	21.79	4.17	52.0
Test 15	90.0	0.1258	24.71	5.78	46.0
Test 16	90.0	0.0949	23.76	4.84	51.0
Test 17	90.0	0.1320	27.41	3.96	30.0
Test 18	90.0	0.0041	8.60	1.58	390.0

In the Table 3.4, σ_y is defined as yield stress as shown in Fig. 3.27; D_y and t_y are displacement and time to yield stress; $\dot{D}$ is the average displacement rate up to the yield point.

Both the stress and displacement rate dependence of the yield stress for conventional tests is presented in Fig. 3.35. The solid lines are correlation obtained from the test data, which are given by

$$\begin{aligned} \sigma_y &= 47.5\dot{D}^{0.321} \\ \sigma_y &= 30.0\dot{\sigma}^{0.319} \end{aligned} \tag{3.7}$$

The above correlation between stress at yield and the indentation rate is almost the same as the relationship between the maximum stress and strain rate proposed by Sinha (1984a) under uniaxial loading condition for first year columnar grained sea ice.

$$\sigma_f = 45.0\dot{\epsilon}^{0.32} \tag{3.8}$$

Figure 3.35 shows that the yield stress increases with the increase of loading rate. However, the angle between the mean c-axis and loading direction has negligible effects on the dependence of the yield stress on the loading rate. Similar conclusion has been drawn by Sinha (1987) with FENCO borehole jack test results.

The stress rate dependence of the yield stress given in Eq. 3.7 agrees quite well with the FENCO borehole jack test results on similar first year oriented columnar grained sea ice (Sinha, 1987).

The indentation rate dependence of the time and deformation to yield or failure is presented in Fig. 3.36 for conventional tests. As shown in Fig. 3.36, a straight line can be used to represent the indentation rate dependence of time at failure. The following relationship between the rate and time at failure is obtained using the least square method.

$$t = 12.04\dot{D}^{-0.66} \tag{3.9}$$

The time to yield decreases with the increase of loading rate. The displacement at yield has a small dependence on the loading rate as shown in Fig. 3.36.

3.4.4 Comparisons between conventional and H test

Figure 3.37 presents a comparison of stress and displacement diagram between the conventional and H tests at about the same displacement rate for an ACL angle 0 degree. Before reaching the maximum stress for H test, the two results are consistent. However, after the maximum stress, the stress starts to decrease for H test, while the stress for conventional test still increases at a very low rate. H test gives a point where the failure occurs, while the conventional test does not.

Similar results are presented in Figs. 3.38 and 3.39 for ACL angle 45 and 90 degrees, respectively.

The comparison of the rate dependence of stress at yield or at failure for both conventional and H tests is presented in Fig. 3.40. In general, result for conventional test gives a higher stress at yield. However, the difference is considered insignificant.

The comparison of the rate dependence of time to failure is presented in Fig. 3.41. The time to yield is higher for conventional test than that for H test.

The comparison of the rate dependence of displacement to yield is presented in Fig. 3.42. Overall, the displacement at yield is higher for conventional test, which implies that the behaviour of sea ice is more ductile under conventional test condition than that under the H test condition.

The rate dependence of the maximum stress or yield stress is related mainly to the viscous strain. In the case of Sinha's creep model without cracking (Sinha, 1978a), the rate dependence of the maximum stress can be given as

$$\frac{\sigma_f}{\sigma_1} = (\frac{\dot{\epsilon}}{\dot{\epsilon}_{v1}})^{\frac{1}{n}} = (\frac{\dot{\epsilon}}{\dot{\epsilon}_{v1}})^{p} \tag{3.10}$$

where σ_f is the maximum stress; σ_1=1.0 MPa is a reference stress; n is the stress power; p is the strain rate power.

Without cracking, the maximum stress is dependent on the strain rate with a power of 0.333. When crack happens, the strain rate will have a stronger dependence on stress as reported as power law break down (Sinha, 1989a). Therefore, with the crack activities, the rate dependence of the maximum stress will be smaller. A strain rate power of less than 0.333 will be expected with the crack activities.

As reported earlier, an indentation rate power of 0.28 is obtained for the rate dependence of the maximum stress in H test. While, a power of 0.32 is obtained for conventional test. This difference in the rate dependence of the maximum stress between conventional and H test may signify that the crack activities in the H test is more pronounced than that in conventional H test.

The similarity of the strain rate power p for fresh water ice under uniaxial con-

stant displacement rate test was investigated by Sinha (1981b). A list of the strain rate power is given in Table 3.5 under different loading conditions for different fresh water ice.

Table 3.5 Strain rate power obtained by different authors

Authors	Power	Test	ice type	Temp.
Michel, 1978a	0.34	CD	S2	-10.0
Frederking, 1977	0.299	CD	S2	-10.0
Gold and Krausz, 1971	0.25	CD	S2	-10.0
Sinha, 1981a	0.33	CD	S2	-10.0
Sinha, 1982	0.345	CD	S2	-10.0
Timco & Frederking, 1982	0.29	CD	S2	-10.0
Mellor & Cole, 1983	0.292	CD	T1	-5.0
Mellor & Cole, 1983	0.332	CS	T1	-5.0

In the above table, CD represents the constant displacement rate test; and CS represents the constant load test. As listed in the Table 3.5, all of the strain rate power p are close to 0.33 except the value obtained by Gold and Krausz. As pointed out by Sinha (1981b), the strain rate power obtained by Gold and Krausz was based on test results on various type of ice.

Similar to fresh water ice, a similarity of strain/indentation rate power is existed among sea ice as shown in Table 3.6.

Table 3.6 Strain/indentation rate power for sea ice

Authors	Power	Test	Ice type	Temp.
Sinha, 1984a	0.27	CD	Frazil	-10.0
Sinha, 1984a	0.32	CD	S3b-0	-10.0
Sinha, 1986	0.28	CD	Frazil	-18.0
Sinha, 1986	0.335	CD	Frazil	-10.0
Timco & Frederking, 1986	0.26	CD	S2b	-2.0
Present study 1992	0.321	BITC	S3b	-10.0
Present study 1992	0.287	BITH	S3b	-10.0

In the above table, the number after the ice type represents the ACL angle; BITC stands for conventional borehole indentation test; BITH is for H type borehole indentation test.

This similarity of the strain/indentation rate power between CD laboratory tests and field conventional tests provides an easy way to convert the field strength data to laboratory strength data. To make the conversion, only a calibration is needed by performing field borehole indentation tests and laboratory constant strain rate tests on the same ice at different rate of loading at the same temperature.

As reported earlier, the following rate dependence for conventional borehole indentation test is obtained for first year columnar grained sea ice at an average temperature 263 K.

$$\sigma_y^B = 47.5\dot{D}^{0.321} \tag{3.11}$$

Laboratory uniaxial constant displacement rate test on similar first year columnar grained sea ice gave a relationship between the strain rate and the stress at failure as follow (Sinha, 1984) at temperature 263 K.

$$\sigma_f^L = 45.0\dot{\epsilon}^{0.32} \tag{3.12}$$

A comparison of the above two equations gave

$$\frac{\sigma_y^B}{\sigma_f^L} = 1.05(\frac{\dot{D}}{\dot{\epsilon}})^{0.32} \tag{3.13}$$

In the Eq. 3.13, superscripts B and L are used to represent the conventional borehole indentation test and laboratory constant displacement rate test. The above equation implies that the strength obtained in a field borehole indentation test at a indentation rate of x $mm.s^{-1}$ is about the strength obtained a uniaxial constant displacement rate tests at a strain rate of x s^{-1} at the same temperature.

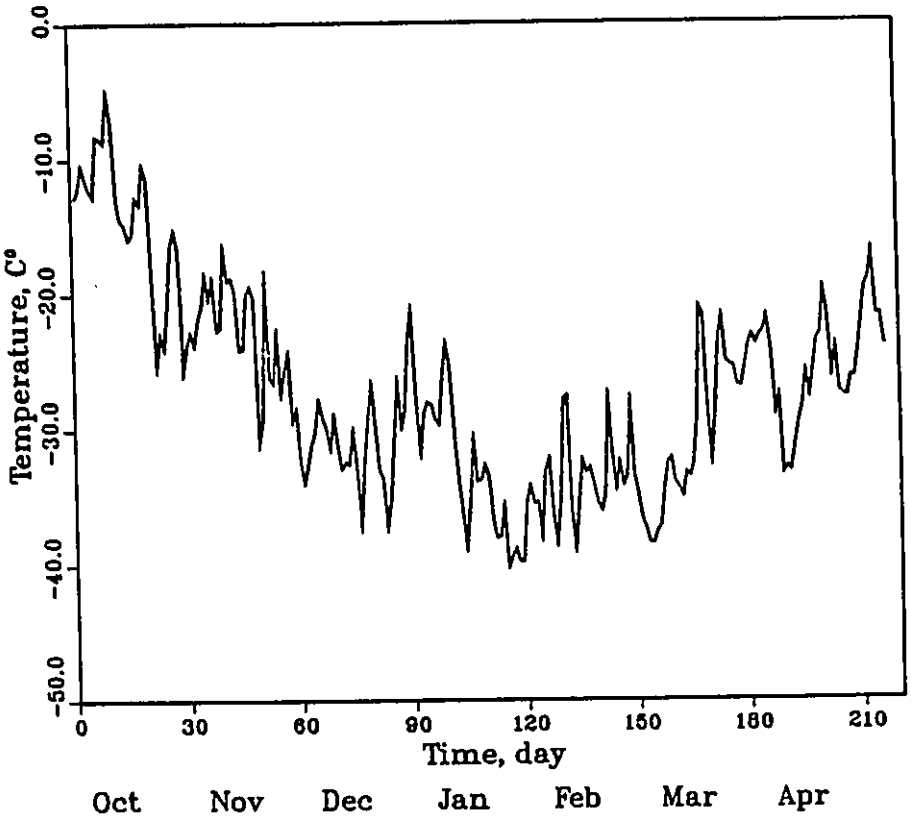

Figure 3.1 Variation of daily mean air temperature winter of 1991–1992 Resolute 74°42'N, 94°50'W, N.W.T., Canada

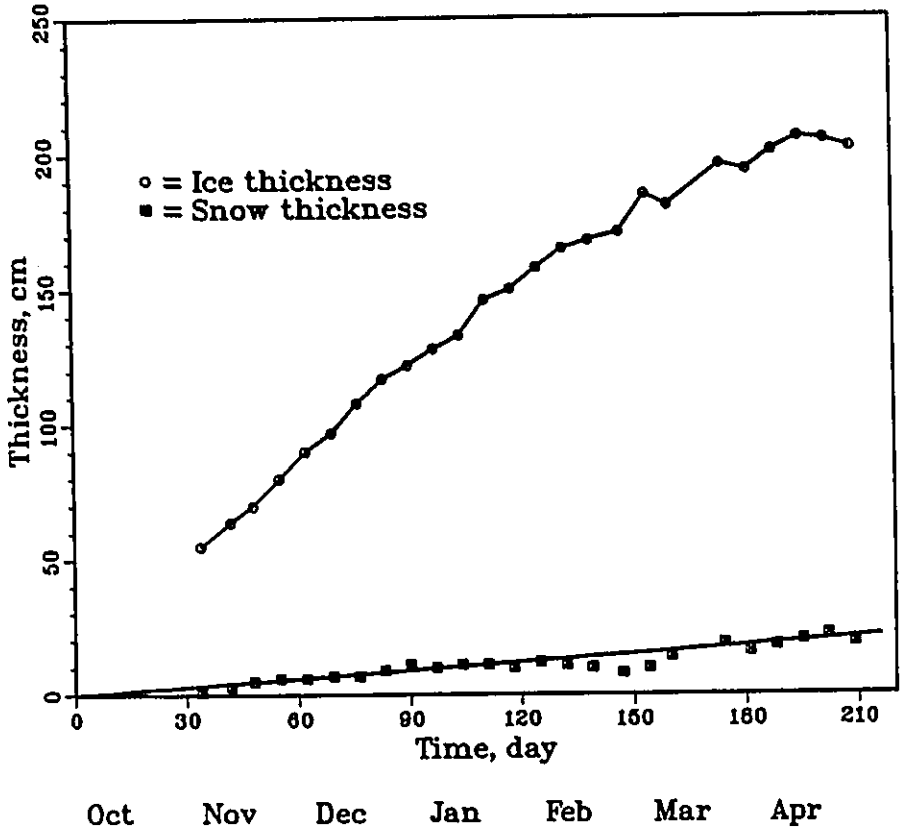

Figure 3.2 Variation of ice and snow thickness during winter of 1991–1992
Resolute 74°42'N, 94°50'W, N.W.T., Canada

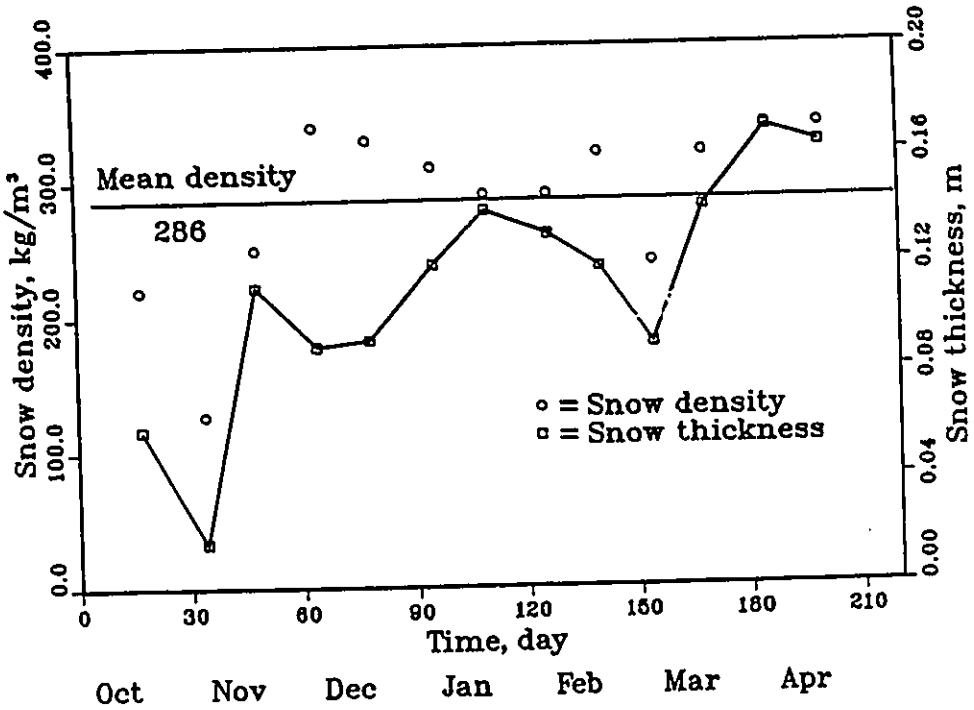

Figure 3.3 Variation of snow density and thickness at a land site during winter of 1991–1992, Resolute, Canada

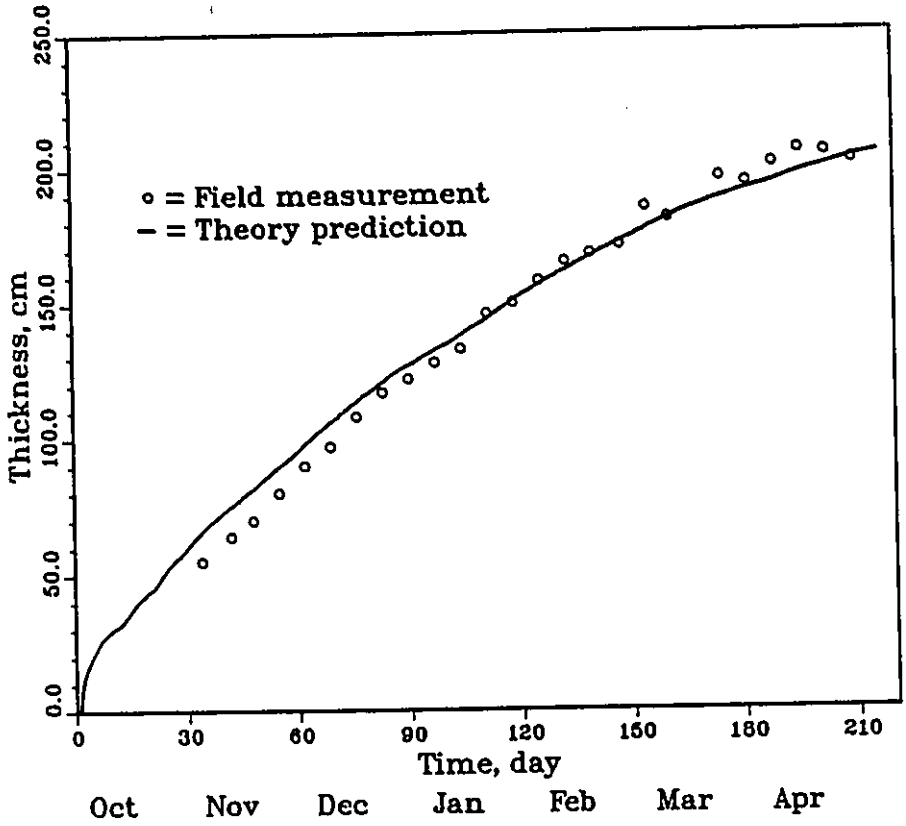

Figure 3.4 Comparison of ice thickness between theory and field measurement for ice in Resolute Bay, Canada

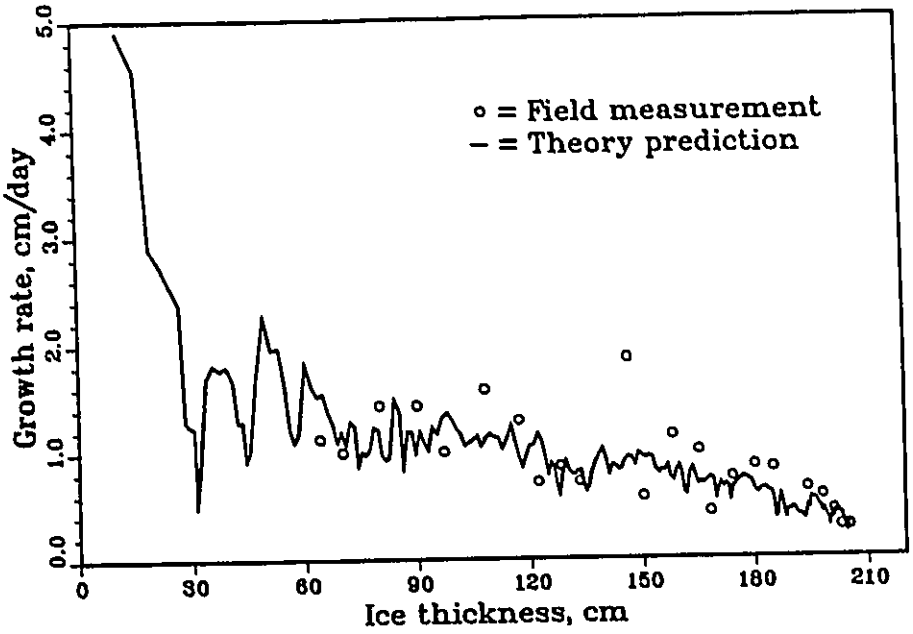

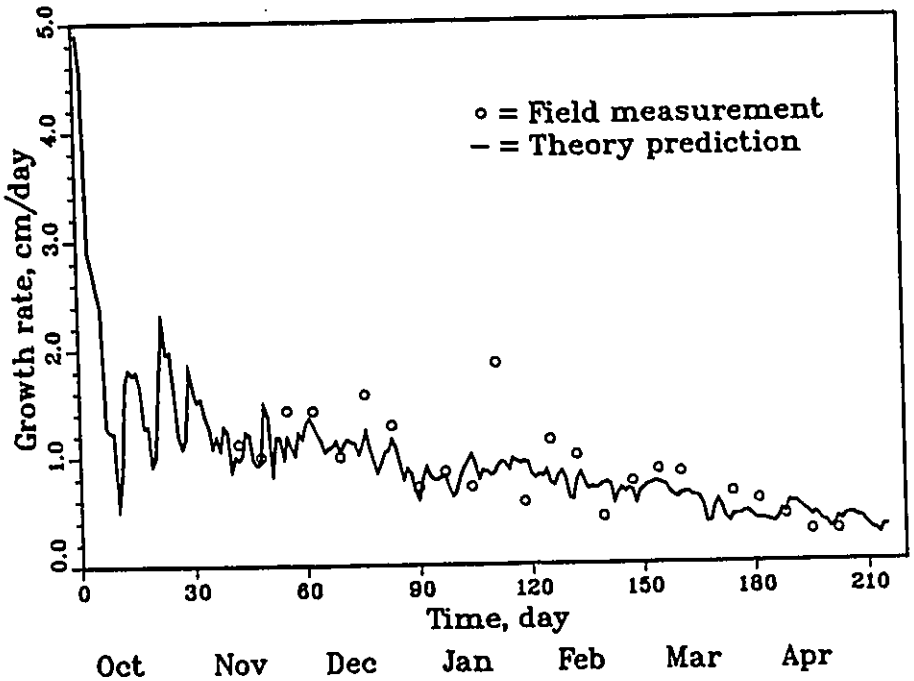

Figure 3.5 Comparison of growth rate in winter of 1991–1992 between theory and field measurement

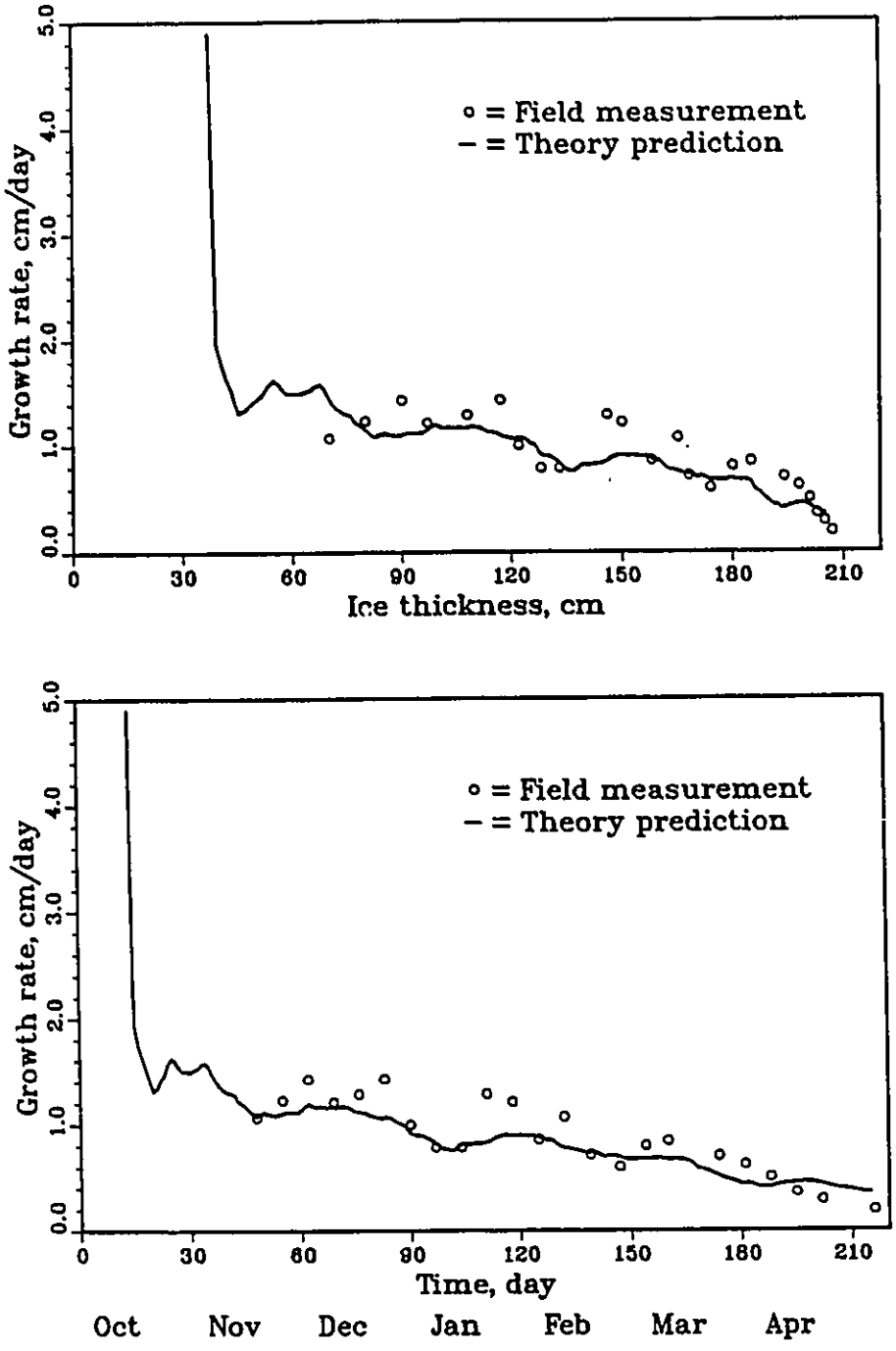

Figure 3.6 Comparison of growth rate in winter of 1991–1992 between theory and field measurement

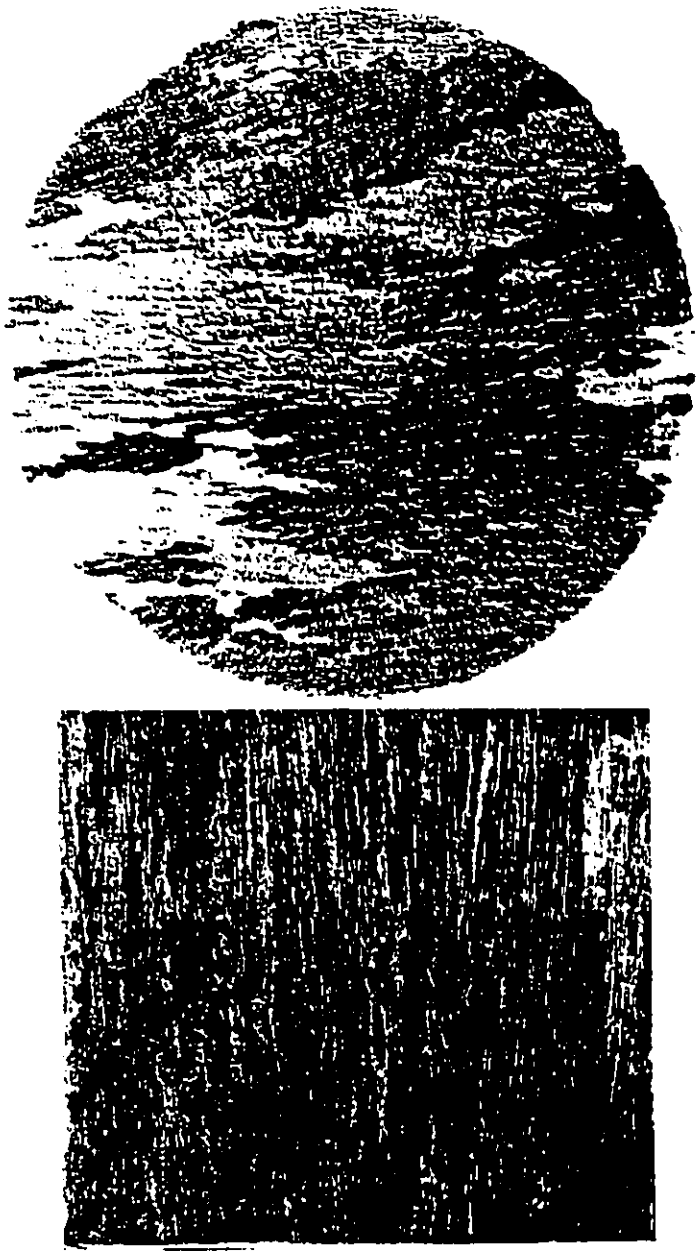

Figure 3.7 Horizontal and vertical thin sections for FY sea ice

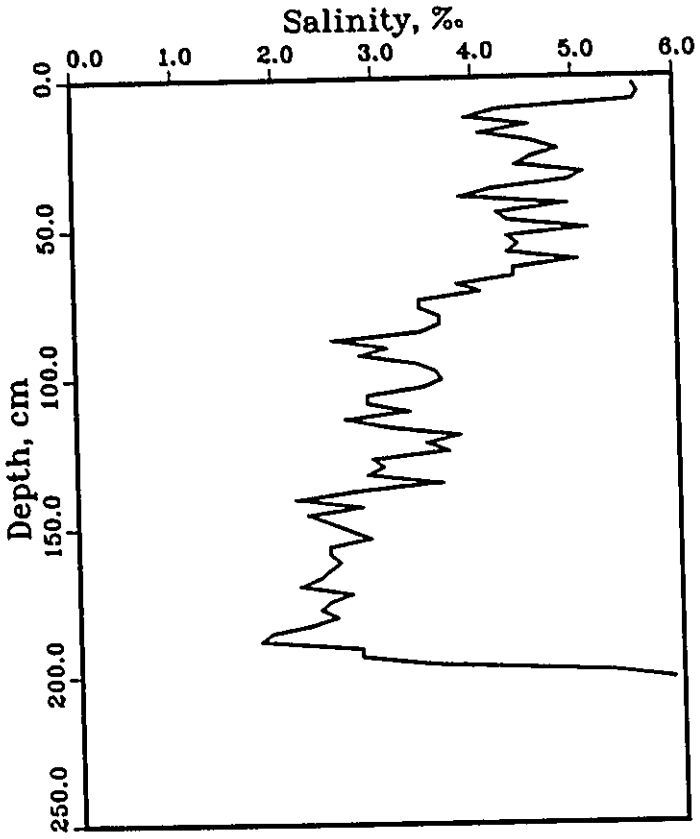

Figure 3.8 Dependence of salinity on depth for FY columnar grained sea ice in Resolute Bay during winter of 1991–1992

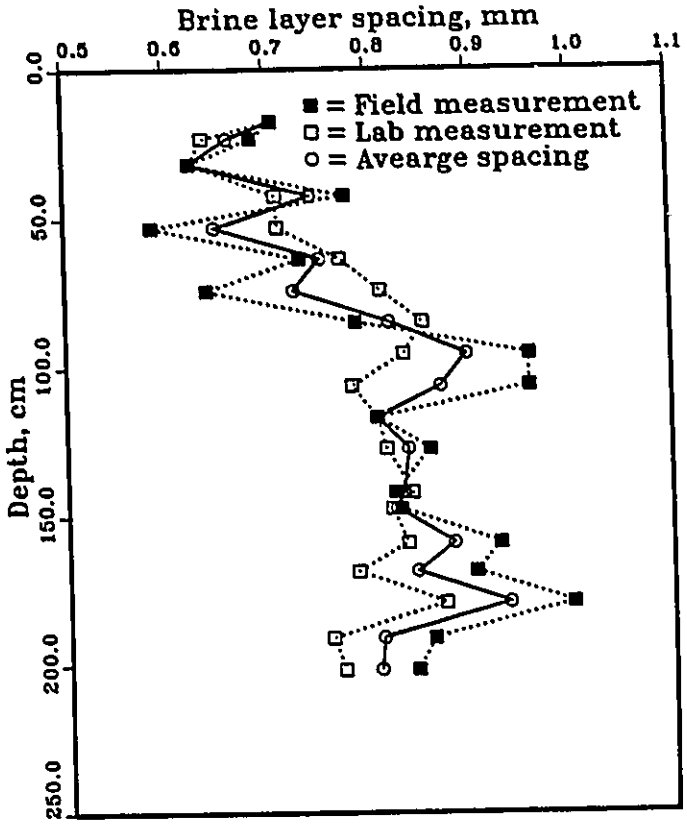

Figure 3.9 Dependence of brine layer spacing on depth of ice in Resolut Bay, Canada

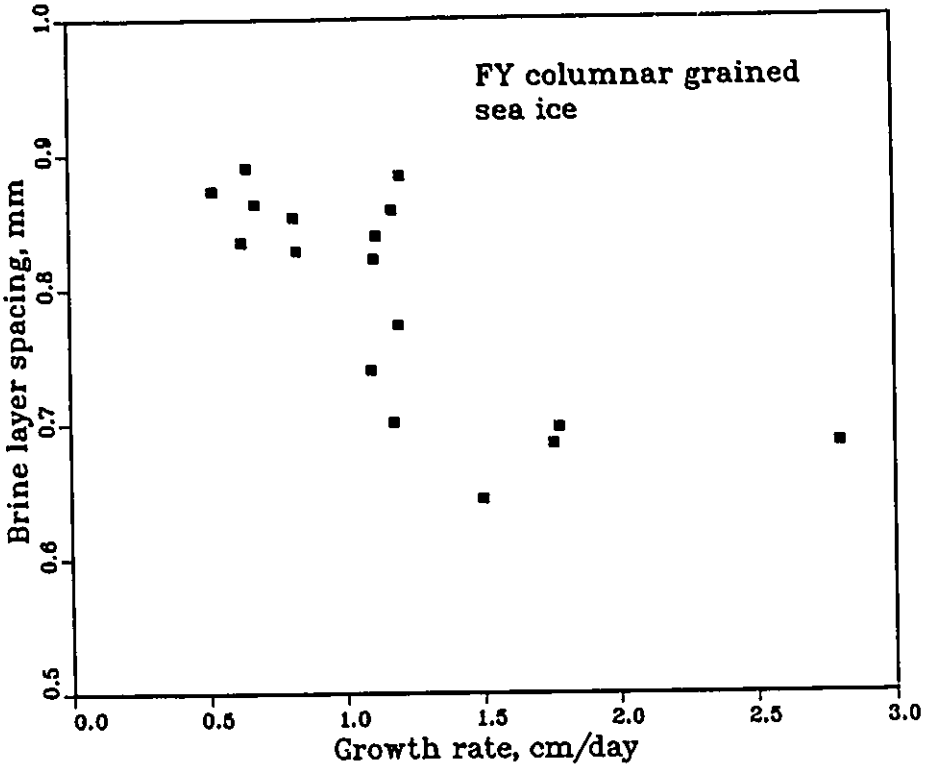

Figure 3.10 Dependence of average brine layer spacing on growth rate during winter of 1991–1992, Resolute Bay Canada

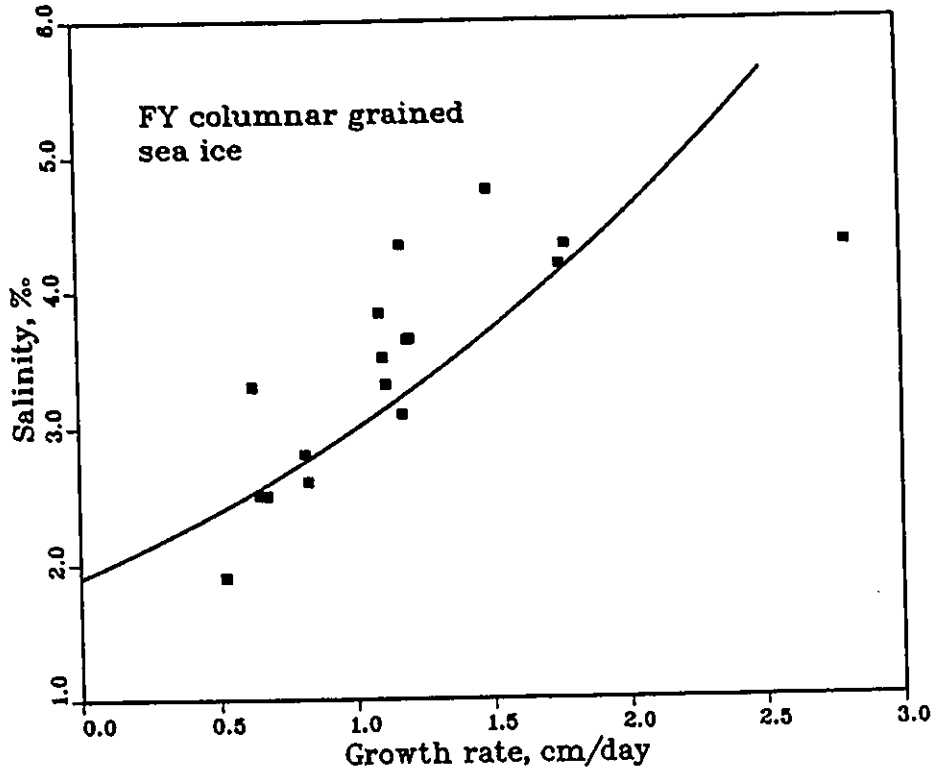

Figure 3.11 Dependence of salinity on growth rate during winter of 1991–1992, Resolute Bay, Canada

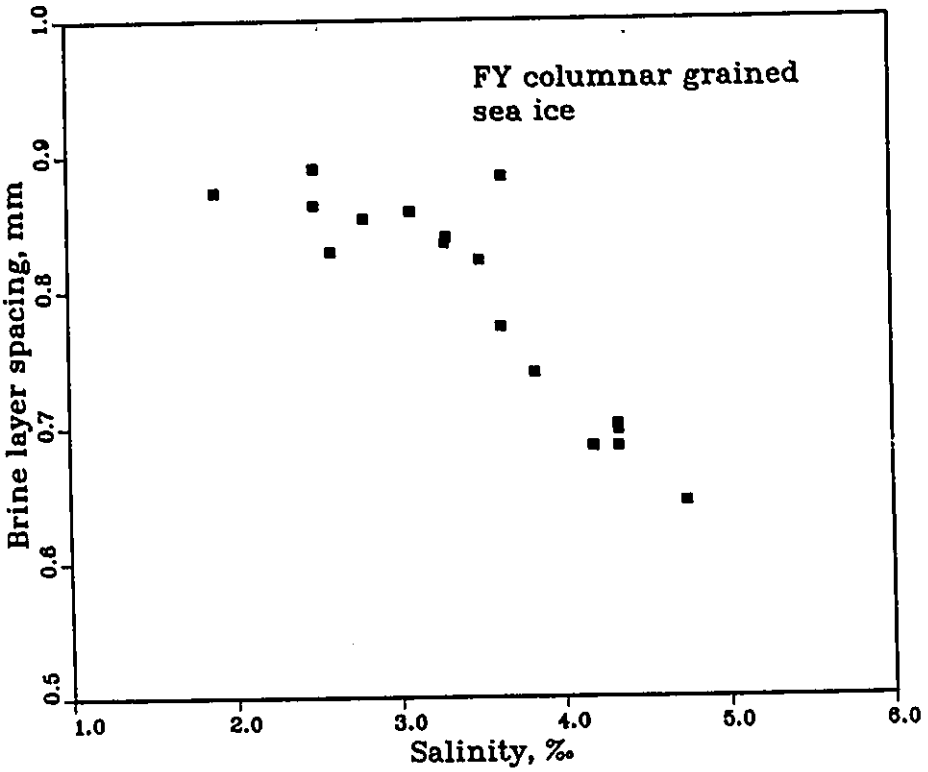

Figure 3.12 Dependence of average brine layer spacing on salinity during winter of 1991–1992, Resolute Bay Canada

Figure 3.13 Field test arrangement with NRCC Borehole indentation test system

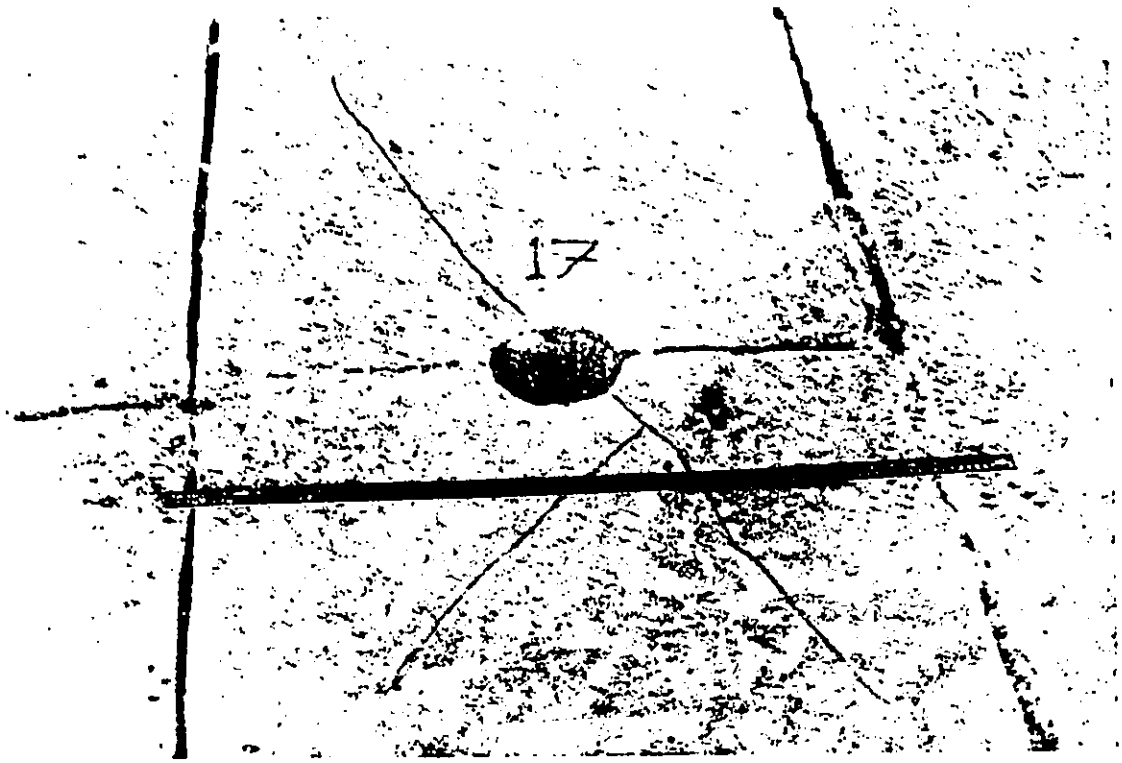

Figure 3.14 Geometry of H test in horizontal plane

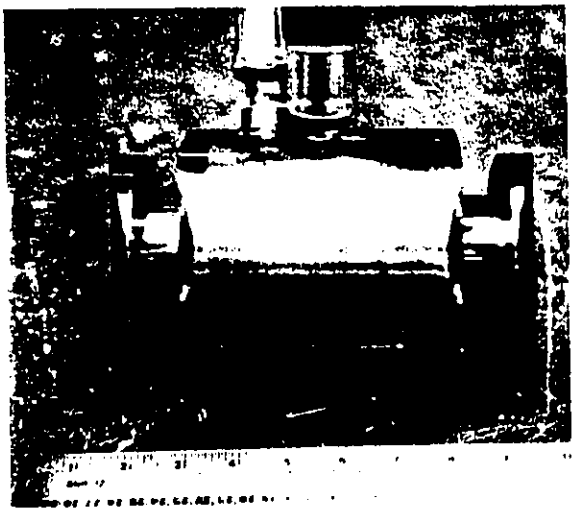

Figure 3.15 NRCC borehole indentor

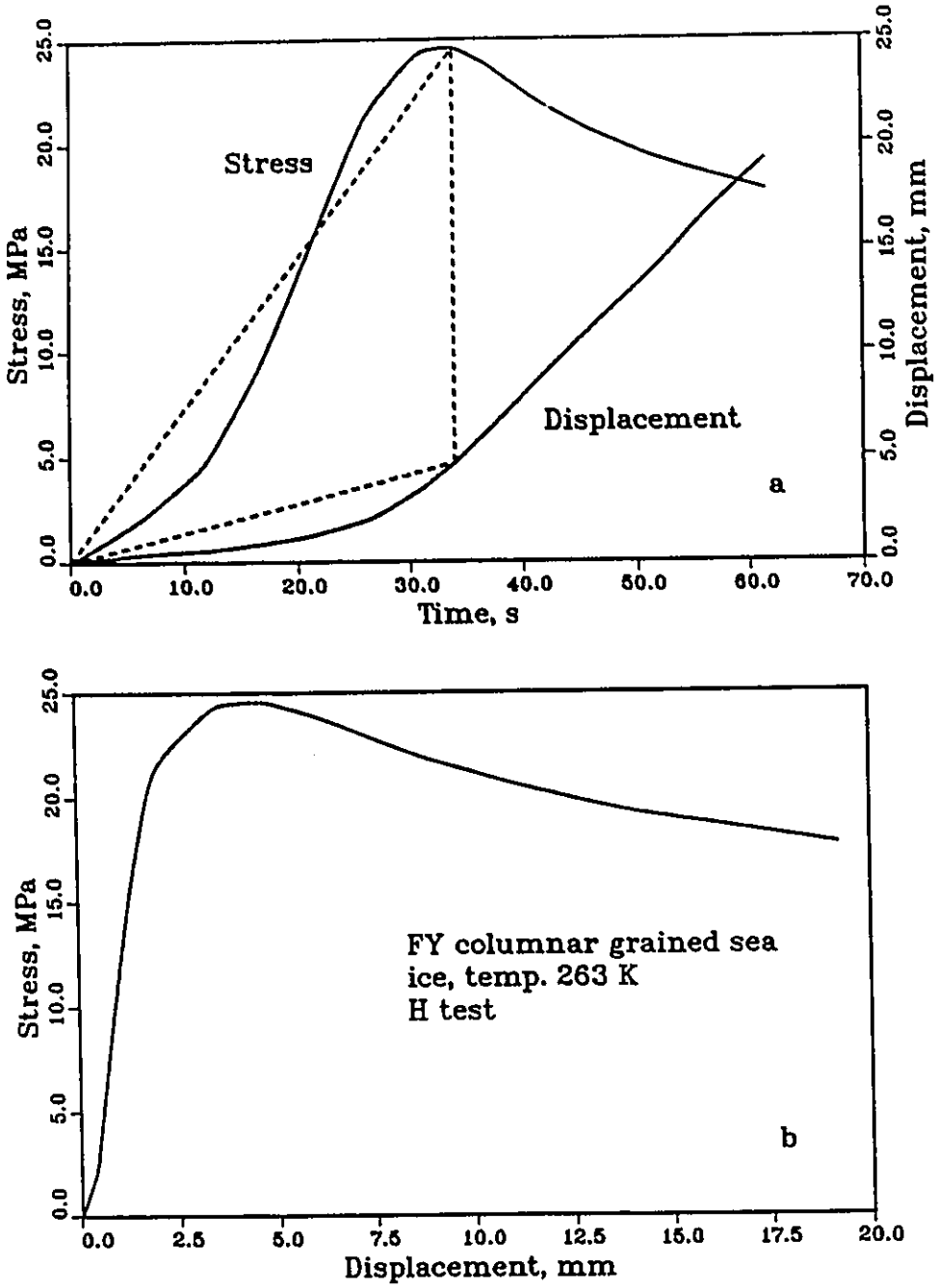

Figure 3.16 H test result with mean c-axis parallel to loading direction
a: Time dependence of stress and displacement
b: Stress and displacement diagram

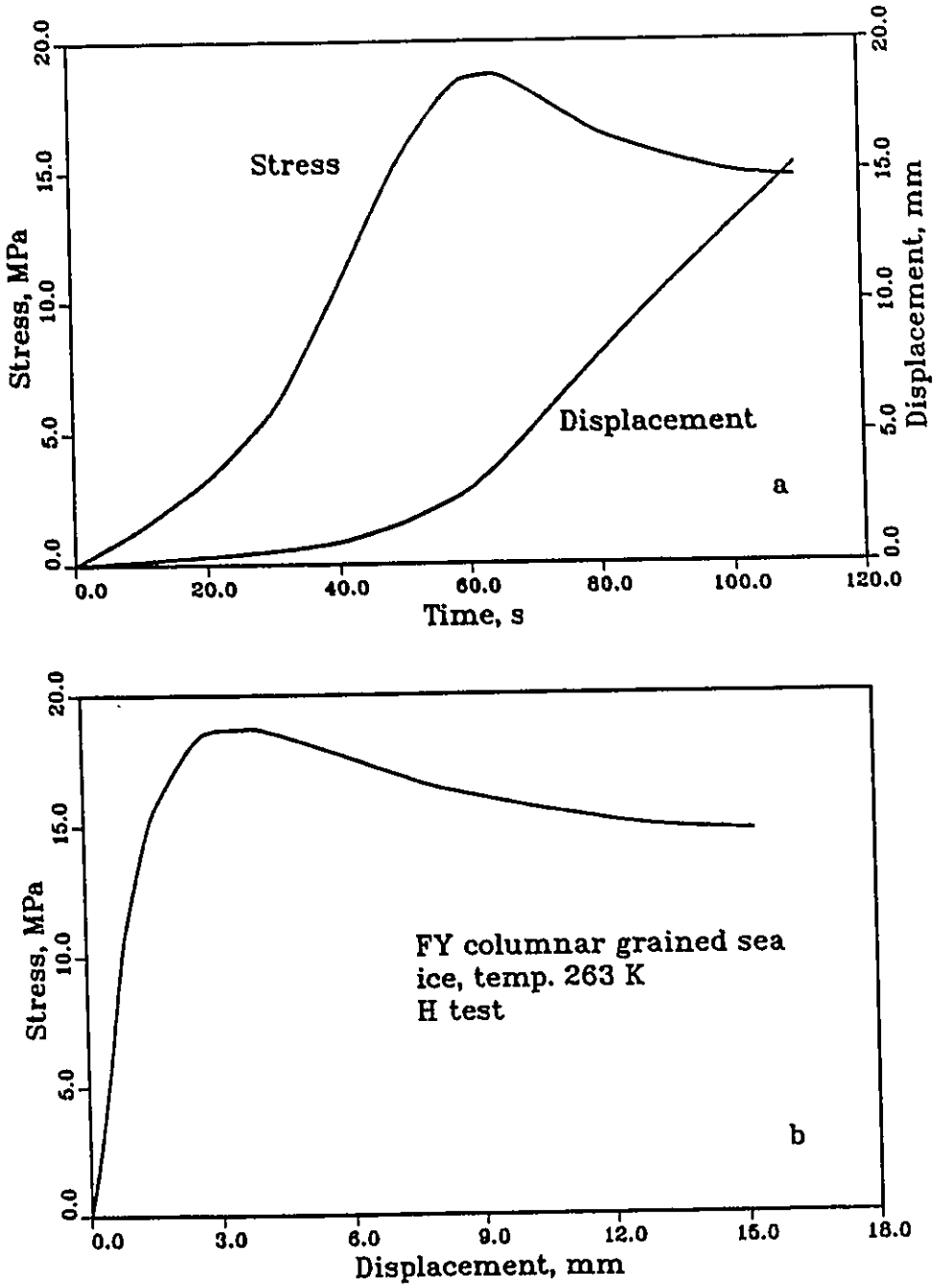

Figure 3.17 H test result with mean c-axis 45 degrees to loading direction
a: Time dependence of stress and displacement
b: Stress-displacement diagram

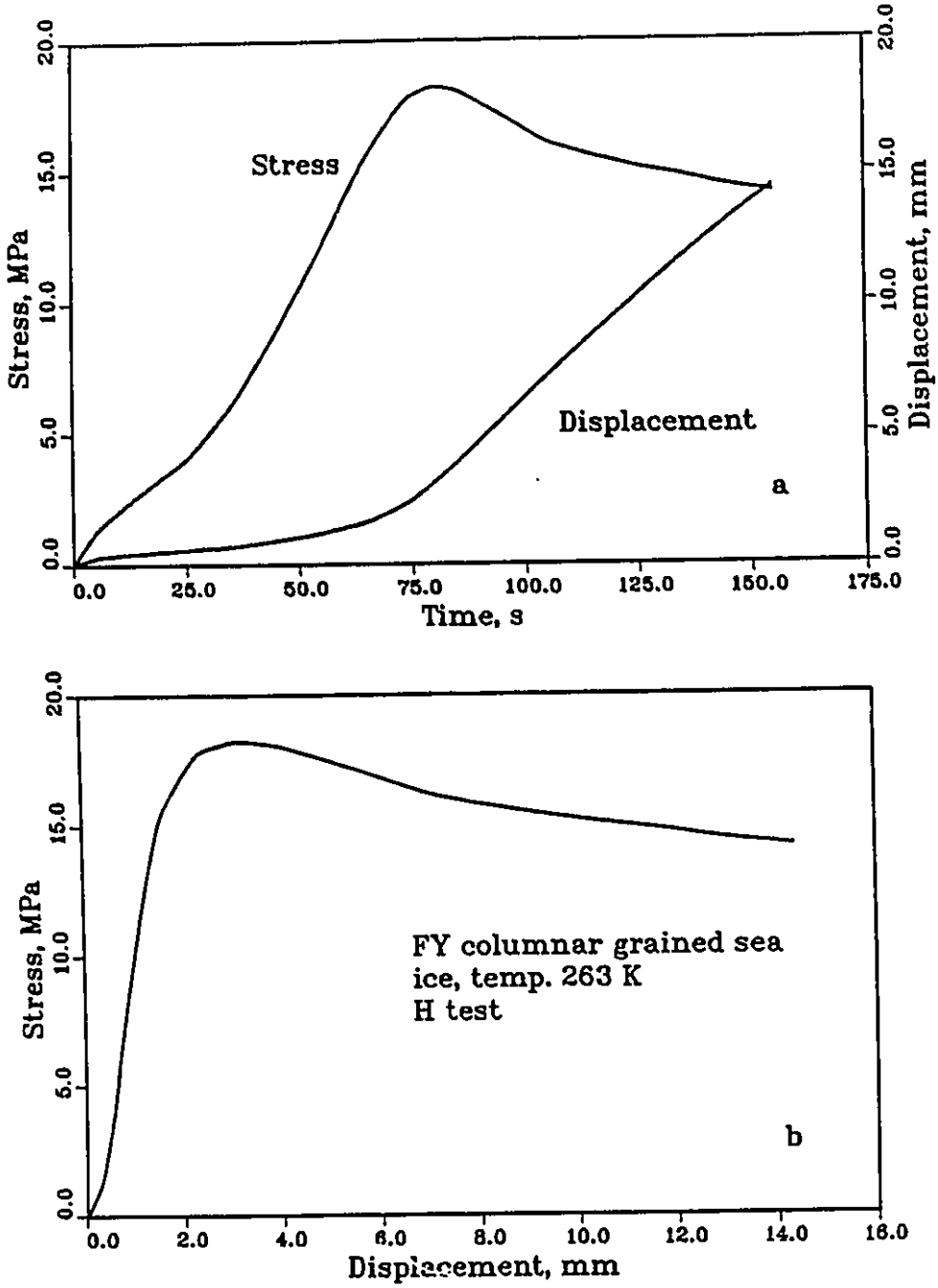

Figure 3.18 H test result with mean c-axis normal to loading direction
a: Time dependence of stress and displacement
b: Stress and displacement diagram

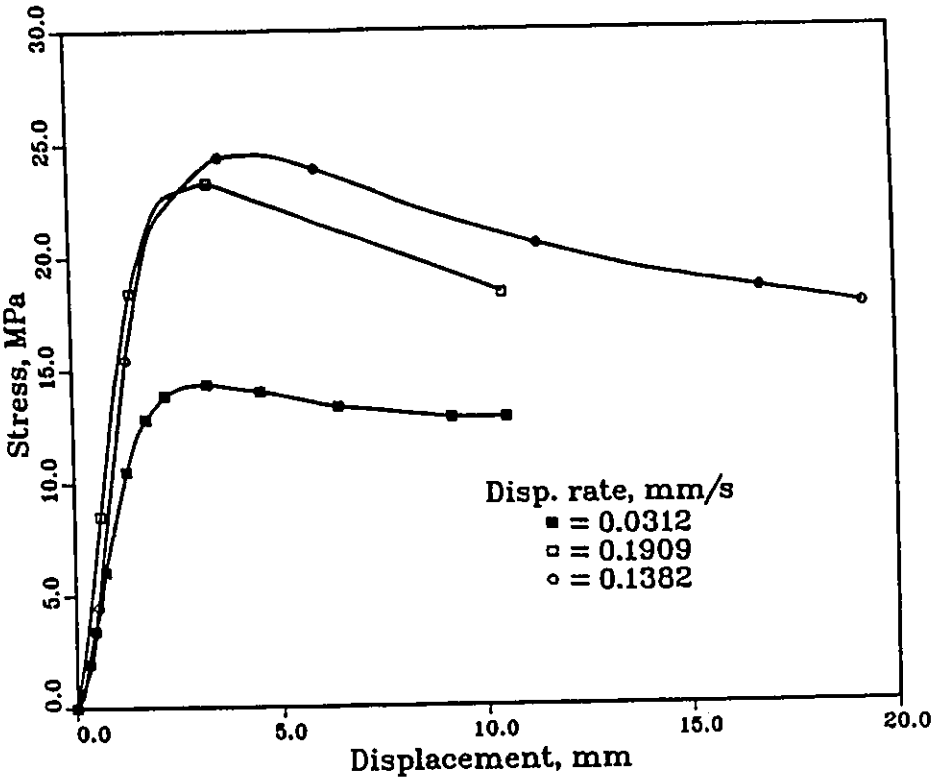

Figure 3.19 Rate dependence of stress–displacement diagrams for H tests with mean c–axis parallel to load axis

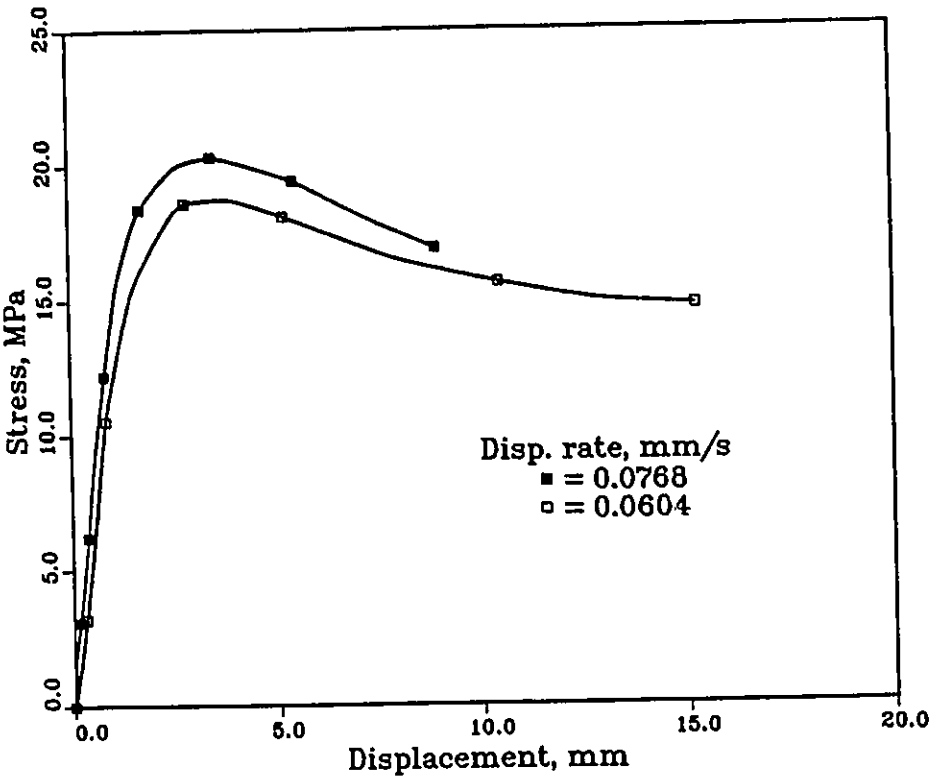

Figure 3.20 Rate dependence of stress–displacement diagrams for H tests with mean c–axis 45 degrees to load axis

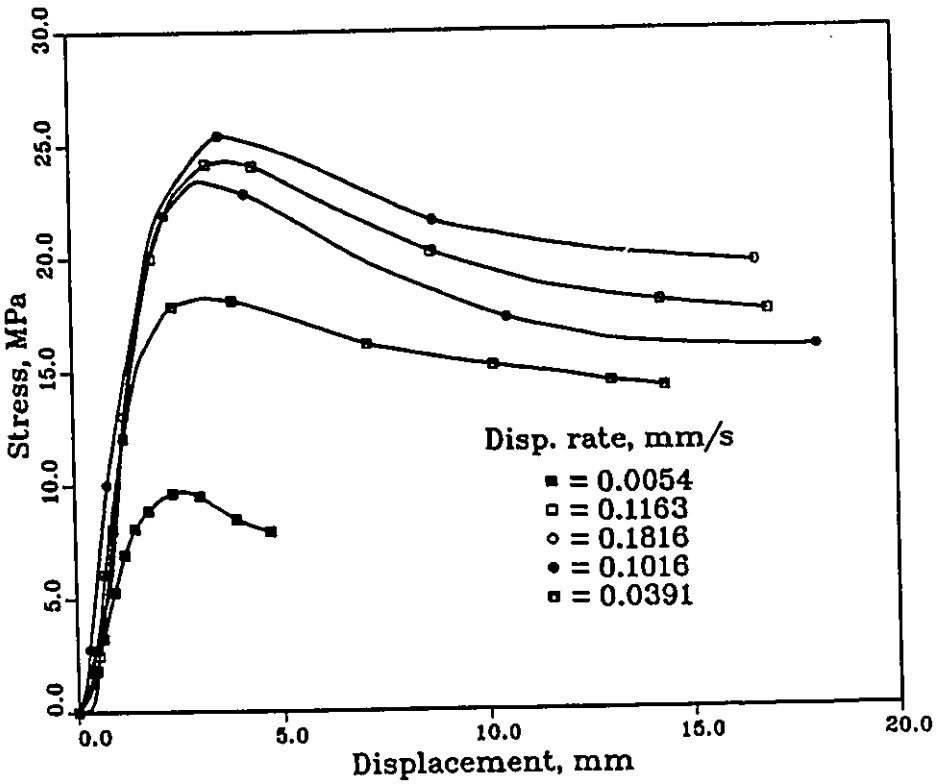

Figure 3.21 Rate dependence of stress–displacement diagrams for H tests with mean c–axis normal to load axis

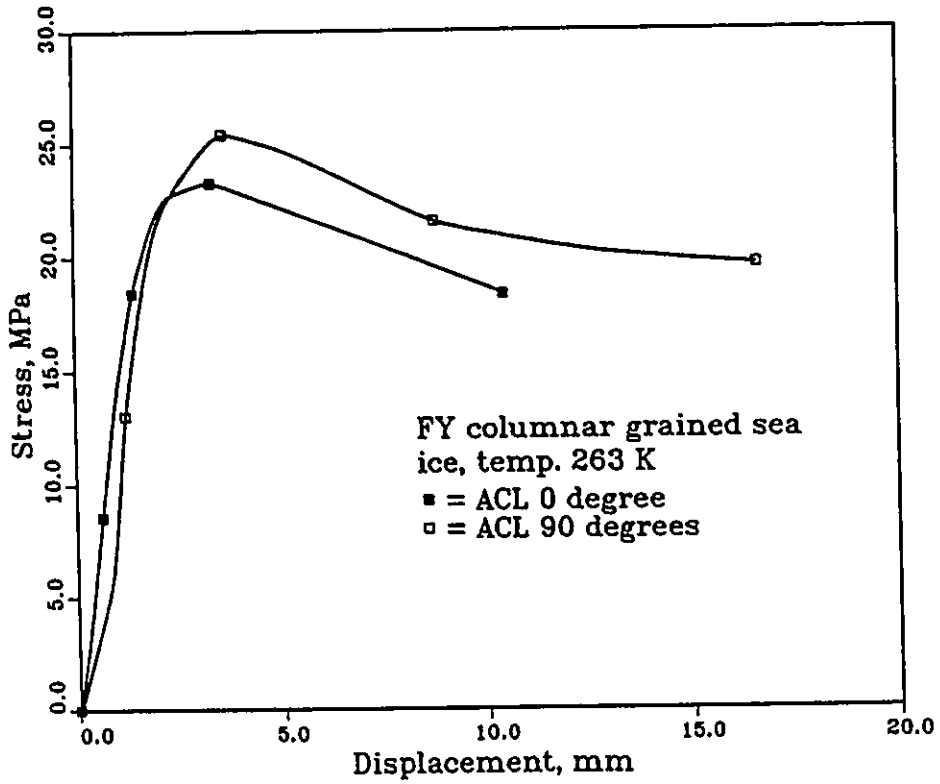

Figure 3.22 Comparisons of stress–displacement diagrams for H tests for two different ACL angles

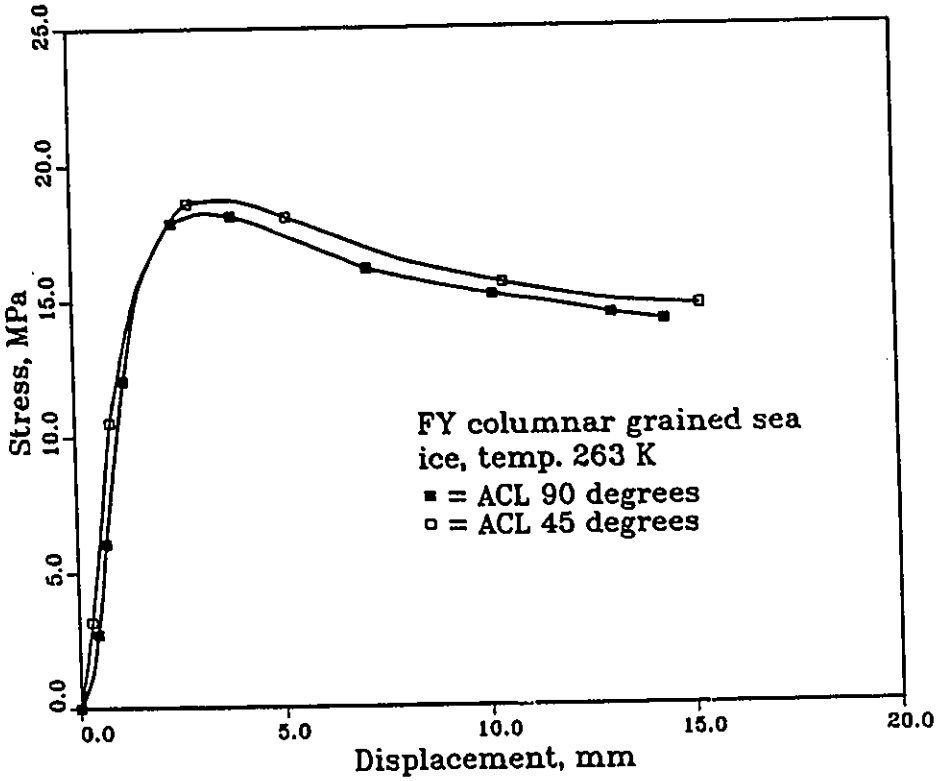

Figure 3.23 Comparisons of stress–displacement diagrams for H tests for two different ACL angles

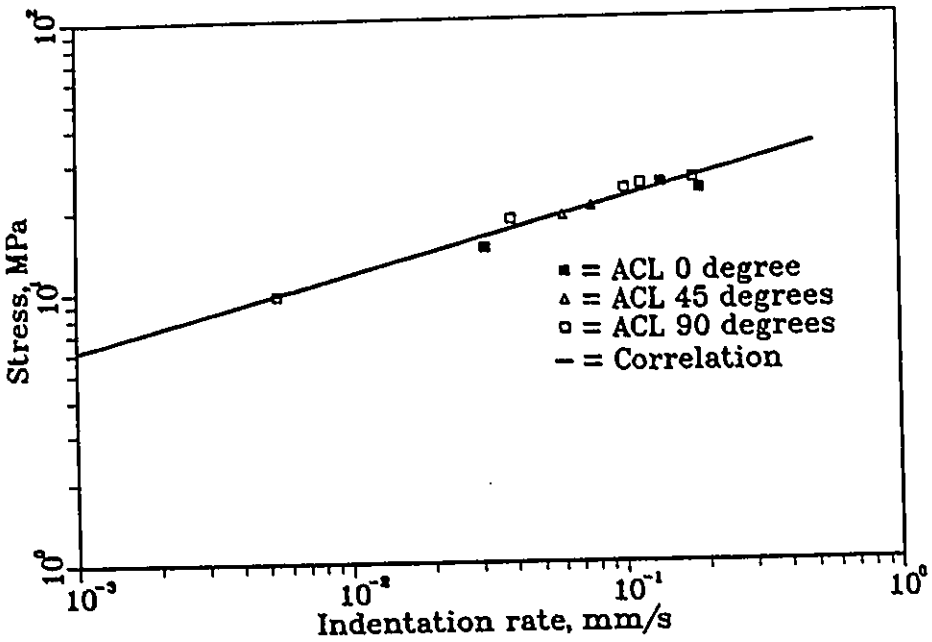

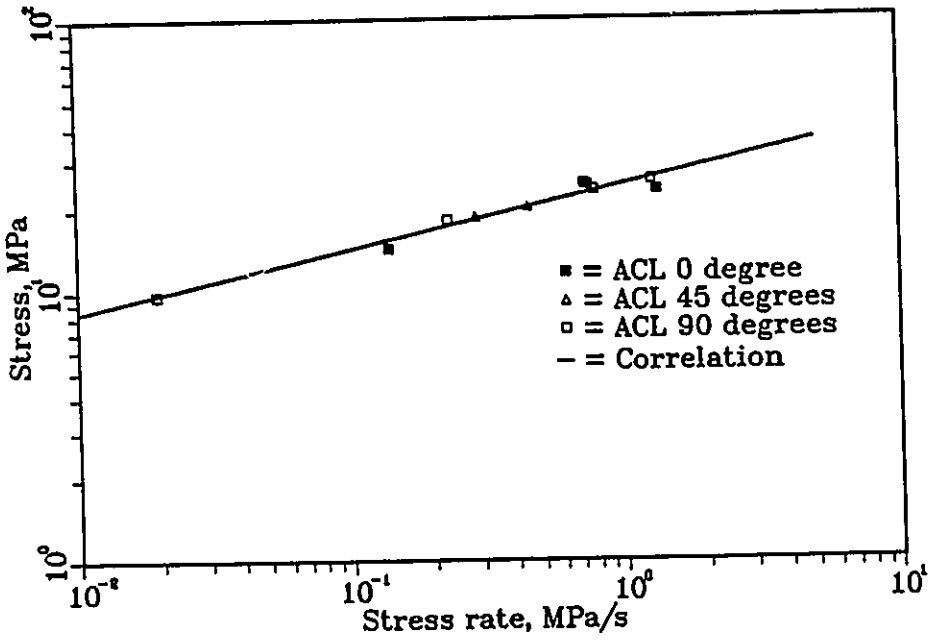

Figure 3.24 Stress and indentation rate dependence of maximum stress for H tests carried out in Resolute Bay, N.W.T., Canada

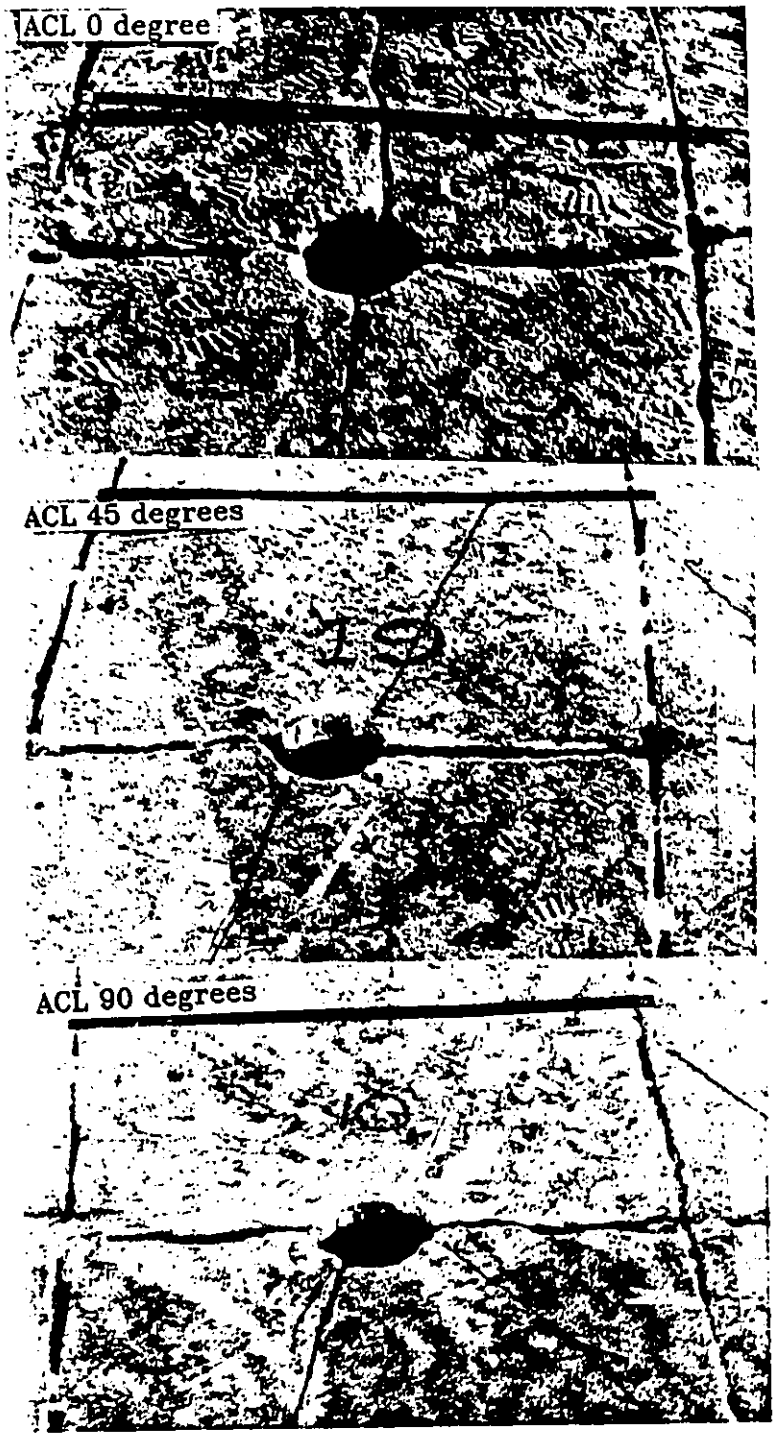

Figure 3.25 Dependence of crack orientation on ACL, angle between mean c–axis and loading direction

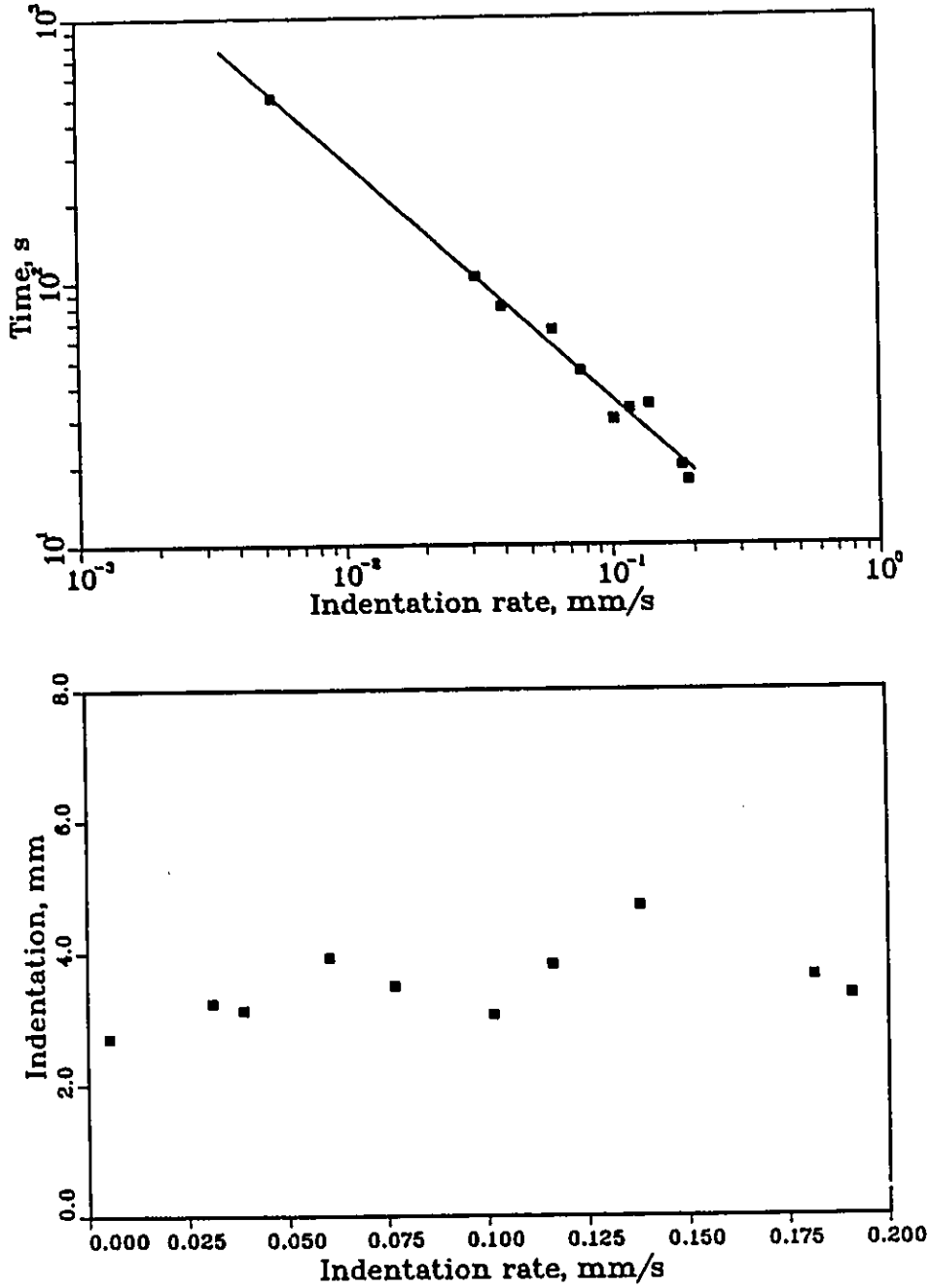

Figure 3.26 Indentation rate dependence of time and displacement at failure for H tests carried out in Resolute Bay, N.W.T., Canada

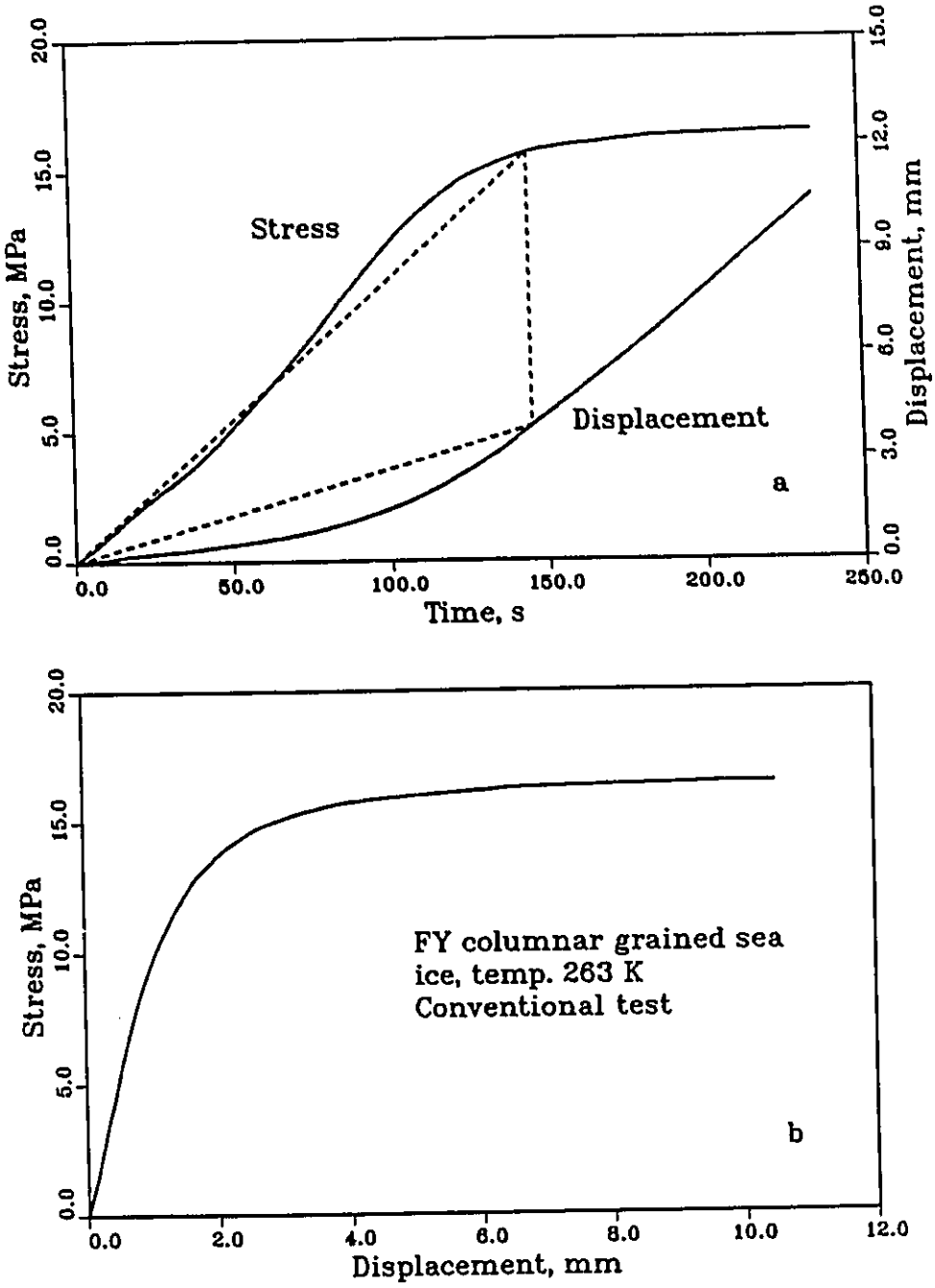

Figure 3.27 Conventional test result with mean c-axis parallel to load axis
a: Time dependence of stress and displacement
b: Stress-displacement diagram

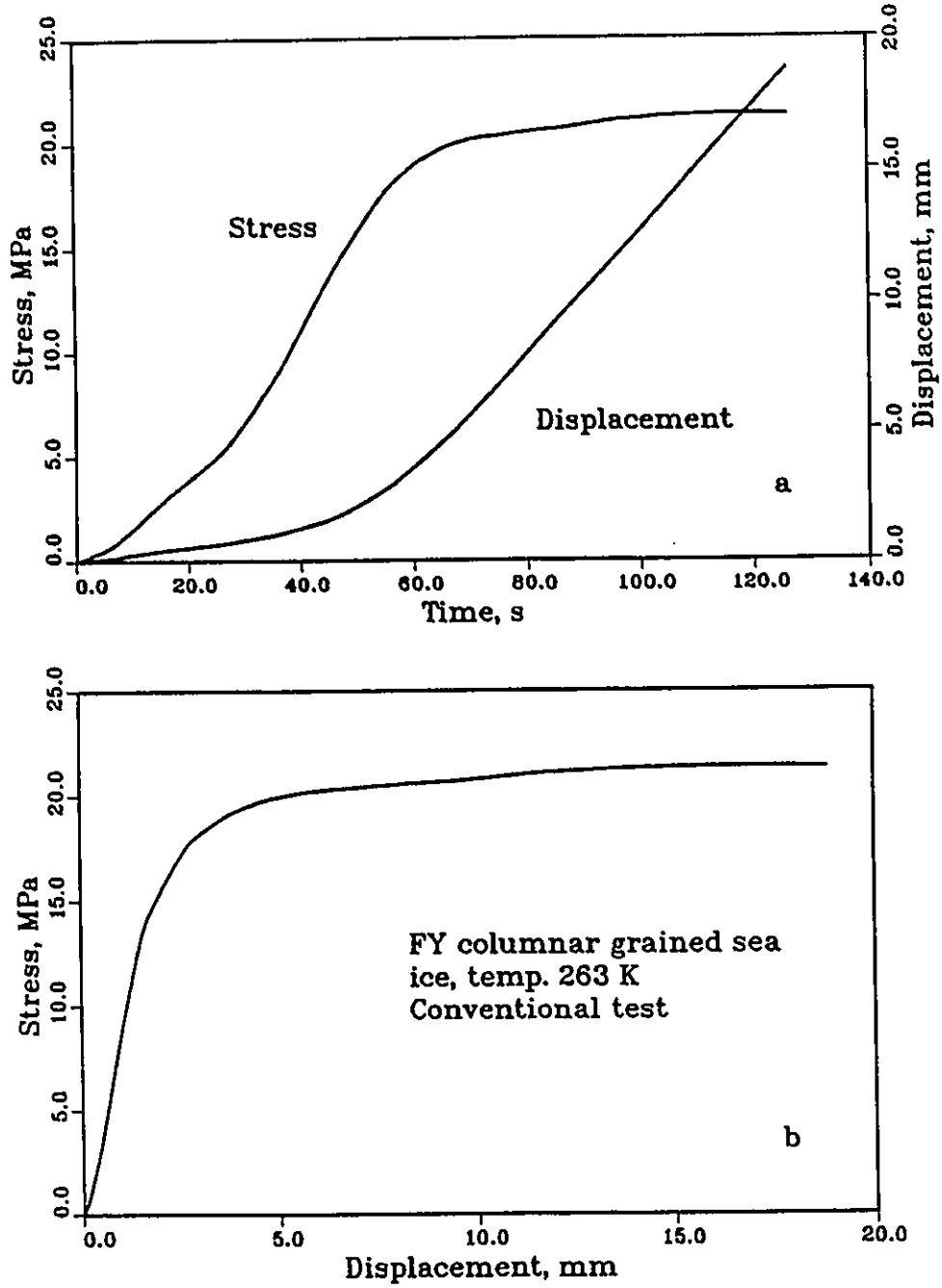

Figure 3.28 Conventional test result with mean c-axis 45 degrees to load axis
a: Time dependence of stress and displacement
b: Stress-displacement diagram

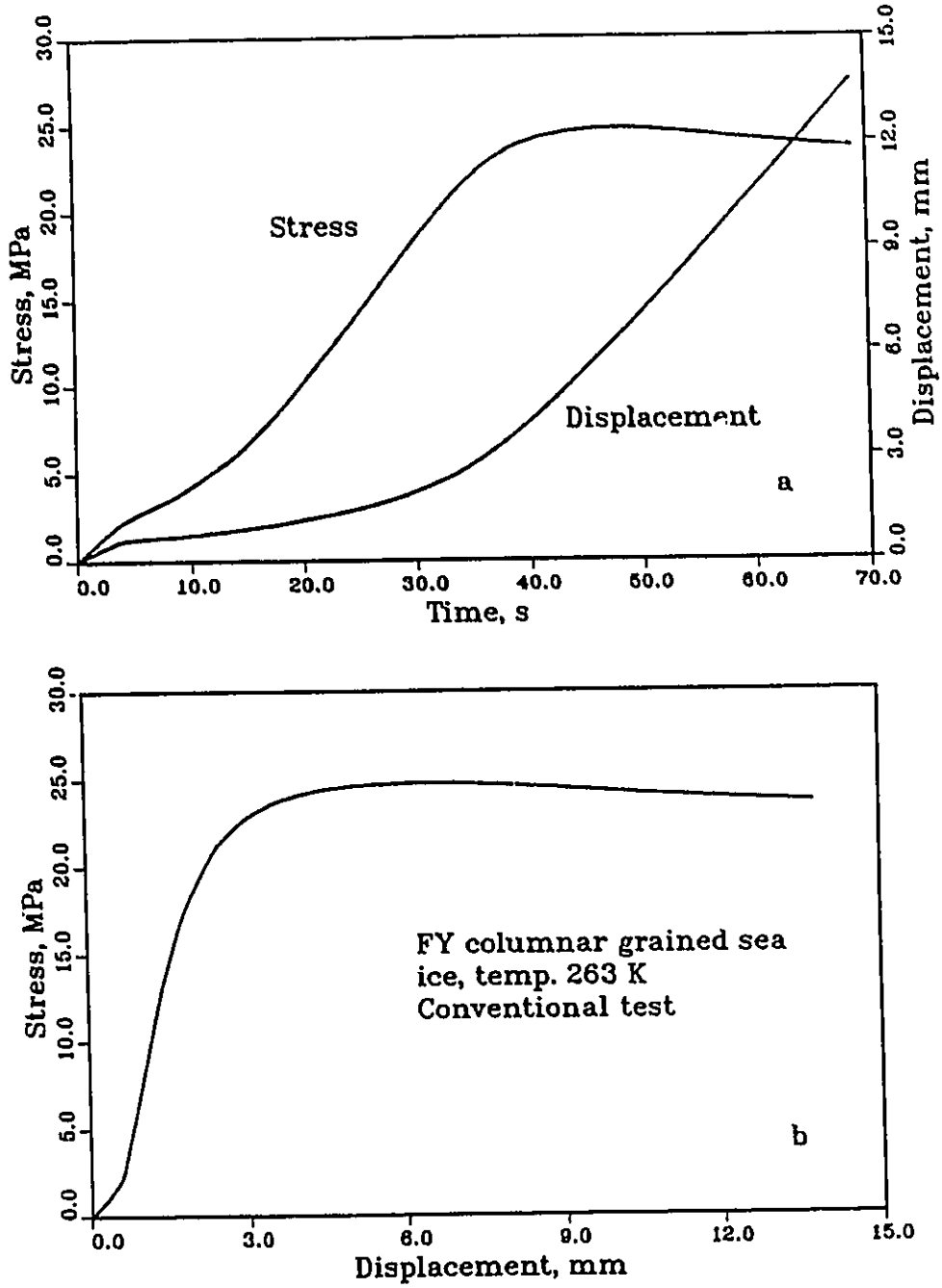

Figure 3.29 Conventional test result with mean c-axis normal to load axis
a: Time dependence of stress a displacement
b: Stress-displacement diagram

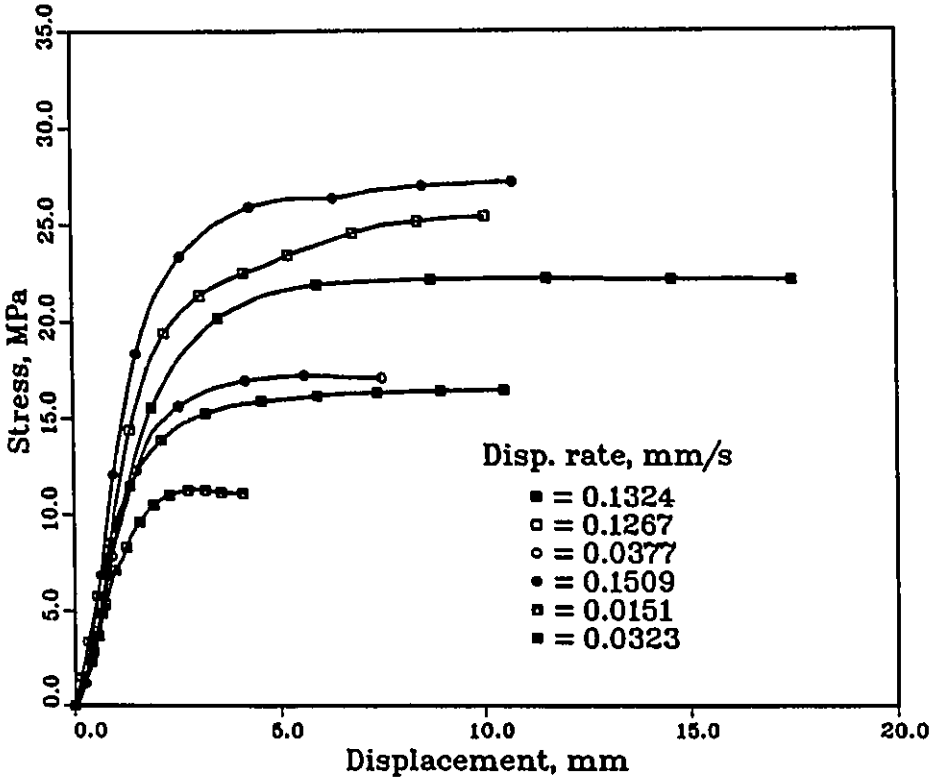

Figure 3.30 Rate dependence of stress–displacement diagrams for field conventional indentations test with mean c–axis parallel to loading direction

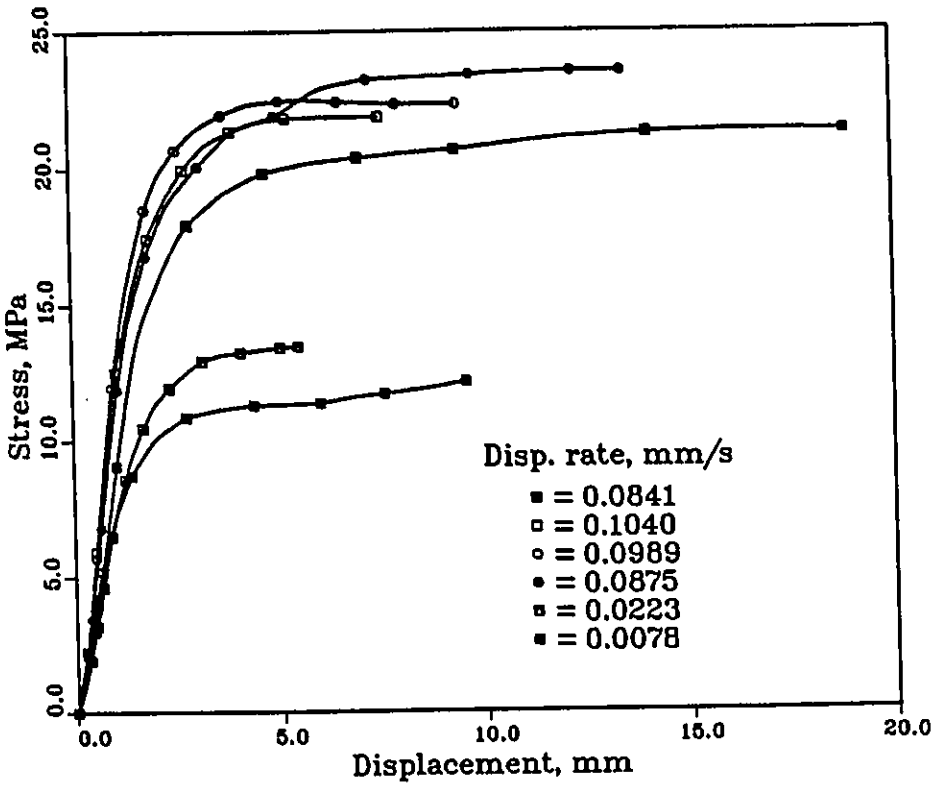

Figure 3.31 Rate dependence of stress–displacement diagrams for field conventional indentation tests with mean c–axis 45 degrees to loading direction

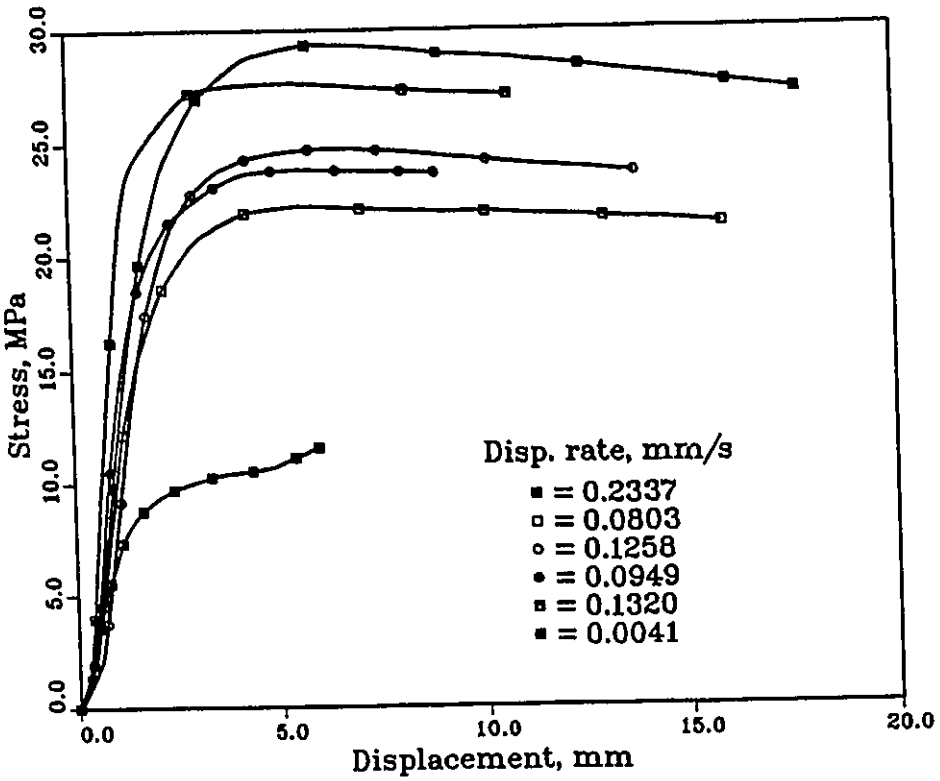

Figure 3.32 Rate dependence of stress–displacement diagrams for field conventional indentation tests with mean c–axis 90 degrees to loading direction

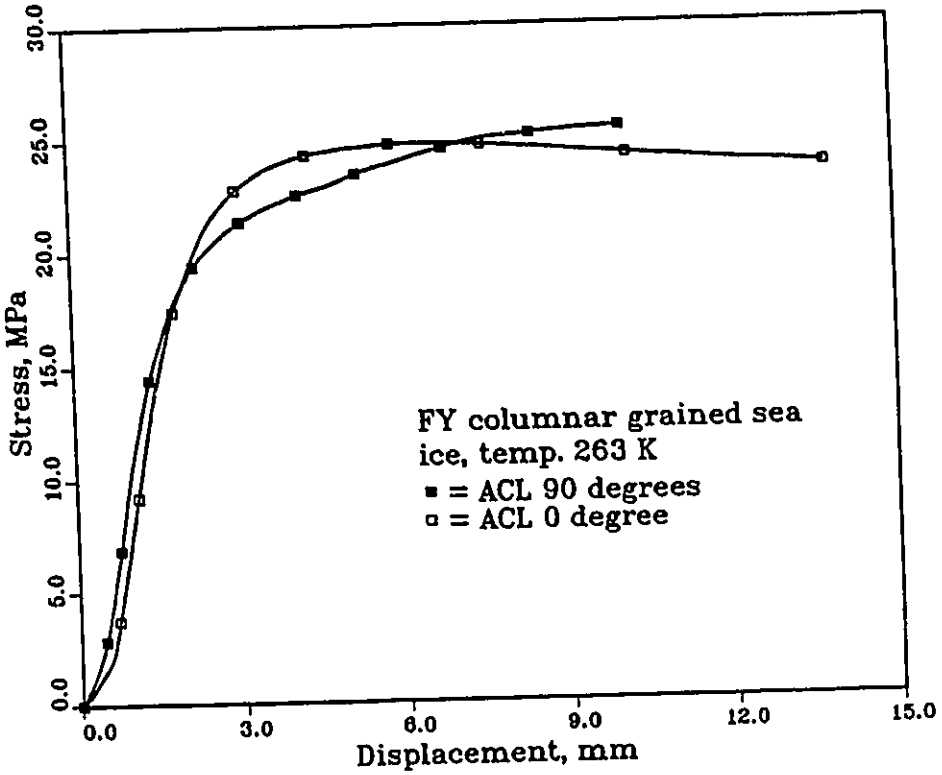

Figure 3.33 Comparisons of stress–displacement diagrams of conventional tests for two different ACL angles

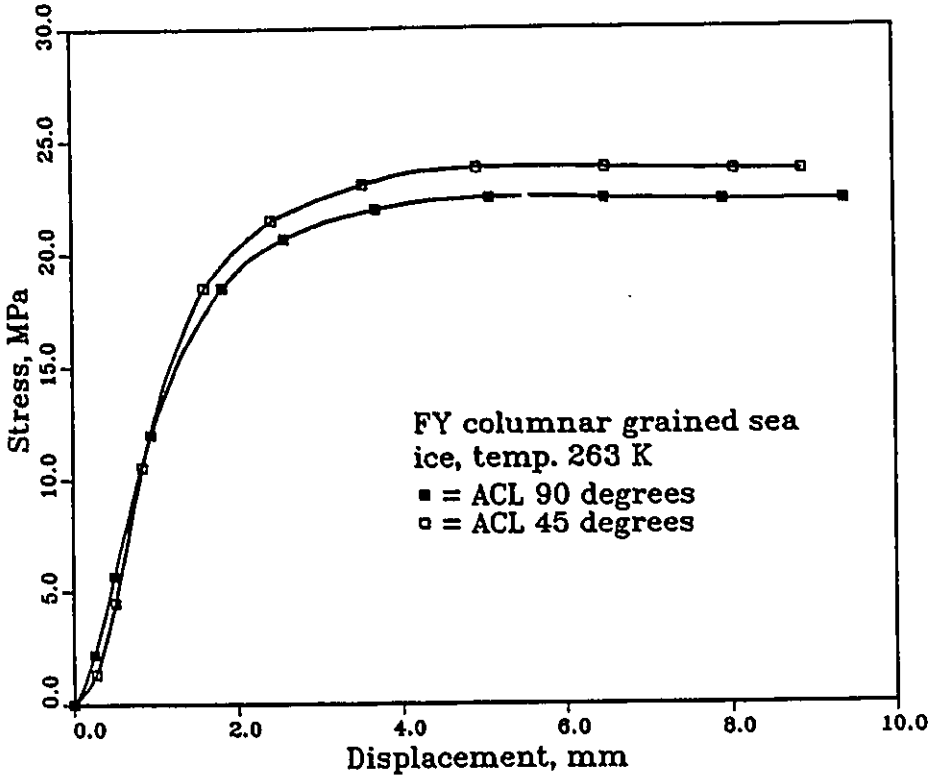

Figure 3.34 Comparisons of stress–displacement diagrams of conventional tests for two different ACL angles

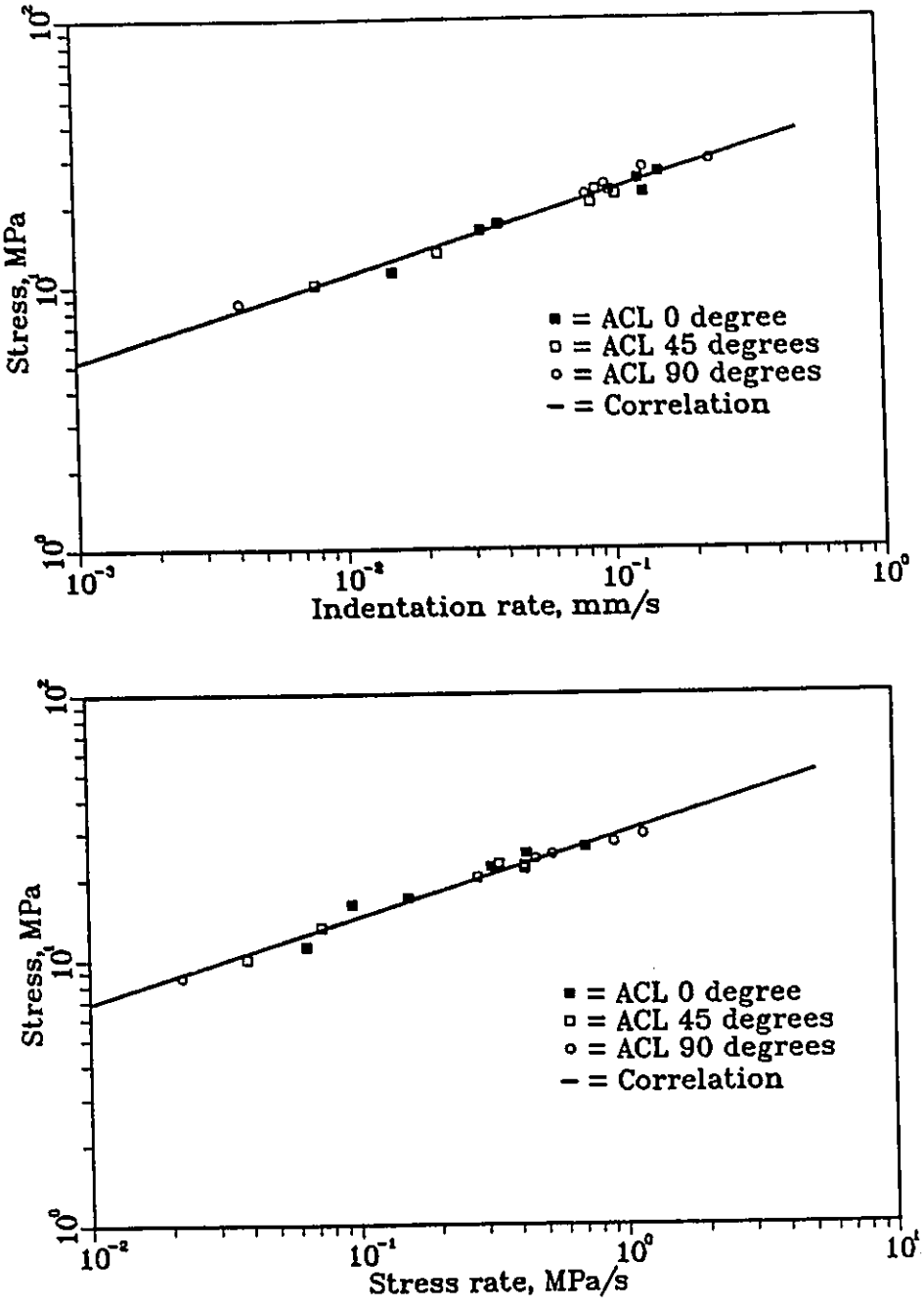

Figure 3.35 Stress and indentation rate dependence of the maximum stress in conventional indentation tests carried out in Resolute Bay, N.W.T., Canada

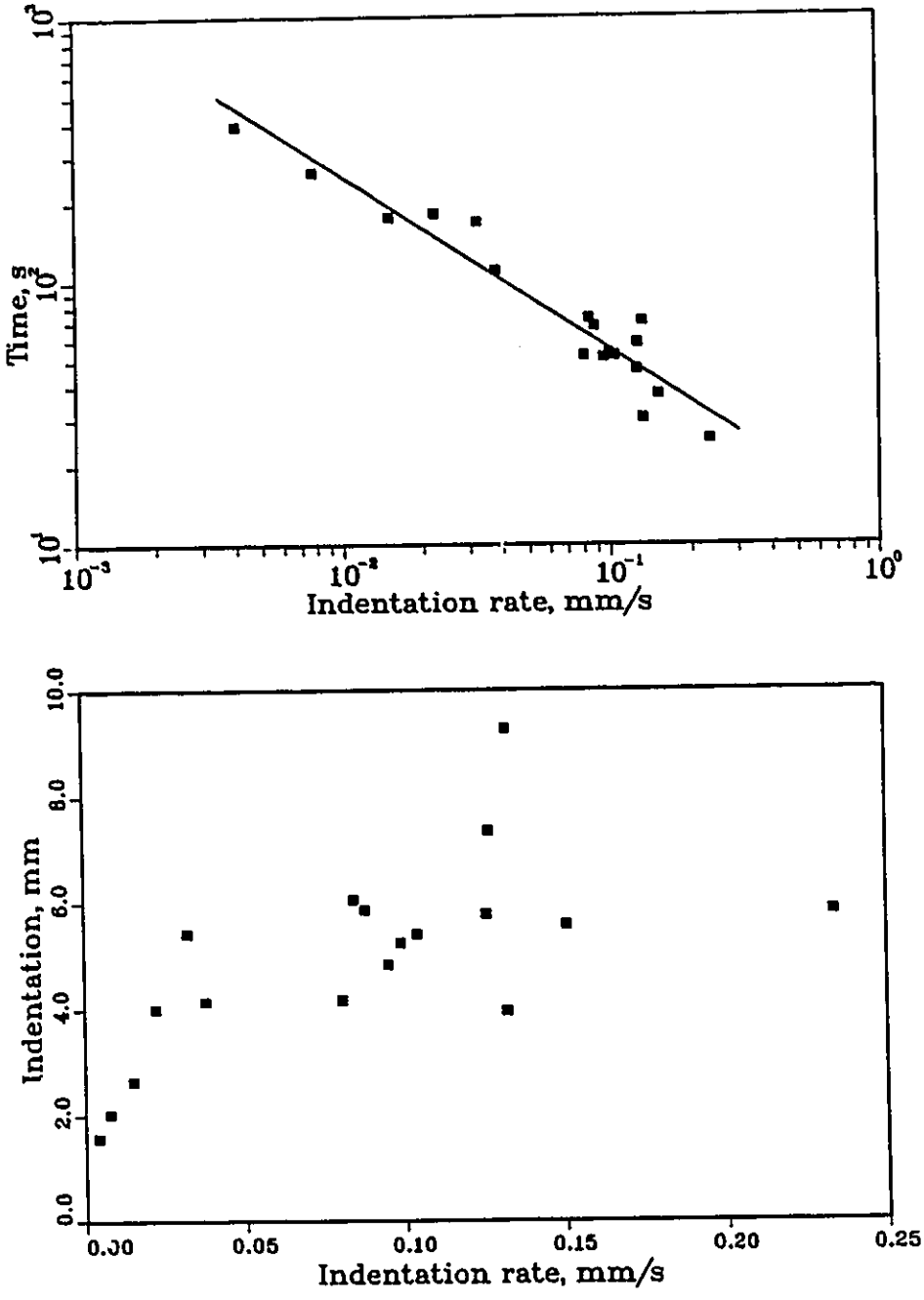

Figure 3.36 Dependence of time and deformation at yield on indentation rate in conventional indentation tests carried out in Resolute Bay, N.W.T., Canada

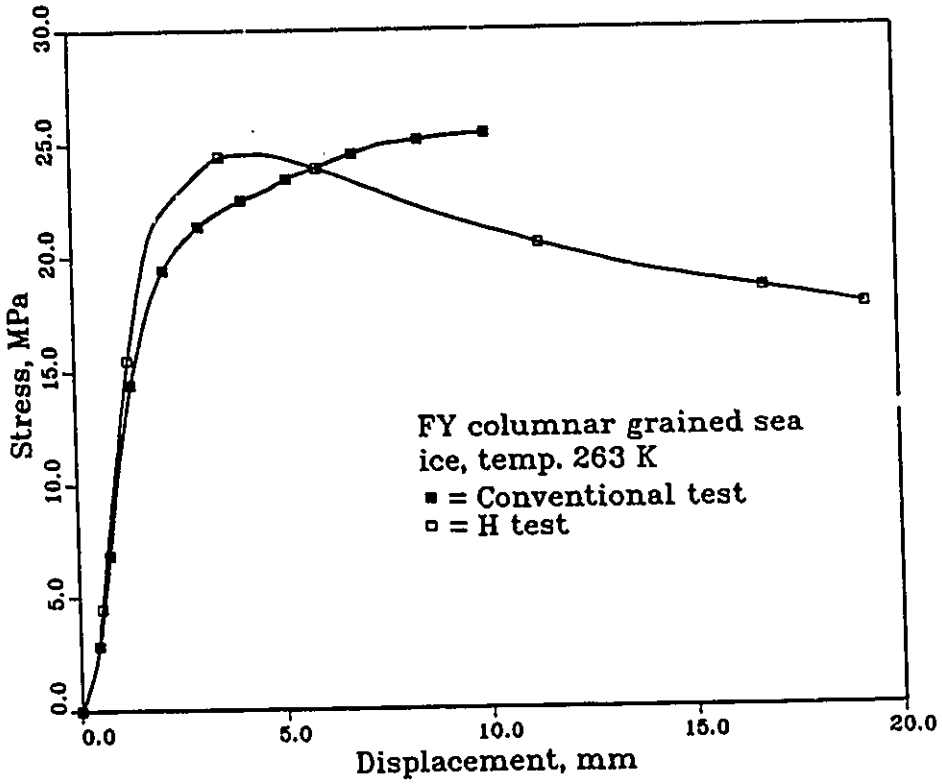

Figure 3.37 Comparisons of stress–displacement diagrams between conventional and H tests

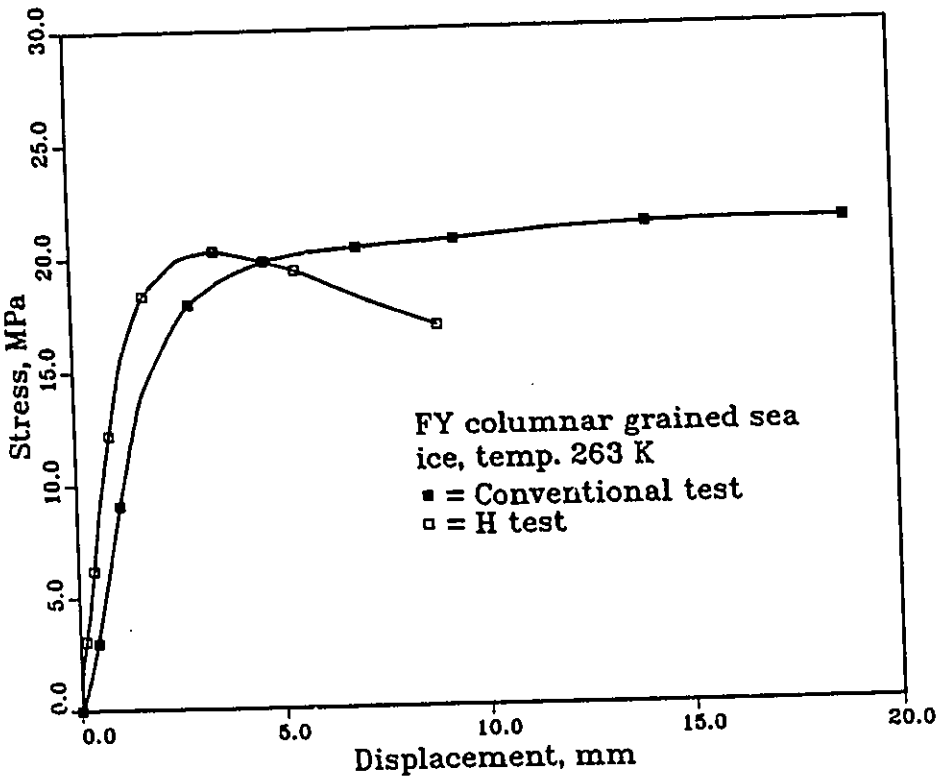

Figure 3.38 Comparisons of stress–displacement diagrams between conventional and H tests

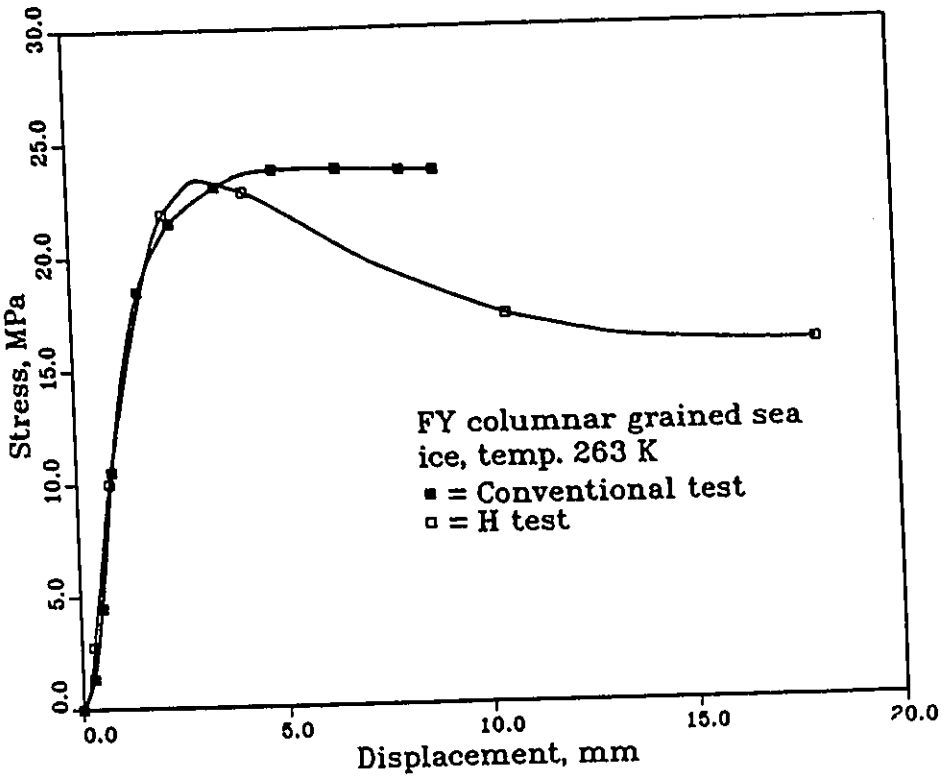

Figure 3.39 Comparisons of stress–displacement diagrams between conventional and H tests

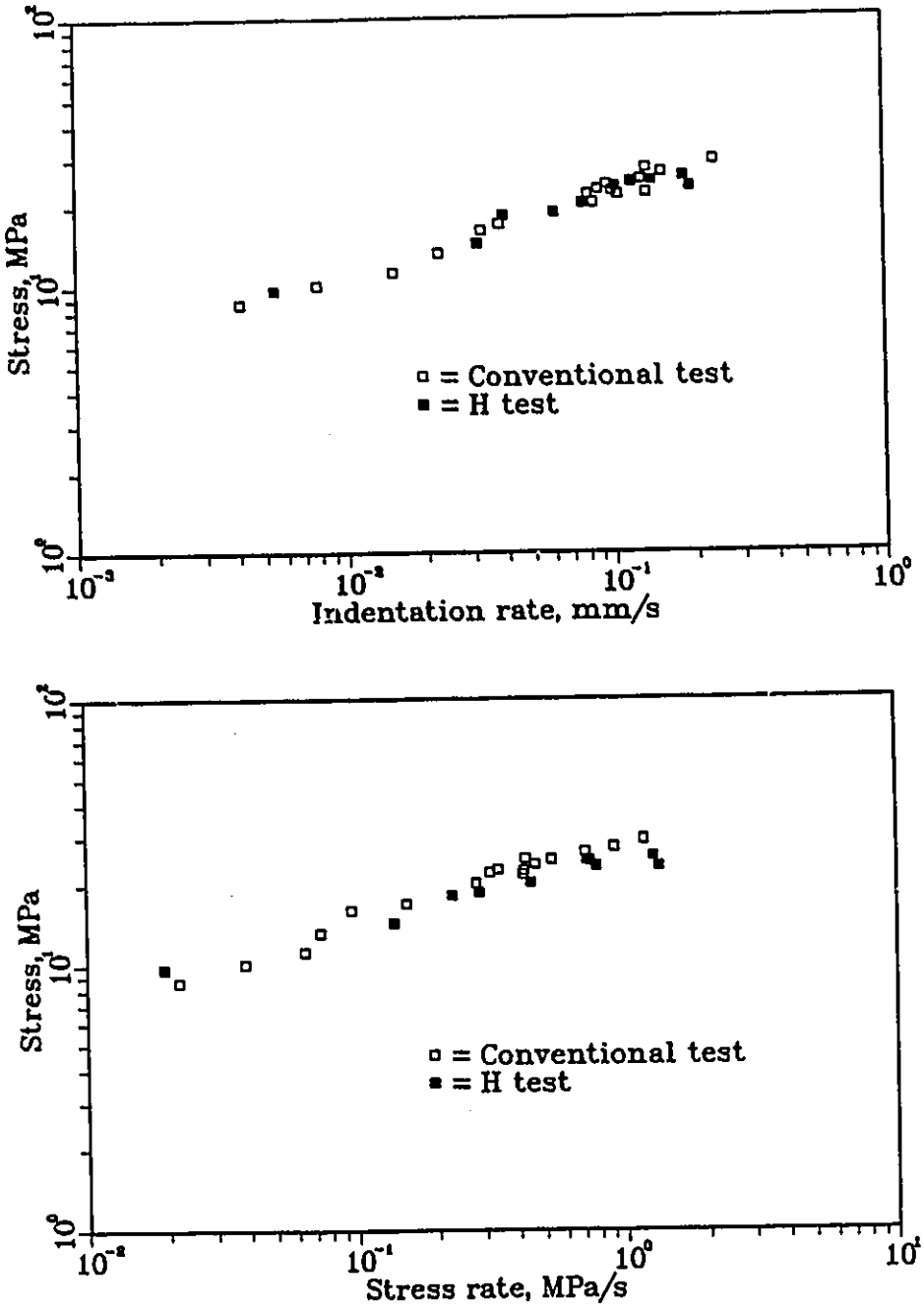

Figure 3.40 Comparisons between conventional tests and H tests for stress and indentation rate dependence of stresses at yield

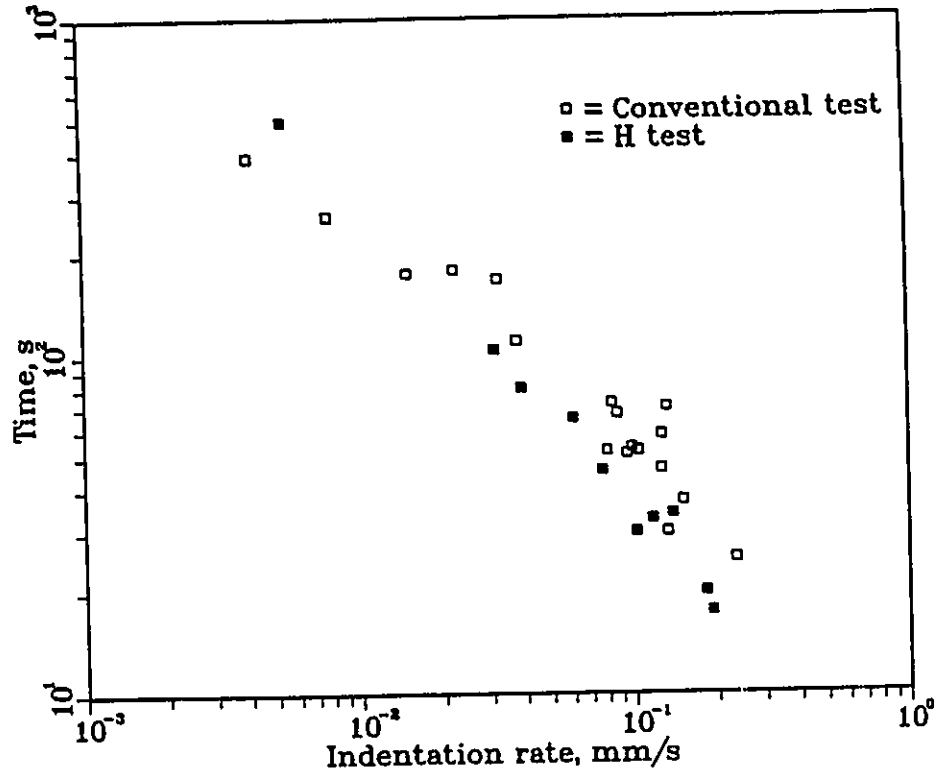

Figure 3.41 Comparisons between conventional tests and H tests for rate dependence of time at yield

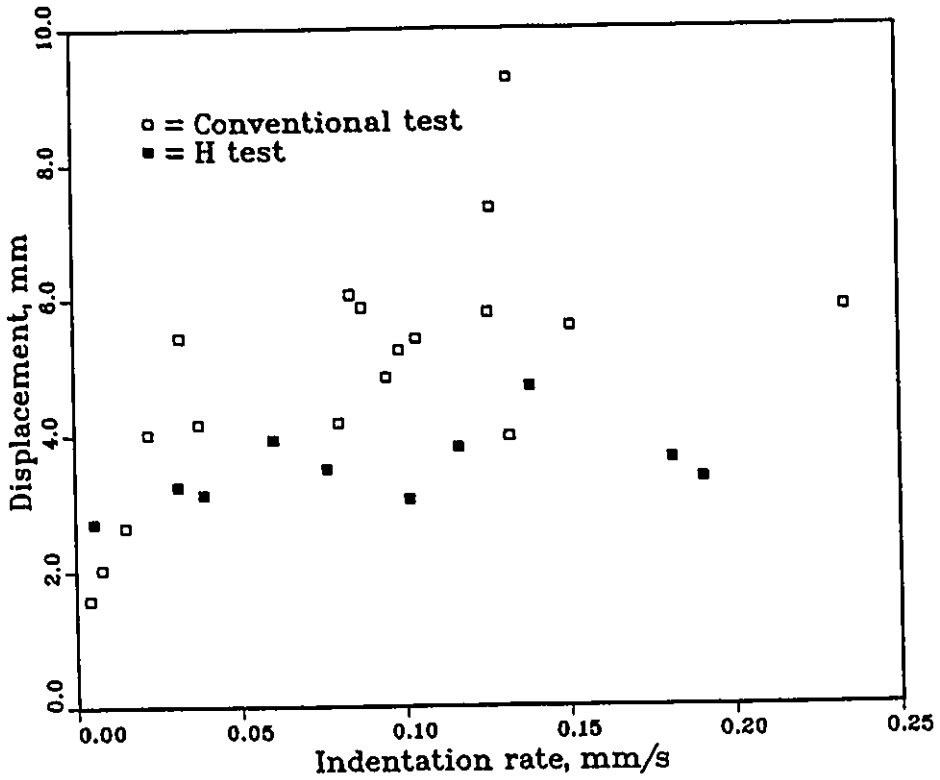

Figure 3.42 Comparisons between conventional tests and H tests for rate dependence of displacements at yield

Chapter 4

3-D anisotropic model for columnar-grained fresh water ice

4.1 Introduction

Most of the ice encountered on the lakes, rivers, and oceans are columnar grained ice. Fresh water columnar-grained ice often exhibits transverse isotropy with c-axis (optic axis) of the grain randomly oriented in the horizontal plane (or the plane normal to the length of the columns). Sea ice, especially land-fast ice, shows c-axis oriented parallel to the water current (Weeks and Gow, 1978; and Nakawa and Sinha, 1984). Columnar grained ice exhibits high anisotropy. An ice sample loaded uniaxially normal to the columns of grains shows negligible strain in the direction of the columns (Wang, 1981; Sinha, 1989a; Sinha, et. al, 1992). Also, a sample loaded uniaxially in the direction parallel to the columns exhibits much higher strength than a sample loaded in the direction normal to the columns (Peyton, 1966; Michel, 1978; Sinha, 1983, 1984a; Frederking and Timco, 1984; Timco and Frederking, 1986). It is, therefore, essential to bring the anisotropic behaviour of the columnar grained ice into the constitutive model.

Many constitutive equations have been developed (Sinha, 1978a; Michel and Testa, 1978; Spring and Morland, 1983; Karr, 1985; Ashby and Duval, 1985; Brown et. al, 1986; Sinha, 1988a, 1990a; Choi and Karr 1989, McKenna et al 1989, Santaoja, 1988, 1989). However, none of the above equations can be used to model

the anisotropic behaviour of columnar grained ice. The equivalent stress concept was used by Ting and Sunder (1985), Sunder and Wu (1989), and Pulkkinen (1989) to model the anisotropy. The problem with this method is that with different fabric, different material parameters are needed. In the case of an anisotropic material without any symmetry, the equivalent stress concept as it was defined is not applicable. Sjolind (1987) employed a fourth order tensor to represent the anisotropy, which requires up to 81 material parameters. The elements of the fourth order tensor have different values for ice with different fabric.

The effects of fabric on the viscous strain rate was formulated by Lile (1978) by introducing an enhancement factor to the viscous strain rate. However, a linear relationship is assumed between the viscous strain rate and the stress, which is not realistic.

In the present model, the anisotropy due to the fabric is formulated in conjunction with the kinetics of microcracking and their effect on the deformation process of columnar grained ice. This model is capable of accounting for the effect of fabric on the deformation as well as the difference between the strength in the vertical and horizontal directions for columnar grained ice. The model is applicable only in the ductile range of material behaviour. Brittle fracture is not considered.

4.2 Present model for columnar grained ice

Five deformation mechanisms were summarized by Sanderson (1988) for polycrystalline ice as follows.

1. elastic deformation due to the atomic bonds lengthening or shortening;
2. delayed elasticity caused by the grain boundary sliding;
3. viscous deformation due to the movement of dislocation within grains;
4. crack deformation;
5. dynamic recrystallization.

In the present model, the total strain tensor increment, $d\epsilon_{ij}$, is divided into four parts based on the deformation mechanisms summarized by Sanderson without considering the dynamic recrystallization.

$$d\epsilon_{ij} = d\epsilon^e_{ij} + d\epsilon^d_{ij} + d\epsilon^v_{ij} + d\epsilon^c_{ij} \tag{4.1}$$

where $d\epsilon^e_{ij}$ is the elastic strain tensor increment; $d\epsilon^d_{ij}$ is the delayed elastic strain tensor increment; $d\epsilon^v_{ij}$ is the viscous strain tensor increment and $d\epsilon^c_{ij}$ is the crack strain tensor increment.

4.2.1 Elastic strain

The elastic strain is calculated from the generalized Hooke's law.

$$d\epsilon^e_{ij} = C_{ijkl} d\sigma_{kl} \tag{4.2}$$

where σ_{kl} is the stress tensor and C_{ijkl} is the stiffness tensor.

For a polycrystalline ice, the stiffness tensor is obtained from the probability distribution of c-axis and the stiffness tensor for a single crystal ice (Sinha, 1989b).

4.2.2 Delayed elastic strain

For a single crystal ice, the delayed elasticity is negligible (Brill and Camp, 1961). In the case of polycrystalline ice, the delayed elasticity can not be neglected (Sinha, 1988a). The importance of delayed elasticity or primary creep for ice engineering problems was discussed in detail by Gold and Sinha (1981).

The delayed elasticity developed under a uniaxial constant stress in a polycrystalline material was attributed to the grain boundary sliding induced stress in the matrix and formulated by Sinha (1979a).

$$\epsilon_d = C_1 \frac{d_1}{d} (\frac{\sigma}{E})^s \{1 - exp(-(a_T t)^b)\} \tag{4.3}$$

where ϵ_d is the delayed elasticity; σ is the stress; E is the elastic modulus; C_1, b, and s are constants; t is the time; d_1 is the reference grain size; d is the grain size of the ice; a_T is a parameter dependent on temperature.

Sinha's equation for delayed elasticity seems to represent the grain size effect (Sinha, 1978b, 1979a). However, Eq. 4.3 consumes a large amount of computer time, due to the history dependence. Based on Eq. 4.3 for s=1 and $b = \frac{1}{n}$ (Sinha, 1979a), the following rate formulation for delayed elasticity under any stress state is proposed for columnar grained ice in a coordinate system (x,y,z) with z axis in the direction of long columns

$$\frac{\partial \epsilon_{ij}^d}{\partial t} = \frac{a_T}{n}\{(\frac{C_1 d_1}{d})^n (\frac{\bar{\sigma}_d}{E\bar{\epsilon}_d})^{n-1} \frac{1}{2E} \frac{\partial \bar{\sigma}_d^2}{\partial \sigma_{ij}} - \epsilon_{ij}^d\} \tag{4.4}$$

where n is a constant; $\bar{\sigma}_d$, $\bar{\epsilon}_d$, and a_T are given in the following equations.

$$\begin{aligned}
\bar{\sigma}_d &= \frac{1}{\sqrt{b_1 + b_2}} \sqrt{b_1(\sigma_x - \sigma_y)^2 + b_2(\sigma_y - \sigma_z)^2 + b_2(\sigma_z - \sigma_x)^2 + 6b_3\tau_{xy}^2} \\
\bar{\epsilon}_d &= \frac{b_1 + b_2}{\sqrt{(2b_1 + b_2)^2 + (2b_2 + b_1)^2 + (b_1 - b_2)^2}} \sqrt{3\epsilon_{ij}^d \epsilon_{ij}^d} \\
a_T &= a_{T_0} exp\{\frac{Q_a}{R}(\frac{1}{T_0} - \frac{1}{T})\}
\end{aligned} \tag{4.5}$$

where $\sigma_x = \sigma_{11}$, $\sigma_y = \sigma_{22}$, $\sigma_z = \sigma_{33}$, and $\tau_{xy} = \sigma_{12}$ are stresses defined in the coordinate system shown in Fig. 4.1; Q_a is the activation energy; R is the universal gas constant; a_{T_0} is the value for a_T at a temperature T_0; T_0 is the reference temperature; b_1, b_2 and b_3 are model parameters used to represent the anisotropy in delayed elasticity as observed in the present laboratory experiments of Chapter 2. The delayed elasticity ϵ_{xz} and ϵ_{yz} are neglected due to the large length of the grains in the z direction (Sinha, 1979a).

4.2.3 Viscous strain

Effective stress for single crystal

The mechanical behaviour of a single crystal ice is quite anisotropic (Glen and Perutz, 1954; Steinmann, 1954; Nakaya, 1958; Butkovich and Landauer, 1958; and Higashi, 1968). Shearing on the basal plane is much easier than the shearing on non-basal planes. The tests done by Higashi (1968) showed that at -19^0C and a strain rate $3 \times 10^{-6} s^{-1}$, the peak uniaxial stress for non-basal slip in a monocrystal ice was between 10 to 20 times higher than the peak stress for basal slip. However, slip in the basal plane does not seem to dependent on any direction (Glen and Perutz, 1954; Steinmann, 1954; and Physics of Ice, page 277, Hobbs, 1974). Single crystal ice can therefore be treated as a transversely isotropic material.

Polycrystalline ice consists of crystals or grains of ice. Suppose (x', y', z') describes the local coordinate system of a crystal with its c-axis parallel to z' axis as shown in Fig. 4.1, the effective stress for a single crystal ice can then be defined as

$$\begin{aligned} \tau^2 &= a_1(\sigma'_x - \sigma'_y)^2 + a_2(\sigma'_y - \sigma'_z)^2 + a_2(\sigma'_z - \sigma'_x)^2 \\ &+6(a_4\tau'^2_{xy} + a_5\tau'^2_{yz} + a_5\tau'^2_{zx}) \end{aligned} \tag{4.6}$$

where τ is the effective stress for single crystal ice; σ'_x, σ'_y, σ'_z, τ'_{xy}, τ'_{xz}, and τ'_{yz} are stresses in the local coordinate system; a_1, a_2, a_4 and a_5 are model parameters.

In order to ensure that the dislocation movement in the basal plane is the dominant mode of deformation, the coefficient a_5 in Eq. 4.6 must be large in comparison to other coefficients.

The material property of a single crystal ice is transversely isotropic, which implies that the definition of the effective stress in Eq. 4.6 has to be invariant when the coordinate system rotates around c-axis. A relationship among model parameters a_1, a_2, and a_4 will be derived below based on this invariant requirement.

From the invariant requirement, a stress state $(\sigma'_x, \sigma'_y, \sigma'_z, \tau'_{xy}, \tau'_{xz}, \tau'_{yz}) = (\sigma, -\sigma, 0, 0, 0, 0)$ will give the same effective stress as a stress state $(0, 0, 0, \sigma, 0, 0)$. From Eq. 4.6, the following relationship can be obtained.

$$3a_4 = 2a_1 + a_2 \tag{4.7}$$

Statement 1: Eq. 4.7 means that among the four parameters in Eq. 4.6, only three of them could be independent.

The following three independent stress invariants as a function of $(\sigma'_x - \sigma'_y)^2$, $(\sigma'_y - \sigma'_z)^2$, $(\sigma'_z - \sigma'_x)^2$, τ'^2_{xy}, τ'^2_{yz}, and τ'^2_{zx} can be obtained when the coordinate system rotates around c-axis.

$$\begin{aligned} I_1 &= (\sigma'_x - \sigma'_y)^2 + (\sigma'_y - \sigma'_z)^2 + (\sigma'_z - \sigma'_x)^2 + 6(\tau'^2_{xy} + \tau'^2_{yz} + \tau'^2_{zx}) \\ I_2 &= (\sigma'_x - \sigma'_y)^2 + 4\tau'^2_{xy} \\ I_3 &= \tau'^2_{xz} + \tau'^2_{yz} \\ I_4 &= .... \end{aligned} \tag{4.8}$$

To satisfy the requirement of invariant for the effective stress when the coordinate system rotates around the c-axis, the effective stress in Eq. 4.6 must be a function of the stress invariants in Eq. 4.8.

$$\tau^2 = k_1 I_1 + k_2 I_2 + k_3 I_3 + ... \tag{4.9}$$

where k_1, k_2, and k_3 are independent constants.

Statement 2: Eq. 4.9 means that among the four parameters in Eq. 4.6, at least three of them are independent.

Considering statement 1 and 2 at the same time, it can be concluded that three parameters among the four parameters a_1, a_2, a_4, and a_5 in Eq. 4.6 are independent. Therefore, one relationship exists among parameters a_1, a_2, a_4, and a_5, which is given in Eq. 4.7. This relationship can also be derived from the following equation.

$$\tau^2 = k_1 I_1 + k_2 I_2 + k_3 I_3 \tag{4.10}$$

For any single crystal of ice in a polycrystalline aggregates with its c-axis defined by direction cosines $(cos\phi cos\theta, cos\phi sin\theta, sin\phi)$ in a global coordinate system (x,y,z) as shown in Fig. 4.1, the effective stress in terms of stresses in the global coordinate system can be obtained by the following equations.

Let σ_x, σ_y, σ_z, τ_{xy}, τ_{xz}, τ_{yz} represent the stresses in the global coordinate system. The relationship between the stresses in the two coordinate systems are given by

$$\sigma'_{ij} = T_{ik}\sigma_{kl}T_{jl} \tag{4.11}$$

where T_{ij} is the coordinate transformation matrix between the global coordinate system (x,y,z) and the local coordinate system (x', y', z').

$$T_{ij} = \begin{pmatrix} l_1 & l_2 & l_3 \\ m_1 & m_2 & m_3 \\ n_1 & n_2 & n_3 \end{pmatrix} = \begin{pmatrix} sin\theta & -cos\theta & 0 \\ sin\phi cos\theta & sin\phi sin\theta & -cos\phi \\ cos\phi cos\theta & cos\phi sin\theta & sin\phi \end{pmatrix} \tag{4.12}$$

The effective stress in Eq. 4.6 can be expressed in terms of stresses in the global coordinate using Eq. 4.11

$$\begin{aligned} \tau^2 &= A_1(\sigma_x - \sigma_y)^2 + A_2(\sigma_y - \sigma_z)^2 + A_3(\sigma_z - \sigma_x)^2 + A_4(\sigma_x - \sigma_y)(\sigma_y - \sigma_z) \\ &+A_5(\sigma_x - \sigma_y)(\sigma_z - \sigma_x) + A_6(\sigma_y - \sigma_z)(\sigma_z - \sigma_x) + A_7\tau_{xy}^2 + A_8\tau_{xz}^2 \\ &+A_9\tau_{yz}^2 + A_{10}(\sigma_x - \sigma_y)\tau_{xy} + A_{11}(\sigma_x - \sigma_y)\tau_{xz} + A_{12}(\sigma_x - \sigma_y)\tau_{yz} \\ &+A_{13}(\sigma_y - \sigma_z)\tau_{xy} + A_{14}(\sigma_y - \sigma_z)\tau_{xz} + A_{15}(\sigma_y - \sigma_z)\tau_{yz} + A_{16}(\sigma_z - \sigma_x)\tau_{xy} \\ &+A_{17}(\sigma_z - \sigma_x)\tau_{xz} + A_{18}(\sigma_z - \sigma_x)\tau_{yz} + A_{19}\tau_{xy}\tau_{xz} + A_{20}\tau_{xy}\tau_{yz} + A_{21}\tau_{xz}\tau_{yz} \end{aligned} \tag{4.13}$$

where A_1, A_2,....., A_{21} are functions of θ and ϕ, which are given in the Appendix A.

Effective stress for polycrystalline ice

Assuming that the stresses are the same in all grains, the effective stress for polycrystalline ice can be obtained by averaging of the effective stresses for all single

crystal ice in a representative volume. The average was performed over τ^2 in Eq. 4.13 for all grains in the polycrystalline ice.

$$\begin{aligned}\tau_p^2 &= B_1(\sigma_x-\sigma_y)^2+B_2(\sigma_y-\sigma_z)^2+B_3(\sigma_z-\sigma_x)^2+B_4(\sigma_x-\sigma_y)(\sigma_y-\sigma_z)\\ &+B_5(\sigma_x-\sigma_y)(\sigma_z-\sigma_x)+B_6(\sigma_y-\sigma_z)(\sigma_z-\sigma_x)+B_7\tau_{xy}^2+B_8\tau_{xz}^2\\ &+B_9\tau_{yz}^2+B_{10}(\sigma_x-\sigma_y)\tau_{xy}+B_{11}(\sigma_x-\sigma_y)\tau_{xz}+B_{12}(\sigma_x-\sigma_y)\tau_{yz}\\ &+B_{13}(\sigma_y-\sigma_z)\tau_{xy}+B_{14}(\sigma_y-\sigma_z)\tau_{xz}+B_{15}(\sigma_y-\sigma_z)\tau_{yz}+B_{16}(\sigma_z-\sigma_x)\tau_{xy}\\ &+B_{17}(\sigma_z-\sigma_x)\tau_{xz}+B_{18}(\sigma_z-\sigma_x)\tau_{yz}+B_{19}\tau_{xy}\tau_{xz}+B_{20}\tau_{xy}\tau_{yz}+B_{21}\tau_{xz}\tau_{yz}\end{aligned} \tag{4.14}$$

where τ_p is the effective stress for polycrystalline ice. The values of B_i are calculated from

$$B_i = \int_0^{\pi}\int_{-\frac{\pi}{2}}^{\frac{\pi}{2}} p(\phi,\theta)A_i cos\phi d\phi d\theta \tag{4.15}$$

where i=1,2,....., 21; $p(\phi,\theta)$ is the probability distribution of c-axis for the polycrystalline ice.

Effective stress for columnar grained ice

In the case of transversely isotropic columnar grained S2 ice (Michel and Ramseier, 1971) with random c-axis orientation in the plane normal to the length of columns, the probability of the c-axis distribution can be expressed as below using the coordinate system shown in Fig. 4.1 with z axis parallel to the long axis of the column.

$$p(\phi,\theta) = \frac{1}{\pi}\delta(\phi) \tag{4.16}$$

where $\delta(\phi)$ is equal to infinite, when ϕ is equal to zero, otherwise $\delta(\phi)$ is zero.

Eq. 4.15 combining with Eq. 4.16 gives nine non-zero values for B_1, B_2, ..., B_9 as follows.

$$
\begin{aligned}
B_1 &= \frac{3}{8}a_1 + \frac{15}{8}a_2 + \frac{a_5}{8} \\
B_2 &= a_1 + a_2 \\
B_3 &= 2a_2 \\
B_4 &= a_1 + 2a_2 \\
B_5 &= 3a_2 \\
B_6 &= 2a_2 \\
B_7 &= \frac{a_1 + 5a_2 + a_5}{2} \\
B_8 &= \frac{a_4 + a_5}{2} \\
B_9 &= \frac{a_4 + a_5}{2}
\end{aligned}
\tag{4.17}
$$

By substituting B_i values into Eq. 4.14, the effective stress for columnar grained ice can be written as

$$
\begin{aligned}
\tau_p^2 &= c_1(\sigma_x - \sigma_y)^2 + c_2(\sigma_y - \sigma_z)^2 + c_2(\sigma_z - \sigma_x)^2 \\
&+ c_4\tau_{xy}^2 + c_5\tau_{yz}^2 + c_5\tau_{zx}^2
\end{aligned}
\tag{4.18}
$$

where c_1, c_2, c_4, and c_5 can be expressed as

$$
\begin{aligned}
c_1 &= \frac{-a_1 + 3a_2 + a_5}{8} \\
c_2 &= \frac{a_1 + a_2}{2} \\
c_4 &= \frac{a_1 + 5a_2 + a_5}{2} \\
c_5 &= \frac{a_4 + a_5}{2}
\end{aligned}
\tag{4.19}
$$

The same as a single crystal ice, S2 ice is transversely isotropic. Therefore, the effective stress derived for S2 ice must be similar in formulation to the effective stress for a single crystal ice, when the coordinate systems are similar. The similarity for the effective stress between single crystal ice and S2 ice can be seen in Eq. 4.6 and Eq. 4.18.

Effective stress for granular ice

In the case of granular ice with random c-axis orientation, the probability distribution of c-axis becomes

$$p(\phi,\theta) = \frac{1}{2\pi} \tag{4.20}$$

Eq. 4.15 combining with Eq. 4.20 gives nine non-zero values for B_1, B_2, ..., B_9 as follows.

$$\begin{aligned}
B_1 &= \frac{7}{10}a_1 + \frac{5}{4}a_2 + \frac{a_4}{24} + \frac{2}{15}a_5 \\
B_2 &= a_1 + a_2 \\
B_3 &= \frac{a_1}{5} + a_2 + \frac{2}{15}a_5 \\
B_4 &= \frac{4}{3}a_1 + \frac{5}{3}a_2 \\
B_5 &= \frac{8}{15}a_1 + \frac{5}{3}a_2 + \frac{2}{15}a_5 \\
B_6 &= \frac{2}{3}a_1 + \frac{4}{3}a_2 \\
B_7 &= \frac{14}{15}a_1 + \frac{5}{3}a_2 + \frac{a_4}{6} + \frac{2}{5}a_5 \\
B_8 &= \frac{4}{15}a_1 + \frac{4}{3}a_2 + \frac{a_4}{3} + \frac{2}{5}a_5 \\
B_9 &= \frac{4}{15}a_1 + \frac{4}{3}a_2 + \frac{a_4}{3} + \frac{2}{5}a_5
\end{aligned} \tag{4.21}$$

Similarly, by substituting these B_i values into Eq. 4.14, the effective stress for granular ice can be written as

$$\begin{aligned}
\tau_p^2 = c\{&(\sigma_x - \sigma_y)^2 + (\sigma_y - \sigma_z)^2 + (\sigma_z - \sigma_x)^2 \\
&+6(\tau_{xy}^2 + \tau_{yz}^2 + \tau_{zx}^2)\}
\end{aligned} \tag{4.22}$$

where $c = \frac{4}{15}a_1 + \frac{1}{3}a_2 + \frac{1}{15}a_5$.

Calculation of viscous strain for polycrystalline ice

With the effective stress defined by Eq. 4.14 for polycrystalline ice, the viscous strain rate can be expressed as follows.

$$\frac{d\epsilon_{ij}^{v}}{dt} = C\frac{\partial \bar{Q}}{\partial \sigma_{ij}} \tag{4.23}$$

where C is a proportionality constant; $\bar{Q}$ is the plastic potential, which can be calculated using Eq. 4.24, similar to the plastic potential used by Leckie and Hayhurst (1977), Betten (1981, 1986), Rees (1983), Leckie (1986), and Sunder and Wu (1989)

$$\bar{Q} = exp(\frac{-Q_a}{RT})\frac{\tau_p^{n+1}}{(n+1)(B_1 + B_3 - B_5)^{\frac{n+1}{2}}} \tag{4.24}$$

where n is the stress power for viscous strain as defined before.

4.2.4 Crack evolution

For polycrystalline ice, crack can be intergranular or intragranular. Crack development has been associated with the pile-up of dislocations by Gold (1972a), grain boundary sliding by Sinha (1984b), and elastic anisotropy by Cole (1988).

In the present model, the material behaviour is in the ductile range, and the elastic anisotropy is not considered as an important mechanism for crack development. In the formulation, the crack development is associated with the grain boundary sliding as well as the viscous flow. The contribution of viscous flow to the crack development is assumed to be related to a partial energy dissipation, W_p, which is defined as

$$W_p = \int \sigma_{ij} d\epsilon_{ij}^{v} - \int \frac{\bar{\sigma}^c}{\bar{\sigma}} \sigma_{ij} d\epsilon_{ij}^{v} \tag{4.25}$$

where $\bar{\sigma} = \sqrt{\frac{3}{2} S_{ij} S_{ij}}$, and S_{ij} is deviatoric stress tensor; $\bar{\sigma}_c$ is the minimum stress for crack to form, which is assumed to be 0.5 MPa.

The following equation is proposed for the crack density, N:

$$\frac{\partial N}{\partial f} = \frac{1}{1.67 + 8.33\alpha}\{\frac{9}{d^2} - N\} \tag{4.26}$$

where α is a confinement parameter; d is the average grain size in meters; f is a variable that accounts for the combined effects of delayed elastic strain and the partial energy dissipation due to viscous flow:

$$\begin{aligned} f &= \frac{5.33}{d^2}\frac{W_p^{1.6828}}{u + W_p^{1.6828}} + \{\frac{\bar{\epsilon}_d d - X_c}{9.0 \times 10^{-8}}\}^p \\ p &= 5.4 - 0.6exp(-3.08 \times 10^{-5}|\bar{\sigma} - 1300|^{1.69}) \\ u &= \frac{6.46 \times 10^{-5}}{d^2}(273 - T)^{0.88} \\ X_c &= 2.67 \times 10^{-6} - 9.0 \times 10^{-9}T \end{aligned} \tag{4.27}$$

where T is the temperature in Kelvin; X_c is the critical grain boundary displacement (Sinha, 1984b); and $\bar{\sigma}$ is in kPa. The parameters in these equations are obtained from the experimental results (Gold, 1972) on crack density.

Crack density for columnar grained fresh water ice is calculated using Eq. 4.26. The comparisons between the results obtained from Eq. 4.26 and Gold's experimental results are shown in Figs. 4.2, 4.3, 4.4 and 4.5 at different stress levels and temperatures. Eq. 4.26 seems to fit Gold's experimental results quite well, however, the crack evolution equation must be verified under multiaxial loading conditions.

4.2.5 Effects of microcracks on deformation

The existence of microcracks will influence the mechanical behaviour of ice mainly by (1) reducing elastic modulus, (2) enhancing viscous strain, and (3) producing crack deformation. In this study, the first factor is not considered significant (Sinha, 1988a).

Effect of microcrack on viscous strain

With increasing microcrack activity, the viscous strain rate will increase. The effect of the crack enhancement on the viscous strain rate was first formulated for ice by Sinha (1988a) using Weertman equation for dilute cracks. Jordaan and McKenna (1990) modified the crack enhancement factor in their ice model to include the crack interaction by using an exponential function.

The following crack enhancement factor is proposed in the present study.

$$F(N) = e^{2\pi N a^2 \sqrt{n}} \tag{4.28}$$

where a is the half width of a crack, which is related to grain size; N is the crack density.

The crack enhancement factor in Eq. 4.28 is the same as that used by Sinha (1988a) for dilute cracks when $Na^2 \ll 1$. With the increase in crack interactions, the higher order of Na^2 becomes important. As discussed by Weertman (1969), for tensile stress normal to crack surface, the enhancement factor to the viscous strain rate is in the order of $(Na^2)^{2n+2}$ at high crack density. While, for shear stresses on the crack surface, the enhancement factor is in the order of $(Na^2)^{n+1}$ at high crack density. Eq. 4.28 is able to cover higher order of Na^2. With the enhancement factor given by Eq. 4.28, the viscous strain rate becomes

$$\frac{d\epsilon_{ij}^v}{dt} = C\frac{\partial \bar{Q}}{\partial \sigma_{ij}} F(N) \tag{4.29}$$

Crack strain

Under the influence of boundary conditions, a crack undergoes sliding along the crack surface and dilating normal to crack surface to cause an opening. The amount of crack deformation is characterized by two parameters. One is the sliding displacement of the crack D_s. The other one is the opening of the crack D_o.

It is reasonable to relate the crack deformation to the strain of the material around the crack. To simplify the problem, it is assumed that the opening of a

crack depends on the strain normal to the crack surface. If the strain is compressive, the size of the opening is zero. If the strain is tensile, the size of the opening can be expressed as follows.

$$D_o = \frac{d\epsilon_n d}{E_N} \tag{4.30}$$

where $d\epsilon_n$ is the strain increment normal to the crack plane, E_N is a model parameter.

Further, it is assumed that the sliding displacement is proportional to the shear strain increment $d\gamma_s$ along the plane of crack. The sliding displacement can be expressed as follows.

$$D_s = \frac{(1+\mu)d\gamma_s d}{E_N} \tag{4.31}$$

Strain caused by crack opening or shear displacement is given by Nemat-Nasser and Obata (1988).

$$\epsilon_{ij}^c = \frac{1}{2V}\int_s \{\bar{n}_i u_j + \bar{n}_j u_i\} ds \tag{4.32}$$

where V is the representative volume, $\bar{n}$ is the normal vector of the crack plane, u is the displacement vector.

For a crack with a unit normal vector $(cos\phi cos\theta, cos\phi sin\theta, sin\phi)$ and crack opening D_o, the strain increment due to the crack opening in the local coordinate system (x', y', z') with z' in the normal direction of the crack surface is given by

$$d\epsilon_{z'}^{lo} = \frac{cD_o}{V} \tag{4.33}$$

where c is the length of the crack in the case of columnar grained ice.

The increment of the rest of the strain tensor components are zero. In the global coordinate system, the strain tensor increment can be expressed as follows.

$$d\epsilon_{ij}^{o} = T_{ki} d\epsilon_{km}^{'o} T_{mj} \tag{4.34}$$

Using the coordinate transformation matrix, T_{ij}, given in Eq. 4.12, the strain tensor increment due to the crack opening can be expressed as

$$d\epsilon_{ij}^{o}(\phi,\theta) = \frac{D_o c}{2V} \begin{pmatrix} 2cos^2\phi cos^2\theta & cos^2\phi sin2\theta & sin2\phi cos\theta \\ cos^2\phi sin2\theta & 2cos^2\phi sin^2\theta & sin2\phi sin\theta \\ sin2\phi cos\theta & sin2\phi sin\theta & 2sin^2\phi \end{pmatrix} \tag{4.35}$$

Similarly, for a crack with a unit normal vector $(cos\phi cos\theta, cos\phi sin\theta, sin\phi)$, the strain tensor increment due to the sliding displacement D_s in the x' direction or y' direction can be expressed as follows, respectively.

$$d\epsilon_{ij}^{s}(\phi,\theta) = \frac{D_s c}{2V} \begin{pmatrix} cos\phi sin2\theta & -cos\phi cos2\theta & sin\phi sin\theta \\ -cos\phi cos2\theta & -cos\phi sin2\theta & -sin\phi cos\theta \\ sin\phi sin\theta & -sin\phi cos\theta & 0 \end{pmatrix} \tag{4.36}$$

$$d\epsilon_{ij}^{s}(\phi,\theta) = \frac{D_s c}{2V} \begin{pmatrix} sin2\phi cos^2\theta & \frac{1}{2}sin2\phi sin2\theta & -cos2\phi cos\theta \\ \frac{1}{2}sin2\phi sin2\theta & sin2\phi sin^2\theta & -cos2\phi sin\theta \\ -cos2\phi cos\theta & -cos2\phi sin\theta & -sin2\phi \end{pmatrix} \tag{4.37}$$

In the case of lots of cracks with the probability distribution $P(\phi,\theta)$ and crack density N, the crack strain tensor increment due to the crack opening and sliding displacement can be expressed as

$$\begin{aligned} d\epsilon_{ij}^{c} &= NV \int_0^{\frac{\pi}{2}} \int_0^{2\pi} P(\phi,\theta) d\epsilon_{ij}^{o}(\phi,\theta) cos\phi d\phi d\theta \\ d\epsilon_{ij}^{s} &= NV \int_0^{\frac{\pi}{2}} \int_0^{2\pi} P(\phi,\theta) d\epsilon_{ij}^{s}(\phi,\theta) cos\phi d\phi d\theta \end{aligned} \tag{4.38}$$

The probability distribution of cracks varies with ice type, time, temperature, and strain (Sinha, 1988a). For the present model, the probability distribution of cracks is assumed to take the following form based on the Gold's experimental data for columnar grained ice (Gold, 1972).

$$
\begin{aligned}
P(\phi,\theta) &= \frac{M}{(|\sigma_1|+|\sigma_2|)^2}\{\sigma_1^2 sin^4(\theta-\theta_1') + 2|\sigma_1\sigma_2| sin^2(\theta-\theta_1') cos^2(\theta-\theta_2') \\
&\quad +\sigma_2^2 cos^4(\theta-\theta_2')\}\delta(\phi) \\
&= G(\theta)\delta(\phi)
\end{aligned} \tag{4.39}
$$

where σ_1 and σ_2 are the maximum and minimum stresses acting on two planes parallel to the long axis of grains; M can be determined by the requirement for the probability function to be equal to one; θ_1' and θ_2' are related to θ_1 and θ_2, which are the orientations of stress σ_1 and σ_2.

$$
\begin{aligned}
\theta_1' &= \begin{cases} \theta_1 & Compression \\ 90^0+\theta_1 & Tension \end{cases} \\
\theta_2' &= \begin{cases} \theta_2 & Compression \\ 90^0+\theta_2 & Tension \end{cases}
\end{aligned} \tag{4.40}
$$

Under uniaxial compression, the crack orientation distribution was measured by Gold (1972) for columnar grained ice. The comparison of crack orientation for both measured as well as calculated from Eq. 4.39 is shown in Fig. 4.6.

Using the probability distribution calculated by Eq. 4.39, the crack strain tensor increment for columnar grained ice due to crack opening and sliding displacement can be expressed as

$$
\begin{aligned}
d\epsilon_{ij}^c = \; & cN\int_0^\pi D_o G(\theta) \begin{pmatrix} 2cos^2\theta & sin2\theta & 0 \\ sin2\theta & 2sin^2\theta & 0 \\ 0 & 0 & 0 \end{pmatrix} d\theta \\
& + cN\int_0^\pi D_s G(\theta) \begin{pmatrix} sin2\theta & -cos2\theta & 0 \\ -cos2\theta & -sin2\theta & 0 \\ 0 & 0 & 0 \end{pmatrix} d\theta
\end{aligned} \tag{4.41}
$$

The sliding displacement of cracks in the direction of long columns is given as zero based on the experimental results (Sinha, 1989a; Sinha et al., 1992).

In the case of uniaxial compression, σ_1 is in the x direction. Eqs. 4.39, 4.30, and 4.31 can be simplified as

$$\begin{aligned} P(\theta,\phi) &= \frac{4}{3\pi} sin^4\theta\delta(\phi) \\ D_o &= \frac{d}{E_N}(d\epsilon_x cos^2\theta + d\epsilon_y sin^2\theta) \\ D_s &= -\frac{(1+\mu)d}{2E_N}(d\epsilon_y - d\epsilon_x) sin2\theta \end{aligned} \tag{4.42}$$

Substituting Eq. 4.42 to Eq. 4.41, the crack strain tensor increment in Eq. 4.41 becomes

$$\begin{aligned} d\epsilon_{ij}^c = \; & \frac{8cdN}{3\pi E_N}\begin{pmatrix} p_1 & 0 & 0 \\ 0 & p_2 & 0 \\ 0 & 0 & 0 \end{pmatrix} + \frac{4(1+\mu)cdN}{3\pi E_N} \\ & (d\epsilon_y - d\epsilon_x)\begin{pmatrix} -p_3 & 0 & 0 \\ 0 & p_3 & 0 \\ 0 & 0 & 0 \end{pmatrix} \end{aligned} \tag{4.43}$$

where p_1, p_2, and p_3 are given by

$$\begin{aligned} p_1 &= 2d\epsilon_x H_1(\theta_1) + 2d\epsilon_y H_2(\theta_1) \\ p_2 &= 2d\epsilon_x H_2(\theta_1) + 2d\epsilon_y H_3(\theta_1) \\ H_1(\theta_1) &= \int_{\theta_1}^{\frac{\pi}{2}} cos^4 x sin^4 dx \\ H_2(\theta_1) &= \int_{\theta_1}^{\frac{\pi}{2}} cos^2 x sin^6 x dx \\ H_3(\theta_1) &= \int_{\theta_1}^{\frac{\pi}{2}} sin^8 x dx \\ p_3 &= \int_0^{\frac{\pi}{2}} sin^2 2x sin^4 x dx \end{aligned} \tag{4.44}$$

in which $\theta_1 = atan(\sqrt{\frac{\epsilon_y}{\epsilon_x}})$.

At this point, the formulations of the constitutive equation of fresh water columnar grained ice are completed. In summary, Eq. 4.2 gives the elastic strain tensor; the delayed elastic strain tensor is given by Eq. 4.4; the viscous strain can be obtained from Eq. 4.29; and the increment of the crack strain tensor is formulated in Eq. 4.41.

4.3 Model validation

Various predictions are made using the model and they are compared with the experimental data to validate the model.

4.3.1 Material constants and model parameters

The elastic strain tensor is formulated for anisotropic material. However, for the following predictions, the ice is treated as an isotropic material for elastic deformations. This is an acceptable approximation for S2 ice (Sinha, 1989b). The material constants for elastic strain are then given by elastic modulus and Poisson's ratio.

For S2 ice, under uniaxial horizontal loading condition, Eq. 4.4 for delayed elasticity in the loading direction can be written as

$$\frac{\partial \epsilon_d^n}{\partial t} = a_T\{(\frac{C_1 d_1 \sigma_x}{Ed})^n - \epsilon_d^n\} \tag{4.45}$$

In the case of instantaneous loading condition, $\sigma_x = \sigma H(t)$, by integrating Eq. 4.45, the delayed elasticity can be obtained as

$$\epsilon_d = \frac{C_1 d_1 \sigma}{Ed}\{1 - exp(-a_T t)\}^{\frac{1}{n}} \tag{4.46}$$

When the $a_T t \ll 1$, the above equation for delayed elasticity becomes identical to Eq. 4.3 for delayed elasticity. Therefore, the material constants in Eq. 4.46 is the same as those in Sinha's equation for delayed elasticity Eq. 4.3.

The other model parameters b_1, b_2, and b_3 (see Eq. 4.5) are used to represent the anisotropy of delayed elastic deformation. Without loss of any generality, b_1

is taken as 1. Similar to Eq. 4.7, for the requirement of symmetry for S2 ice, the following relationship exists among b_1, b_2, and b_3.

$$3b_3 = 2b_1 + b_2 \tag{4.47}$$

Therefore, only one model parameter needs to be determined from a creep test for delayed elasticity in the present model.

For viscous strain, n is the stress power, which is about 3 for polycrystalline ice. C is the proportionality constant which is determined from a uniaxial constant load test result.

The model parameters a_1, a_2, a_4, and a_5 are used to represent the anisotropy of viscous strain of single ice crystals. Without loss of any generality, a_1 can be taken as 1. From Eq. 4.7, only two parameters need to be determined from creep tests on single crystal ice.

There is only one model parameter for crack strain tensor, which can be estimated based on the crack size given by Sinha (1990a). The model parameters related to crack density are obtained from Gold's experimental results (1972).

In summary, the following material constants and model parameters shown in Table 4.1 are used in the predictions for temperature 263 K.

Table 4.1: Material properties for fresh water columnar grained ice

Elastic modulus E	9.5 GPa
Poisson's ratio μ	0.33
For delayed elasticity, C_1 and a_T at 263 K	9.0, 0.00025 s^{-1}
For delayed elasticity, b_2	0.2
For viscous strain C, n	$1.43 \times 10^6 s^{-1}$, 3
For viscous strain a_2, a_5	0.3, 50.0
For crack strain E_N	1.0

In the Table 4.1, E, C_1, a_T, n are the same material constants used by Sinha (1978a, 1979a) for columnar grained ice. The model parameter b_2 represents the anisotropy in delayed elasticity, which is given a value of 0.2 based on the constant load test results on first year columnar grained sea ice (Sinha et al., 1992). The

model parameters for viscous strain, a_2 and a_5, are assumed to be 0.3 and 50.0 based on the test results on single ice crystals (Butkovich and Laudauer, 1958). In Chapter 6, the present constitutive model is extended to sea ice. The same model parameters a_2, a_5 and b_2 are used for sea ice model. Good agreement between test results and model predictions is achieved. E_N is given as 1.0 based on the width of crack estimated by Sinha (1990a). It must be mentioned that the model parameters b_2, a_2 and a_5 will not affect the predicted strain and stress in the loading direction under uniaxial loading condition for S2 ice loaded in the horizontal plane.

4.3.2 Prediction of constant load test

The stress and time dependence of axial and volumetric strains predicted from the present model are presented in Fig. 4.7 for 263 K. The ice is transversely isotropic S2 ice with grain size 2 mm. It was loaded uniaxially normal to the long axis of grains. The test results from Sinha (1990a) is also presented in the figure. Good agreement between the model predictions and test results is achieved, although the model predictions are a little bit smaller than the experimental results.

Strain along the long columns of grains is insignificant compared to the strains in other two directions as predicted from the model and obtained from experiments (Sinha, 1989a; Sinha et al., 1992). It can, therefore, be concluded that good agreements between model predictions and test results in Fig. 4.7 for both axial and volumetric strains suggest that the present model can predict the anisotropic deformation of columnar grained ice.

As an example, the time dependence of axial, lateral and volumetric strains calculated from the model is presented in Fig. 4.8 for columnar grained S2 ice with a grain size 1.0 mm. It was loaded normal to the long axis of the grains with a stress 2.0 MPa at 263 K. The results show that the behaviour of the columnar grained ice is highly anisotropic. The deformation is primarily two dimensional. This prediction agrees with previous experimental investigation by (Wang, 1981; Sinha, 1989a; Sinha, et. al, 1992). Strain along the column ϵ_3 is very small compared to the other two. Strain ϵ_2 is significantly higher than the axial strain ϵ_1 during the tertiary creep. Due to this, a large amount of volumetric strain is

produced. By looking at the axial strain, it can be concluded that the model is capable of describing the primary, secondary, and tertiary creep of ice.

The stress and time dependence of axial strain rate predicted from the present model is presented in Fig. 4.9 at 263 K. The ice is S2 ice with a grain size 4.5 mm. It was loaded uniaxially normal to the long axis of grains. The dash line is a connection of points for the minimum strain rate at 8 different stress levels. This line means that the minimum strain rate increases with the increase of stress, which has been reported in a number of experimental studies.

4.3.3 Prediction of constant displacement rate test

Sinha (1982) carried out a series constant strain rate tests on fresh water columnar grained S2 ice with a closed-loop MTS machine. The load was applied normal to the long columns. The average grain size is 4.5 mm. The tests were conducted at a temperature of 263 K (-10^0C).

Figure 4.10 shows the strain rate dependence of stress and strain diagram at 263 K predicted from the present model. The experimental results (Sinha, 1982) are also shown as the square maker in the figure. In general, the two results agree quite well, especially, at low strain rate. However, the model prediction is higher at lower strain but lower at higher strain.

4.3.4 Prediction of grain size effect

The grain size and time dependence of the axial strains are calculated using the present model and the results are presented in Fig. 4.11. It is for S2 ice loaded normal to the long axis of grains at 263 K. The test results by Sinha (1989a) under the same condition are also shown in the figure as the square markers. Both the test results and the model predictions show that strain rate for smaller grain size is higher than that for larger grain size initially, but, the reverse is true after primary creep. Although the strain predicted from the present model is smaller than the experimental results, the agreement between the model predictions and test results is fair.

Figure 4.12 shows the grain size dependence of stress strain diagram for S2 ice loaded uniaxially normal to the long axis of the grains at 263 K. The strain rate is

$5 \times 10^{-5} s^{-1}$. With the decrease of grain size, the material becomes more ductile. In addition, the grain size dependence of the maximum stress is negligible. This is in agreement with the test result reported by Jones and Chew (1983) for man-made fresh water granular ice. However, the experimental result on fresh water man-made granular ice by Cole (1987) suggest that there is a grain size dependence of the maximum stress. This contradiction could be due to the existence of air bubbles generated during the process of making ice samples.

4.3.5 Prediction of strength anisotropy

Figure 4.13 shows the strength dependence on the angle between the mean c-axis and the loading direction. The ice is oriented columnar grained S3 ice with a grain size 4.5 mm. The simulation is carried out at three different strain rates. It is known that for oriented columnar grained ice, the strength is highly dependent on the angle between the mean c-axis and the loading direction (Peyton, 1966; Wang, 1979a; Sinha, 1985). Due to the lack of test data on S3 ice, no direct comparison is given. However, the shape of the curves are quite similar to the test results obtained by Wang (1979b). The present model was extended to sea ice in Chapter 5, where direct comparison between the sea ice model prediction and the test results by Richter-Menge (1991) for S3b ice shows good agreement.

For S2 ice, it was known that under uniaxial compression, the maximum stress is about 2 to 4 times higher when the ice is loaded parallel to the long axis of the grains than that when it is loaded normal to the long axis of the grains (Peyton, 1966; Michel, 1978; Sinha, 1983, 1984a; Frederking and Timco, 1984; Timco and Frederking, 1986). Fig. 4.14 shows the theoretical prediction from the present model. It shows that the vertical strength is about 3 times higher than the horizontal strength at strain rate 5×10^{-5} for grain size 4.5 mm. Two reasons can be given to this high vertical strength from the constitutive model. One is that the loading in the vertical direction is in a position to cause hard glide. The other one is that cracking is happened in planes parallel to the loading direction. Therefore, there is no contribution of the crack strain to the strain in the loading direction.

4.3.6 Correspondence between CS and CD test

The strain rate dependence of the maximum stress and stress dependence of minimum strain rate are presented in Fig. 4.15 for two different stress paths. One is a stress path for constant stress test (CS). The other is a stress path for constant displacement rate test (CD). It shows that there is no difference for the maximum stress when the strain rate is lower than $4 \times 10^{-5} s^{-1}$. While, the CS results shows a higher rate dependence after that strain rate. Similar conclusions have been reached, based on the experimental investigations, for fresh water columnar grained ice (Sinha, 1981b), for fresh water granular ice (Mellor and Cole, 1982, 1983), and for first year columnar grained ice (Chapter 2).

The dependence of strain at failure for the two stress paths is presented in Fig. 4.16. In general, the strain at failure for CS test is lower than that for CD test. However, the difference is small. This is in agreement with the experimental investigation by Mellor and Cole (1983).

The dependence of time at failure for the two stress paths is presented in Fig. 4.17. In general, the time at failure for CS test is lower than that for CD test. The experimental investigation by Mellor and Cole (1983) shows similar trend.

4.7 Prediction of strength under multiaxial loading

The effect of confinement on the deformation of ice has been investigated by a number of researchers experimentally (Frederking, 1977; Hausler, 1982; Jones, 1982; Nawwar et al., 1983; Blanchet and Hamza, 1983; Timco and Frederking 1983; Sinha, 1985; and Richter-Menge, 1991). Sinha (1991a) used his constitutive model to predict the stress-strain curve under biaxial proportional loading. However, no direct comparison for the rate dependence of strength between model prediction and test data was given. The rate dependence of strength is presented in Fig. 4.18. The ice is S2 ice with grain size 1 mm. It is loaded in the plane parallel to the long axis of grains, and confined in another plane which is also parallel to the long axis of grains. The third plane which is normal to the long axis of grains is free. Two solid lines are for two different confinements. The upper line is for 85 percent of confinement $\frac{\sigma_2}{\sigma_1} = 0.85$. The lower line is for 57 percent of confinement. The two different confinements are chosen based on the measurements by Sinha

(1985). The experimental results from Frederking (1977) and Sinha (1985) are also presented in the figure. Frederking's results are for fresh water S2 ice. Sinha's results are for second year columnar grained sea ice with zero salinity. So, the ice can be treated as fresh water ice. For strain rate above $10^{-5}s^{-1}$, the test results are well within the model predictions. However, for strain rate lower than $10^{-5}s^{-1}$, the strength value predicted from the model is lower than the experimental value. One reason could be the effectiveness of the confinement. It would be expected that at lower strain rate, the confinement would be more effective than that at higher strain rate for the plane strain tests performed. Another reason could be due to the effect of the first invariant of stress on viscous strain rate, which is not considered in the model.

Figure 4.19 shows the effect of confinement at different direction for S2 ice on the stress strain diagram. The strain rate is 10^{-5}. The ice is loaded in the horizontal plane in the x direction. It shows that the strength for the confinement in both y direction and z direction (long column direction) is the highest. The strength for no confinement and confinement normal to the long axis of grains is about the same which are the lowest. The strength under confinement parallel to the long axis of grains are in between. The small difference between no confinement and the confinement in the direction normal to the long axis of the grains was reported by Timco and Frederking (1986).

4.3.8 Prediction of temperature effect

The temperature dependence of stress strain diagram predicted from present model is presented in Fig. 4.20 at strain rate $5 \times 10^{-5}s^{-1}$. The ice is S2 ice with grain size 4.5 mm loaded uniaxially normal to the long axis of grains. In general, it shows that with the decrease of temperature, the maximum stress, time and strain to failure increase.

Figures 4.21 and 4.22 show the temperature and time dependence of axial strain, volumetric strain and axial strain rate for a constant stress of 3.0 MPa. It show that the rate of deformation is much smaller at low temperature at a given time.

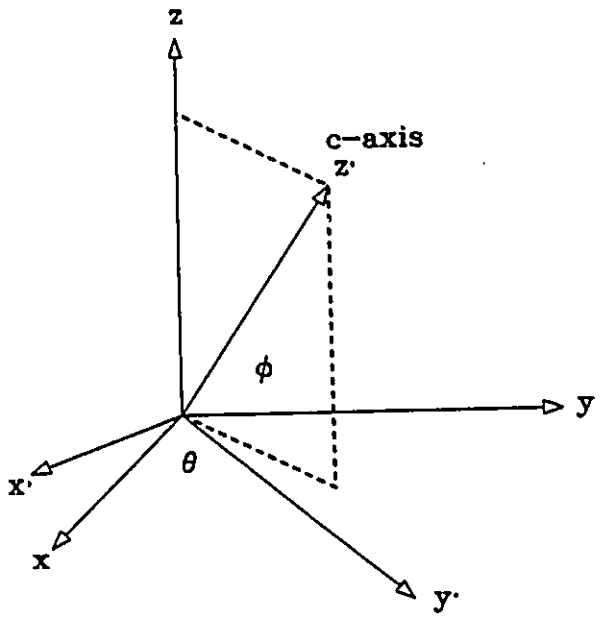

Figure 4.1 Global and local coordinate systems

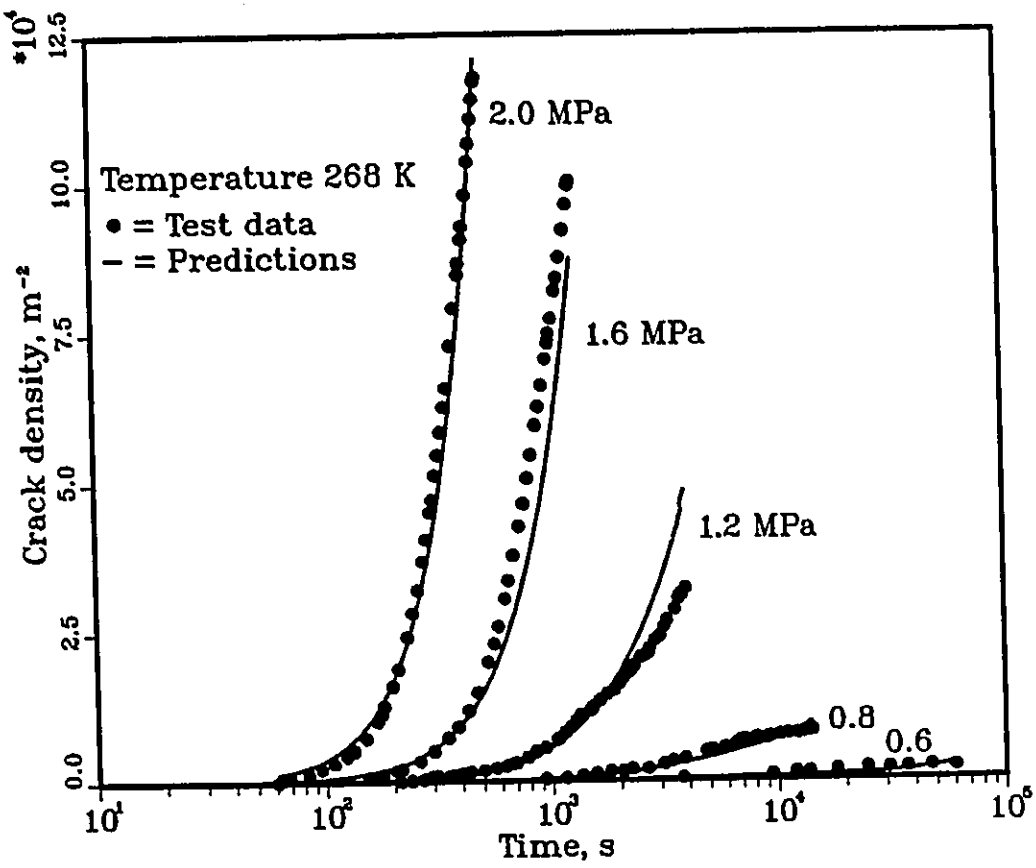

Figure 4.2 Comparisons of crack density between model predictions and experimental data at 268 K

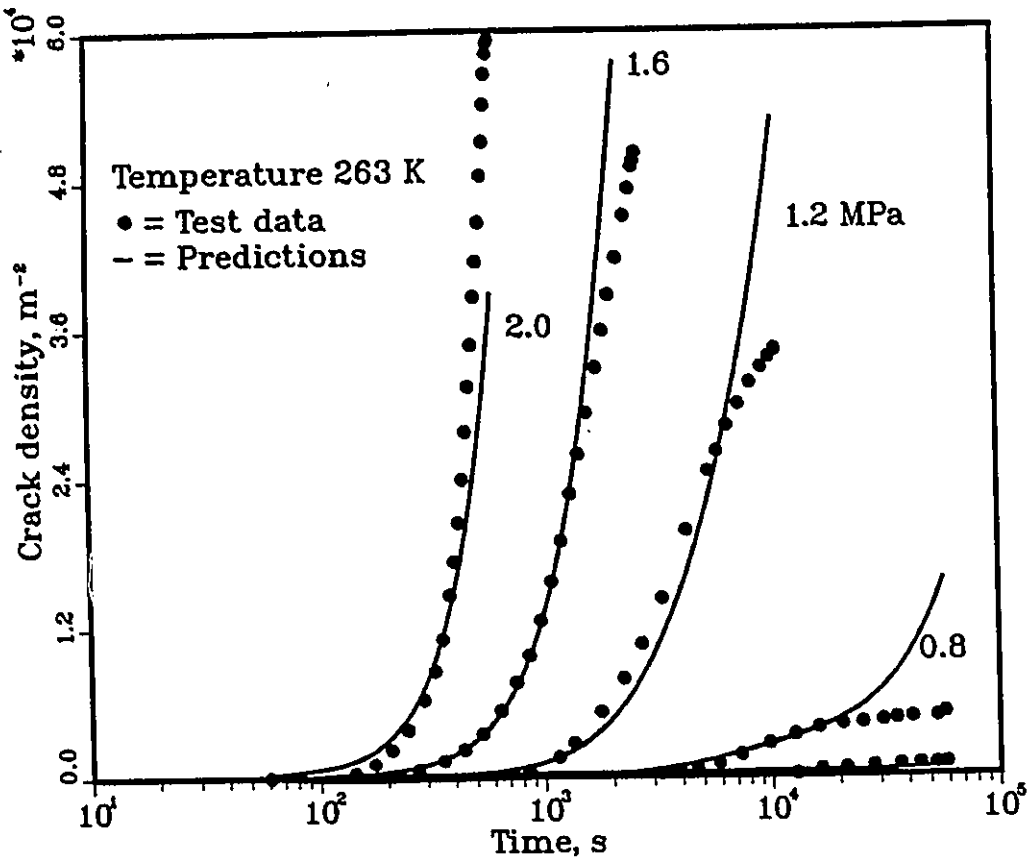

Figure 4.3 Comparisons of crack density between model predictions and test data at 263 K

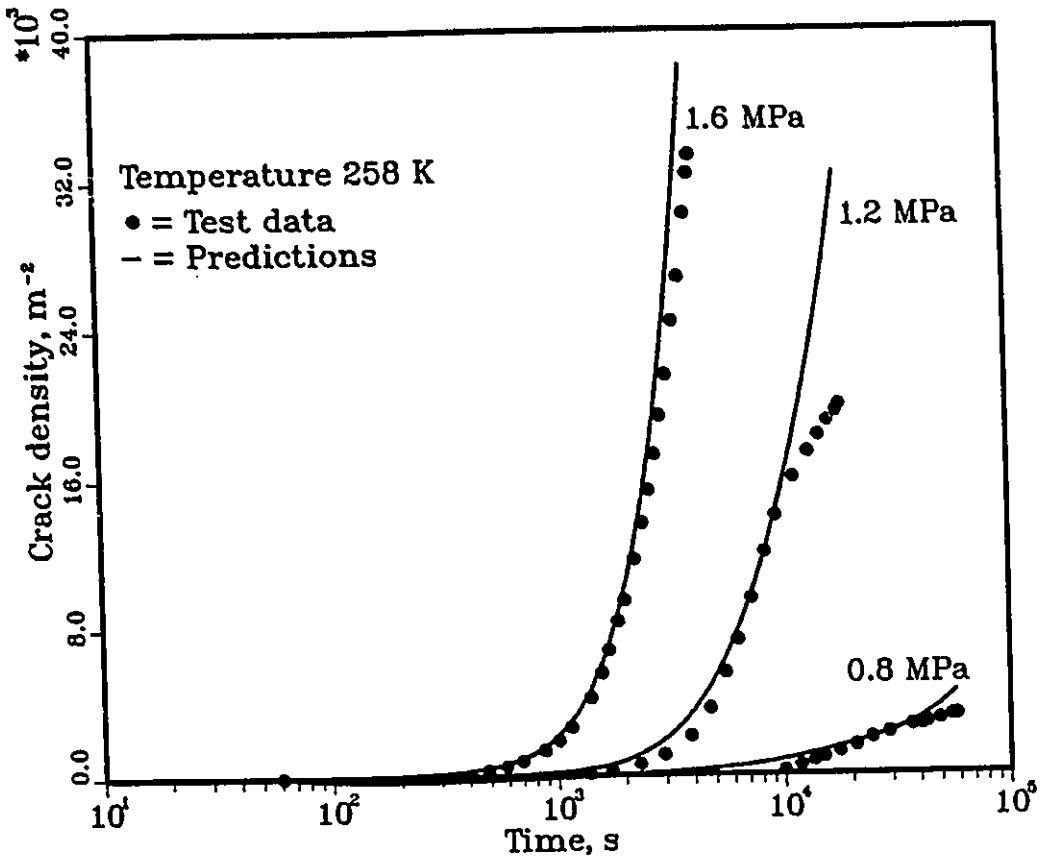

Figure 4.4 Comparisons of crack density between model predictions and experimental data at 253 K

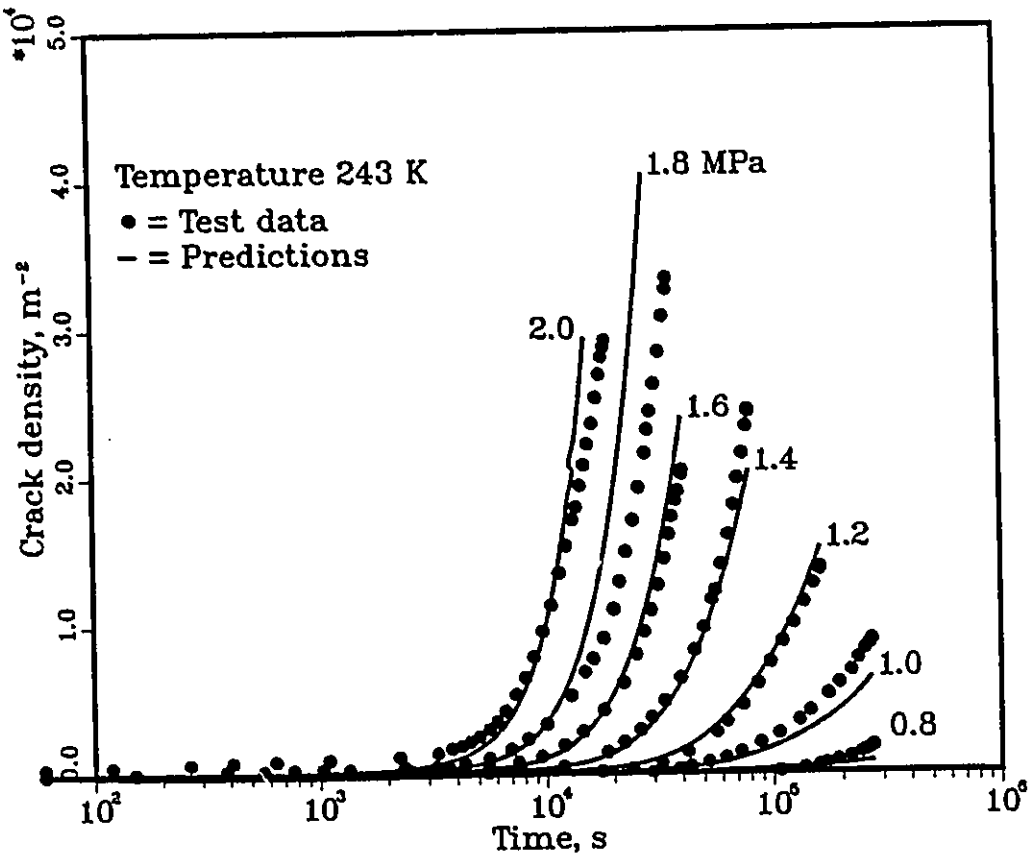

Figure 4.5 Comparisons of crack density between model predictions and experimental data at 242 K

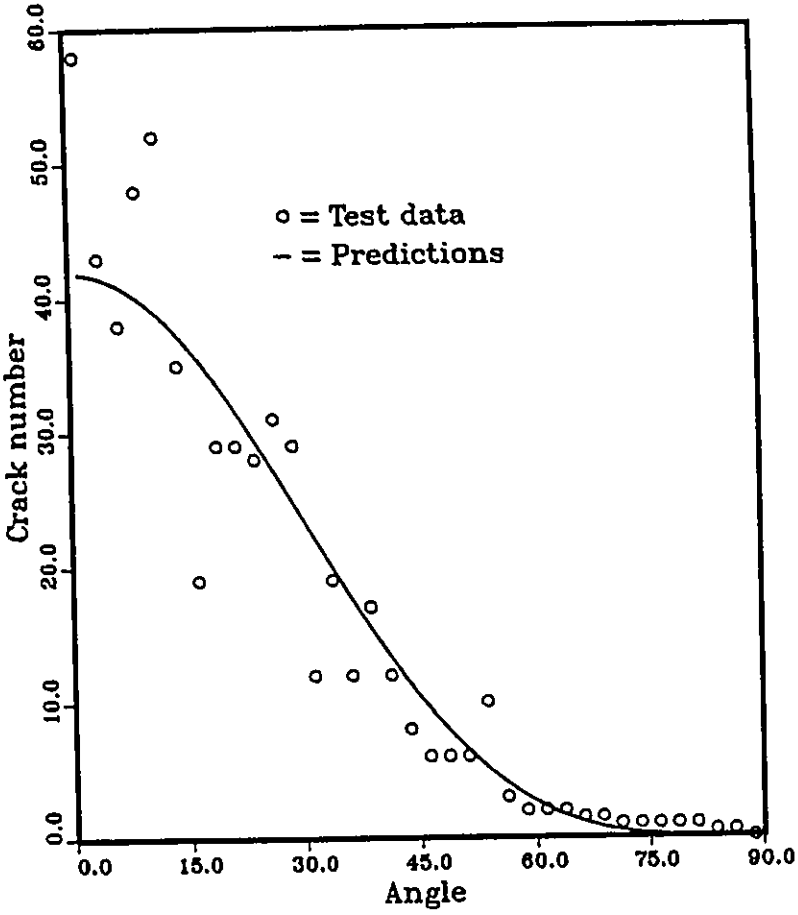

Figure 4.6 Comparisons between test data and predictions for crack orientations

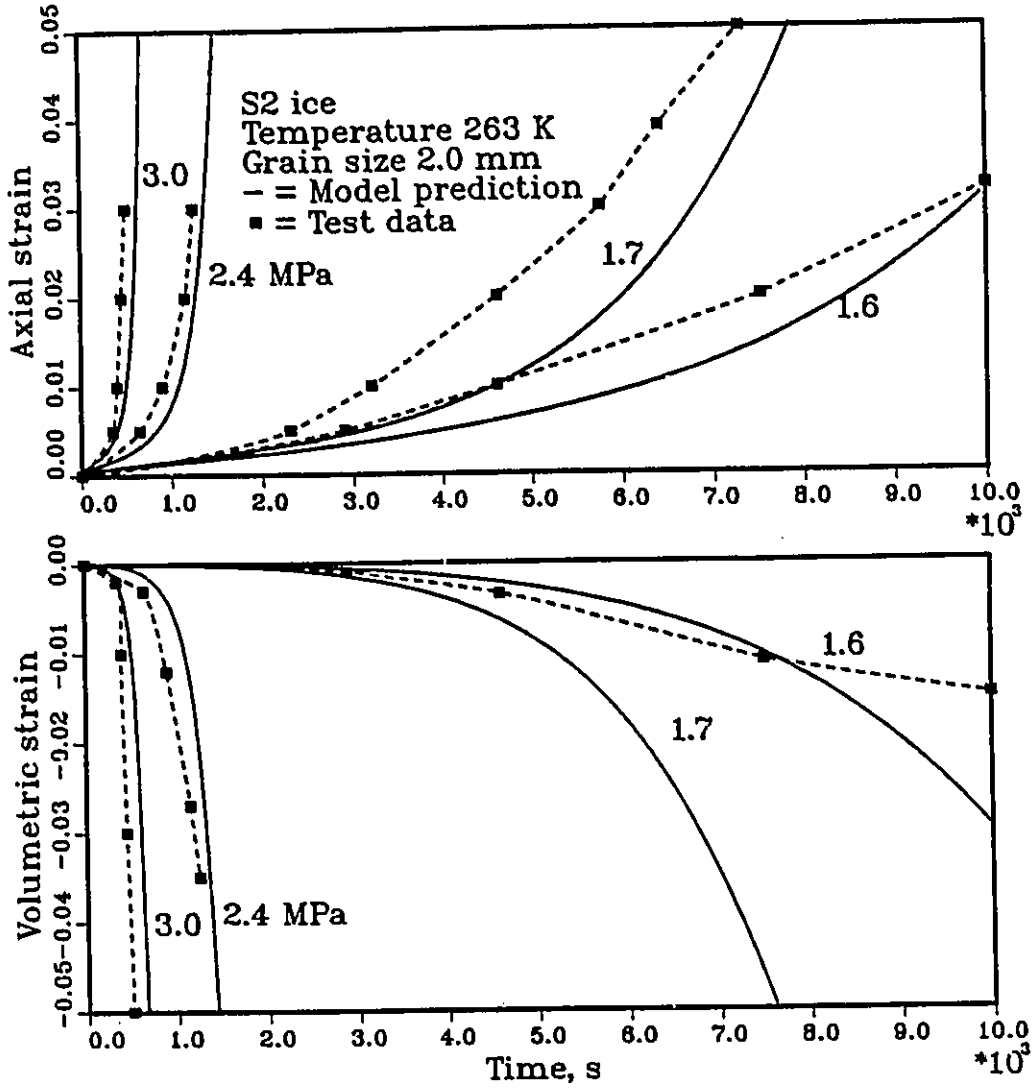

Figure 4.7 Comparisons between model predictions and test results for time dependence of axial and volumetric strains

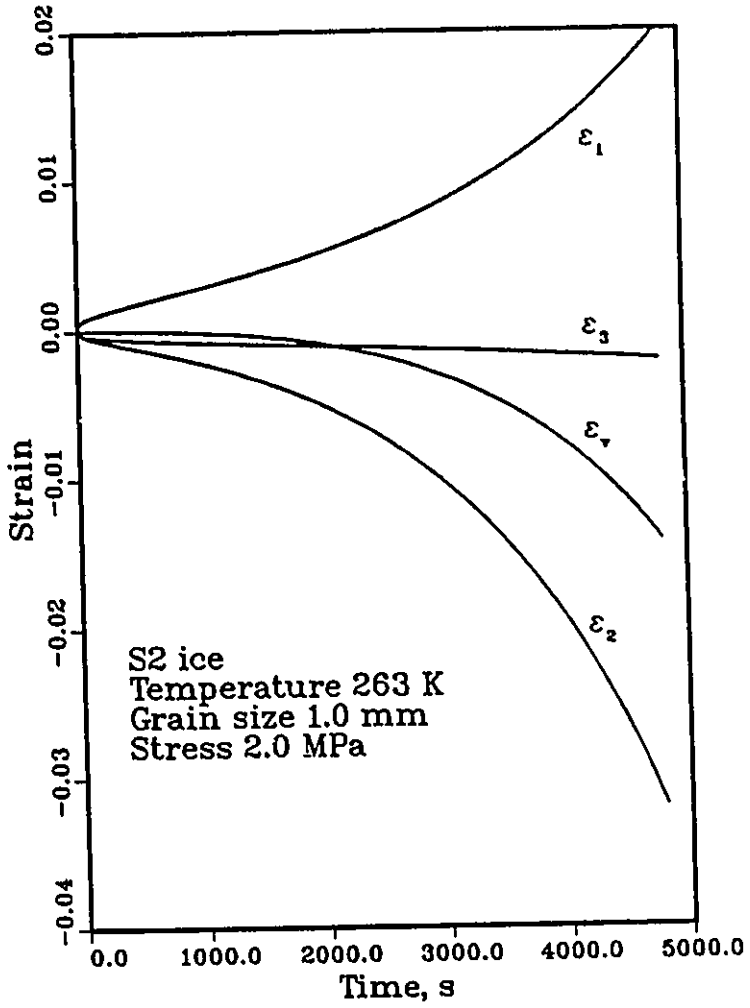

Figure 4.8 Model predictions for the time dependence of axial lateral and volumetric strains

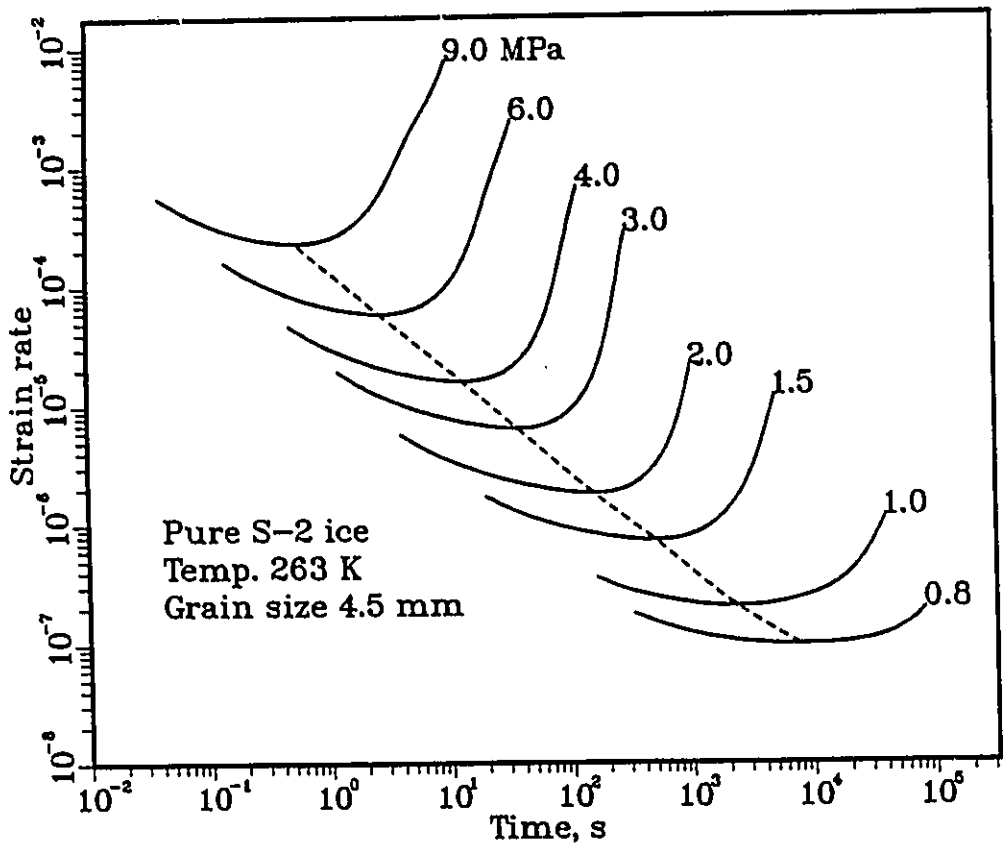

Figure 4.9 Time and stress dependence of axial strain rate predicted from present model

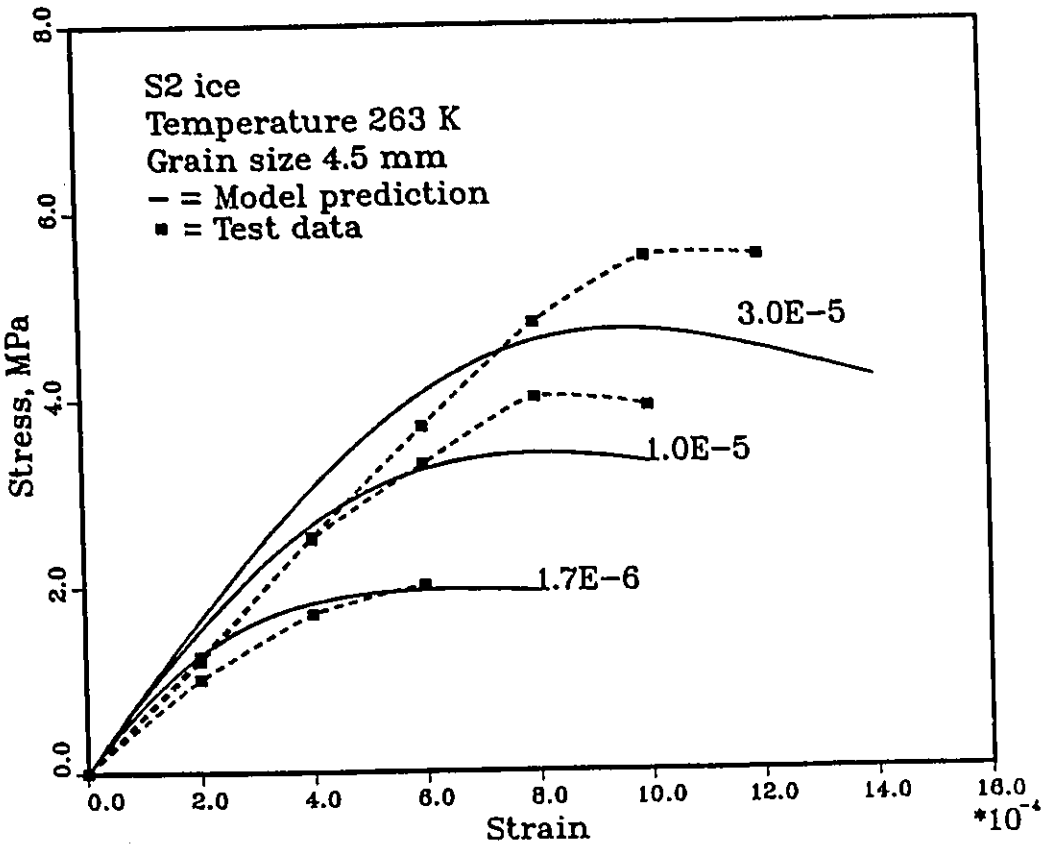

Figure 4.10 Comparisons between model predictionsand test results for stress–strain diagrams

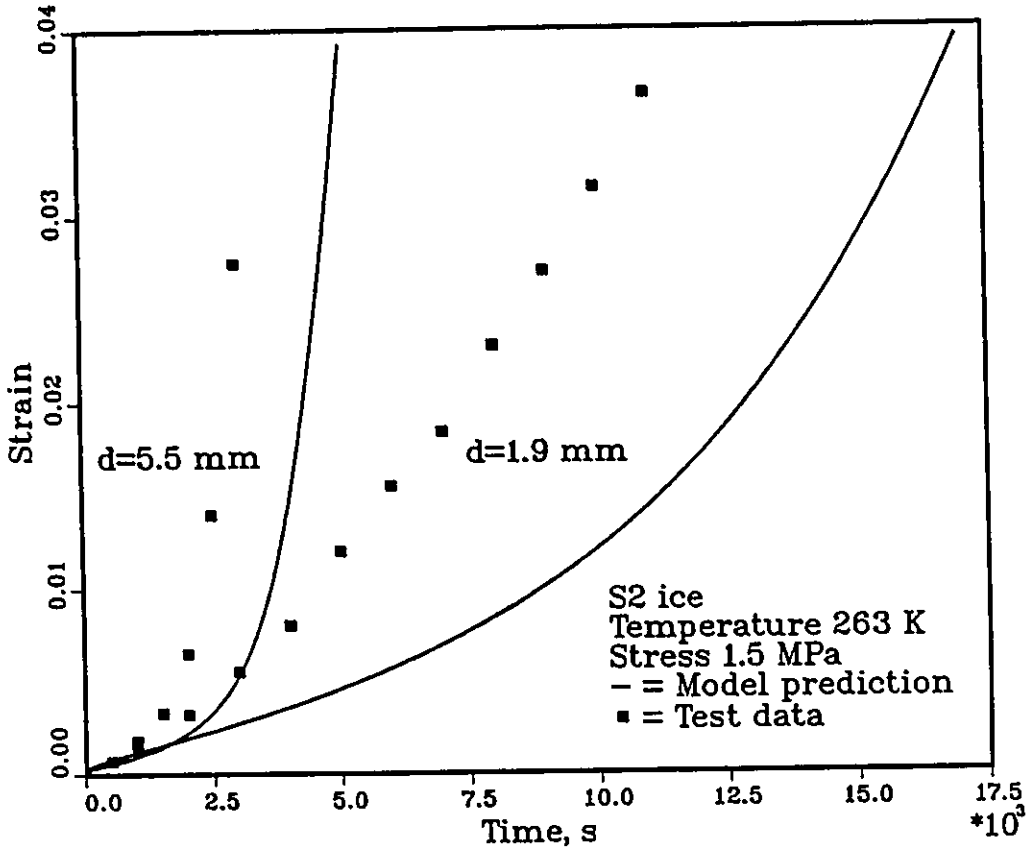

Figure 4.11 Comparisons between model predictions and test data for time and grain size dependence of axial strains

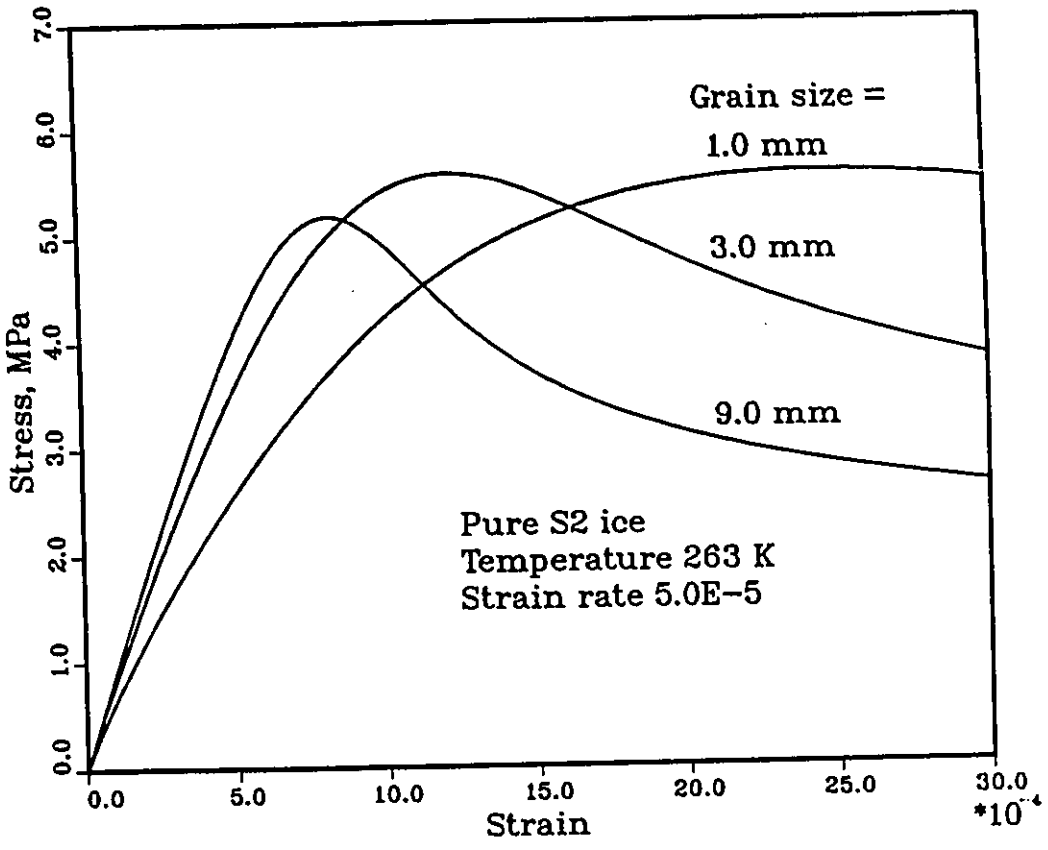

Figure 4.12 Grain size dependence of stress–strain diagrams predicted from present model

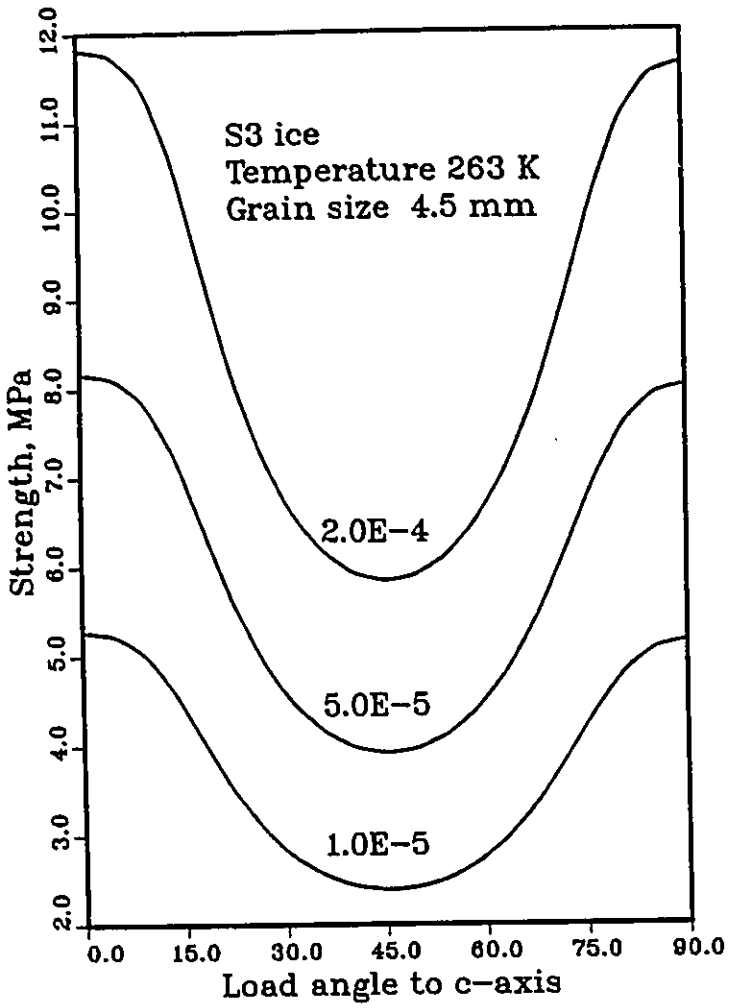

Figure 4.13 Strength dependence on angle between mean c−axis and loading direction

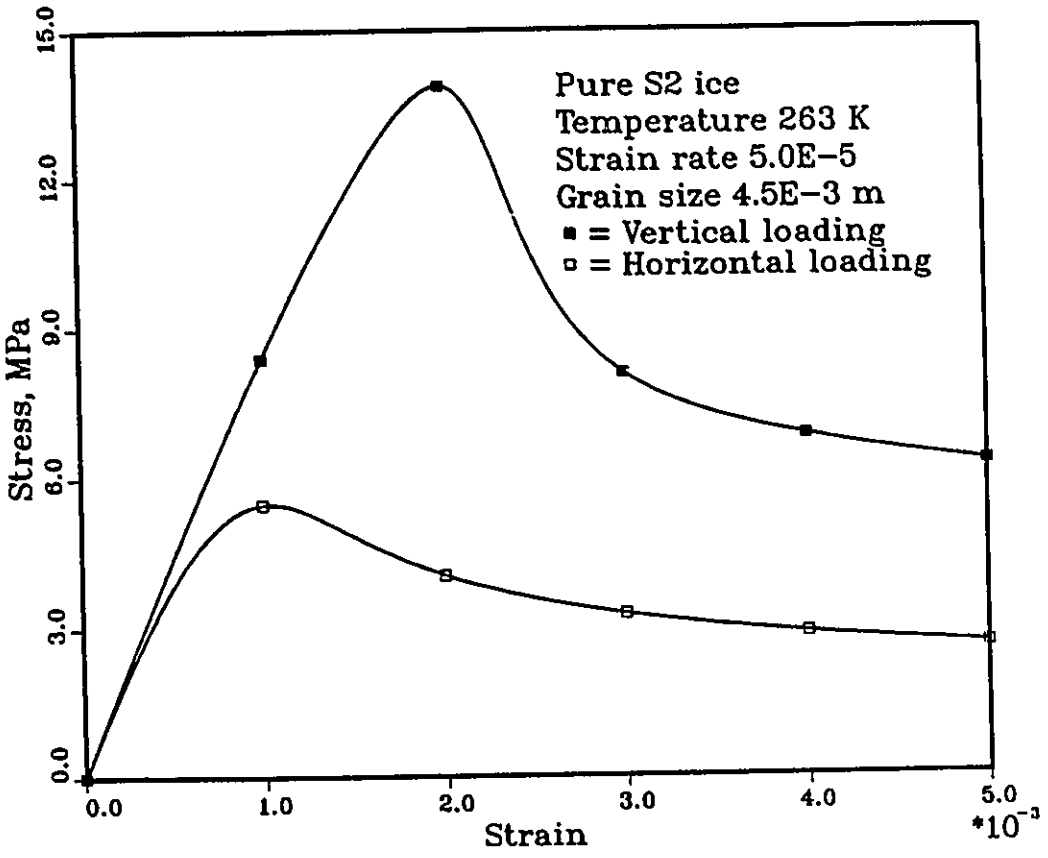

Figure 4.14 Comparisons for stress–strain diagrams between horizontal and vertical loading predicted from present model

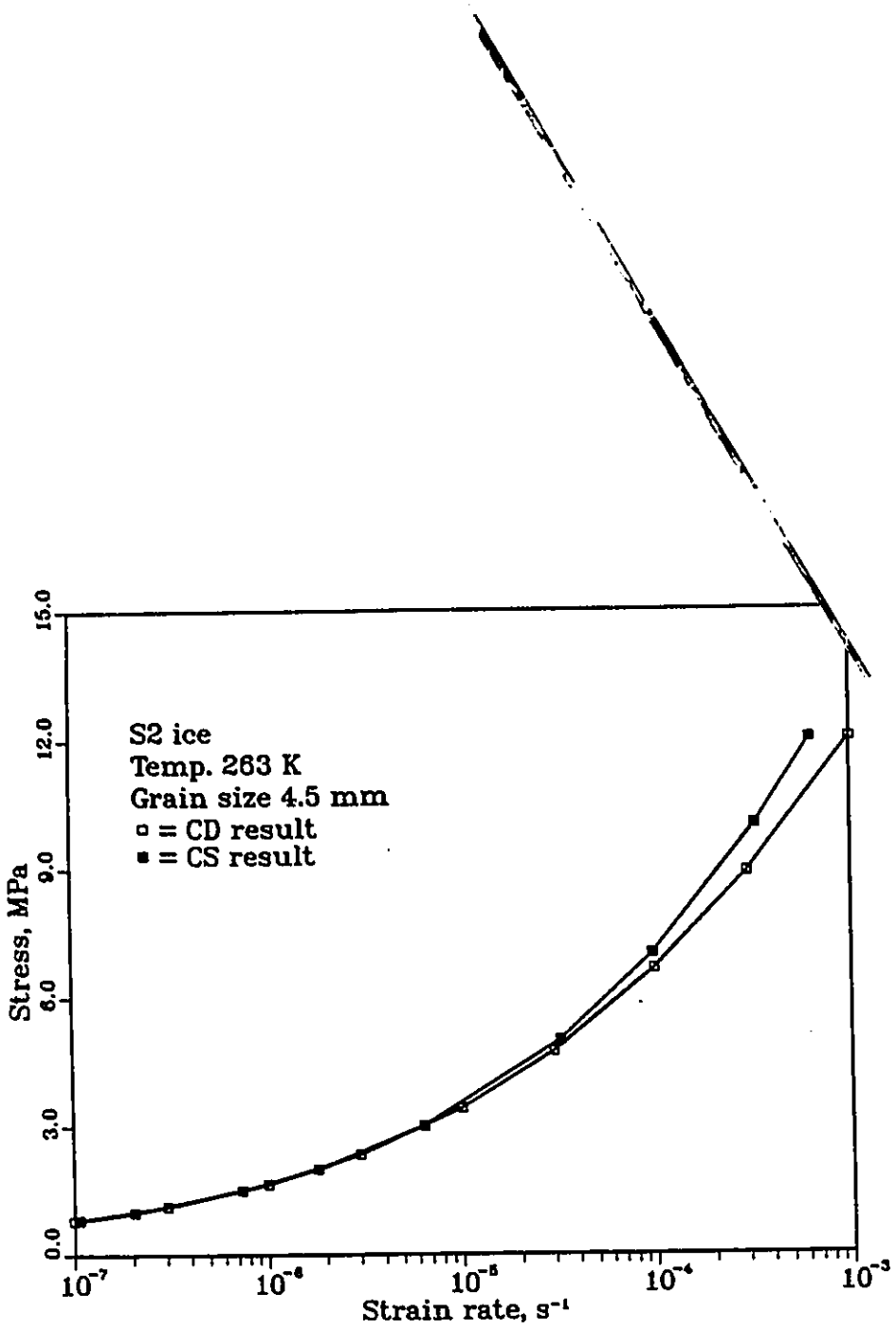

Figure 4.15 Correlations between rate dependence of strength in CD test and stress dependence of minimum strain rate in CS test

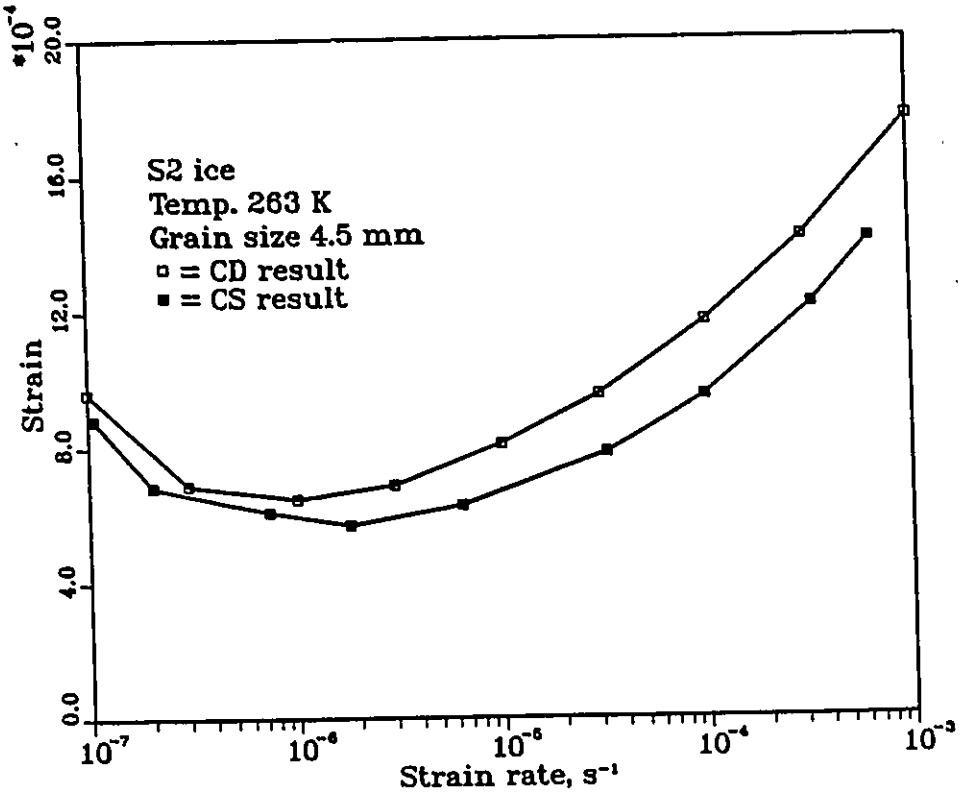

Figure 4.16 Dependence of strains at failure on strain rate for both CD and CS tests predicted from present model

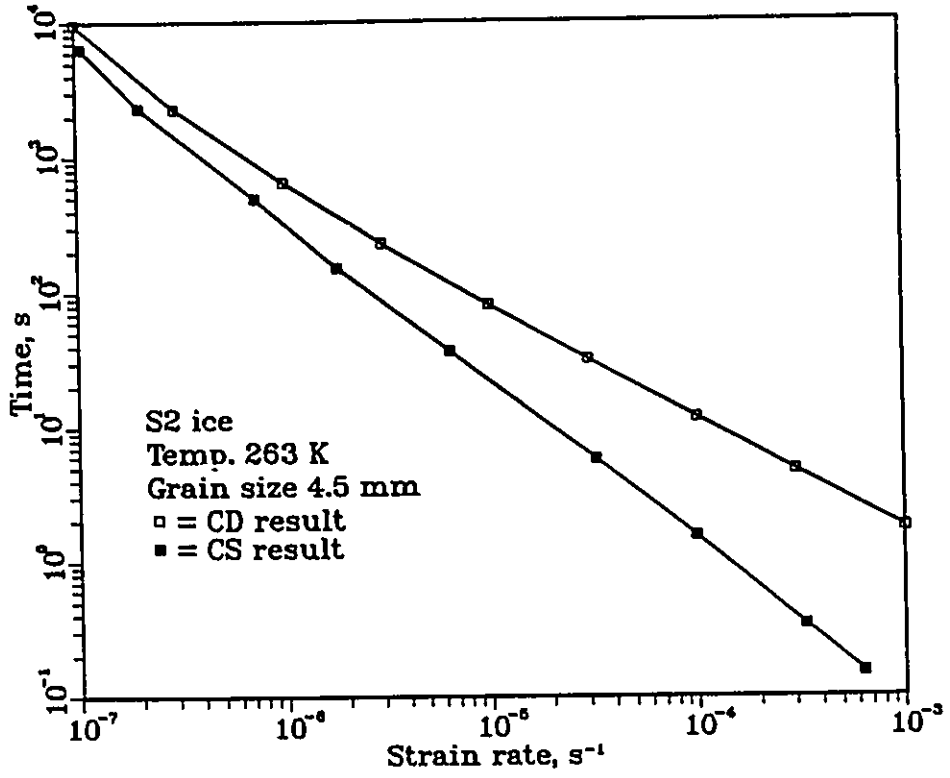

Figure 4.17 Dependence of time at failure on strain rate for both CD and CS tests predicted from present model

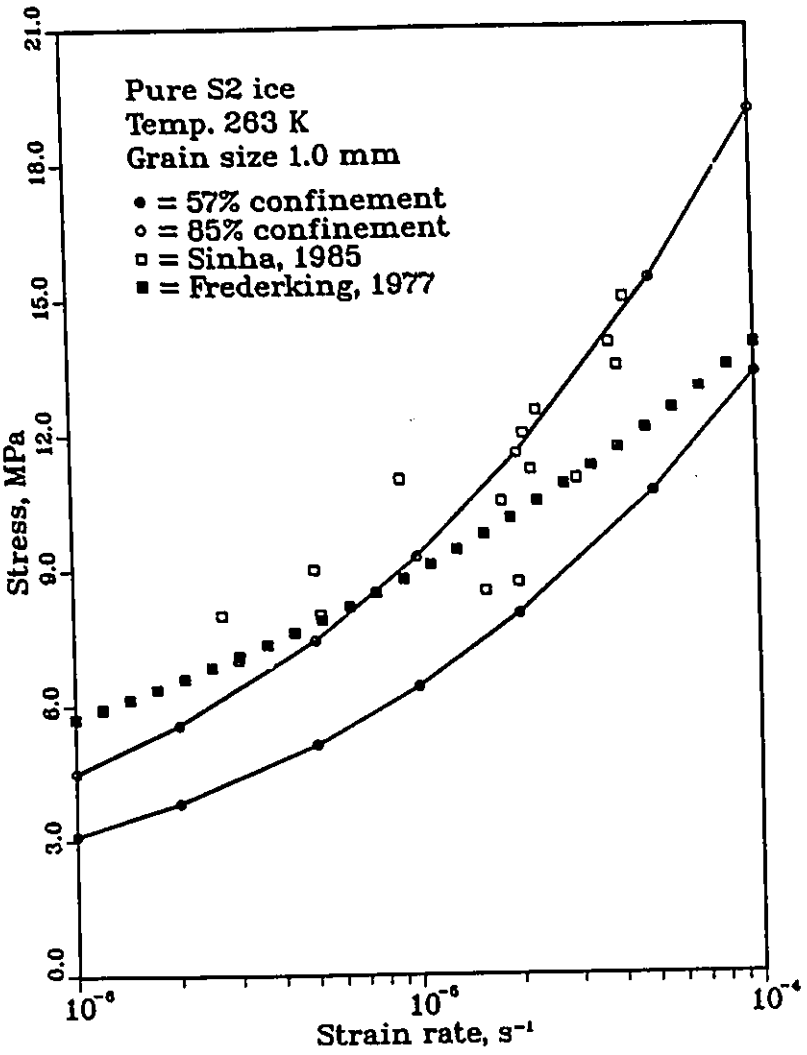

Figure 4.18 Comparisons between model predictions and test data for rate dependence of strength

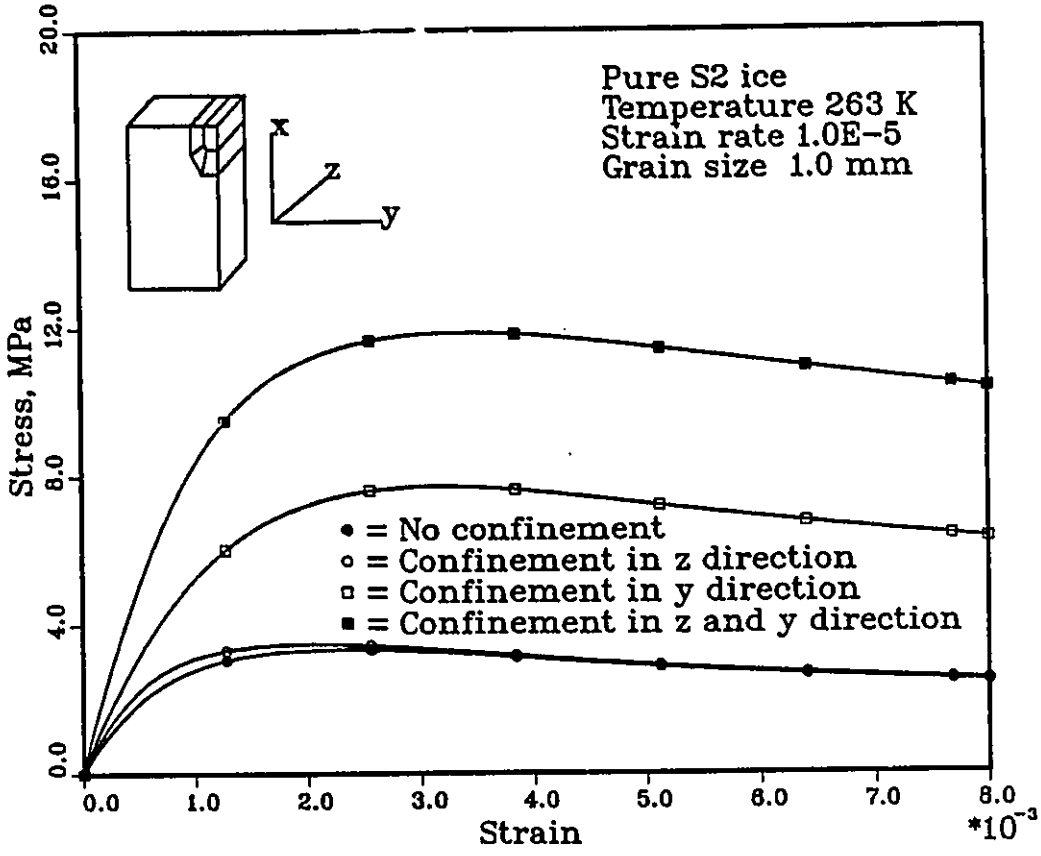

Figure 4.19 Stress–strain diagrams at different confinement predicted from present model

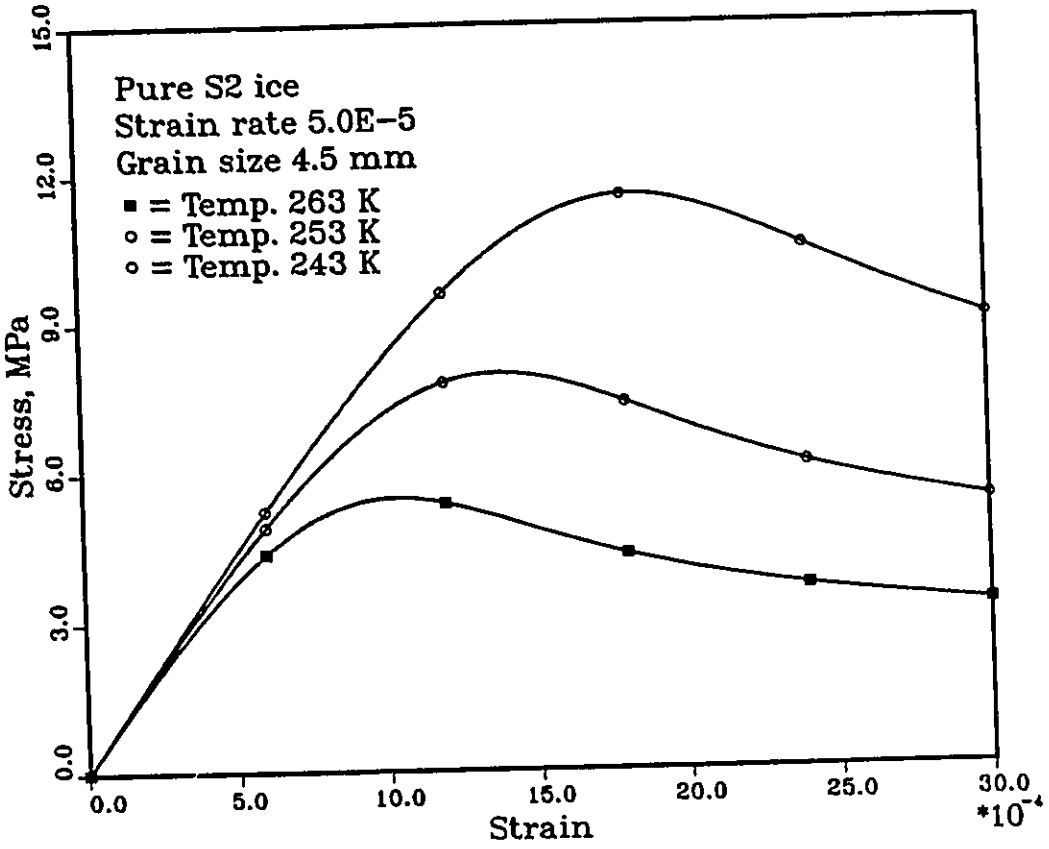

Figure 4.20 Temperature dependence of stress–strain diagrams predicted from present model

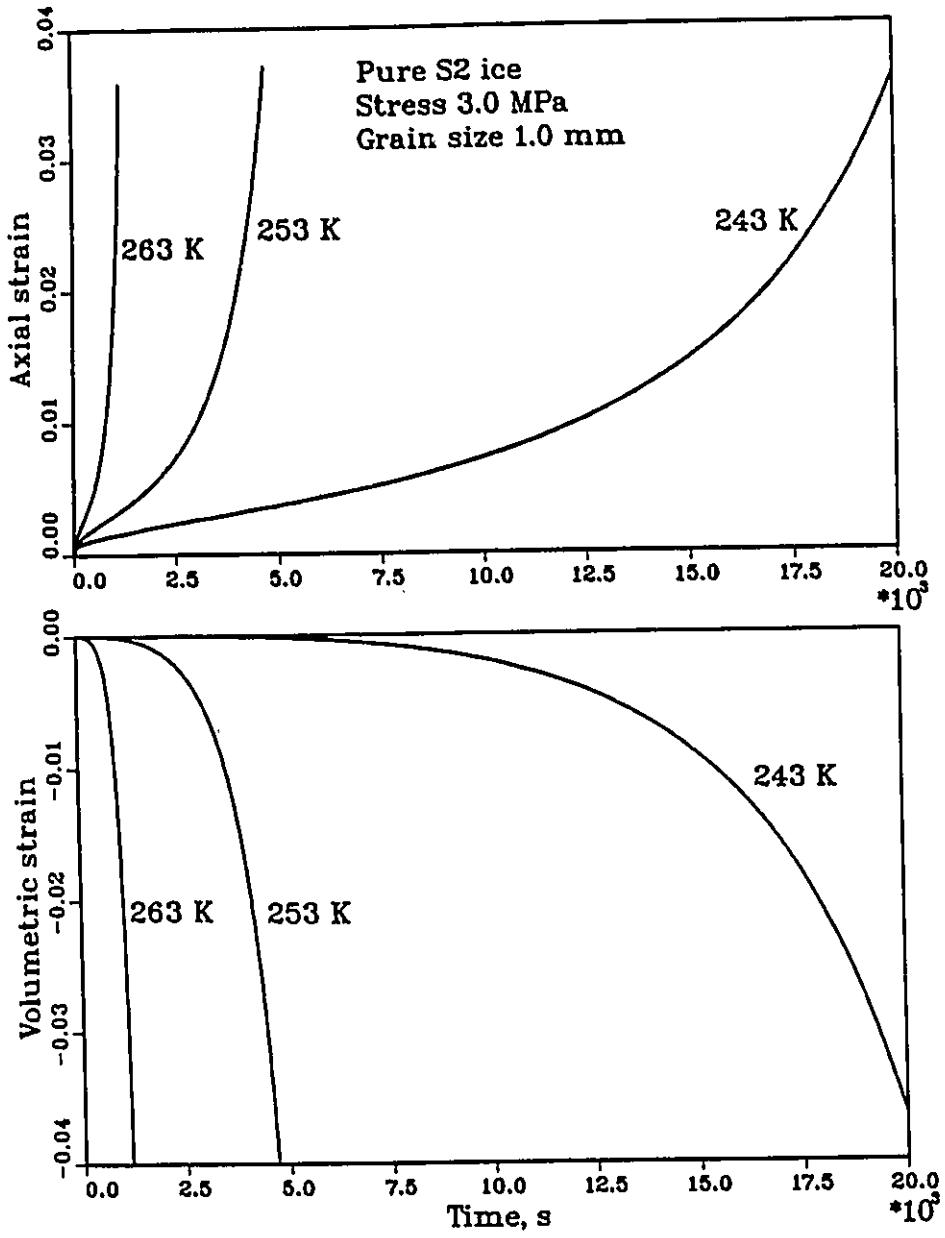

Figure 4.21 Temperature and time dependence of axial and volumetric strains predicted from present model

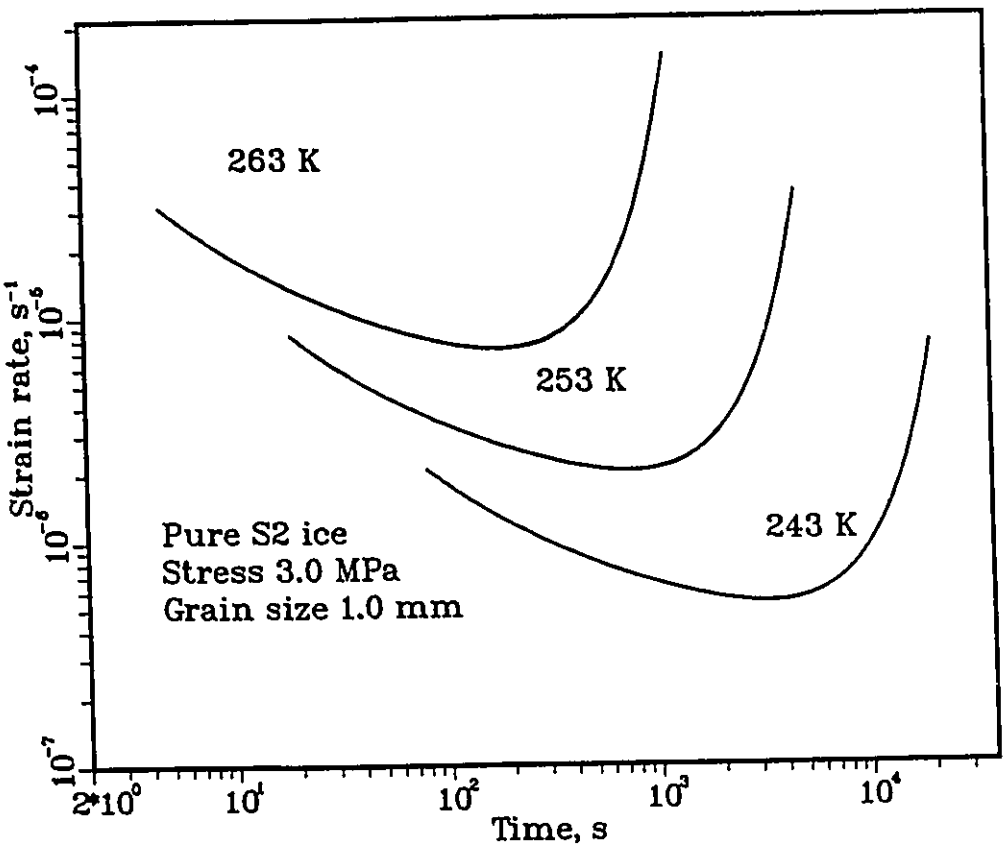

Figure 4.22 Temperature and time dependence of strain rate predicted from present model

Chapter 5

3-D anisotropic model for columnar grained sea ice

5.1 Introduction

The effect of brine pockets on the strength of sea ice was investigated by Assur (1958), Anderson and Weeks (1958), and Anderson (1958, 1960). A geometric model of ice and brine pockets was used in the theoretical development. The following relationship was obtained for the strength of sea ice based on the effective area concept. The effective area was calculated by subtracting the total area of brine pockets from the total cross sectional area.

$$\frac{\sigma_f}{\sigma_0} = 1 - (\frac{v_b}{v_0})^{\frac{1}{n}} \tag{5.1}$$

where σ_0 is the strength of sea ice with zero brine volume; σ_f is the strength of sea ice; v_0 and n are parameters, which are obtained from experimental data.

It was found that n=2 gives best results for the strength of columnar grained sea ice (Weeks and Ackley, 1982). Eq. 5.1 with n=2 has been used by many researchers listed in Table 5.1. The values of σ_0 and v_0 are obtained by linear regression analysis of test data for a certain range of salinity. Table 5.1 shows the values for σ_0 and v_0 determined by different authors.

Table 5.1 σ_0 and v_0 for columnar grained sea ice

Authors	σ_0 (MPa)	v_0	Comments
Weeks and Assur, 1967	1.67	0.275	Compressive
Timco and Frederking, 1986	$39\dot{\epsilon}_n^{0.26}$	0.32	Compressive
Dykins, 1971	1.03	0.209	Flexural
Nadreau and Michel, 1984	0.75	0.202	Flexural
Dykins, 1970	0.82	0.142	Tensile
Michel, 1978	$0.079d^{-0.5}$	0.25	Tensile

In general, the values for σ_0 and v_0 are different for different types of tests. For example, the v_0 value for compressive strength is higher than that for flexural strength, which is higher than that for tensile strength. The difference of v_0 value under different stress states signifies that the brine pockets have a bigger effect on the tensile strength than that on compressive strength. The rate effect to Eq. 5.1 was introduced by Timco and Frederking (1986). However, no consideration was given to the effect of fabric and texture of sea ice on the strength.

The above model is simple and easy to use. However, it is only applicable to columnar grained ice with load applied in the horizontal direction. The effect of brine pockets on strength in other directions was not considered. In addition, the anisotropy due to the specific distribution of brine pockets in each single grain of sea ice was not accounted for either.

In the present investigation, a new relationship is developed for the mechanical behaviour of sea ice to account for the effect of brine pockets. This constitutive model is based on an assumed geometric pattern for the distribution of brine pockets in a single grain of sea ice. An initial defect tensor for a single grain of sea ice is defined based on the geometric pattern. Subsequently, the initial defect tensor for polycrystalline ice is obtained from the initial defect tensor for a single grain of sea ice and the probability distribution of c-axis. The effect of the initial defect on the response of sea ice to different type of loading is expressed by introducing two additional tensors. One is called the influence tensor for deviatoric stresses, and the other one is the influence tensor for hydrostatic stresses.

5.2 Experimental observations on sea ice substructure

Sea ice can easily be distinguished from fresh water ice by the presence of the cellular substructures, which consist of evenly spaced ice platelets or subgrains separated by small angle boundaries (Weeks and Ackley, 1982). These small angle boundaries are more or less in the basal plane. A bunch of the subgrains separated from each other at the small angle boundaries constitute a single grain of sea ice. Brine pockets are present in a form of gas, liquid or solid along the boundaries of the subgrains in both basal planes as well as planes parallel to the c-axis as reported by Sinha (1979b). A horizontal thin section of first year sea ice is shown in Fig. 5.1. It clearly shows the substructure of sea ice.

Brine layer spacing a_0 is an important parameter which characterizes the substructures of sea ice. Brine layer spacing was measured by Weeks and Hamilton (1962), and Nakawo and Sinha (1984). Bolling and Tiller (1960) developed a theoretical relationship between a_0 and the growth rate. According to this relationship, The higher the growth rate is, the lower the brine layer spacing is. A typical value for a_0 is about 0.4 mm near the top of an ice sheet and it is about 1.0 mm near the bottom of a first year ice sheet. As reported by Weeks and Hamilton (1962), the distribution of a_0 is approximately normal at a given level in an ice sheet. Further, Nakawo and Sinha (1984) reported that at a given depth, the brine layer spacing becomes greatest when the optical axes of the crystals are in the favorable direction for ice growth.

Compared to the brine layer spacing, very few data are available about the shape of brine pockets. This is mainly due to the technique used in making thin sections. The shape of the original brine pocket is destroyed due the hot plate used in making thin sections. A new technique was developed by Sinha (1977) to avoid this problem. It was found that the majority of brine pockets are irregular. Fig. 5.2 shows the shape of a brine pocket in the vertical plane (Sinha,1979b). This specific brine pocket has an elliptical shape in the vertical plane.

For the development of the constitutive relation in the present investigation, the shape of brine pockets is assumed to be an ellipsoid. Therefore, the geometric pattern is formed in a single grain of sea ice by spheroidal cavities aligning them-

selves along the subgrain boundaries. The projections of the brine pockets on three orthogonal plane are shown in Fig. 5.3. In this figure and Fig. 5.4, a single grain of sea ice consists of four subgrains, with its c-axis in z direction and long columns in x direction. The shape of each subgrain is assumed to be rectangular. The size of each subgrain is assumed to be $(a_0, 4a_0, 8a_0)$ in the subsequent calculations.

5.3 Constitutive model for columnar grained sea ice

The constitutive equations for columnar grained sea ice are the same as those for fresh water columnar grained ice, except that an effective stress tensor, which will be defined later in this section is used in the sea ice constitutive equations to replace the stress tensor in the model for fresh water ice. In addition, the brine layer spacing is used to replace the grain size in the constitutive equations (Sinha, 1981).

5.3.1 Definition of initial defect tensor

Initial defect tensor for single crystal sea ice

An initial defect tensor is introduced to represent the material defect in a single grain of sea ice due to the existence of brine pockets. For a single grain of sea ice with c-axis in the z direction, and the long axis of grain or the growth direction in x direction as shown in Fig. 5.4, the material defect due to the brine inclusions is defined below following Krajcinovic (1985).

$$\begin{aligned} \omega_i &= A_x f(8a_0, A_x) N_i^1 + A_y f(2a_0, A_y) N_i^2 + A_z f(a_0, A_z) N_i^3 \\ N_i^1 &= (1,0,0) \\ N_i^2 &= (0,1,0) \\ N_i^3 &= (0,0,1) \end{aligned} \tag{5.2}$$

where ω_i is a vector used to represent material defect; A_x is the area ratio in (y, z)

plane; A_y is the area ratio in (x, z) plane; A_z is the area ratio in the basal plane or (x, y) plane; N_i^1, N_i^2 and N_i^3 are unit vectors in x, y, and z directions; f(x,y) is a function which is introduced to account for the effect of brine layer spacing on the material defect.

If there is no influence between the neighboring brine layers, f(x,y) is equal to one. The function f(x,y) is chosen as

$$f(x,y) = 1 + (\frac{1}{y} - 1)exp(-k_1 x^{\frac{1}{3}} - \frac{k_2}{y}) \tag{5.3}$$

where k_1 and k_2 are parameters. k_2 is given as 0.6. The term related to k_2 in Eq. 5.3 is introduced to reduce the effect of brine layer spacing on the material defect, when the area ratio is small.

Based on the geometric pattern of brine pockets distribution shown in Fig. 5.3, the area ratios A_x, A_y and A_z can be determined. The total volume of a subgrain with dimensions $(n_1 a_0, n_2 a_0, a_0)$ can be obtained by the following equation.

$$V = n_1 n_2 a_0^3 \tag{5.4}$$

As shown in Fig. 5.3, in average, two brine pockets are present at the boundary of each subgrain. One is in the basal plane. The other one is in the plane normal to the basal plane. The size of each brine pocket is defined by the dimensions of the ellipsoid along the three symmetry axes. For the brine pocket lying on the basal plane, the dimensions are assumed to be $(rn_1 a_0, rn_2 a_0, m_1 a_0)$. The dimensions for the other one is $(rn_1 a_0, m_1 a_0, ra_0)$. The total brine volume for the two brine pockets is

$$V_b = \frac{\pi r^2 m_1 (1 + n_2)}{6 n_2} n_1 n_2 a_0^3 \tag{5.5}$$

where r and m_1 are the rations between the dimensions of brine pocket ellipsoid and the dimensions of subgrain.

The total porosity due to the brine inclusions can be written as

$$v_b = \frac{V_b}{V} = \frac{\pi r^2 m_1 (1+n_2)}{6n_2} \tag{5.6}$$

The area ratios A_x, A_y, and A_z are determined by the following equations.

$$\begin{aligned} A_x &= \frac{\pi r m_1 (1+n_2)}{4n_2} \\ A_y &= \frac{\pi r}{8}(r+m_1) \\ A_z &= \frac{\pi}{4} r^2 \end{aligned} \tag{5.7}$$

In order to obtain the area ratios in Eq. 5.7, it is necessary to know r, m_1, and n_2. n_2 is one of the dimensions of a subgrain, which can be measured. There is one relationship existed between r and m_1 as shown in Eq. 5.6. Therefore, the following relationship is assumed between r and the porosity.

$$r = (\frac{v_b}{v_0})^m \tag{5.8}$$

where v_0 is the reference porosity; m is a parameter related to the shape of the brine pockets, which is assumed to be 0.15.

If v_0 is defined as the porosity when ice loses all of its shear strength on the basal plane, the area ratios A_x, A_y and A_z are then defined as

$$\begin{aligned} A_x &= \frac{6v_b}{\pi r} \\ A_y &= \frac{r}{2}\{r + \frac{6n_2 v_b}{\pi r^2 (1+n_2)}\} \\ A_z &= (\frac{v_b}{v_0})^{2m} \end{aligned} \tag{5.9}$$

Following Krajcinovic (1985) and Murakami (1988), the initial defect tensor D^k for a single grain of sea ice due to the existence of brine pockets is defined as follows:

$$D^k = A_x(8a_0, A_x)N_i^1 \otimes N_i^1 + A_y f(2a_0, A_y)N_i^2 \otimes N_i^2 + A_z f(a_0, A_z)N_i^3 \otimes N_i^3$$
$$= \begin{pmatrix} A_x f(8a_0, A_x) & 0 & 0 \\ 0 & A_y f(2a_0, A_y) & 0 \\ 0 & & A_z f(a_0, A_z) \end{pmatrix} \tag{5.10}$$

The initial defect tensor given in Eq. 5.10 is obtained for a single grain of sea ice in a specific coordinate with c-axis in z direction and the long axis of grain in x direction. If the c-axis is in an arbitrary direction as defined by the direction cosines $(cos\phi cos\theta, cos\phi sin\theta, sin\phi)$ with the long axis of grain still lying in the x-y plane, the initial defect tensor D^l can be obtained using the tensor transformation.

$$D_{ij}^l = T_{ki} D_{kl}^k T_{lj} \tag{5.11}$$

where T_{ij} is given by

$$T_{ij} = \begin{pmatrix} sin\theta & -cos\theta & 0 \\ sin\phi cos\theta & sin\phi sin\theta & -cos\phi \\ cos\phi cos\theta & cos\phi sin\theta & sin\phi \end{pmatrix} \tag{5.12}$$

By substituting the T_{ij} in Eq. 5.12 into Eq. 5.11, the initial defect tensor becomes

$$\begin{aligned} D^l \;\; = & A_z f(a_0, A_z) \begin{pmatrix} cos^2\phi cos^2\theta & \frac{sin2\theta}{2} cos^2\phi & \frac{sin2\phi}{2} cos\theta \\ \frac{sin2\theta}{2} cos^2\phi & cos^2\phi sin^2\theta & \frac{sin2\phi}{2} sin\theta \\ \frac{sin2\phi}{2} cos\theta & \frac{sin2\phi}{2} sin\theta & sin^2\phi \end{pmatrix} \\ & + A_y f(2a_0, A_y) \begin{pmatrix} sin^2\phi cos^2\theta & \frac{sin2\theta}{2} sin^2\phi & -\frac{sin2\phi}{2} cos\theta \\ \frac{sin2\theta}{2} sin^2\phi & sin^2\phi sin^2\theta & -\frac{sin2\phi}{2} sin\theta \\ -\frac{sin2\phi}{2} cos\theta & -\frac{sin2\phi}{2} sin\theta & cos^2\phi \end{pmatrix} \\ & + A_x f(8a_0, A_x) \begin{pmatrix} sin^2\theta & -\frac{sin2\theta}{2} & 0 \\ -\frac{sin2\theta}{2} & cos^2\theta & 0 \\ 0 & 0 & 0 \end{pmatrix} \end{aligned} \tag{5.13}$$

Initial defect tensor for polycrystalline sea ice

In the case of polycrystalline sea ice, the initial defect tensor can be obtained by averaging the initial defect tensors for all grains in a representative volume. Given the probability distribution of c-axis orientation $p(\phi,\theta)$, the initial defect tensor for polycrystalline sea ice can be obtained by the following integration, assuming that the area ratio A_x, A_y, A_z, and the brine layer spacing a_0 are independent of the c-axis orientation.

$$
\begin{aligned}
D_{ij} &= \int_0^{2\pi}\int_{-\frac{\pi}{2}}^{\frac{\pi}{2}} p(\phi,\theta) D^I_{ij} cos\phi d\phi d\theta \\
&= A_z f(a_0, A_z) \int_0^{2\pi}\int_{-\frac{\pi}{2}}^{\frac{\pi}{2}} p \begin{pmatrix} cos^2\phi cos^2\theta & \frac{sin2\theta}{2} cos^2\phi & \frac{sin2\phi}{2} cos\theta \\ \frac{sin2\theta}{2} cos^2\phi & cos^2\phi sin^2\theta & \frac{sin2\phi}{2} sin\theta \\ \frac{sin2\phi}{2} cos\theta & \frac{sin2\phi}{2} sin\theta & sin^2\phi \end{pmatrix} cos\phi d\phi d\theta \\
&+ A_y f(2a_0, A_y) \int_0^{2\pi}\int_{-\frac{\pi}{2}}^{\frac{\pi}{2}} \begin{pmatrix} sin^2\phi cos^2\theta & \frac{sin2\theta}{2} sin^2\phi & -\frac{sin2\phi}{2} cos\theta \\ \frac{sin2\theta}{2} sin^2\phi & sin^2\phi sin^2\theta & -\frac{sin2\phi}{2} sin\theta \\ -\frac{sin2\phi}{2} cos\theta & -\frac{sin2\phi}{2} sin\theta & cos^2\phi \end{pmatrix} cos\phi d\phi d\theta \\
&+ A_x f(8a_0, A_x) \int_0^{2\pi}\int_{-\frac{\pi}{2}}^{\frac{\pi}{2}} \begin{pmatrix} sin^2\theta & -\frac{sin2\theta}{2} & 0 \\ -\frac{sin2\theta}{2} & cos^2\theta & 0 \\ 0 & 0 & 0 \end{pmatrix} cos\phi d\phi d\theta
\end{aligned} \tag{5.14}
$$

In the case of S2b columnar grained sea ice, the probability distribution of c-axis orientation is $p(\phi,\theta) = \frac{1}{2\pi}\delta(\phi)$. Therefore, the initial defect tensor can be expressed as follows.

$$
\begin{aligned}
D &= \{A_z f(a_0, A_z) + A_x(8a_0, A_x)\} \begin{pmatrix} 0.5 & 0.0 & 0.0 \\ 0.0 & 0.5 & 0.0 \\ 0.0 & 0.0 & 0.0 \end{pmatrix} \\
&+ A_y f(2a_0, A_y) \begin{pmatrix} 0.0 & 0.0 & 0.0 \\ 0.0 & 0.0 & 0.0 \\ 0.0 & 0.0 & 1.0 \end{pmatrix}
\end{aligned} \tag{5.15}
$$

5.3.2 Definition of effective stresses

The effect of the initial defect or damage on stress state is represented by using an effective stress concept. The constitutive equations for sea ice are derived from the constitutive equations for fresh water ice by replacing the stress components in the equations for fresh water ice with the corresponding effective stress components. This procedure is based on the hypothesis of strain equivalence (Lemaitre and Chaboche, 1978, 1985). Following Murakami (1988), the relation between the effective stress tensor and the Cauchy stress tensor is given as

$$\sigma^* = (1 - D)^{-1}\sigma \tag{5.16}$$

The effective stress tensor defined above is asymmetric. Due to the difficulty involved in using an asymmetric stress tensor in both constitutive and numerical modelling, it is necessary to symmetrize the effective stress tensor. The effective stress tensor is defined below following Murakami (1988).

$$\sigma^* = \frac{1}{2}\{(1 - D)^{-1}\sigma + \sigma(1 - D)^{-1}\} \tag{5.17}$$

5.3.3 Influence tensors for deviatoric and hydrostatic stresses

It is known from Table 5.1 that the effect of brine pockets on different stress states is different. This implies that a different damage tensor must be defined for different stress states. The effective stress definition is modified in the present study to take into account the effect of the type of loading on the effective stress tensor. Eq. 5.17 can be rewritten as

$$\sigma^* = (1 - D)^{-1}p + \frac{1}{2}\{(1 - D)^{-1}S + S(1 - D)^{-1}\} \tag{5.18}$$

where p is the hydrostatic stress; S is the deviatoric stress tensor.

In the above equation, the effect of the initial defect on the deviatoric stresses and hydrostatic stresses is represented by the same tensor D. It is known that the

initial defect has different effects under different types of loading. To account this effect, the effective stress definition Eq. 5.18 is modified as

$$\sigma^* = (1 - D^h)^{-1} p + \frac{1}{2}\{(1 - D^s)^{-1} S + S(1 - D^s)^{-1}\} \tag{5.19}$$

where D^h and D^s are the influence tensors for hydrostatic and deviatoric stresses, respectively.

The influence tensor for deviatoric stresses is defined in the principal stress space with the coordinate transformation tensor B_{ij}. In the principal stress space, the deviatoric stress tensor can be divided into three pure shear stress states.

$$\begin{pmatrix} 2\sigma_1 - \sigma_2 - \sigma_3 & 0 & 0 \\ 0 & 2\sigma_2 - \sigma_1 - \sigma_3 & 0 \\ 0 & 0 & 2\sigma_3 - \sigma_1 - \sigma_2 \end{pmatrix} = \begin{pmatrix} \sigma_1 - \sigma_2 & 0 & 0 \\ 0 & \sigma_2 - \sigma_1 & 0 \\ 0 & 0 & 0 \end{pmatrix}$$
$$+ \begin{pmatrix} 0 & 0 & 0 \\ 0 & \sigma_2 - \sigma_3 & 0 \\ 0 & 0 & \sigma_3 - \sigma_2 \end{pmatrix} + \begin{pmatrix} \sigma_1 - \sigma_3 & 0 & 0 \\ 0 & 0 & 0 \\ 0 & 0 & \sigma_3 - \sigma_1 \end{pmatrix} \tag{5.20}$$

The three pure shear stress operate in three different sets of coordinate systems, which can be expressed in terms of the coordinate transformation tensors.

$$B^1_{ij} = \begin{pmatrix} 0.7072 & 0.7072 & 0.0 \\ -0.7072 & 0.7072 & 0.0 \\ 0.0 & 0.0 & 1.0 \end{pmatrix} \tag{5.21}$$

$$B^2_{ij} = \begin{pmatrix} 1.0 & 0.0 & 0.0 \\ 0.0 & 0.7072 & 0.7072 \\ 0.0 & -0.7072 & 0.7072 \end{pmatrix} \tag{5.22}$$

$$B^3_{ij} = \begin{pmatrix} -0.7072 & 0.0 & 0.7072 \\ 0.0 & 1.0 & 0.0 \\ 0.7072 & 0.0 & 0.7072 \end{pmatrix} \tag{5.23}$$

The influence tensor for deviatoric stresses is then defined as an average of the initial defect tensor in the above three coordinate systems weighted by using the magnitude of the shear stresses in each coordinate system.

$$\begin{aligned} D^s_{ij} &= \frac{1}{(\sigma_1-\sigma_2)^2+(\sigma_2-\sigma_3)^2+(\sigma_3-\sigma_1)^2}\{(\sigma_1-\sigma_2)^2 B^1_{ik} D^p_{kl} B^1_{lj} \\ &+(\sigma_2-\sigma_3)^2 B^2_{ik} D^p_{kl} B^2_{lj} + (\sigma_3-\sigma_1)^2 B^3_{ik} D^p_{kl} B^3_{lj}\} \end{aligned} \tag{5.24}$$

where D^p_{ij} is the initial defect tensor in the principal stress space coordinate, which is related to D_{ij} in the global coordinate system as below.

$$D^p_{ij} = B_{ik} D_{kl} B_{jl} \tag{5.25}$$

When an ice sample is subjected to a uniaxial compressive load, the strains in other two directions are in extension. It is expected that brine pockets with normal vectors in the loading direction will close, while brine pockets with normal vectors normal to the loading direction will open. The influence tensor for compressive hydrostatic stresses is, therefore, assumed to be

$$\begin{aligned} D^h_{11} &= K\frac{D^p_{22}+D^p_{33}}{2} \\ D^h_{22} &= K\frac{D^p_{11}+D^p_{33}}{2} \\ D^h_{33} &= K\frac{D^p_{22}+D^p_{11}}{2} \end{aligned} \tag{5.26}$$

The rest of D^h_{ij} are zero. In Eq. 5.26, K is a parameter between 0 and 1. For the subsequent calculations, K is given as 0.25. For negative hydrostatic stress, D^h_{ij} is given as:

$$\begin{aligned} D^h_{ii} &= D^p_{ii} \\ D^h_{ij} &= 0 \; i \neq j \end{aligned} \tag{5.27}$$

5.4 Model validation

The material constants and model parameters for the sea ice model are the same as those for fresh water ice. However, two more model parameters are needed to define the initial defect tensor. All material constants and model parameters are given in Table 5.1 for temperature 263 K.

Table 5.2 Material properties for columnar grained sea ice

Elastic modulus E	9.5 GPa
Possion's ratio μ	0.33
For delayed elasticity,C_1 and a_T at 263 K	9.0, 0.00025 s^{-1}
For delayed elasticity, b_2	0.2
For viscous strain C, n	$1.43 \times 10^6 s^{-1}$, 3
For viscous strain a_2, a_5	0.3, 50.0
For crack strain E_N	1.0
For initial defect tensor v_0, k_1	0.16, 0.02

The value of v_0 is given as 0.16, which represents that the sea ice with a porosity of 16% loses all of its strength. The value of k_1 is determined by fitting the test data of the minimum strain rate at -10^0 for a stress level 2.5 MPa.

Columnar grained sea ice is usually found to be oriented due to the action of current during the growth. Therefore, the available test data are mainly for oriented columnar grained sea ice or S3b sea ice as classified by Nadreau and Michel (1984). The strength and deformation for oriented columnar grained sea ice is quite anisotropic (Wang, 1981; Sinha, 1983b, 1984a; Richter-Menge, 1991; Sinha et. al, 1992) depending on the fabric, texture, and the loading direction. In general, for a test data to be meaningful, information on temperature, rate of loading, fabric, texture, and brine volume is needed. There are lots of test data available on strength of sea ice. However, none of the test data provided all the necessary information, especially the fabric of the ice. For the model prediction given below, the fabric of S3b ice is described by two angles. One of them is the mean c-axis angle, and the other one is called the scatter angle (Sinha, 1989b). In

this case, the probability distribution of c-axis can be expressed by the following equation.

$$p(\phi,\theta) = \begin{cases} 0 & |\theta-\theta_1| > \theta_2 \\ \frac{1}{2\theta_2\pi}\delta(\phi) & |\theta-\theta_1| < \theta_2 \end{cases} \tag{5.28}$$

where θ_1 and θ_2 are the mean c-axis angle and scatter angle, respectively.

5.4.1 Predictions of constant displacement rate test result

A comparison is given in Fig. 5.5 between the model predictions and the test data from Sinha (1984a) for an average strain rate $5.2 \times 10^{-5}s^{-1}$. The temperature is -10^0C. The ice is S3b columnar grained sea ice with the scatter angle about 25^0 as measured by Sinha. Considering that the majority of the c-axis for different grains are lying not on the horizontal plane but close to, a scatter angle of 30^0 is used in the model prediction. The load is applied in the horizontal plane parallel to the mean c-axis direction. The brine layer spacing a_0 is assumed to be 1 mm. The salinity is 6 parts per thousand. In general, the model prediction is good considering the uncertainty about the brine layer spacing, the exact angle between c-axis and loading direction, and the existence of brine channels in the ice sample.

The strain rate dependence of the maximum stress is predicted with the sea ice model for S3b columnar grained sea ice as shown in Fig. 5.6. The scatter angle, salinity, and brine layer spacing a_0 of the ice are given as 30^0, 6.0 parts per thousand, and 1.0 mm, respectively. The load is applied in the horizontal plane parallel to the mean c-axis. The temperature is -10^0C. The data points in the figure are test results from Sinha (1984a); Wang (1983); and Chen and Lee (1986) on first year columnar grained sea ice. It shows that the model gives a good prediction for the rate dependence of the maximum stress.

Figure 5.7 presents the rate dependence of stress-strain curves predicted by the present sea ice model. It shows that the maximum stress increases with the increase of strain rate.

5.4.2 Predictions of constant load test results

The results of the constant load tests carried out as part of the present study are presented in Chapter 2. Predictions were made for the constant load tests at -10^0C. The predictions were for the S3b columnar grained sea ice with the salinity 5 parts per thousand, brine layer spacing 0.6 mm, and the scatter angle 30^0. The load was applied in the horizontal plane parallel to the mean c-axis.

Figure 5.8 shows the test results and model predictions for the time and stress dependence of axial strain. The agreement between the test results and model predictions is good. However, the rate of deformation predicted from the constitutive model is higher than that of the experiment, especially in the later stage of the predictions.

The comparison of model prediction and test result for the dependence of the minimum strain rate on stress is shown in Fig. 5.9. The agreement is good between the model prediction and test result.

Comparisons between the model predictions and test results for axial, lateral, and volumetric strains are shown in Fig. 5.10 for an axial stress of 2.5 MPa. The correspondence between the model predictions and test results is close for axial strain less than 1.0%.

5.4.3 Prediction of strength anisotropy under multiaxial loading

The sea ice model is developed for three dimensional problem. A set of comparisons between the model predictions and test data are necessary under three dimensional loading. Recently, Richter-Menge (1991) published some triaxial test data for the oriented columnar grained sea ice with information on the brine volume. The tests were carried out at -10^0C under two different strain rates. The maximum stress σ_1 was applied in the horizontal plane with the angle between the mean c-axis and loading direction ranging from 0 to 90 degrees. Other principal stresses, σ_2 and σ_3 are equal.

The predictions were made in this study for the same oriented columnar grained sea ice. The brine volume is chosen as 0.0327, which was about an average value given in Table 2 (Richter-Menge, 1991). The scatter angle and brine layer spacing

were assumed to be 10^0 and 1 mm, respectively.

Figure 5.11 shows the comparisons between the model predictions and test results at strain rate $10^{-5}s^{-1}$ under four different stress ratios, $\frac{\sigma_2}{\sigma_1}$, i.e., 0.0, 0.25, 0.5, 0.75. As shown in the figure, the model provides very good predictions for the dependence of strength on the angle between the mean c-axis and loading direction under the three dimensional stress state.

Similar to Fig. 5.11, Fig. 5.12 shows the comparisons at strain rate $10^{-3}s^{-1}$. A fair agreement is achieved between model predictions and test results. The strength values predicted by the model were less than experimental values.

5.4.4 Prediction of strength dependence on fabric

The effect of the scatter angle on the prediction of the stress-strain diagrams is shown in Fig. 5.13 at temperature -10^0C. The load is applied in the horizontal plane parallel to the mean c-axis. The brine volume is given as 0.0327. The figure shows that peak stress is higher when the scatter angle is smaller.

The effect of fabric on strength of S3b columnar grained sea ice is presented in Fig. 5.14 for temperature -10^0C, strain rate $10^{-5}s^{-1}$. The angle between the mean c-axis and loading direction, ACL, is zero for one of the curve and 45 degrees for the other curve. As shown in the figure, the difference between the two lines becomes smaller when the scatter angle approaches 45 degrees. When the scatter angle is 45 degrees, there is no difference between the two results. For the scatter angle between 45 and 90 degrees, the difference between the two lines is small. However, the strength for ACL=45 degrees is higher than that for ACL=0 degree. Again, the two lines cross each other at 90 degrees.

Figure 5.1 Horizontal thin section shown substructure of sea ice

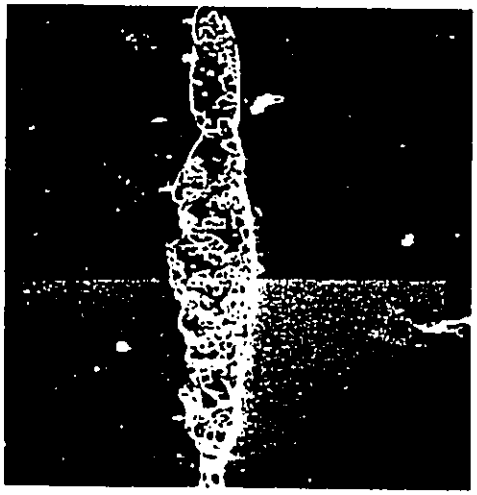

Figure 5.2 Shape of brine pocket in vertical plane, after Sinha, 1979

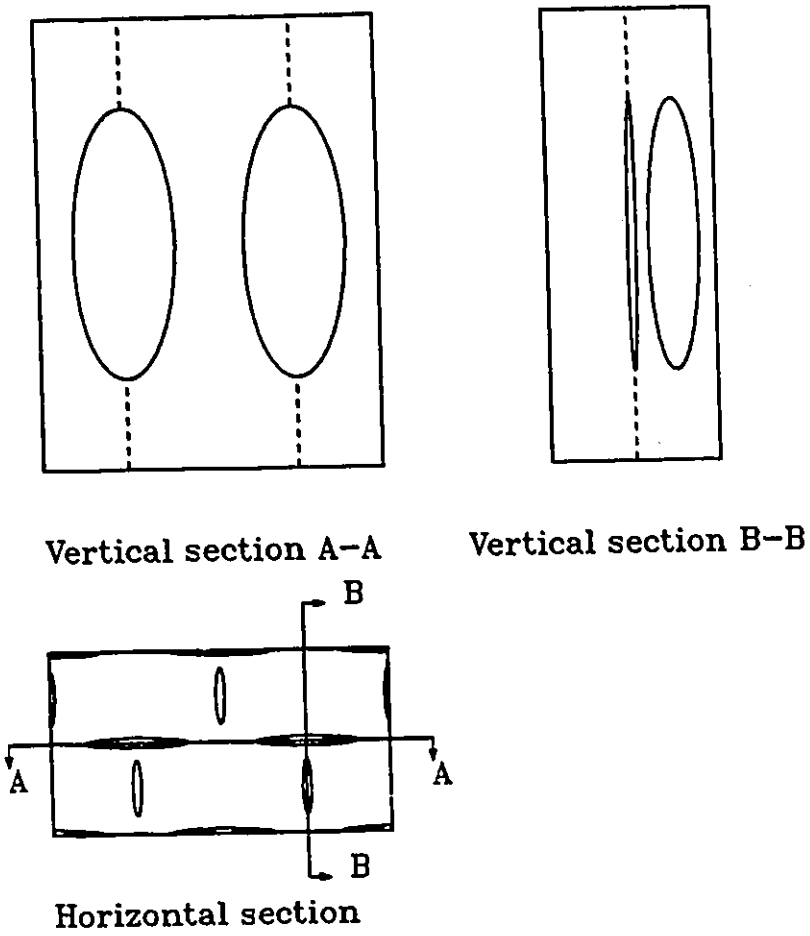

Figure 5.3 Geometric pattern of brine pockets distribution in a single grain of sea ice

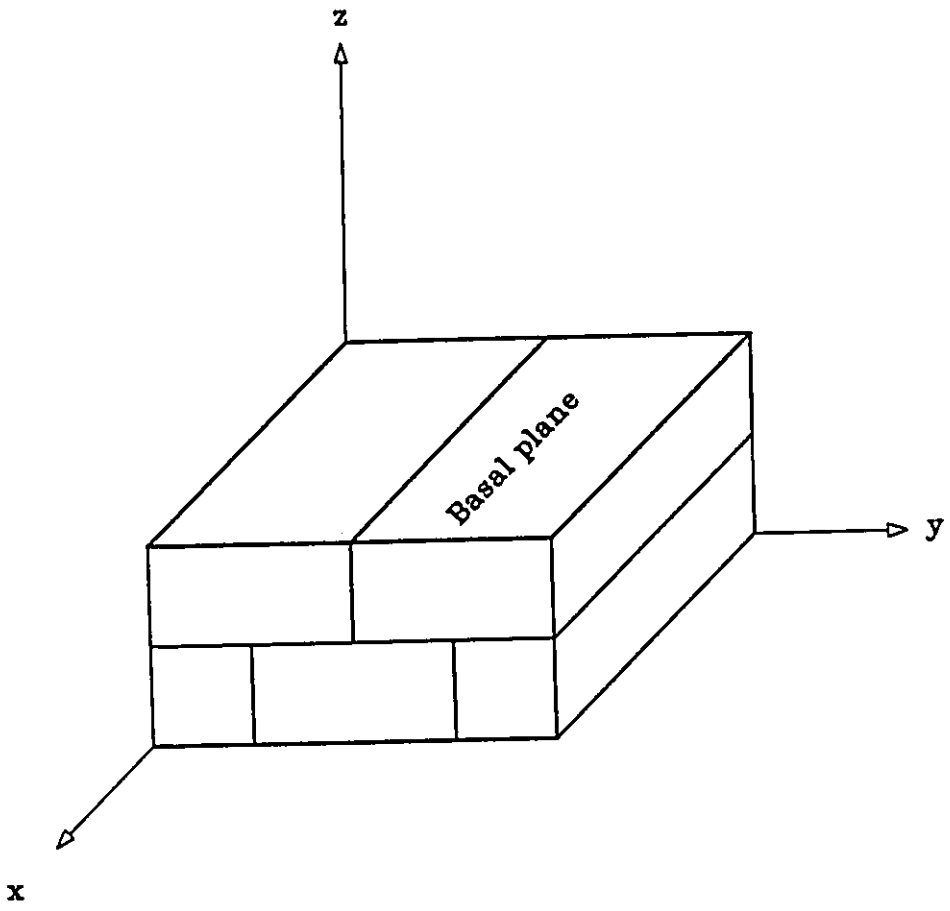

Figure 5.4 Single grain of sea ice

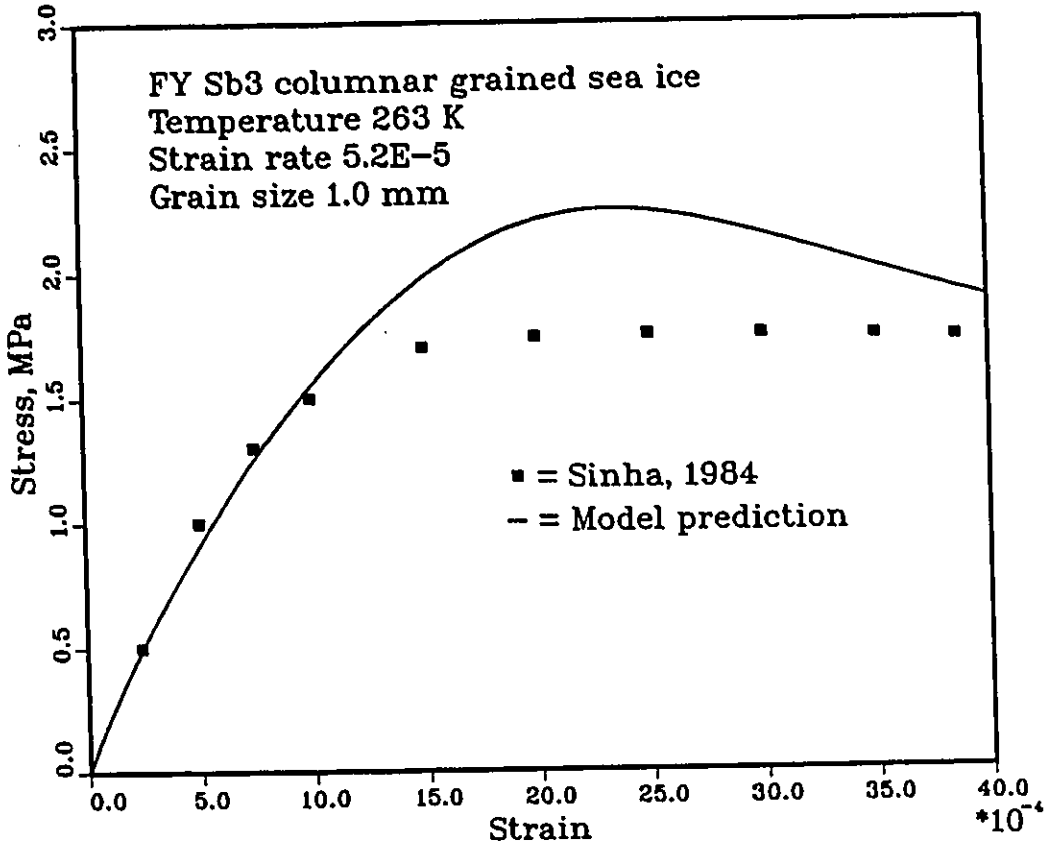

Figure 5.5 Comparisons between model predictions and test data for stress–strain diagrams

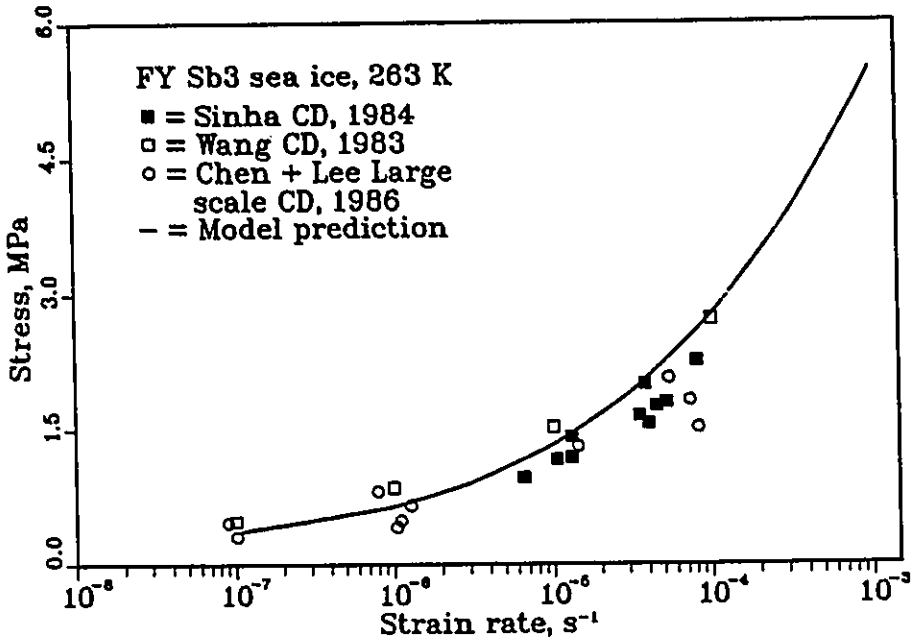

Figure 5.6 Comparisons between model predictions and test data for rate dependence of strength

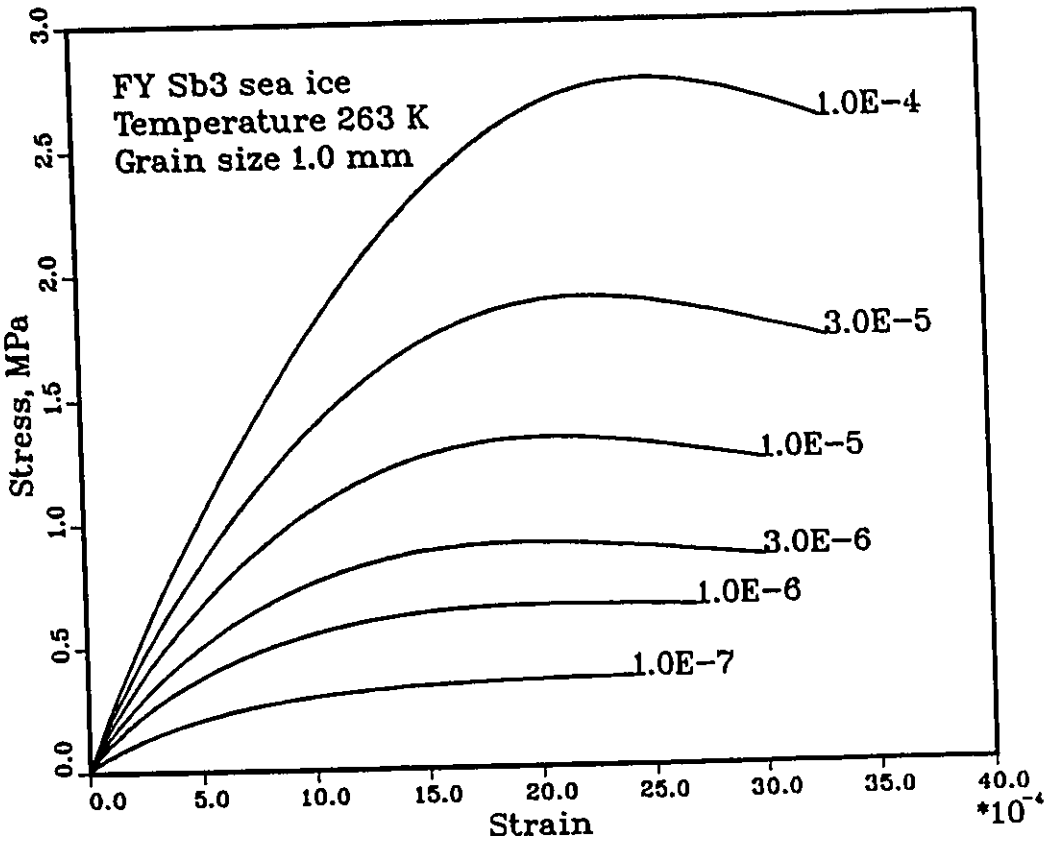

Figure 5.7 Strain rate dependence of stress–strain diagrams predicted from present model for sea ice

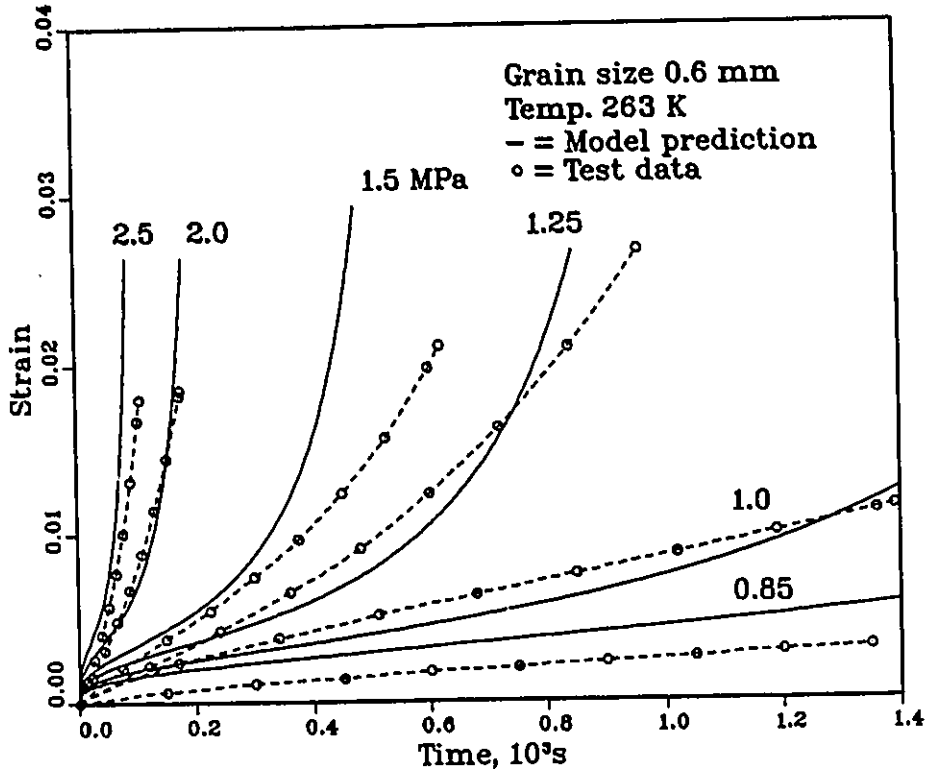

Figure 5.8 Comparisons between model predictions and test data for time dependence of axial strains

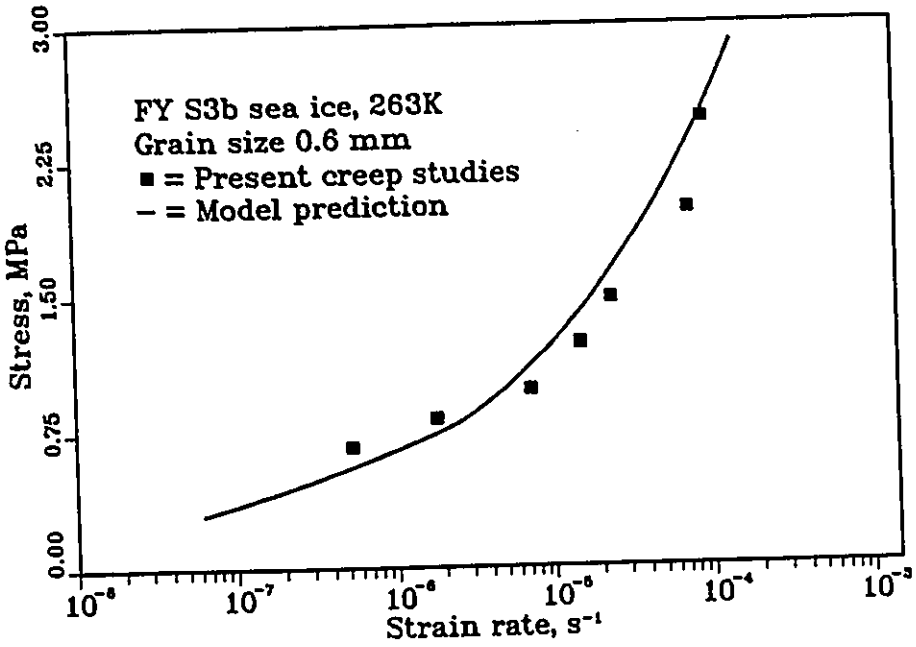

Figure 5.9 Comparisons between model predictions and test data for stress dependence of minimum strain rate

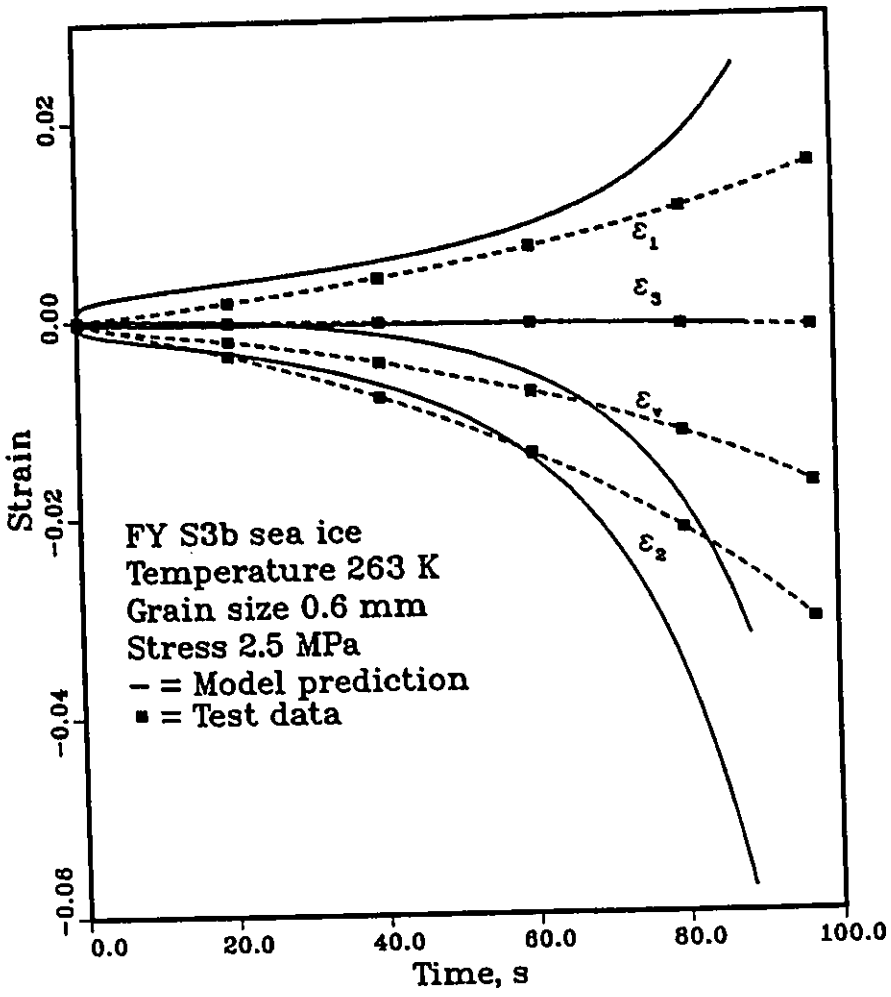

Figure 5.10 Comparisons between model predictions and test data for time dependence of axial, lateral and volumetric strains

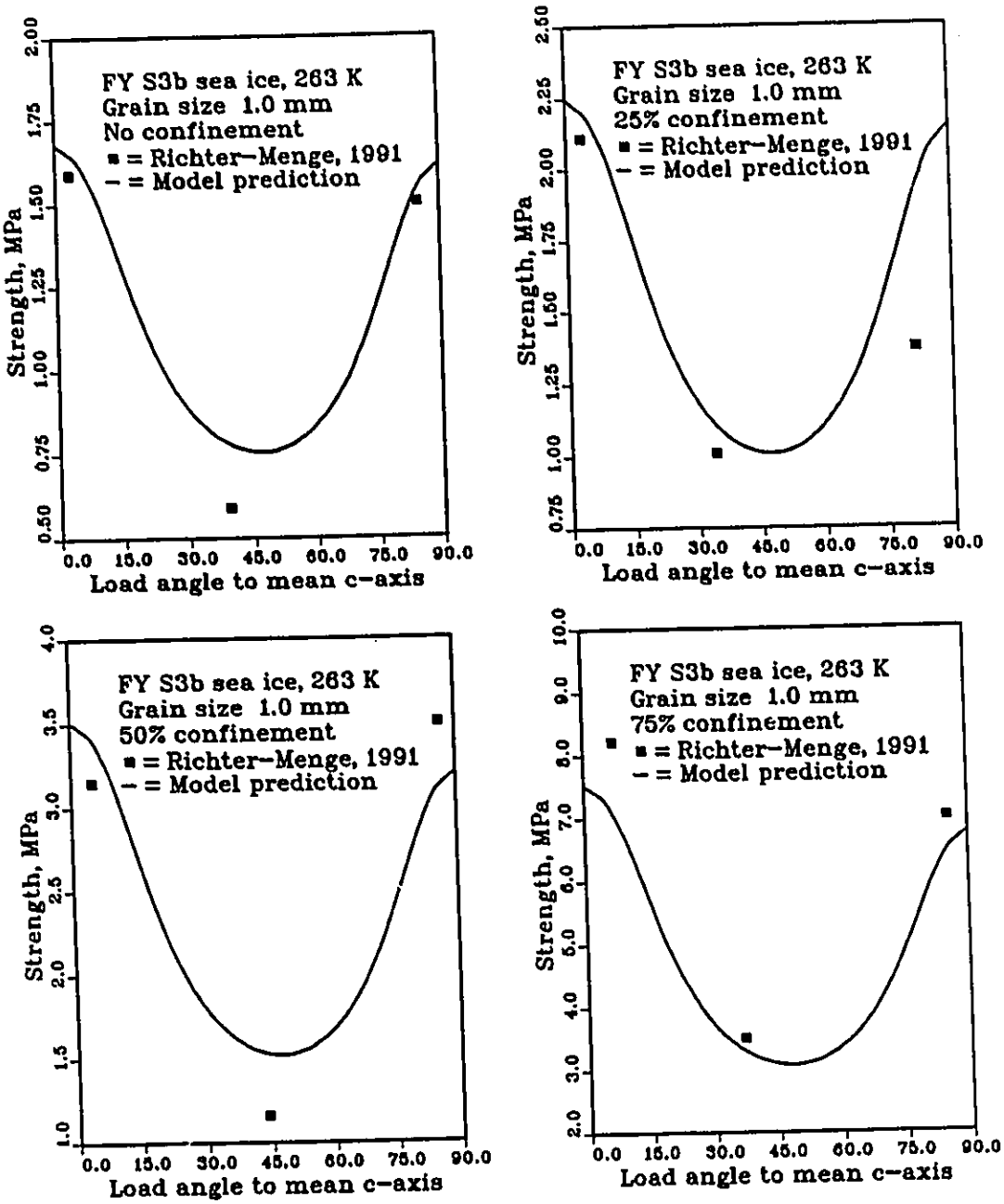

Figure 5.11 Comparisons between model predictions and test data for strength dependence on ACL at strain rate 10E–5

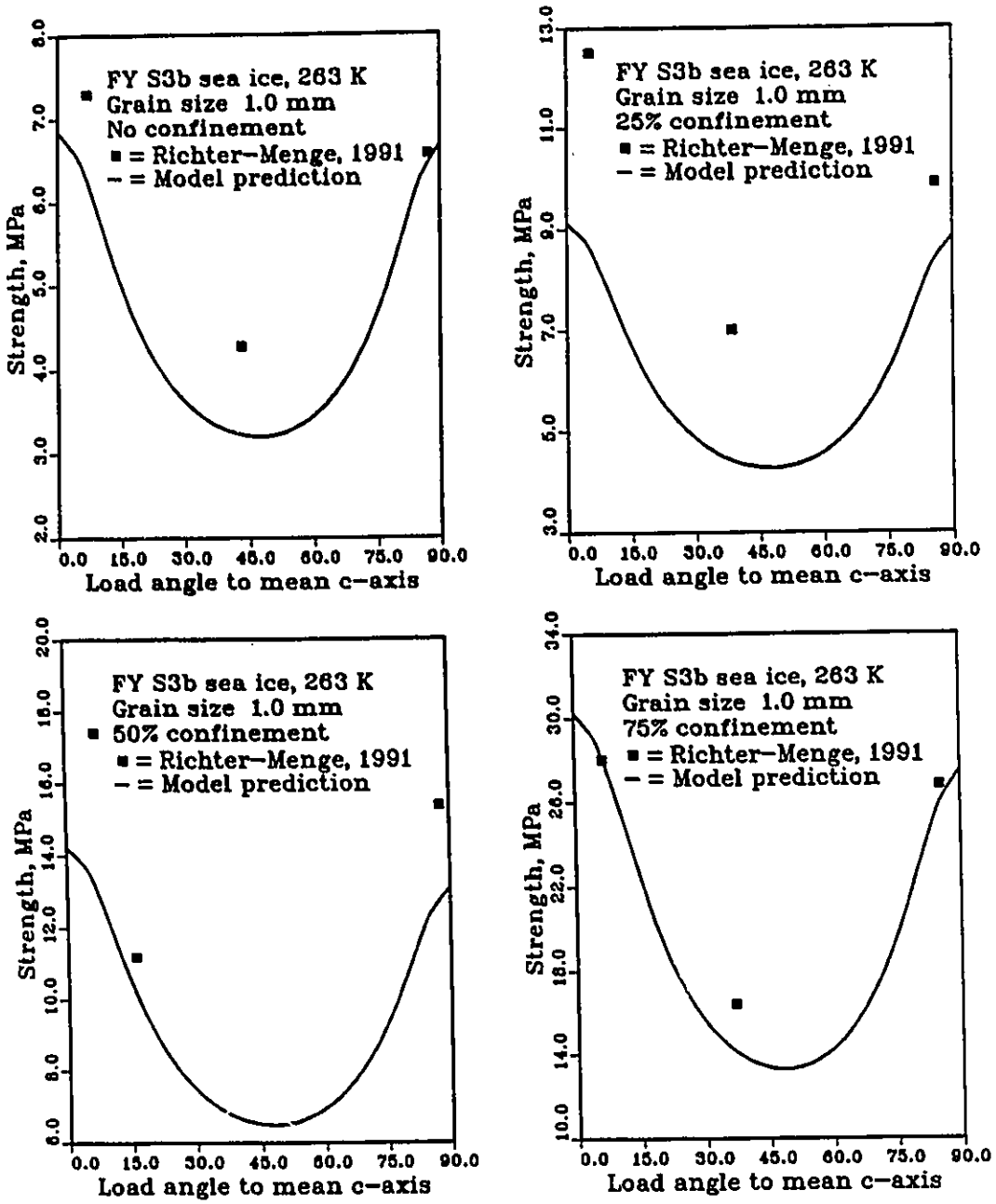

Figure 5.12 Comparisons between model predictions and test data for strength dependence on ACL at strain rate 10E–3

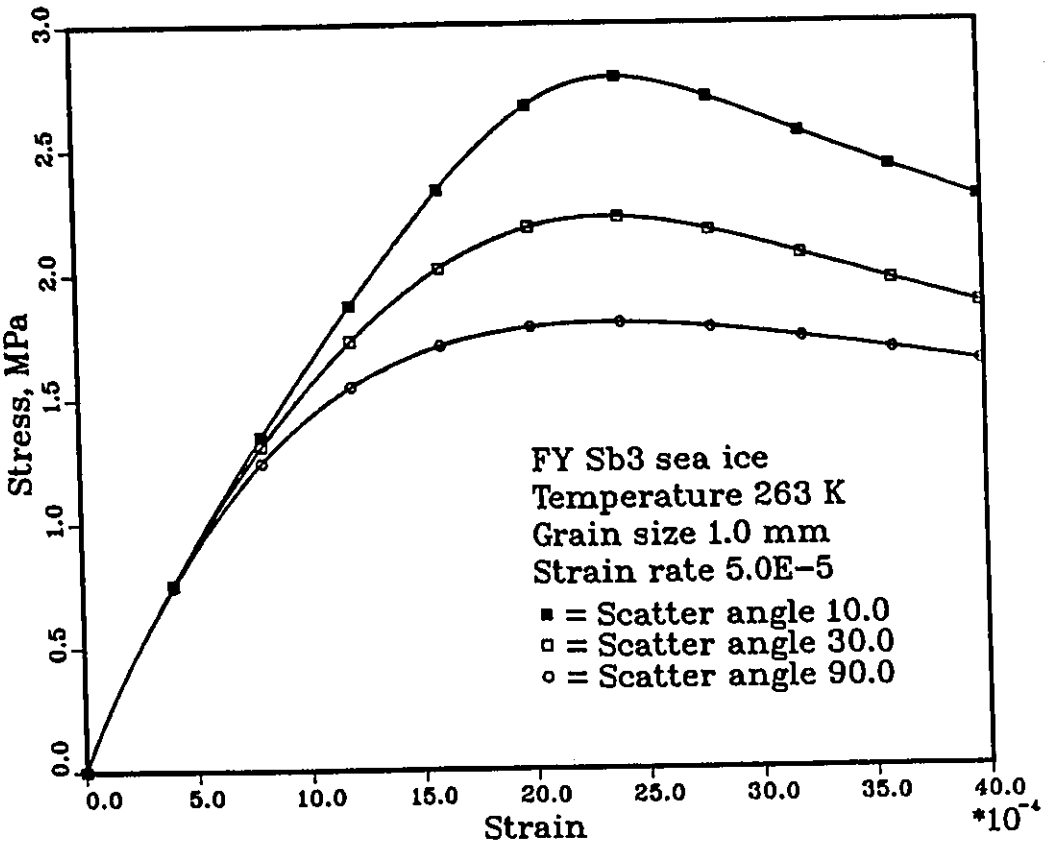

Figure 5.13 Dependence of stress–strain diagrams on scatter angle predicted from sea ice model

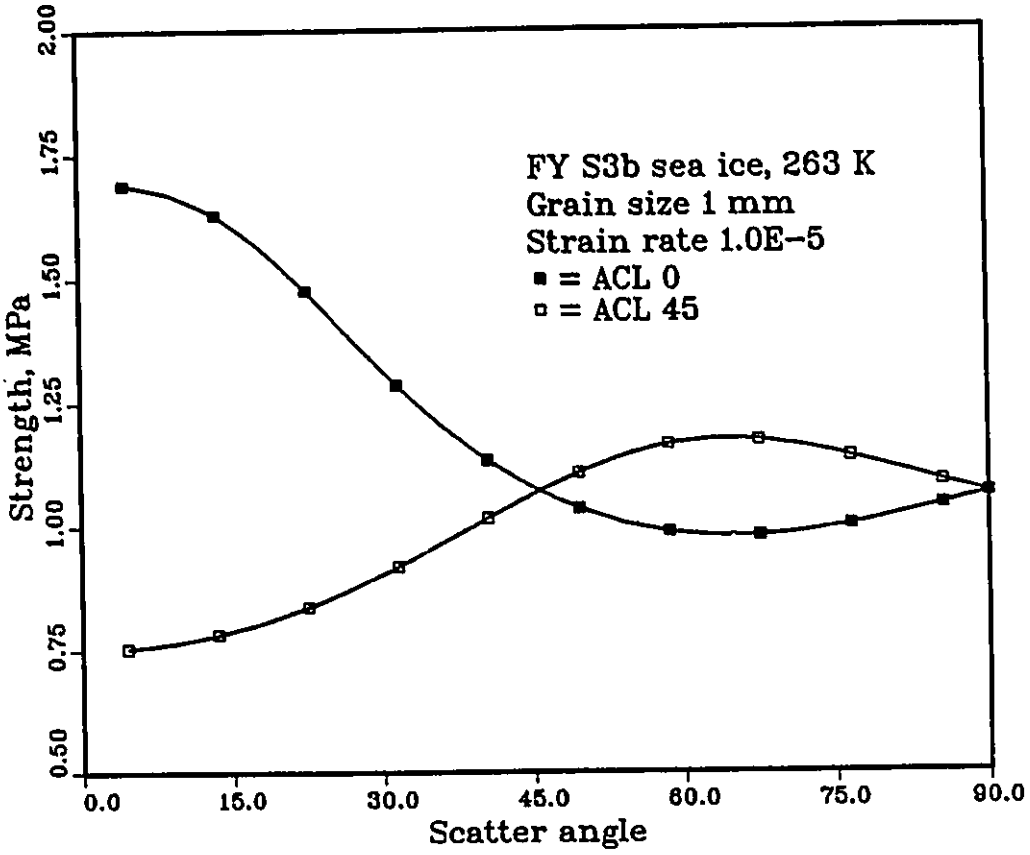

Figure 5.14 Effect of scatter angle on strength for S3b ice predicted from sea ice model

Chapter 6

Analyses of borehole indentation test results

6.1 Introduction

A three dimensional finite element program is developed with the generalized Sinha's model implemented. The program is used to analyze the borehole indentation test data.

Finite element method is a powerful numerical method. It is designed mainly for the analysis of continuum mechanics problems. Some studies have been carried out on ice related problems based on various constitutive models such as elasticity (Sodhi and Hamza, 1977; Svec and Frederking, 1985; Frederking and Evgin, 1990), plasticity (Ralston 1978; Prodavic 1979; Kormann and Brown 1992), viscoelasticity (Katona and Vaudrey, 1975; Emery and Mirza, 1980; Sjolind, 1985; Brown et. al 1986; Jordaan, 1986; Vinogradov and Masterson, 1989; Evgin et. al, 1991; Mahreholtz et. al, 1991), viscoelasticity with damage (Tomin et. al 1986; Pulkkinen 1989; Xiao et. al, 1991).

The output of a finite element analysis is highly dependent on the constitutive model. In order to get a meaningful result, a constitutive model which can represent the material behaviour has to be used. Sinha's model is one of the best constitutive models for ice. Therefore, the model is chosen to be generalized and implemented into the finite element program.

The aim of the present numerical study is to implement the generalized Sinha's creep model with cracking into a three dimensional finite element program and to use it to analyse the borehole indentation test results.

6.2 Generalization of Sinha's model to 3-D

Sinha's creep model with cracking is a one dimensional model. In order to use the model in the analyzing two or three dimensional problems, a generalization to three dimension is necessary. The generalization was done for isotropic ice. The dilation caused by the crack opening is not considered.

6.2.1 Sinha's model

A phenomenological ice creep model was developed by Sinha (1978a). The total strain was divided into three parts: elastic, delayed elastic, and viscous strain. The delayed elasticity in the model is related to grain boundary sliding (Sinha, 1979a). In 1988 and 1989, Sinha extended the 1978 creep model by adding (1) a crack enhancement factor to the viscous strain and (2) a volumetric strain due to the crack opening. The one dimensional creep model with cracking is given as below.

$$\begin{aligned}
\epsilon &= \frac{\sigma}{E} + C_1\frac{d_1}{d}\frac{\sigma}{E}\{1 - exp(-(a_T t)^b)\} + \dot{\epsilon}_{v1}(\frac{\sigma}{\sigma_1})^n \int_0^t p(N)dt \\
\epsilon_{vol} &= \frac{1-2\mu}{E}\sigma + v(N) \\
N &= N_c\{exp\{\psi(\frac{\epsilon_d d}{K} - x_c)\} - 1\}
\end{aligned} \tag{6.1}$$

For granular ice, p(N) and v(N) can be expressed as follows.

$$\begin{aligned}
p(N) &= 1 + 0.083Nd^3n^{\frac{1}{2}} \\
v(N) &= \pi a^2 wN
\end{aligned} \tag{6.2}$$

For columnar grained ice, p(N) and v(N) are expressed as

$$
\begin{aligned}
p(N) &= 1 + 0.5Nd^2n^{\frac{1}{2}} \\
v(N) &= 2awN
\end{aligned}
\tag{6.3}
$$

where σ and ϵ are stress and strain; σ_d is delayed elastic strain; E is elastic modulus; C_1 and b are constants; d_1 is reference grain diameter; d is the average grain diameter; t is time; σ_1 is the unit stress; $\dot{\epsilon}_{v1}$ is the viscous strain rate for unit stress; N is crack density; w is the opening of the cracks; a is half length of the crack, which is equal to 0.275d for a hexagonal crystal; n is the stress power; N_c, ψ and K are constants; a_T and $\dot{\epsilon}_{v1}$ are dependent on the temperature as follows.

$$
\begin{aligned}
a_T(T_1) &= \frac{a_T(T_2)}{S_{1,2}} \\
\dot{\epsilon}_{v1}(T_1) &= \frac{\dot{\epsilon}_{v1}(T_2)}{S_{1,2}} \\
S_{1,2} &= exp\{\frac{Q}{R}(\frac{1}{T_1} - \frac{1}{T_2})\}
\end{aligned}
\tag{6.4}
$$

where Q is activation energy, R is the universal gas constant, T_1 and T_2 are absolute temperature.

Sinha's model has been successfully used to predict (1) the rate and grain size dependence of the effective modulus (Sinha, 1978b, 1989c); (2) the rate dependence of the strain ratios (Sinha, 1989c); (3) the rate dependence of the maximum stress (Sinha, 1988a); (4) the power law breakdown (Sinha, 1989a); (5) the grain size effect on time dependence of creep strain (Sinha, 1989d). However, the model is only applicable to one dimensional problems. It is therefore necessary to generalize the model to three dimension, in order to use it for engineering problems.

6.2.2 Generalization of Sinha's model to 3-D

To generalize Sinha's model to 3-D, the extension of the damage evolution equation to 3-D becomes necessary. In Sinha's model, the crack density is related to the grain boundary sliding. In the case of a three dimensional problem, the second

invariant of the delayed elasticity strain tensor is a good measure of the overall shear strain at the grain boundary. For three dimensional problems, the following equation for crack density is used.

$$N = N_c\{exp\{\psi(\frac{\bar{\epsilon}_d d}{K} - x_c)\} - 1\} \tag{6.5}$$

where $\bar{\epsilon}_d$ is the second invariant of delayed elasticity strain tensor, which can be obtained by the following equation.

$$\bar{\epsilon}_d = \sqrt{\frac{3}{2}\epsilon^d_{ij}\epsilon^d_{ij}} \tag{6.6}$$

Two assumptions are made to generalize Sinha's model to 3-D.

1. The relation between hydrostatic stress and volumetric strain is linear.
2. The elements of deviatoric stress tensor are functions of the corresponding elements of deviatoric strain tensor, the second invariant of the deviatoric stress tensor, temperature, crack density, and time. In addition, the function is the same for each deviatoric stress element.

The above assumptions can be written mathematically as follows.

$$\begin{aligned} \epsilon_{ii} &= \frac{1-2\mu}{E}\sigma_{ii} \\ e_{ij} &= F(s_{ij}, J, T, N, t) \end{aligned} \tag{6.7}$$

where J is the second invariant of the deviatoric stress tensor, s_{ij} and e_{ij} are the deviatoric stress and strain tensors, respectively.

Eq. 6.7 is the generalization of Sinha's one dimensional creep model to three dimension. In the case of one dimensional problems, Eq. 6.7 must be consistent with Sinha's model. The following equation can be obtained by simplifying Eq. 6.7 to one dimension.

$$\epsilon_x = \frac{1-2\mu}{3E}\sigma_x + F(\frac{2\sigma_x}{3}, J, T, N, t) \tag{6.8}$$

A comparison of Eq. 6.8 with Sinha's model provides the unknown function F(s,J,T,N,t).

$$F(s,J,T,N,t) = \frac{1+\mu}{E}s + C_1\frac{d_1}{d}\frac{3s}{2E}\{1-exp(-(a_T t)^b)\}$$
$$+kJ^{\frac{n-1}{2}}s\int_0^t p(N)dt \tag{6.9}$$

in which, $k = \frac{1}{2}3^{\frac{n+1}{2}}\dot{\epsilon}_{v1}(\frac{1}{\sigma_1})^n$.

In the case of complicated stress histories, other than a constant stress history, Eqs. 6.5 and 6.7 become

$$\epsilon_{ii} = \frac{1-2\mu}{E}\sigma_{ii}$$
$$e_{ij} = \frac{1+\mu}{E}s_{ij} + C_1\frac{d_1}{d}\frac{3}{2E}f(s_{ij},T,t) + \int_0^t kJ^{\frac{n-1}{2}}s_{ij}p(N)dt \tag{6.10}$$
$$N = MAX\{N_c\{exp(\psi(\frac{\bar{\epsilon}_d d}{K} - x_c)) - 1\}$$

where $f(s_{ij},T,t)$ can be written as

$$f(s_{ij},T,t) = s_{ij}(0)\{1-exp(-(a_T t)^b)\} + \int_0^t\{1-exp(-(a_T(t-\tau))^b)\}\frac{\partial s_{ij}}{\partial \tau}d\tau$$

6.2.3 Prediction in 3-D

The generalized Sinha's model is used to predict the material behaviour under three dimensional loading. The material properties listed in Table 6.1 on page 234 are used in the predictions. Comparisons are given between the generalized Sinha's model and the present model for fresh water columnar grained ice developed in Chapter 4. The same material properties as listed in Table 6.1 are used for the present fresh water ice model.

The comparisons of the predictions between the generalized Sinha's model and the present model are given. The ice is columnar grained ice with random c-axis distribution in the horizontal plane. The grain size is 1 mm. The ice is loaded normal to the long columns and confined in the other two planes. The confining pressure σ_3 is proportional to the loading stress σ_1 with $\frac{\sigma_3}{\sigma_1} = 0.5$. The ice temperature is 263 K.

Figure 6.1 presents the comparison of the predicted stress strain diagram between the present model and the generalized Sinha's model. This figure shows that before the failure, there is no difference between the two models, however, after failure, the stress decreases a little bit faster for the generalized model.

Figure 6.2 presents the comparison of the rate dependence of strength between the present model and the generalized Sinha's model. This figure shows that there is almost no difference between the two models for the predicted rate dependence of strength.

6.3 Three dimensional finite element program

A nonlinear problem can generally be expressed as a set of algebraic equations as follows (Zienkerwicz, 1977).

$$\psi(a) \equiv k(a)a + f = 0 \tag{6.11}$$

where a is an unknown vector; f is a given vector; k is a function of vector a.

Various methods, such as direct iteration method, Newton-Raphson method, tangential stiffness method, modified Newton-Raphson method, have been used to solve nonlinear algebraic equations. In this study, the modified Newton-Raphson method is utilized. The advantage of using the modified Newton-Raphson method is that it can be employed in situations where the materials exhibit negative tangential stiffness.

6.3.1 Modified Newton-Raphson method

Assuming that a^n is the nth approximate solution to Eq. 6.11, the (n+1)th approximate solution can be obtained by using Taylor's series expansion as below.

$$\psi(a^{n+1}) \equiv \psi(a^n) + (\frac{\partial \psi}{\partial a})_n da^n = 0 \tag{6.12}$$

Eq. 6.12 can be rewritten to obtain da^n.

$$da^n = -(K^n)^{-1}\psi(a^n) \tag{6.13}$$

where $K^n = k(a^n) + (\frac{\partial k}{\partial a^n})_n a^n$.

To overcome the difficulty of solving the new equation each time, approximation is made by writing

$$K^n = K^0 \tag{6.14}$$

By using this approximation, the equation for the modified Newton Raphson method can be expressed as

$$da^n = -(K^0)^{-1}\psi(a^n) \tag{6.15}$$

6.3.2 Formulation of creep in FE analysis

If the initial stresses and strains are neglected, the equilibrium equation of a body can be expressed as

$$\int_V B^T \sigma dV + f = 0 \tag{6.16}$$

where B is strain displacement matrix; f is the force vector; σ is the stress tensor.

Consider that the solution to Eq. 6.16 has already been obtained at time t=t_m. The nonlinear problem is characterized by a set of nodal displacements a_m, stresses σ_m, and nodal forces f_m. The equilibrium equation for time $t_{m+1} = t_m + dt_m$ can be written as follows.

$$\psi_{m+1} \equiv \int B^T \sigma_{m+1} dV + f_{m+1} = 0 \tag{6.17}$$

where ψ_{m+1} is the unbalanced load. Although above equation is set to be zero, due to the approximation in calculating $d\sigma_{m+1}$, it is not equal to zero. If Eq. 6.17 is written in incremental form, the following equation can be obtained.

$$\psi_{m+1} \equiv \psi_m^L + \int B^T d\sigma_{m+1} dV + df_{m+1} = 0 \tag{6.18}$$

where ψ_m^L is the final unbalanced load at the end of the mth time interval.

The stress increment $d\sigma_{m+1}$ in Eq. 6.18 for a creep problem can be expressed as follows.

$$\begin{aligned} d\sigma_{m+1} &= D(\epsilon_{m+1} - \epsilon_m^e) - D(\epsilon_{c,m+1} - \epsilon_{c,m}^e) \\ &= DBda_{m+1} - D(\epsilon_{c,m+1} - \epsilon_{c,m}^e) \end{aligned} \tag{6.19}$$

where superscript e means the exact solution from the mth time increment; a is the node displacement vector; ϵ is the total strain; ϵ_c is the creep strain; D is the elastic matrix.

Similar to Eq. 6.11, Eq. 6.19 can be rewritten as

$$\phi_{m+1} \equiv \sigma_{m+1} - \sigma_m^e - DB(a_{m+1} - a_m^e) + D(\epsilon_{c,m+1} - \epsilon_{c,m}^e) = 0 \tag{6.20}$$

The incremental form of the above equation is as follows.

$$\phi_{m+1} = \phi_m^L + \sigma_{m+1} - \sigma_m^L - DB(a_{m+1} - a_m^L) + D(\epsilon_{c,m+1} - \epsilon_{c,m}^L) \tag{6.21}$$

where σ_m^L, a_m^L and ϕ_m^L are the stress, nodal displacement and the unbalanced load at the end of mth time step.

Implementation of generalized Sinha's model

For the generalized 3-D Sinha's model, the components of creep strain tensor, in general, can be expressed as follows.

$$\epsilon_c = \epsilon_d(\sigma, t) + \beta(\sigma, N)t \tag{6.22}$$

If the stress σ_m^L and displacement a_m^L are obtained at time t_m, the stress increment from time step m to time step m+1 can be obtained by the following equations.

Let $\sigma_{m+1}^0 = \sigma_m^L$ and $a_{m+1}^0 = a_m^L$, Eq. 6.21 can be expressed as below using Eq. 6.22.

$$\begin{aligned} \phi_{m+1}^0 &= \phi_m^L + D(\epsilon_d(\sigma_{m+1}^0, T, t+dt) - \epsilon_d(\sigma_m^L, T, t)) \\ &\quad + D dt \beta(\sigma_{m+1}^0, N_{m+1}^0) \end{aligned} \tag{6.23}$$

For the first iteration, Eq. 6.21 becomes

$$\begin{aligned} \phi_{m+1}^1 &= \phi_{m+1}^0 + d\sigma_{m+1}^0 - DBda_{m+1}^0 + D(\frac{\partial \epsilon_d}{\partial \sigma})_m^L d\sigma_{m+1}^0 + Ddt(\frac{\partial \beta}{\partial \sigma})_m^L \theta d\sigma_{m+1}^0 \\ &\quad + Ddt(\frac{\partial \beta}{\partial N})_m^L \theta dN_{m+1}^0 \end{aligned} \tag{6.24}$$

where θ is a parameter with a value between 0 and 1.

Because the value for dN_{m+1}^0 is unknown, zero initial value is assumed for the calculation. By rearranging Eq. 6.24, the stress increment can be expressed as

$$\begin{aligned} d\sigma_{m+1}^0 &= \bar{D}^{-1}\{DBda_{m+1}^0 - \psi_{m+1}^0\} \\ \bar{D} &= I + D(\frac{\partial \epsilon_d}{\partial \sigma})_m^L + Ddt\theta(\frac{\partial \beta}{\partial \sigma})_m^L \end{aligned} \tag{6.25}$$

where I is a unit tensor.

The displacement increment da^0_{m+1} can be obtained by substituting Eq. 6.25 into Eq. 6.18. The stress and displacement at the end of the first iteration can be written as

$$\begin{aligned} \sigma^1_{m+1} &= \sigma^0_{m+1} + d\sigma^0_{m+1} \\ a^1_{m+1} &= a^0_{m+1} + da^0_{m+1} \end{aligned} \tag{6.26}$$

With the stresses and displacements, the crack density increment dN^0_{m+1} can be obtained. For the (n+1)th iteration, the unbalanced load at the end of nth iteration can be expressed as follows.

$$\begin{aligned} \phi^n_{m+1} &= D\{\epsilon_d(\sigma^n_{m+1}, T, t+dt) - \epsilon_d(\sigma^{n-1}_{m+1}, T, t+dt)\} - D(\frac{\partial \epsilon_d}{\partial \sigma})^{n-1}_{m+1} d\sigma^{n-1}_{m+1} \\ &+ Ddt(\frac{\partial \beta}{\partial N})^{n-1}_{m+1} \theta dN^{n-1}_{m+1} \end{aligned} \tag{6.27}$$

The nonlinear Eq. 6.21 for the (n+1)th iteration becomes

$$\begin{aligned} \phi^{n+1}_{m+1} &= \phi^n_{m+1} + d\sigma^n_{m+1} - DBda^n_{m+1} + D(\frac{\partial \epsilon_d}{\partial \sigma})^n_{m+1} d\sigma^n_{m+1} \\ &+ D(\frac{\partial \beta}{\partial \sigma})^n_{m+1} \theta d\sigma^n_{m+1} + D(\frac{\partial \beta}{\partial N})^n_{m+1} \theta dN^n_{m+1} \end{aligned} \tag{6.28}$$

Since the value for dN^n_{m+1} is unknown, zero initial value is assumed for the calculation. The stress increment in Eq. 6.28 can be obtained as

$$\begin{aligned} d\sigma^n_{m+1} &= \bar{D}\{DBda^n_{m+1} - \psi^n_{m+1}\} \\ \bar{D} &= (I + D(\frac{\partial \epsilon_d}{\partial \sigma})^n_{m+1} + D\theta(\frac{\partial \beta}{\partial \sigma})^n_{m+1})^{-1} \end{aligned} \tag{6.29}$$

The displacement increment da^n_{m+1} can be calculated by substituting Eq. 6.29 into Eq. 6.18. The stress and displacement at the end of (n+1)th iteration are give as

$$\sigma_{m+1}^{n+1} = \sigma_{m+1}^{n} + d\sigma_{m+1}^{n}$$
$$a_{m+1}^{n+1} = a_{m+1}^{n} + da_{m+1}^{n} \tag{6.30}$$

In the program, for the simplicity, only one time step is used. In addition, θ is given as zero. Therefore, for the (m+1)th time step, similar to the discussion from Eq. 6.23 to Eq. 6.26, the following equations are used.

Let $\sigma_{m+1}^{0} = \sigma_{m}^{L}$ and $a_{m+1}^{0} = a_{m}^{L}$, Eq. 6.21 can be expressed as below using Eq. 6.22.

$$\begin{aligned}\phi_{m+1}^{0} &= \phi_{m}^{L} + D(\epsilon_d(\sigma_{m+1}^{0}, T, t+dt) - \epsilon_d(\sigma_{m}^{L}, T, t)) \\ &\quad + D dt \beta(\sigma_{m+1}^{0}, N_{m+1}^{0})\end{aligned} \tag{6.31}$$

The nonlinear Eq. 6.21 can be expressed as below for the first iteration.

$$\begin{aligned}\phi_{m+1}^{1} &= \phi_{m+1}^{0} + d\sigma_{m+1}^{0} - DBda_{m+1}^{0} + D(\frac{\partial \epsilon_d}{\partial \sigma})_{m}^{L} d\sigma_{m+1}^{0} + Ddt(\frac{\partial \beta}{\partial \sigma})_{m}^{L} \theta d\sigma_{m+1}^{0} \\ &\quad + Ddt(\frac{\partial \beta}{\partial N})_{m}^{L} \theta dN_{m+1}^{0}\end{aligned} \tag{6.32}$$

In the approximation, only the following value is required to be zero in the program.

$$\bar{\phi}_{m+1}^{1} = \phi_{m+1}^{0} + d\sigma_{m+1}^{0} - DBda_{m+1}^{0} = 0 \tag{6.33}$$

By rearranging Eq. 6.33, the stress increment can be obtained.

$$d\sigma_{m+1}^{0} = DBda_{m+1}^{0} - \phi_{m+1}^{0} \tag{6.34}$$

The displacement increment da_{m+1}^{0} can be obtained by substituting Eq. 6.34 and Eq. 6.18. The stress and displacement at the end of the first iteration can be obtained from

$$\sigma^1_{m+1} = \sigma^0_{m+1} + d\sigma^0_{m+1}$$
$$a^1_{m+1} = a^0_{m+1} + da^0_{m+1} \tag{6.35}$$

The unbalanced load at the end of the first iteration becomes

$$\begin{aligned}\phi^1_{m+1} &= D(\epsilon_d(\sigma^1_{m+1}, T, t+dt) - \epsilon_d(\sigma^L_m, T, t)) \\ &+ Ddt(\frac{\partial\beta}{\partial\sigma})^L_m \theta d\sigma^0_{m+1} + Ddt(\frac{\partial\beta}{\partial N})^L_m \theta dN^0_{m+1}\end{aligned} \tag{6.36}$$

This unbalanced load is applied in the next time step.

6.4 Verification of FE program

The development of the finite element code is based on a three dimensional linear elastic finite element program. First, the correctness of the linear elastic program was tested. Then, spring elements to be used at the boundaries were added to the program. This addition was considered necessary for simulating the buoyancy effects. Finally, the generalized creep model of Sinha was implemented into the program.

The verification of the FE program is given in this section. According to the development of the program, three types of verifications are performed: (1) verification of the elastic part of the program; (2) verification of the implementation of the spring elements; (3) verification of the implementation of the generalized Sinha's model.

All problems used for the verification purpose are for columnar grained ice at temperature -10^0C. The material properties for the ice are listed in Table 6.1. In the linear viscoelastic analysis, the stress power n and constant b are assumed equal to one.

Two different finite element meshes used in the verification are shown in Fig. 6.3. The first mesh is used to simulate the load displacement response of a cubical ice sample subjected to a uniaxial loading. The second one is used for the analysis of a thick cylinder.

Table 6.1 Material properties of fresh water columnar grained ice

Elastic modulus E	9.5 GPa
Possion's ratio μ	0.33
For delayed elasticity, c_1 and a_T	9.0, 0.00025 s^{-1} (263 K)
For delayed elasticity, b	0.333
For viscous strain $\dot{\epsilon}_{v1}$	1.76×10^{-7}
For crack density, N_c, ψ, K	550.0, 1.33×10^7, 1.0
For crack density X_c	4.7×10^{-7} m
Stress power n	3.0

6.4.1 Elastic analysis

The elastic analysis was carried out to verify the correctness of the elastic part of the finite element program. This analysis is not intended to verify the correct implementation of the generalized Sinha's model into the finite element code.

Figure 6.4 shows the comparisons of stress and displacement along the radial direction between the analytical solution and the FE results for a thick cylinder subjected to an internal pressure. The results agree quite well.

6.4.2 Spring elements

For the purpose of simulating the buoyancy effects in the analysis of ice engineering problems, a spring elements was added to the program. The implementation of the spring elements is explained below.

In general, the following equation is solved in a finite element analysis.

$$M\delta = f \tag{6.37}$$

where M is the stiffness matrix; δ is the nodal displacements vector; f is the force vector.

By separating the nodal displacements δ_s at the spring boundary from the rest δ_r and rearranging the stiffness matrix, Eq. 6.37 can be rewritten as

$$\begin{pmatrix} A & B \\ C & D \end{pmatrix} \begin{pmatrix} \delta_s \\ \delta_r \end{pmatrix} = \begin{pmatrix} -k\delta_s \\ f \end{pmatrix} \tag{6.38}$$

The above equation can be rearranged as follows.

$$\begin{pmatrix} A+k & B \\ C & D \end{pmatrix} \begin{pmatrix} \delta_s \\ \delta_r \end{pmatrix} = \begin{pmatrix} 0 \\ f \end{pmatrix} \tag{6.39}$$

Eq. 6.39 shows that the spring boundary can be treated as a free boundary by modifying the elements, of the stiffness matrix, which are corresponding to the spring boundary.

The following example is designed to verify the implementation of the spring boundary. A thick cylinder subjected to an external pressure with elastic springs at the internal boundary is analyzed. The comparisons of the results of FE analysis and an analytical solution for stresses and displacement along the radial direction are presented in Fig. 6.5. The FE results agree with the analytical results, which shows that the implementation of the spring elements is correct.

6.4.3 Verification of ice model implementation

Three different types of problems were analyzed to verify the numerical implementation of the generalized Sinha model. The first one is a linear viscoelastic problem. The second one is a nonlinear viscoelastic problem. And the last one is nonlinear viscoelastic problems with cracking.

Linear viscoelastic analysis

In this analysis, stresses and displacements are calculated for a thick cylinder subjected to internal pressure. The material is represented by a linear viscoelastic model. If the value of n and b in Sinha's equation are one, the mathematical expression for Sinha's creep equation becomes similar to a four-parameter linear viscoelastic fluid material, which can be expressed as below.

$$\epsilon = \frac{\sigma}{E_1} + \frac{\sigma}{E_2}\{1 - exp(-a_T t)\} + \beta\sigma t \qquad (6.40)$$

The comparisons between the analytical solution and FE results for the stresses and displacement are shown in Fig. 6.6. An unloading analysis was performed to show that the program can follow any loading path. The agreement between the FE results and the analytical solution is very good.

Nonlinear viscoelastic analysis

The verifications performed above is for a linear viscoelastic material. In addition, no stress transformation was occurring between elements in the previous verification. It is therefore necessary to check the nonlinear part of the program further.

It is difficult to obtain an analytical solution for Sinha's model, When the parameters n and b are not equal to one. However, a steady state solution for a thick cylinder subjected to internal pressure under plane strain condition was obtained using the generalized Sinha's model (see Appendix B). The steady state is defined as a state where the stress does not change with time anymore.

Figure 6.7 presents the comparison between finite element results and the analytical solution for the radial stress σ_r. The finite element result is obtained at a creep time of about 7 hours. This figure shows that the two results are very close. The comparisons between finite element results and the analytical solution for the circumferential stress σ_θ and the intermediate stress σ_z are shown in Figs. 6.8 and 6.9, respectively. Good agreements are achieved.

Nonlinear viscoelastic analysis with cracking

Two problems are solved using the generalized Sinha's model with cracking. The first one is for a cubical ice sample subjected to a constant uniaxial load. The second one is a simulation of a constant strain rate test.

Figure 6.10 shows the comparisons between the model prediction and FE results for the time dependence of strain at three different stress levels. The FE results are in good accord with the model prediction.

Figure 6.11 shows the comparisons between the model prediction and FE results for the rate dependence of stress and strain at three different strain rates. These results are also in good agreement.

The analysis of the example problems given in this section indicates that the model implementation was done correctly.

6.5 Analysis of borehole indentation test data

The three dimensional finite element program developed in this study is used to analyse the borehole indentation test results. Due to the limitations, however, in terms of storage and speed of the mainframe computer at the University of Ottawa, three dimensional elastic and two dimensional creep analysis are carried out. The finite element analyses are performed to find explanations for the following results observed in the borehole indentation tests.

1. Negligible dependence of the maximum stress, measured during the borehole indentation test, on the angle between the mean c-axis and loading direction.

2. Strong dependence of the large crack orientation in the horizontal plane on the angle between the mean c-axis and loading direction.

Two analyses are carried out. One is the three dimensional elastic analysis of the stress distribution around the borehole indentor. The purpose of this analysis is to determine the stress distribution and the angle between the mean c-axis and the principal stress axis at different location around the borehole indentor. The other one is a plane strain creep analysis as a simplification of the borehole indentation test. The purpose of this analysis is to study the change of the principal stresses and its orientation with time. The material properties listed in Table 6.1 are used in the finite element analysis. The grain size of the ice is chosen as 1.0 mm, which is close to the measured values in the field.

6.5.1 3-D elastic analysis

In the three dimensional elastic analysis, a quarter of the ice mass around the borehole indentor is discretized as shown in Fig. 6.12. The borehole indentor is

assumed to be rigid. A displacement boundary condition is applied at the surface between the borehole indentor and the ice mass.

The principal stress distribution in the horizontal plane at the level of the borehole indentor is presented in Fig. 6.13. The maximum tensile stress occurs in the element G in Fig. 6.13. The angle between the mean c-axis and loading direction (ACL) is 45 degrees. This analysis shows that the angle between the mean c-axis and the principal stress axis (ACP), which is the primary factor affecting the strength of ice, is different at different locations. It happens only in a small area around the borehole indentor where the ACP angel is close to the ACL angle 45 degrees. Further, the principal stresses shown in the figure are in a horizontal plane passing through the middle of the borehole indentor. The deviation of the ACP angle from the 45 degrees in other horizontal planes would be larger most likely. In the case of the mean c-axis parallel to the loading direction, large deviations of the ACP angle from 0 degree would be expected in most areas in the ice sheet around the borehole indentor. It can be concluded that the deviation of the ACP angle from the ACL angle narrows down the effects of the ACL angle on the maximum stress in the borehole indentation test.

With the principal stress distribution in the Fig. 6.13, the following explanation can be given for the dependence of the orientation of large cracks on the ACL angle.

Two mechanisms are operating at the same time to decide which direction the crack goes. One is that the plane parallel to the c-axis is a cleavage plane. Therefore, it is easy for a crack to develop in these planes. The other one is that the maximum tensile stress is in vertical planes almost 45 degrees to the loading direction as obtained from finite element analysis.

For ACL angle 0 degree, the large crack is parallel to the mean c-axis. In this case, the first mechanism is the main cause. For ACL angle 45 degrees, the large crack tends to orientate to the direction of the mean c-axis. This is caused by the combination of both mechanisms discussed above. For ACL angle 90 degrees, the large cracks are in a plane about 45 degrees to the loading direction. This is mainly due to the second mechanism.

The deformed mesh in the horizontal plane at the same level of the borehole indentor is presented in Fig. 6.14. In the figure, the dashed line is the mesh after the load is applied.

6.5.2 Plane strain creep analysis

A plane strain creep analysis is conducted to investigate the time dependence of the principal stresses and their orientations. Half of the ice in the horizontal plane is discretized as shown in Fig. 6.15. Six elements close to the borehole indentor were labeled for the presentation of stresses in these elements later. A displacement boundary is applied at the surface between the borehole indentor and the ice sheet. The displacement increases with time at a constant rate. The analysis is done on fresh water columnar grained ice with a grain size of 1 mm at temperature of 263 K. The indentation rate is given as 0.02 mm/s.

Figure 6.16 presents the principal stresses and their orientations at a creep time of 100 seconds. Similar to the three dimensional elastic analysis, the orientations of the principal stresses are different in different locations. The deformation at the same time is presented in Fig. 6.17. The dashed line is the deformed mesh.

The time dependence of the principal stresses and their orientation are presented in Fig. 6.18 for the elements labeled in Fig. 6.15. In these figures, α represents the angle between the first principal stress σ_1 and x direction. It can be seen from this figure that the time dependence of the principal stress orientation is negligible. Except the stresses in elements A and B, all major principal stresses σ_1 increase with time to a maximum and then decrease. This is quite similar to the increase and decrease of the average stress measured in H test reported in Chapter 3. In addition, a maximum tensile stress of -4.0 MPa occurs in element C as shown in Fig. 6.18. This is the place where a large crack occurred in borehole indentation test for ACL 45 and 90 degrees.

The time and displacement dependence of the maximum shear stresses $\frac{\sigma_1-\sigma_3}{2}$ for the labeled six elements are shown in Figs. 6.19 and 6.20, respectively. Although the principal stresses are quite different in different elements, the time dependence of the maximum shear stresses is quite similar. With the increase of time, the maximum shear stress increases to a maximum and then decreases. It is very interesting to see that after the maximum shear stress decreases for a while, it becomes about the same value in all elements as shown in Fig. 6.20. This redistribution of stress among elements to make the maximum shear stress the same among all elements is due to that the maximum shear stress is the main driving

force for the time dependent plastic deformation.

The plane strain analysis shows that the time dependence of the principal stress orientation is negligible. As pointed out in the three dimensional elastic analysis, the ACP angle in most area is different from ACL angle at time zero. This will be true at any creep time if the ACP angle does not change with time. That is what is found in the plane strain creep analysis.

Similar to the results shown in Figs. 6.19 and 6.20, the time and displacement dependence of the maximum shear stresses at an indentation rate 0.04 mm/s are presented in Figs. 6.21 and 6.22, respectively, for the labelled six elements.

The comparison of the maximum shear stress versus displacement diagrams at two indentation rates are presented in Fig. 6.23. This figure shows that with the increase of indentation rate, the maximum shear stress increases.

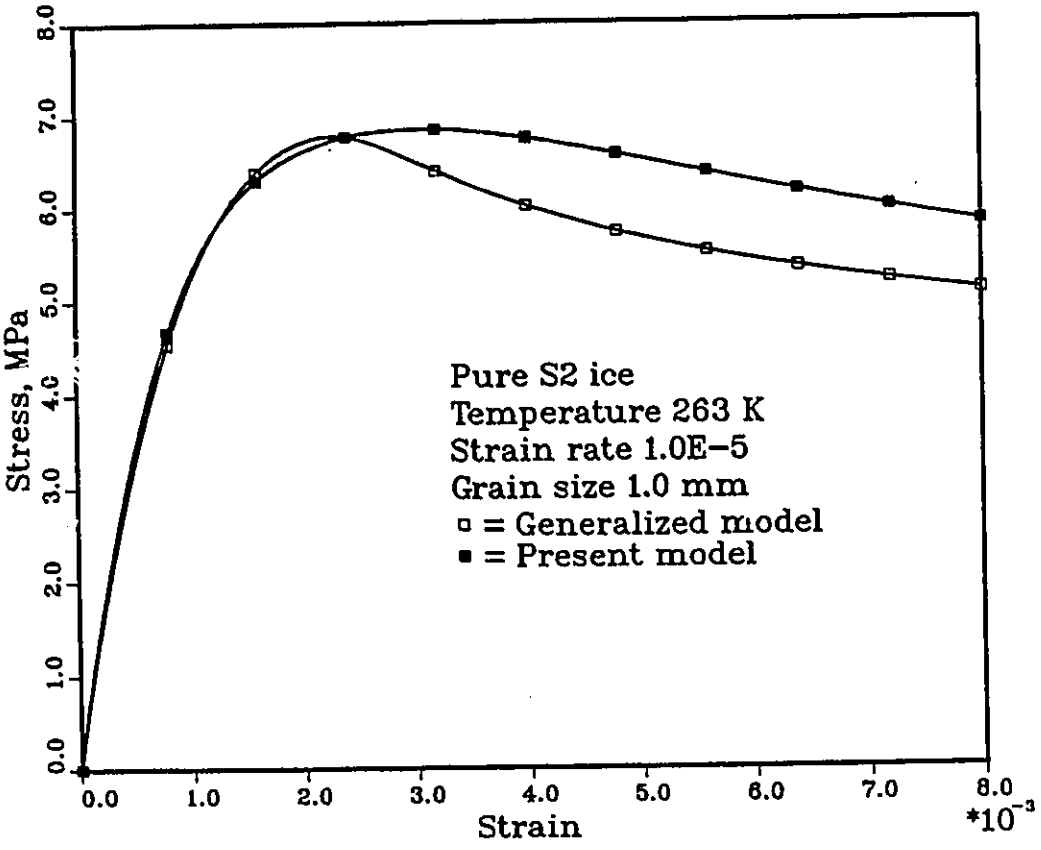

Figure 6.1 Comparisons for predicted stress–strain diagrams between present model and generalized model under 3–D loading with 50% confinement

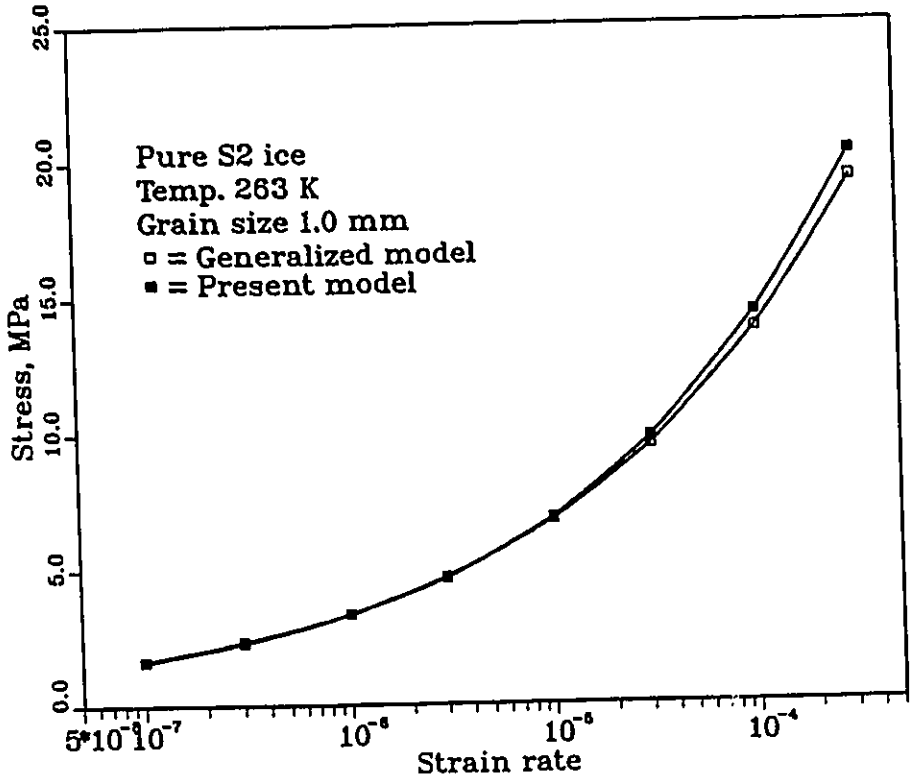

Figure 6.2 Comparisons between present model and generalized model predictions for rate dependence of strength under 3–D loading with 50% confinement

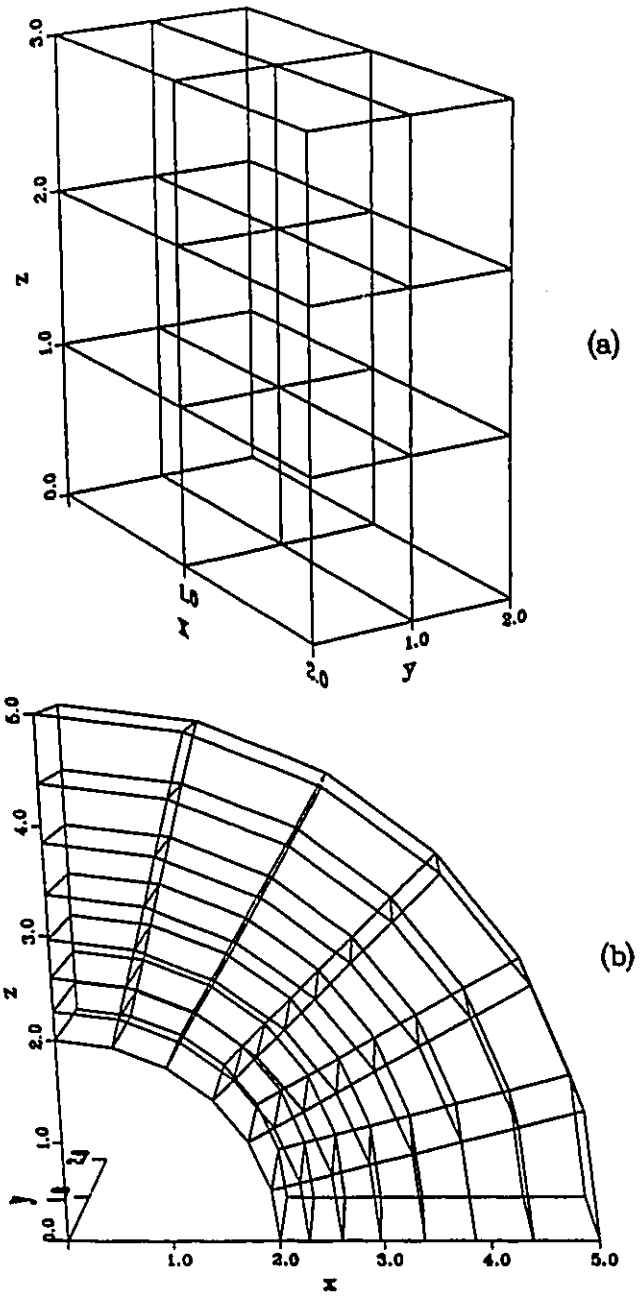

Figure 6.3 Three dimensional finite element mesh
a: cubical ice sample
b: thick cylinder

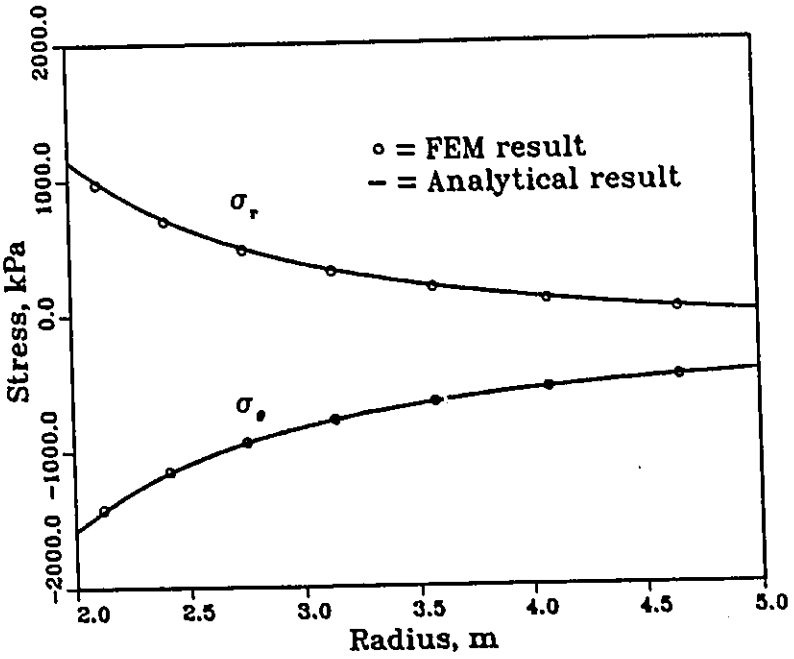

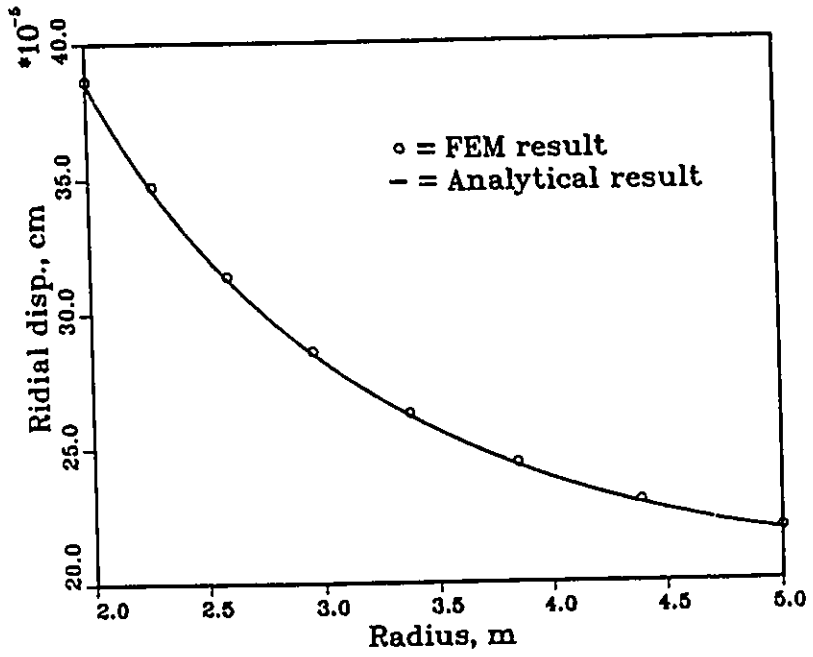

Figure 6.4 Comparison between FE result with analytical solution for elastic thick cylinder subjected to internal pressure

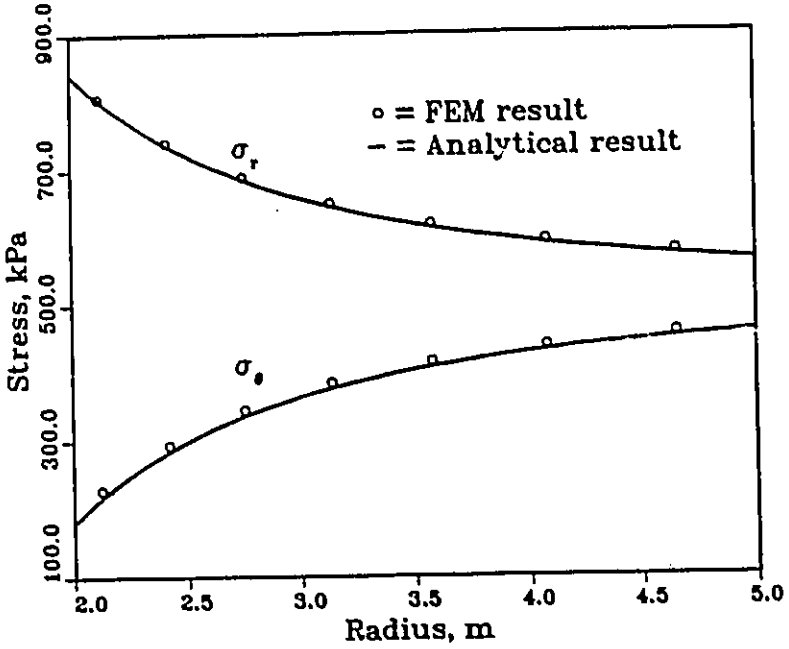

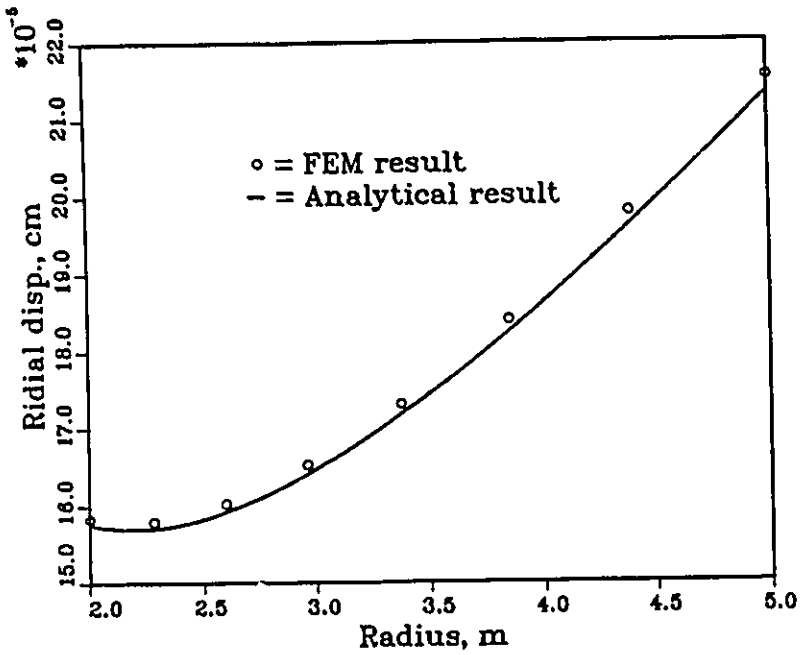

Figure 6.5 Comparison between FE result with analytical solution for elastic thick cylinder with internal elastic foundation bounary subjected to external pressure

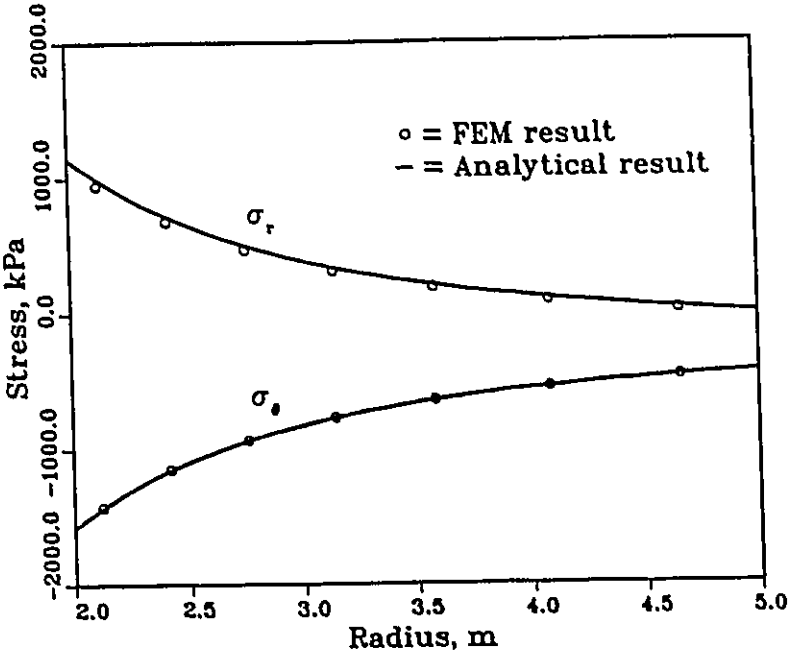

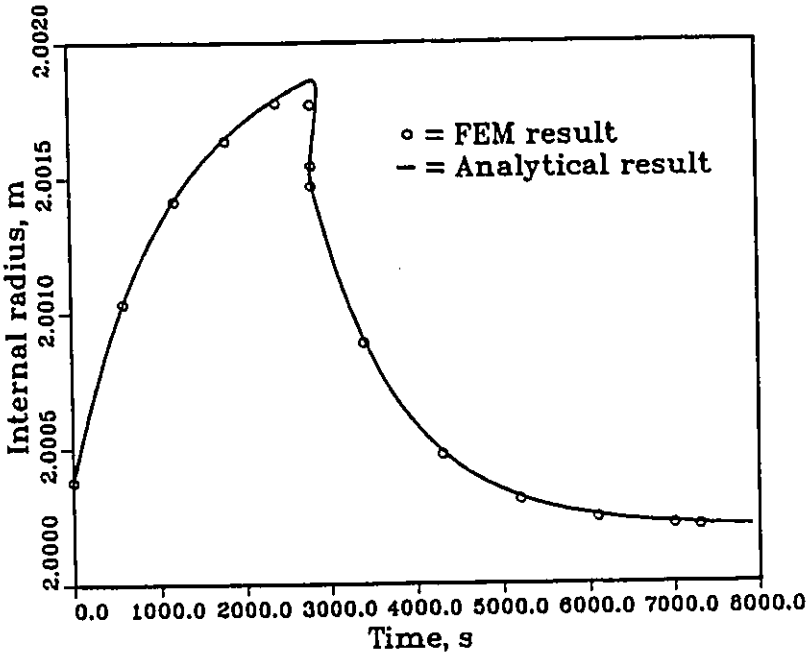

Figure 6.6 Comparison between FE result and analytical solution for linear viscoelastic problem

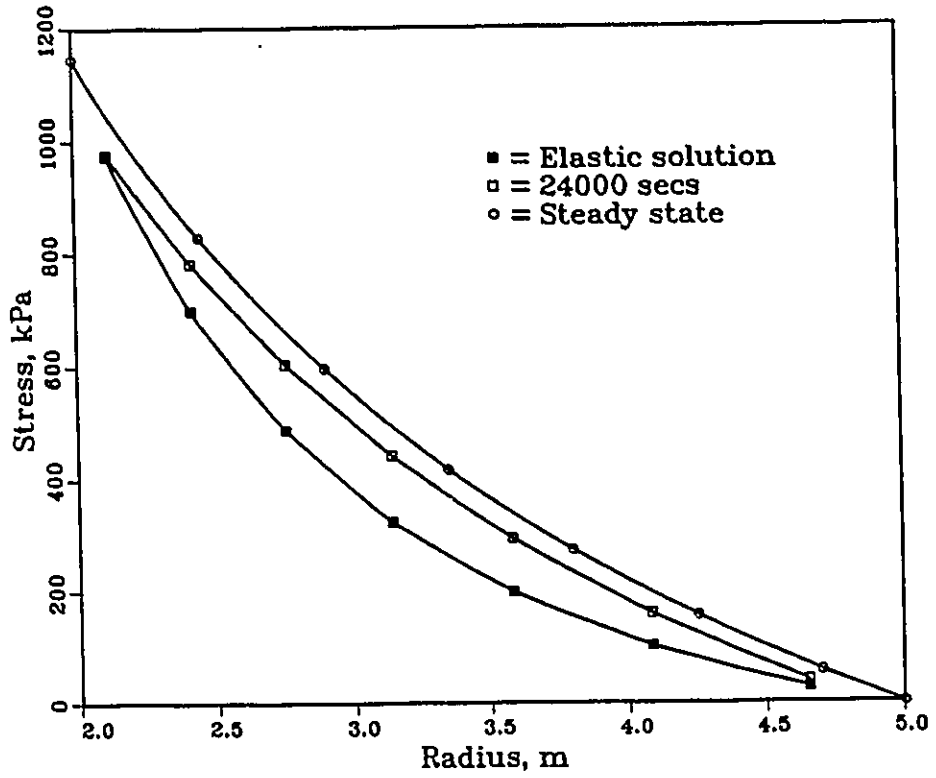

Figure 6.7 Comparison of radial stress between FE analysis and analytical solution for thick cylinder subjected to internal pressure under plane strain condition

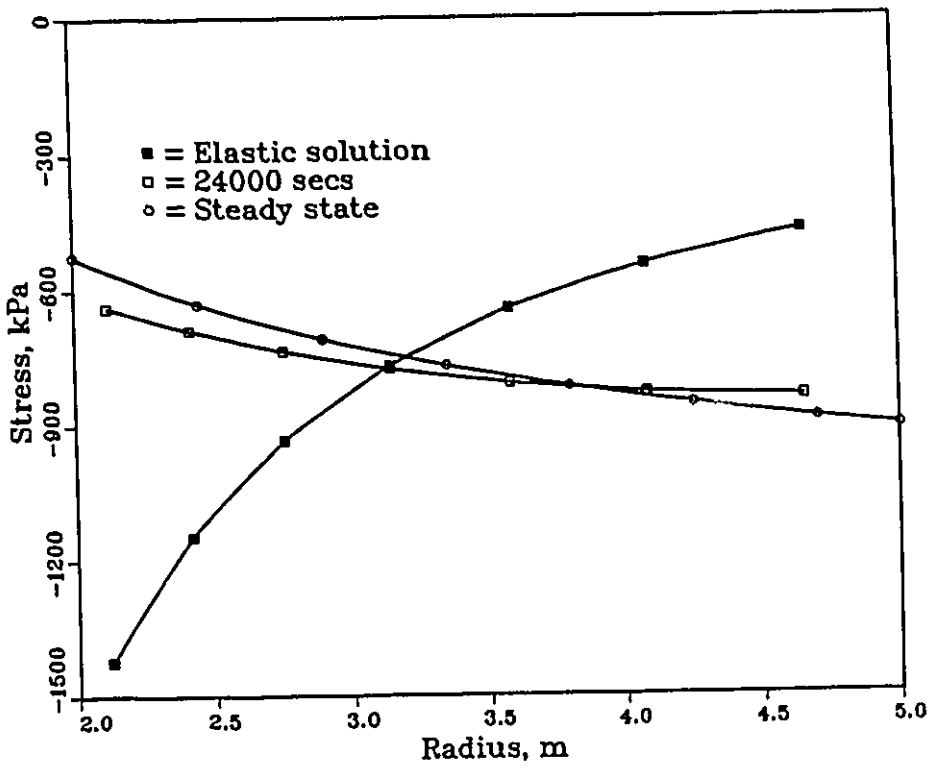

Figure 6.8 Comparison of circumferential stress between FE results and analytical solution for thick cylinder subjected to internal pressure under plane strain condition

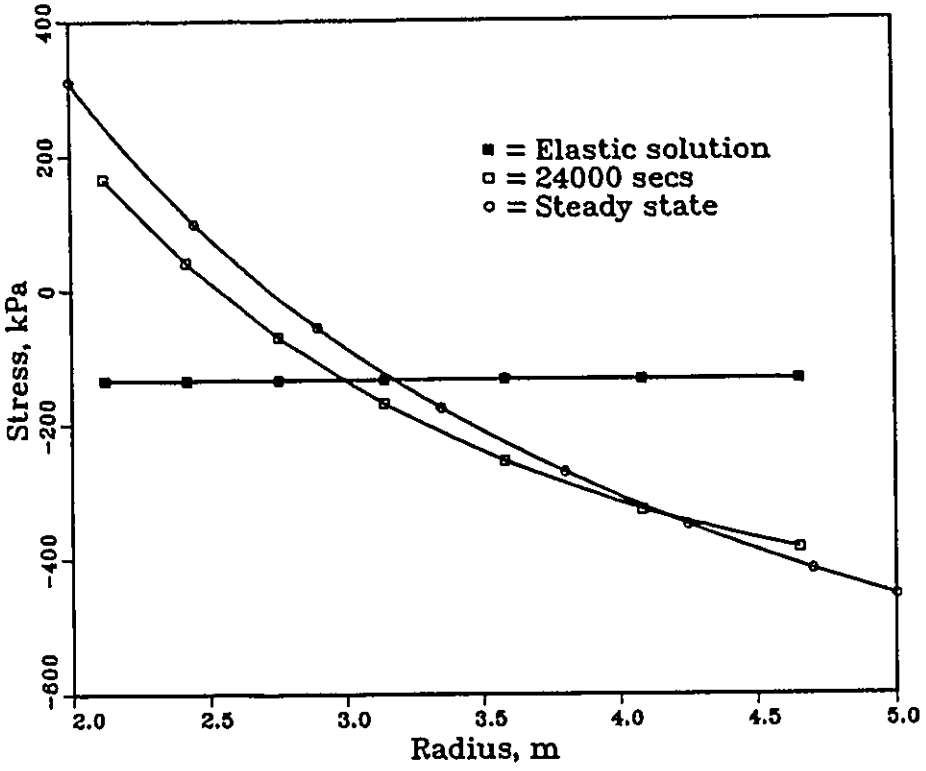

Figure 6.9 Comparison of middle stress between FE analysis and analytical solution for thick cylinder subjected to internal pressure under plane strain condition

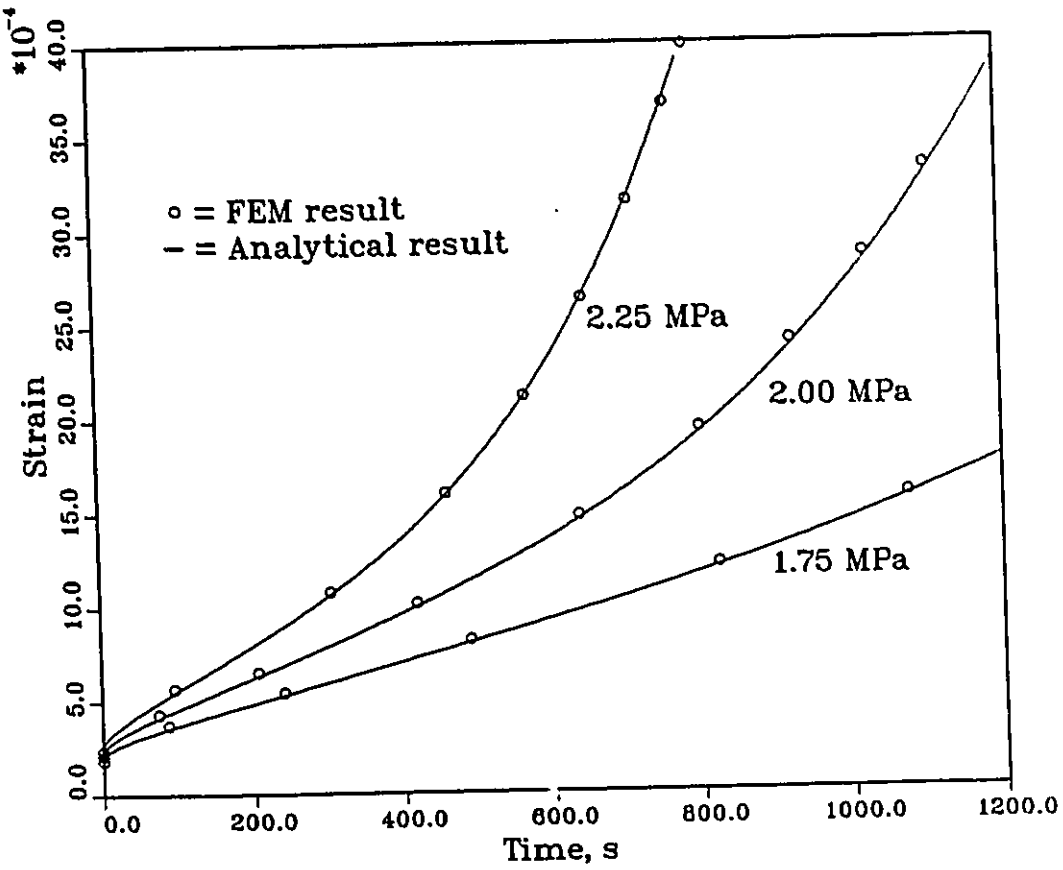

Figure 6.10 Comparisons between FE result and model predictions for time dependence of strains under constant load

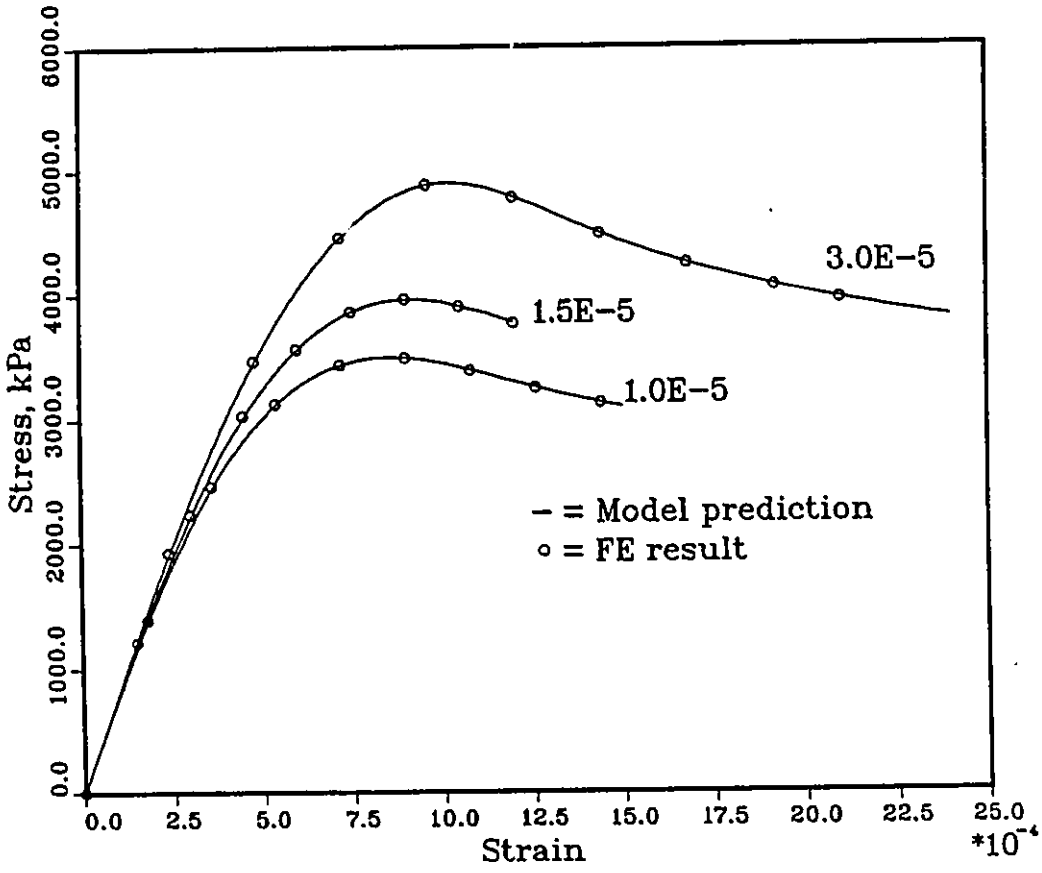

Figure 6.11 Comparisions between FE results and model predictions for stress–strain diagrams

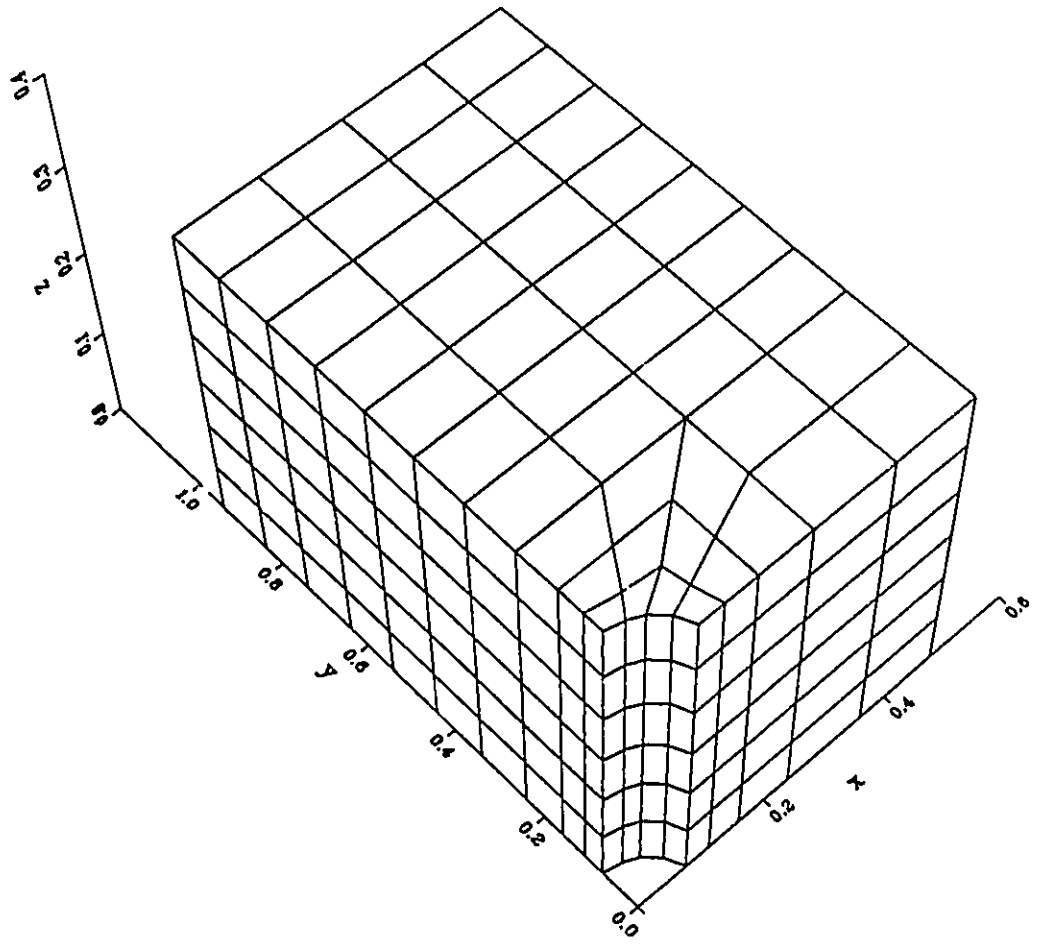

Figure 6.12 Three dimensional finite element mesh for borehole indentation test

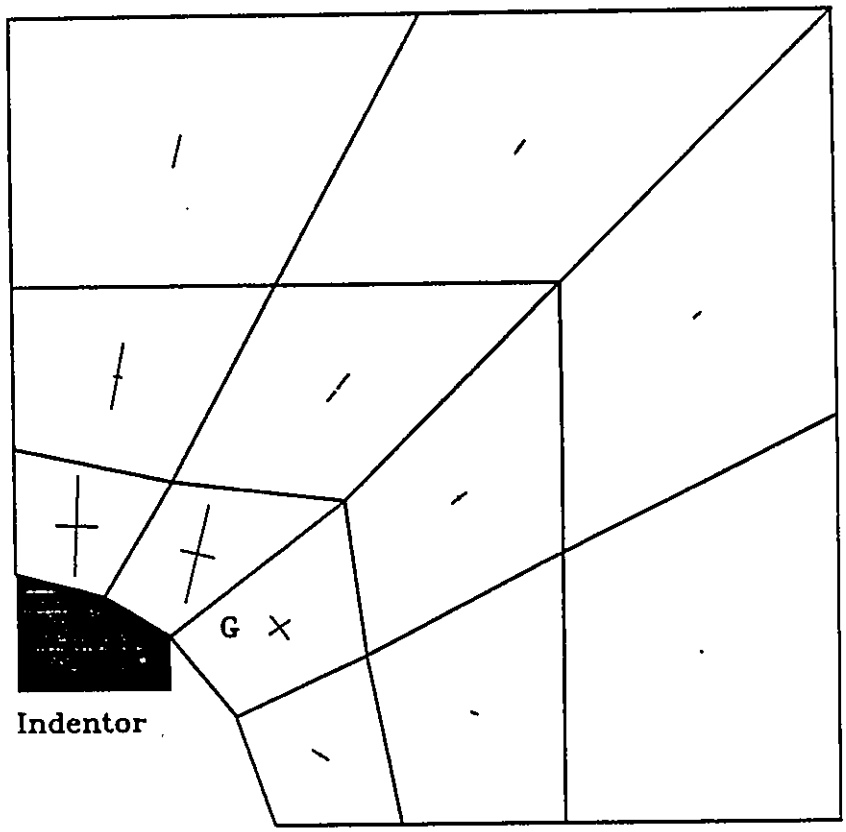

Figure 6.13 Elastic stress distribution around borehole indentor

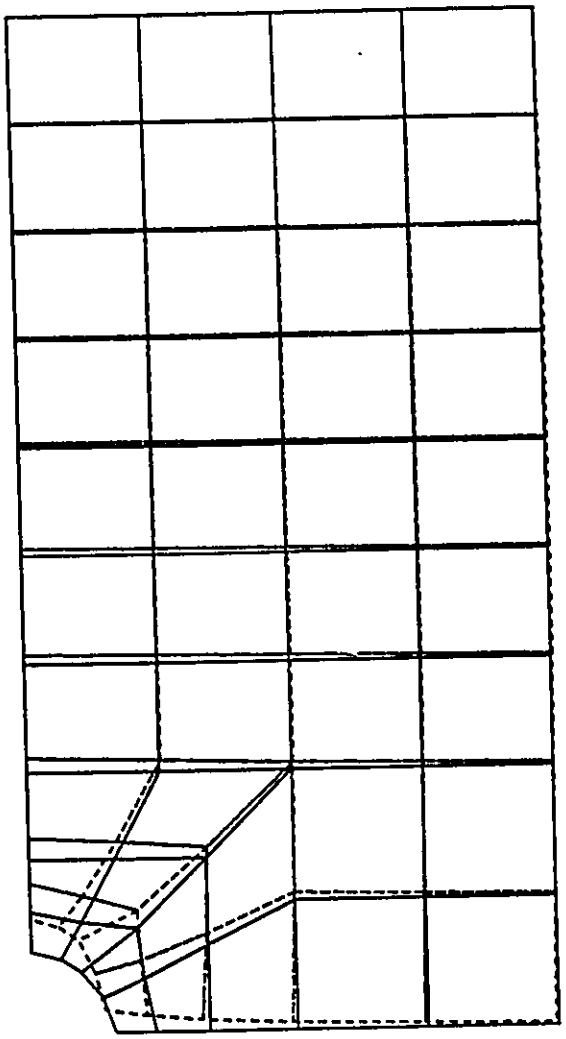

Figure 6.14 Deformation of ice in horizontal plane at level of borehole indentor

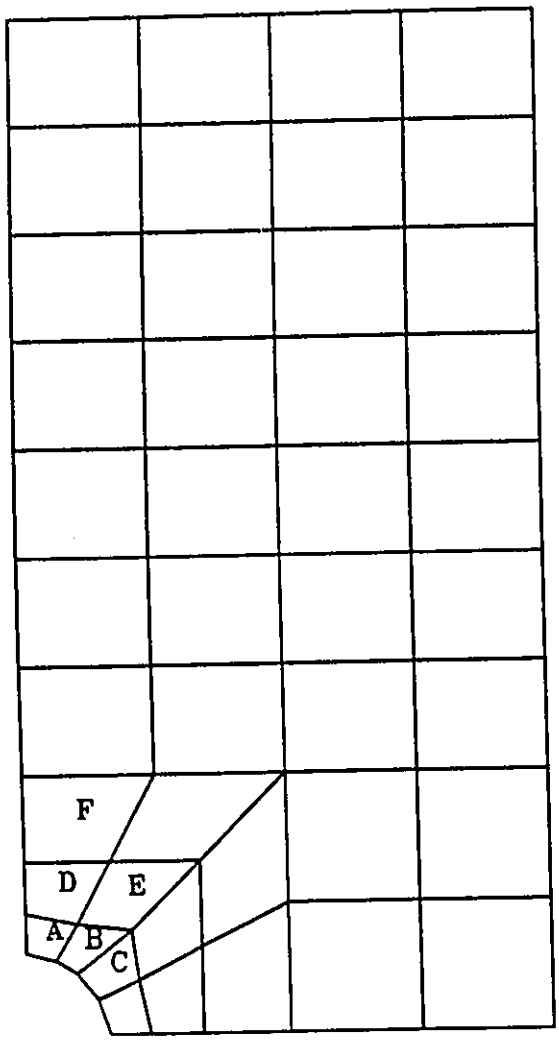

Figure 6.15 Finite element mesh for borehole indentation test under plane strain condition

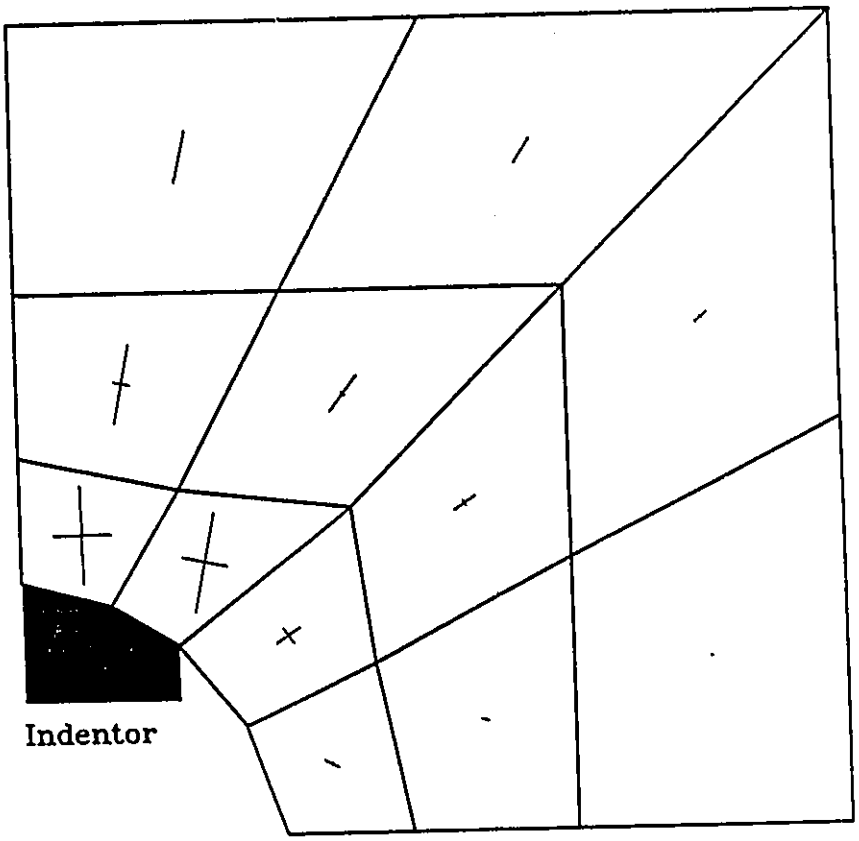

Figure 6.16 Elastic stress distribution around borehole indentor under plane strain condition

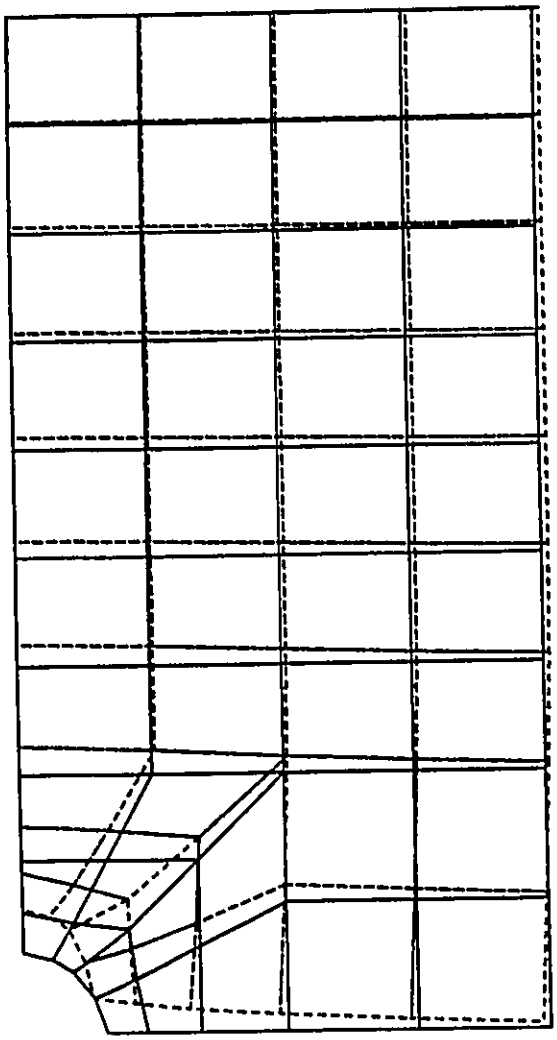

Figure 6.17 Deformation of mesh at time close to zero for simulation of borehole indentation test under plane strain condition

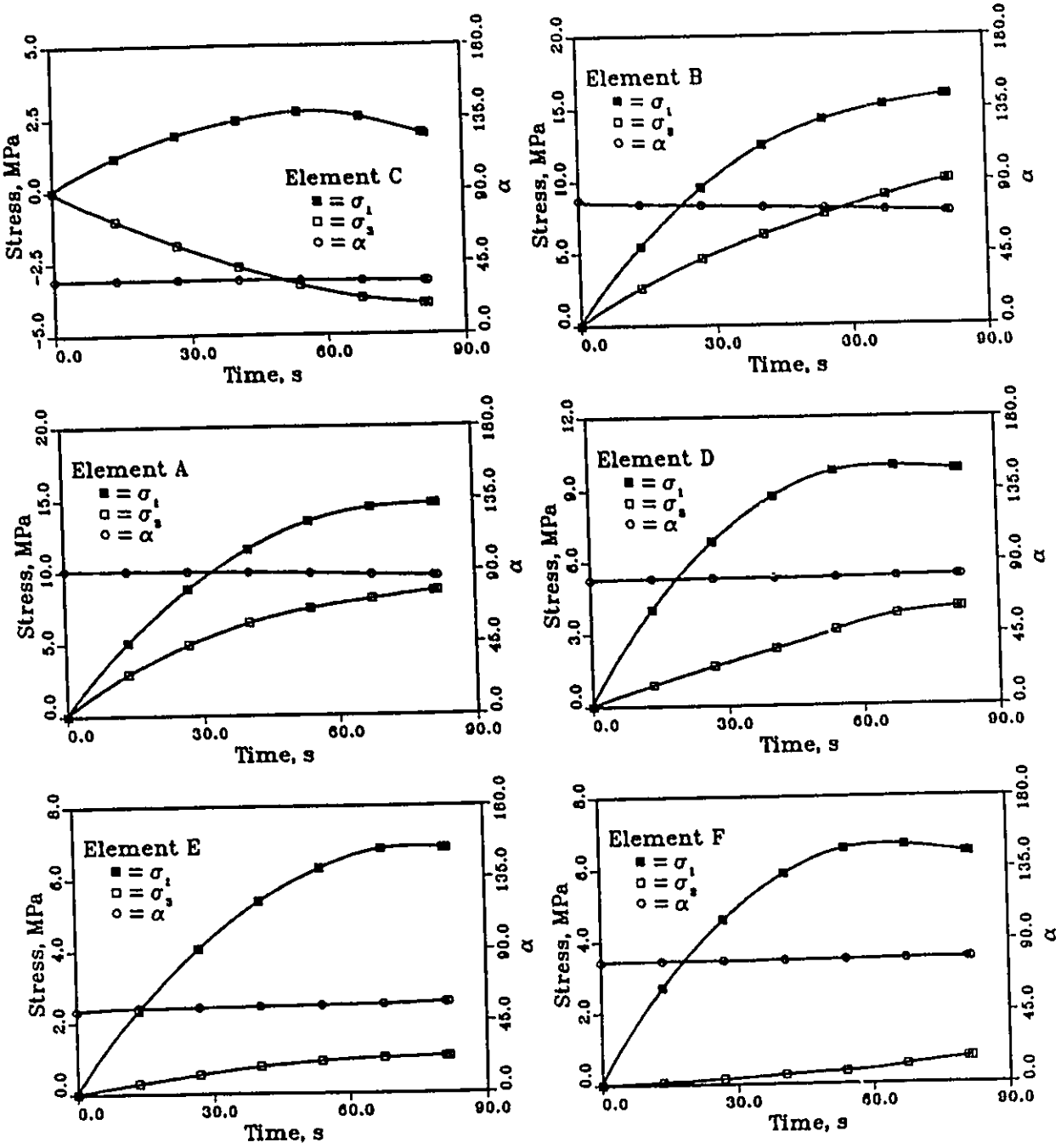

Figure 6.18 Time dependence of principal stresses and their orientations for borehole indentation test

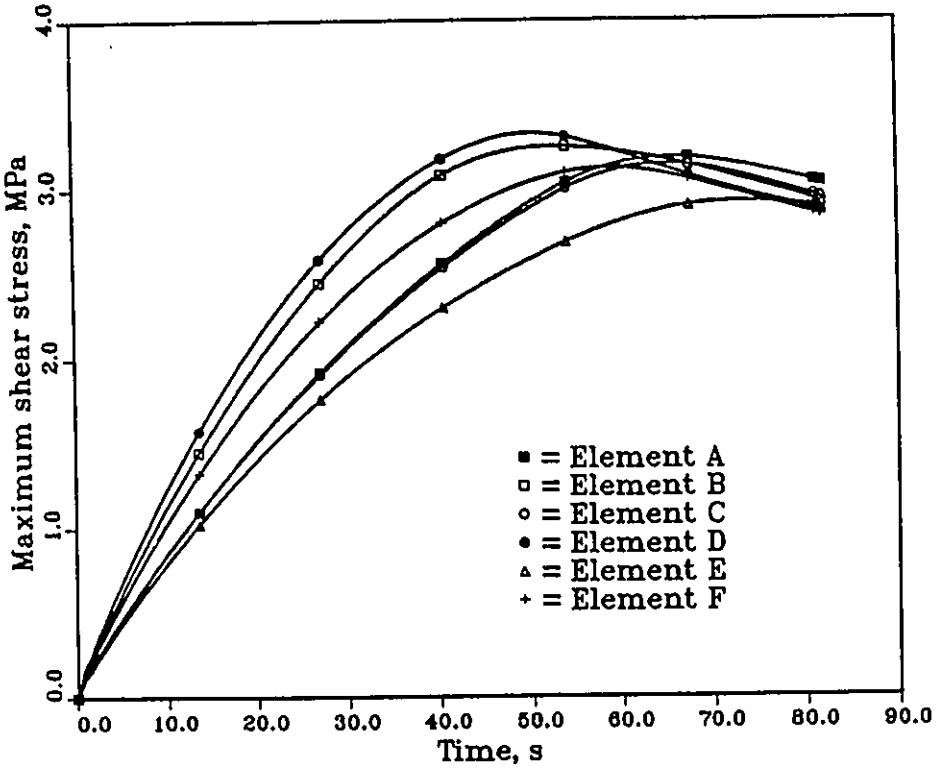

Figure 6.19 FE simulation of time dependence of maximun shear stress in borehole indentation test under plane strain condition at indentation rate 0.02 mm/s

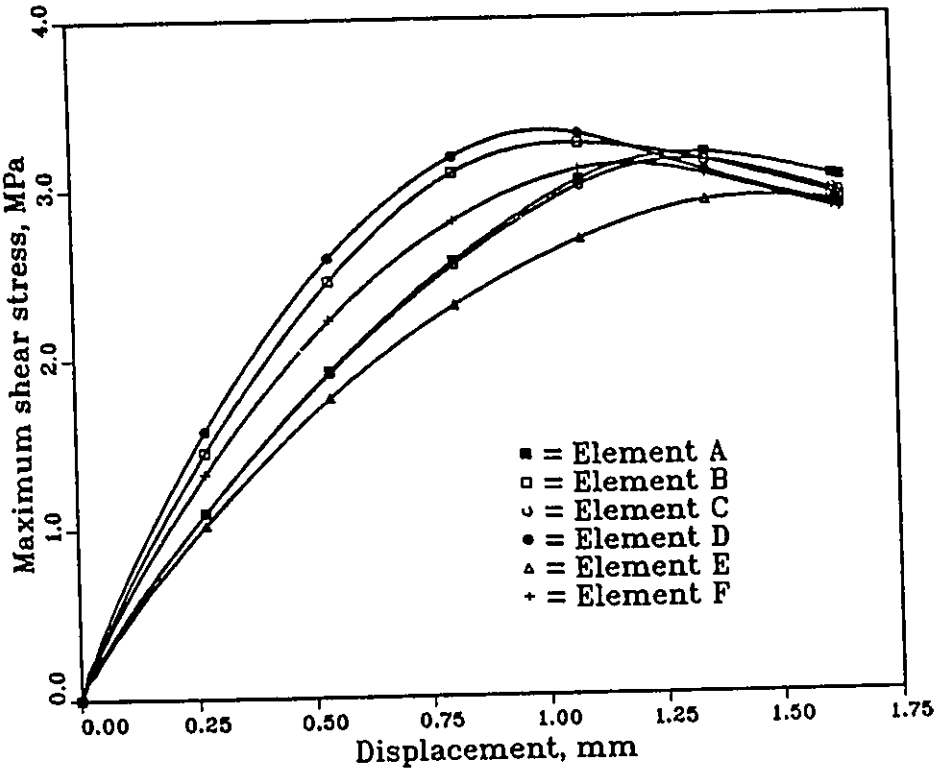

Figure 6.20 FE simulation of maximum shear stress and displacement diagram in borehole indentation test under plane strain condition at indentation rate 0.02 mm/s

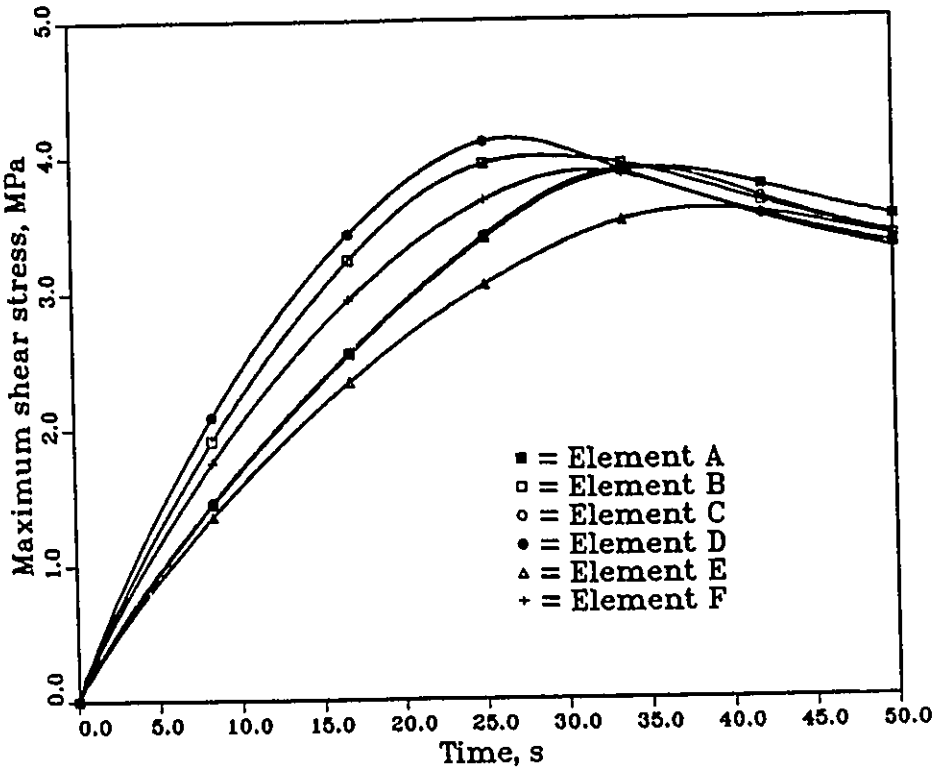

Figure 6.21 FE simulation of time dependence of maximun shear stress in borehole indentation test under plane strain condition at indentation rate 0.04 mm/s

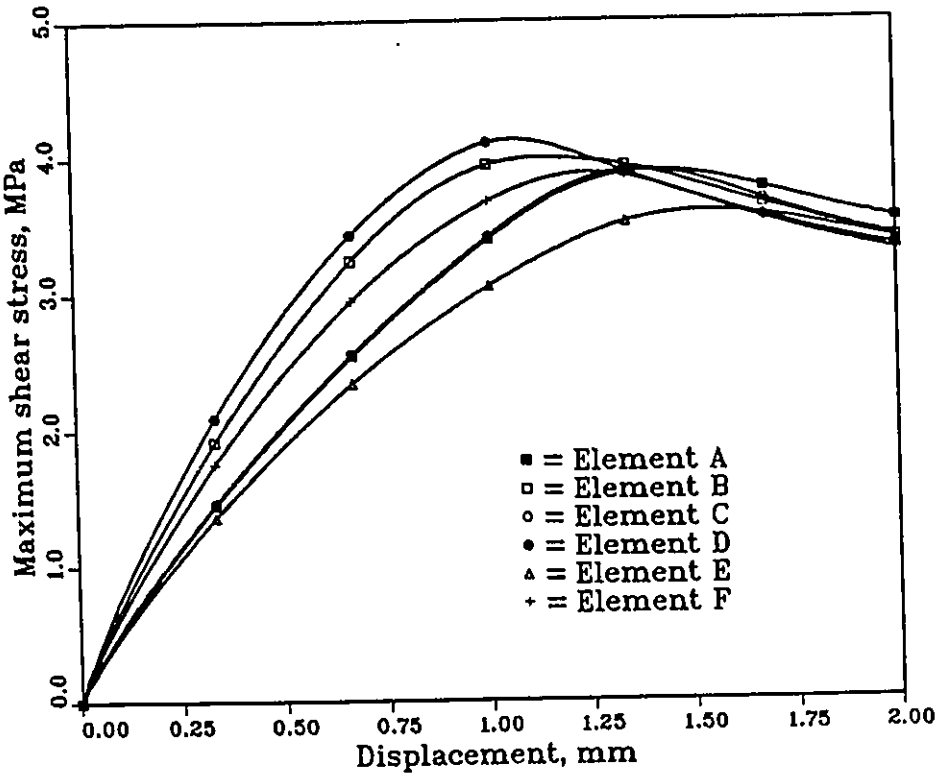

Figure 6.22 FE simulation of maximum shear stress and displacement diagram in borehole indentation test under plane strain condition at indentation rate 0.04 mm/s

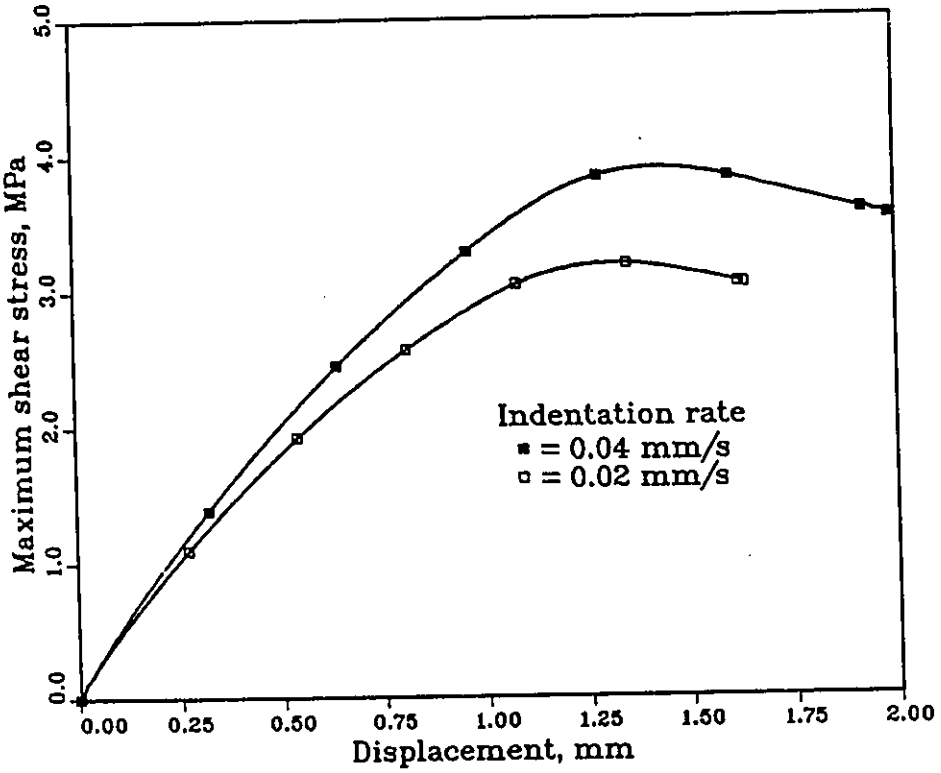

Figure 6.23 Comparison of maximum shear stress and displacement diagram in borehole indentation test at two indentation rates for element A

Chapter 7

Conclusions

The conclusions of this research work are presented in this Chapter. Recommendations for future work are also provided.

7.1 Laboratory experiments

Uniaxial constant compressive stress (CS) tests were carried out at temperature -10^0, -20^0 and -30^0C with the stress ranging from 0.7 to 2.5 MPa. Axial and lateral strains were measured and acoustic emission data were recorded. The conclusions are given below.

1. Very similar to fresh water polycrystalline ice, sea ice also shows the three creep stage; primary, transitory and tertiary. The creep rate decreases with time until reaching a minimum value, and then increases with further deformation.

2. The deformation of columnar grained first year sea ice is anisotropic, which is primarily two dimensional. When an uniaxial load is applied normal to the length of the columns of grains, the strain along the columns is very small. However, the lateral strain normal to the columns of grains is significantly larger than the axial strain during the tertiary creep stage. These observations are the indications of the fact that the microcracks formed during the deformation and that the geometry of the cracks were essentially two dimensional.

3. Results from creep tests show that the sea ice behaviours are highly non-linear. This non-linearity can be examined by plotting the effective modulus as a function of time. The effective modulus decreases with the increase in creep time. The higher the stress, the lower the effective modulus at a given time, which further confirms the nonlinearity of the sea ice behaviour.

4. The recovery curve after unloading shows small but measurable amount of delayed elastic strain. The delayed volumetric strain, associated with delayed elastic strain, is almost zero. The magnitude of the axial recovery strain at the time of unloading in the tertiary creep range (1.0 to 2.5% strain) is between 10 to 25 times higher than the axial elastic strain. The delayed elastic strain also shows significant anisotropy, the delayed elastic strain along the length of the columns of grains is much smaller than that in the other two directions.

5. The stress dependence of the minimum strain rate can be expressed by a power law with a stress power close to 4.0.

6. One to one correspondence has been shown between the dependence of minimum strain rate on stress observed during the present compressive creep tests at 263 K and the previous data on the dependence of the maximum stress or upper yield (compressive strength) on strain rate in constant closed-loop controlled strain rate (CD) tests. The significance of this conclusion is that one can simply perform a series of constant stress tests to obtain the rate dependence of the strength obtained from CD tests. CD tests require expensive closed-loop machine; CS tests can be performed using inexpensive simple dead load system.

7. The ductility at failure decreases with an increase in stress; the strain at minimum creep rate (failure) decreases with an increase in stress. This is in contradiction with the test results on fresh water granular ice.

8. The time at failure decreases with the increase in stress or temperature.

9. The apparent activation energy for minimum creep rate does not depend on stress from 0.7 to 2.5 MPa and temperature between 263 and 253 K. At

low temperatures between 253 and 243 K, however, the apparent activation energy decreases rapidly with the increase of stress level at low stresses and approaches a constant value at stress levels higher than about 1.5 MPa. The apparent activation energy at higher temperature is higher than that at lower temperature with stress level higher than about 1.5 MPa.

10. The apparent activation energy obtained here are similar to the values reported for fresh water ice. The presence of brine in sea ice does not significantly affect the apparent activation energy.

11. The acoustic emission data showed that with an increase in stress or temperature, the crack activity increases.

12. Microstructure studies after the creep tests in compression showed that the majority of the cracks were parallel to the loading axis.

7.2 Field tests

Field tests were carried out in Resolute Bay in May, 1992. The ice cover in the bay was extremely flat and uniform. Two studies were carried out. One is the microstructure studies of first year sea ice. The other one is borehole indentation test.

7.2.1 Growth and microstructures of first year sea ice

1. Sinha and Nakawo's model was found to be applicable in estimating the growth of first year sea ice in Resolute Bay.

2. The ice is highly oriented columnar grained sea ice with the mean c-axis parallel to the shore line.

3. The brine layer spacing in the first year ice sheet increases with an increase in ice thickness. This is further related to the growth rate of the ice sheet. The vertical salinity distribution exhibits a "C" type of curve with higher salinity near the top and the bottom surfaces. In the bulk of the ice, the

salinity decreases with an increase in ice thickness. This decrease in salinity with depth is related to the decrease in the growth rate of ice.

7.2.2 Borehole indentation tests

1. The maximum or the upper yield stress on the indentation rate can be expressed by a power law This indentation rate power was found to be about 0.3, which is very similar to the strain rate power in CD or CS tests.

2. The upper yield stress does not depend on the ACL angle (angle between the mean c-axis and loading direction) in both conventional and H borehole indentation tests.

3. Stress decreases during the post failure in H tests, however, the stress continues to increase after the yield in conventional tests. The H tests give a maximum stress value which can be characterized as failure, while the conventional test does not.

4. The conventional tests showed a stronger indentation rate dependence of the upper yield stress than the H tests.

5. Large cracks form in the H tests, which are not observed in the conventional tests. The large crack orientation depends strongly on the ACL angle in the H tests.

6. A link between the conventional borehole indentation tests and the laboratory uniaxial constant strain rate tests can be established. This link can be used to relate the field strength test to the laboratory strength test.

7.3 Constitutive model for fresh water ice

A three dimensional constitutive model for the ductile behaviour of fresh water columnar grained ice is developed. The model can account the inherent anisotropy due to fabric, the crack evolutions, the deformation of cracks, the effect of cracks on viscous strain, temperature and the grain size effect.

1. The model can predict the primary, transitory and tertiary creep of ice.

2. The proposed formulation for delayed elasticity reduces computer time significantly compared with Sinha's creep equation.

3. The effect of fabric on viscous strain rate is formulated. It is demonstrated that the model can predict the strength dependence on the ACL angle, anisotropic deformation, and the difference between vertical strength and horizontal strength.

4. The crack density is related to the grain boundary sliding and the plastic flow. A rate formulation is established based on the test results. The comparisons between the test data and the predictions showed that the crack density is formulated correctly.

5. A simple formulation is given for crack enhancement factor to viscous strain rate for both dilute and interacting cracks. Good agreements, between model predictions and test data on the rate dependence of strength, stress strain diagram, and time dependence of strains, imply that the crack enhancement factor is reasonable.

6. The crack deformation is formulated. Crack opening produces dilation. Volumetric strain predictions were in good agreement with the test data.

The model was developed to account for temperature effects. However, the model validation was done only at -10^0C temperature. Further validation at other temperatures is necessary.

7.4 Constitutive model for sea ice

The constitutive equations developed in this study for fresh water columnar grained ice is extended to columnar grained sea ice by introducing an initial defect tensor based on the microstructure of sea ice.

Comparisons between the model predictions and test data were in agreement for the rate dependence of strength, stress strain diagram, time dependence of

strains, and strength dependence on the angle between the mean c-axis and loading direction under both uniaxial and multiaxial loading conditions.

7.5 FE analyses of borehole indentation test data

1. Sinha's model is generalized to 3-D and implemented to a FE program. Comparisons between analytical solutions and finite element results showed that the model implementation was done correctly.

2. 3-D elastic analysis showed that the maximum tensile stress occurs at vertical planes almost 45 degrees to the loading axis. This founding explained the dependence of the large crack orientation on the ACL angle.

3. 3-D elastic analysis shows that for a given ACL angle, the angle between the principal stress and the mean c-axis is different in different locations around the borehole indentor. This was used to explain the negligible dependence of the maximum stress on the ACL angle.

4. Plane strain creep analysis shows that the time dependence of the principal stress orientations is negligible.

7.6 Recommendations

The following recommendations are offered.

1. The crack density is formulated based on Gold's experimental results under uniaxial loading conditions. Further data are required to verify the formulation under multiaxial loading conditions.

2. The proposed constitutive model must be implemented into a finite element program, in order to solve engineering problems.

3. Laboratory tests on single crystal ice and S3 ice with measurements of strains in all directions are needed to estimate the material constants a_2, a_5 and b_2.

4. Laboratory tests on columnar grained sea ice with measurements of strains combined with microstructure studies are needed to further verify the sea ice model.

5. In order to investigate the anisotropy of oriented columnar grained sea ice, further H test should be performed with the width of H similar to the size of the borehole indentor.

6. Further analysis of the acoustic emission data is required.

Bibliography

[1] Anderson, D.L. and Weeks, W.F., 1958. A theoretical analysis of sea ice strength. Transactions American Geophysical Union, 39(4), pp. 632-640.

[2] Anderson, D.L., 1958. A model for determining sea ice properties. Arctic Sea Ice, US National Academy of Science, National Research Council, Pub. 598, pp. 148-152.

[3] Anderson, D.L., 1960. The physical constants of sea ice. Research, 13(S), pp. 310-318.

[4] Assur, A., 1958. Composites of sea ice and its tensile strength. Arctic Sea Ice, US National Academy of Science, National Research Council, Pub. 598, pp. 106-138.

[5] Ashby, M.F. and Duval, P., 1985. The creep of polycrystalline ice. Cold Regions Sciences and Technology, 11, pp. 285-300.

[6] Betten, J., 1981. Creep theory of anisotropic solids. Journal of Rheology, 25(6), pp. 565-581.

[7] Betten, J., 1986. Applications of tensor functions in the formulation of constitutive equation involving damage and initial anisotropy. Engineering fracture mechanics, Vol 25, No, 5/6, pp. 573-584.

[8] Brill, R. and Camp, P.R., 1961. Properties of Ice. Research Report 68, U.S. Army Snow, Ice and Permafrost Research Establishment.

[9] Blanchet, D. and Hamza, H., 1983. Plane strain compressive strength of first year Beaufort sea ice. Proceedings of the 7th International Conference on Port and Ocean Engineering under Arctic Conditions, Vol. 3, pp. 84-96.

[10] Bolling, G.F. and Tiller, W.A., 1960. Growth from the melt II, Cellular interface morphology. Journal of Applied Physics, Vol. 31, pp. 2040-2045.

[11] Burton, J.A., Prim, R.C. and Slichter, W.P., 1953. The distribution of solute in crystals grown from melt, Part 1 Theoretical. Journal of Chemical Physics, Vol. 21, pp. 1987-1991.

[12] Brown, R.L., Richter-Menge, J.A. and Cox, G.F.N., 1986. A comparison of two constitutive theories for compressive deformation of columnar sea ice. Proceedings of the International Association for Hydraulic Research Symposium on Ice, pp. 241-252.

[13] Brown, T.J., Cheung, M.S., and Bercha, F.G., 1986. Ice rheology finite element models. Proceedings of 5th International Conference on Offshore Mechanics and Arctic Engineering, Vol.4, pp. 583-588.

[14] Butkovich T.R. and Landauer, J.K., 1958. The flow law for ice, IASH Pub., 47, pp. 318-327.

[15] Chen, A.C.T., and Lee J., 1986. Large scale ice strength tests at slow strain rate. Proceedings of 5th International Conference on Offshore Mechanics and Arctic Engineering, Vol.4, pp. 374-378.

[16] Cole, D.M., 1983. The relationship between creep and strength behavior of ice at failure. Cold Regions Science and Technology, 8, pp. 189-197.

[17] Cole, D.M., 1987. Strain rate and grain size effects in ice. Journal of Glaciology, Vol. 33, No. 15, pp. 274-280

[18] Cole, D.M., 1988. Crack nucleation in polycrystalline ice. Cold Regions Science and Technology, 15, pp. 79-87.

[19] Cox, G.F.N., and Weeks, W.F., 1975. Brine drainage and initial entrapment in sodium chloride ice. USA, CRREL, Research Report, 354, 85p.

[20] Choi, K., and Karr, D.G., 1989. A damage mechanics model for uniaxial creep and cyclic loading of polycrystalline ice. Proceedings of the 8th International Conference on Offshore Mechanics and Arctic Engineering, Vol. 4, pp. 75-82.

[21] Duval, P. and Kalifa, P., 1991. Viscoelasticity and compressive failure of polycrystalline ice. Proceeding of the 6th International Specialty Conference, Edited by D.S. Sodhi, pp. 494-503.

[22] Dykins, J.E., 1970. Ice engineering, tensile properties of sea ice grown in a confined system. US Naval Civ. Eng. Lab., Technical Report, R687, Port Hueneme.

[23] Dykins, J.E., 1971. Ice engineering, mechanical properties of saline ice for a limited range of condition. US Naval Civ. Eng. Lab., Technical Report, R720, Port Hueneme.

[24] Emery, J.J, and F.A. Mirza, 1980. Finite element method simulation of large ice mass flow behaviour. IUTAM Symposium, 1979, pp. 82-90.

[25] Evgin, E., C. Zhan, and R.W.M. Frederking, 1991, Nonlinear analysis of stress distribution in an ice floe, Proceedings of 10th International Conference on Offshore Mechanics and Arctic Engineering, Vol. 4, pp. 55-82.

[26] Frederking, R.M.W., 1977. Plane strain compressive strength of columnar grained and granular-snow ice. Journal of Glaciology, 18(80), pp. 505-516.

[27] Frederking, R., and Timco, G.W., 1983. Uniaxial compressive strength and deformation of Beaufort sea ice. Proceedings of the 7th International Conference on Port and Ocean Engineering under Arctic Conditions, Vol. 1, pp. 89-98.

[28] Frederking, R., and Timco, G.W., 1984. Compressive behaviour of Beaufort sea ice under vertical and horizontal loading. Proceedings of 3rd International Conference on Offshore Mechanics and Arctic Engineering, Vol. 3, pp. 145-149.

[29] Frederking, R.W.M., and E. Evgin, 1990. Analysis of stress distribution in an ice floe. Proceedings of 9th International Conference on Offshore Mechanics and Arctic Engineering, Vol. 4, pp. 83-87.

[30] Glen, J.W., and Perutz, M.F., 1954. The growth and deformation of ice crystals. Journal of Glaciology, Vol. 2, pp. 397-403.

[31] Glen, J.W., 1955. The creep of polycrystalline ice. Proc. Roy. Soc., London, A228, pp. 519-538.

[32] Gold L.W. and Krausz, A.S., 1971. Investigation of the mechanical properties of St. Lawrence river ice. Canadian Geotechnical Journal, 8(2), pp. 163-169.

[33] Gold L., 1972a. The failure process in columnar grained ice. Technical Report, Report No. 369, NRC Ottawa, 13Sp.

[34] Gold L., 1972b. Activation energy for creep of columnar grained ice. Physics and Chemistry of Ice, pp. 363-364.

[35] Gold L. and Sinha, N.K., 1981. The rheological behaviour of ice at small strains. Physics and Mechanics of Ice, Edited by P. Tryde, pp. 117-128.

[36] Gold, L.W., Jones, S.J. and Slade, T.D., 1992. A comparison of crack initiation for columnar grained and granular ice. Proceedings of the International Association for Hydraulic Research Symposium on Ice, pp. 200-209.

[37] Hagashi, T., 1968. Mechanics properties of ice crystals. Physics of Ice, International Conference on Physics of Ice, pp. 197-212.

[38] Hausler, F.U., 1982. Multiaxial compressive strength test on saline ice with brush type loading platens. Proceedings of the International Association for Hydraulic Research Symposium on Ice, Vol. 2, pp. 526-539.

[39] Hobbs, P.V., 1974. Physics of Ice. Clarenden Press, Oxford.

[40] Jones, S.J., 1982. Confined compressive strength of polycrystalline ice. Journal of Glaciology, Vol. 28, No. 98, pp. 171-177.

[41] Jones, S.J., and Chew, H.A.M., 1983. Effects of sample and grain size on the compressive strength of ice. Annuals of Glaciology, 4, pp. 129-132.

[42] Jordaan, I.J., 1986. Numerical and finite element techniques in calculation of ice structure interaction. Proceedings of the International Association for Hydraulic Research Symposium on Ice, pp. 405-441.

[43] Jordaan, I.J. and McKenna, R.F., 1989. Process of deformation and fracture of ice in compression. Proc. of IUTAM/IAHR Symp. on Ice Structure Interaction, St John's, Newfoundland, Canada.

[44] Karr, D.G., 1985. A damage mechanics model for uniaxial deformation of ice. Journal of Energy Resources Technology, 107, pp. 363-368.

[45] Katona, M.G., and Vaudrey, K.D., 1975. Viscoelastic finite element analysis of sea ice sheets. Proceedings of the International Association for Hydraulic Research Symposium on Ice, Hanover, pp. 515-525.

[46] Kormann, J.P., and Brown, T.G., 1992. Numerical solution of indentation problem. Proceedings of 11th International Conference on Offshore Mechanics and Arctic Engineering, Vol. 4, pp. 297-302.

[47] Krajcinovic, D., 1985. Continuous damage mechanics: Basic concepts and definition. Journal of Applied Mechanics, Vol. 52, No. 4, pp. 529-534.

[48] Lainey, L., and, Tinawi, R., 1984. The mechanical properties of sea ice : A compilation of available data. Canadian Journal of Civil Engineering, Vol. 11, No.4, pp. 884-923.

[49] Leckie, F.A. and Hayhurst, D.R., 1977. Constitutive equation for creep rapture. Acta Metallurgica, pp. 1059-1070.

[50] Leckie, F.A., 1986. The micro and macromechanics of creep rapture. Engineering Fracture Mechanics, Vol 25, No, 5/6, pp. 505-521.

[51] Lemaitre, J. and Chaboche, J.L., 1978. Aspect phenomenologique de la rapture par endoommagement. Journal de Mecanique Appliquee, Vol. 2, pp. 317-365.

[52] Lemaitre, J. and Chaboche, J.L., 1985. Mecanique des materianx solides. Dunod, Paris.

[53] Li, Z. and et al., 1991. Experimental creep behaviour of the sea ice. Proceedings of the 10th International Conference on Offshore Mechanics and Arctic Engineering, Vol. 4, pp. 83-86.

[54] Lile, R.C., 1978. The effects of anisotropy on the creep of polycrystalline ice. Journal of Glaciology, Vol. 21, No. 85, pp. 475-484

[55] Mahrenholtz, O.H. and Wu, Z., 1991. Numerical simulation of viscoelastic behaviour of ice structures. Proceedings of the 11th International Conference on Port and Ocean Engineering under Arctic Conditions, pp. 416-427.

[56] McKenna, R.F., Meyssonnier, J. and Jordaan, I.J., 1989. Peak pressure from a damage model for ice in compression. Proceedings of the 8th International Conference on Offshore Mechanics and Arctic Engineering, pp. 67-74.

[57] Mellor, M., 1977. Engineering properties of snow. Journal of Glaciology, 19(81), pp.15-66.

[58] Mellor, M. and Cole, D.M., 1982. Deformation and failure of ice under constant stress and constant strain rate. Cold Regions Science and Technology, 5, pp. 201-219.

[59] Mellor, M. and Cole, D.M., 1983. Stress/strain/time relations for ice under uniaxial compression. Cold Regions Science and Technology, 6, pp. 207-230.

[60] Michel, B. and Ramseier, R., 1971. Classification of river and lake ice. Canadian Geotechnical Journal, 8(1), pp. 36-45.

[61] Michel B. and Testa, R., 1978. A mechanical model of creep of polycrystalline ice. Canadian Geotechnical Journal, 15(2), pp. 155-171.

[62] Michel B., 1978a. Ice mechanics. Les Presses de L'universite Laval, Quebec

[63] Michel B., 1978b. The strength of polycrystalline ice. Canadian Journal of Civil Engineering, 5(3), pp. 285-300.

[64] Murakami, S., 1988. Mechanical modelling of material damage. Journal of Applied Mechanics, Vol. 55, pp. 280-286.

[65] Nadreau, J.P., and Michel, B., 1984. Ice properties in relation to ice forces. Proceedings of 2nd state of the art IAHR working group, Vol. 4, Chapter 1, Hamburg, pp. 1-53.

[66] Nakawo, M., and Sinha, N.K., 1981. Growth rate and salinity profile of first year sea ice in High Arctic. Journal of Glaciology, Vol. 27, pp. 315-330.

[67] Nakawo, M., and Sinha, N.K., 1984. A note on brine layer spacing of first year sea ice. Atmosphere Ocean, 22(2), pp. 193-206.

[68] Nakaya, U., 1958. Mechanical properties of single crystal of ice. SIPRE, Res. Pub. 28.

[69] Nawwar, A.M., Nadreau, J.P., and Wang, Y.S., 1983. Triaxial compressive strength of sea ice. Proceedings of the 7th International Conference on Port and Ocean Engineering under Arctic Conditions, Vol. 1, pp.243-253.

[70] Nemat-Nasser, S., and Obata, M., 1988. A microcrack model of dilatancy in brittle materials, Journal of Applied Mechanics, Vol. 55, pp. 24-35.

[71] Peyton, H.R., 1966. Sea ice strength. University of Alaska, Geophysical Institute Report Series UAG-R-182.

[72] Pitman, D., and Zuckerman, B., 1967. Effective thermal conductivity of snow at -88^0, -27^0, and -5^0. Journal of Applied Physics, 38(6), pp. 2698-2699.

[73] Prodanovic, A., 1979. Two dimensional limit analysis of ice failure described by a quadratic yield criteria. Research Advances in Engineering Sciences, pp. 515-519.

[74] Pulkkinen, E., 1989. Rate sensitive damage and cracking model for ice. Proceedings of the 8th International Conference on Offshore Mechanics and Arctic Engineering, pp. 47-54

[75] Ralston, T.D., 1978. An analysis of ice sheet indentation. Proceedings of the International Association for Hydraulic Research Symposium on Ice, pp.13-31.

[76] Ramseier, R.O., 1972. Growth and mechanical properties of river and lake ice. Ph.D. thesis, Laval University.

[77] Rees, D.W.A., 1983. The potential theory of creep. Engineering Approaches to High Temperature Design, Edited by Wilshire, B. and Owen, D.R.J., Pinerridge Press, Swansea, U.K., pp.57-84.

[78] Richter-Menge, J.A., 1991. Confined compressive strength of horizontal first year sea ice. Journal of Offshore Mechanics and Arctic Engineering, Vol. 113, pp. 344-351.

[79] Sanderson, T.J.O., 1988. Ice Mechanics, Risk to Offshore Structures. Graham and Trotman, London.

[80] Santaoja, K., 1988. Three dimensional ductile constitutive equation for ice. Proceedings of the 7th International Conference on Offshore Mechanics and Arctic Engineering, Vol. 4, pp. 1-10.

[81] Santaoja, K., 1989. Continuum damage mechanics approach to describe the multidirectional microcracking of ice. Proceedings of the 8th International Conference on Offshore Mechanics and Arctic Engineering, Vol. 4, pp. 55-67.

[82] Schwerdtfeger, P., 1963. The thermal properties of sea ice. Journal of Glaciology, 4(36), pp. 789-807.

[83] Sinha, N.K., 1977. Dislocation in ice as revealed by etching. Philosophical Magazine, 36(6) pp. 1385-1404.

[84] Sinha, N.K., 1978a. Rheology of columnar-grained ice. Experimental Mechanics, 18(12), pp. 1-7.

[85] Sinha, N.K., 1978b. Grain size influences on effective modulus of ice. Workshop on the Bearing Capacity of Ice Covers, Winnipeg, Manitoba, pp. 65-78.

[S6] Sinha, N.K., 1978c. Observation of basal dislocations by etching and replicating. Journal of Glaciology, 21(85), pp. 385-395.

[S7] Sinha, N.K., 1979a. Grain boundary sliding in polycrystalline materials. Philosophical Magazine, 40(6) pp. 825-842.

[S8] Sinha, N.K., 1979b. Technique for studying structures of sea ice. Journal of Glaciology, 18(79), pp. 315-323.

[S9] Sinha, N.K., and Nakawo, M., 1981. Growth of first year sea ice, Eclipse Sound, Baffin Island, Canada. Canadian Geotechnical Journal, 18(2), pp. 17-23.

[90] Sinha, N,K., 1981a. Rate sensitivity of compressive strength of columnar grained ice. Experimental Mechanics, 21(6), pp. 209-218.

[91] Sinha, N,K., 1981b. Comparative study of ice strength data. Proceedings of the International Association for Hydraulic Research Symposium on Ice, Vol. 2, pp. 581-595.

[92] Sinha, N.K., 1982. Constant strain and stress rate compressive strength of columnar grained ice. Journal of Material Science, 17, pp. 785-802.

[93] Sinha, N,K., 1983a. Field test 1 of compressive strength of first year sea ice. Annals of Glaciology, 4, pp. 253-259.

[94] Sinha, N,K., 1983b. Field tests on rate sensitivity of vertical strength and deformation of first year columnar grained sea ice. Proceedings of the 7th International Conference on Port and Ocean Engineering under Arctic Conditions, Helsinki, Finland, Vol. 1, pp. 231-242.

[95] Sinha, N.K., 1984a. Uniaxial compressive strength of first year and multi-year sea ice. Canadian Journal of Civil Engineering, Vol. 11, No.1, pp. 82-91.

[96] Sinha, N.K., 1984b. Intercrystalline cracking grain boundary sliding and delayed elasticity. Journal of Material Science, 16, pp. 359-376.

[97] Sinha, N.K., 1984c. Delayed-elasticity model for initiation and Accumulation of creep cavitation at high temperature. Proceeding of 6th International Conference on Fracture, pp. 2295-2302.

[98] Sinha, N.K., 1985. Confined strength and deformation of second year columnar grained sea ice in Mould Bay. Proceedings of 4th International Conference on Offshore Mechanics and Arctic Engineering, pp. 209-219.

[99] Sinha, N.K., 1986. Young Arctic frazil sea ice, field and laboratory strength tests. Journal of Material Science, 21(5), pp. 1533-1546.

[100] Sinha, N.K.. 1987, The borehole jack, is it a useful Arctic tool? Journal of Offshore Mechanics and Arctic Engineering, Transactions of the ASME, Vol. 109, pp. 391-397.

[101] Sinha, N.K., 1988a. Crack enhanced creep in polycrystalline material strain rate sensitive strength and deformation of ice. Journal of Material Science, 23, pp. 4415-4428

[102] Sinha, N.K., 1988b. Anisotropy of Possion's ration and young's modulus. Experimental Mechanics, 23, pp. 4415-4428

[103] Sinha, N.K., 1989a. Microcrack-enhanced creep in polycrystalline material at elevated temperature. Acta Metallurgy, 37(11), pp. 3107-3118.

[104] Sinha, N.K., 1989b. Elasticity of natural types of polycrystalline ice. Cold Regions Science and Technology, Vol. 17, No. 2, pp. 127-135.

[105] Sinha, N.K., 1989c. Experiments on anisotropic and rate sensitivity strain ratio and modulus of columnar grained ice. Journal of Offshore Mechanics and Arctic Engineering, Vol. 111, pp. 354-360.

[106] Sinha, N.K., 1989d. Ice and steel, a comparison of creep and failure. Proceeding of Euromech-239, Leicester, U.K., pp. 201-212.

[107] Sinha, N.K., 1990a. Microcracking and creep dilation in polycrystalline columnar-grained and equiaxied ice. Proceeding of 4th International Conference on Creep and Fracture of Engineering Materials and Structures, Swansea, U.K., pp.345-354.

[108] Sinha, N.K., 1990b. Ice cover strength decay using borehole indentor. Proceedings of the International Association for Hydraulic Research Symposium on Ice, Vol. 2, pp. 735-744.

[109] Sinha, N.K., 1991a. Microstructures and mechanical behaviour of ice. Proceeding of the 6th International Specialty Conference, Edited by D.S. Sodhi, pp. 519-528.

[110] Sinha, N.K., 1991b. In situ multi-year sea ice strength using NRCC Borehole indentor. Proceedings of the 10th International Conference on Offshore Mechanics and Arctic Engineering, Vol. 4, pp. 239-246.

[111] Sinha, N,K., Zhan, C., and Evgin, E., 1992. Creep of sea ice. Proceedings of the 11th International Conference on Offshore Mechanics and Arctic Engineering, Vol. 4, pp. 261-266.

[112] Shokr, M.E., and Sinha, N.K., 1992. Sea ice microstructural characteristics relevant to ice microwave scattering. Proceedings of the 11th International Conference on Offshore Mechanics and Arctic Engineering, Vol. 4, pp. 319-328.

[113] Sjolind, S.G., 1985. Visco-elastic buckling analysis of thick ice sheet. Cold Regions Science and Technology, 11(3), pp. 224-246.

[114] Sjolind, S.G., 1987. A constitutive model for ice as a damage visco-elastic material. Cold Regions Science and Technology, 41, pp. 247-262.

[115] Sodhi, D.S., and H.E. Hamza, 1977. Buckling analysis of semi-infinite ice sheet. Proceedings of the 4th International Conference on Port and Ocean Engineering under Arctic Conditions, pp. 593-604.

[116] Spring, U., and Morland, L.W., 1983. Integral representations for the viscoelastic deformation of ice. Cold Regions Science and Technology, 6, pp. 185-193.

[117] Steinmann, S., 1954. Results on preliminary experiments on plasticity of ice crystals. Journal of Glaciology, Vol. 2, pp. 404-412.

[118] Sunder, S., and Wu, M.S., 1989. A multiaxial differential model of flow of orthotropic polycrystalline ice. Cold Regions Science and Technology, 16, pp. 223-235

[119] Svec, O.J., Frederking, R.W.M., 1985. Cantilever beam tests in an ice cover, influence of plate effects at the root. Cold Regions Science and Technology, 4, pp. 93-101.

[120] Tabata, T., 1958. Studies on visco-elastic properties of sea ice. U.S. National Academy of Sciences, National Research Council Publications 598-"Arctic Sea ice", pp. 139-147.

[121] Timco, G.W., and Frederking, R.W.M., 1982. Comparative strength of fresh water ice. Cold Regions Science and Technology, 6, pp. 21-27.

[122] Timco, G.W., and Frederking, R.W.M., 1983. Confined compressive strength of sea ice. Proceedings of the 7th International Conference on Port and Ocean Engineering under Arctic Conditions, Vol. 1, pp. 243-253.

[123] Timco, G.W., and Frederking, R.W.M., 1986. Confined compressive tests outlining the failure envelope of columnar sea ice. Cold Regions Science and Technology, 12, pp. 13-28.

[124] Tomin, M.J., Cheung M., Jordaan I.J., and Cormeau A., 1986. Analyses of failure modes and damage processes of fresh water ice in indentation tests. Proceedings of 5th International Conference on Offshore Mechanics and Arctic Engineering, Vol. 4, pp. 453-460.

[125] Ting, S-K, and Shyam Sunder, S., 1985. Constitutive modelling of sea ice with application to indentation problem. CSEOE Report No. 3, MIT, 255p.

[126] Vinogradov, A.M., and D.M. Masterson, 1989. Time dependent settlement of ice and earth offshore structures. Proceedings of the 8th International Conference on Offshore Mechanics and Arctic Engineering, Vol. 4, pp. 263-268.

[127] Wang, Y.S., 1979a. Crystallographic studies and strength tests of field ice in the Alaska Beaufort Sea. Proceedings of the 5th International Conference on Port and Ocean Engineering under Arctic Conditions, Vol. 1, pp. 651-665.

[128] Wang, Y.S., 1979b. Sea ice properties. Technical Seminar on Alaska Beaufort Sea Gravel Island Design, Exxon Company, USA.

[129] Wang, Y.S., 1981. Uniaxial compressive testing of Arctic sea ice. Proceedings of the 6th International Conference on Port and Ocean Engineering under Arctic Conditions, pp. 346-355.

[130] Wang, Y.S., 1983. A rate dependent of stress strain relation for sea ice. Journal of Energy Resources and Technology, Vol. 105, pp. 2-5.

[131] Weeks, W.F., and Hamilton, W.L., 1962. Petrographic characteristics of young sea ice, Point Barrow, Alaska. Am. Minerals, Vol. 47, pp. 945-961.

[132] Weeks, W.F., and Lofgren, G., 1967. The effective solute distribution coefficient during freezing of N_aCl solution. Physics of Snow and Ice, Vol. 1, No. 1, pp. 579-597.

[133] Weeks, W.F. and Gow, A.J., 1978. Preferred crystal orientation along the margins of the Arctic ocean. Journal of Geophysics Research, Vol. 84, No. C10, pp. 5105-5121.

[134] Weeks, W.F. and Assur, A., 1967. Mechanical properties of sea ice. CRREL Monograph IIC3, Hanover, NH.

[135] Weeks, W.F. and Ackley, S.F., 1982. The growth, structure, and properties of sea ice. CRREL Monograph 82-1.

[136] Weertman, J., 1969. Effect of cracks on creep rate. Transactions of the ASM, 62(2), pp. 502-511.

[137] Xiao, J. I. Jordaan, R.F. McKenna, and R.M.W. Frederking, 1991. Finite element modelling of spherical indentation test on ice. Proceedings of the 11th International Conference on Port and Ocean Engineering under Arctic Conditions, pp. 471-485.

[138] Zienkiewicz, O.C., 1977. The finite element method. McGraw-Hill Book Company Limited, UK

Appendix A

Determination of A_i

$$
\begin{aligned}
A_1 = \;& a_1 sin^4\theta(1+sin^2\phi)^2 + a_2 sin^4\theta(2sin^2\phi + 5cos^4\phi) + \frac{a_4}{4} sin^2\phi sin^2 2\theta \\
& + a_5 cos^2\phi sin^2\theta(1 - cos^2\phi sin^2\theta) \\
A_2 = \;& a_1 + a_2 \\
A_3 = \;& a_1 sin^4\phi + a_2(cos^4\phi + cos^2 2\phi) + \frac{a_5}{4} sin^2 2\phi \\
A_4 = \;& 2a_1 sin^2\theta(1+sin^2\phi) + 2a_2 sin^2\theta(1+cos^2\phi) \\
A_5 = \;& 2a_1 sin^2\theta(1+sin^2\phi)sin^2\phi + 2a_2 sin^2\theta(5cos^4\phi - 3cos^2\phi + 1) \\
& + \frac{a_5}{2} sin^2 2\phi sin^2\theta \\
A_6 = \;& 2a_1 sin^2\phi + 2a_2 cos^2\phi \\
A_7 = \;& a_1 sin^2 2\theta(1+sin^2\phi)^2 + a_2 sin^2 2\theta(2sin^2\phi + 5cos^4\phi) + a_4 sin^2\phi cos^2 2\theta \\
& + a_5 cos^2\phi(1 - cos^2\phi sin^2 2\theta) \\
A_8 = \;& a_1 cos^2\theta sin^2 2\phi + 5a_2 cos^2\theta sin^2 2\phi + a_4 sin^2\theta cos^2\phi \\
& + a_5(sin^2\phi sin^2\theta + cos^2\theta cos^2 2\phi) \\
A_9 = \;& (a_1 + 5a_2) sin^2\theta sin^2 2\phi + a_4 cos^2\theta cos^2\phi \\
& + a_5(sin^2\phi cos^2\theta + sin^2\theta cos^2 2\phi) \\
A_{10} = \;& -2a_1 sin^2\theta sin2\theta(1+sin^2\phi)^2 - 2a_2 sin^2\theta sin2\theta(5cos^4\phi + 2sin^2\phi) \\
& - a_4 sin^2\phi sin2\theta cos2\theta - a_5 cos^2\phi sin2\theta(cos^2\theta - cos2\phi sin^2\theta) \\
A_{11} = \;& 2a_1 sin^2\theta cos\theta sin2\phi(1+sin^2\phi)^2 - 2a_2 sin^2\theta cos\theta sin2\phi(5cos^4\phi - 1)
\end{aligned}
$$

$$
\begin{aligned}
& -\frac{a_4}{2} sin2\phi sin2\theta sin\theta + a_5 sin2\phi sin2\theta sin\theta cos^2\phi \\
A_{12} = \; & 2a_1 sin^3\theta sin2\phi(1 + sin^2\phi) - 2a_2 sin^3\theta sin2\phi(5cos^2\phi - 1) \\
& + \frac{a_4}{2} sin2\phi sin2\theta cos\theta + a_5 sin2\phi sin\theta(sin^2\theta cos2\phi - cos^2\theta) \\
A_{13} = \; & -2a_1 sin2\theta(1 + sin^2\phi) - 2a_2 sin2\theta(1 + cos^2\phi) \\
A_{14} = \; & 2(a_1 - a_2) cos\theta sin2\phi \\
A_{15} = \; & 2(a_1 - a_2) sin\theta sin2\phi \\
A_{16} = \; & -2a_1 sin2\theta sin^2\phi(1 + sin^2\phi) - 2a_2 sin2\theta(5cos^4\phi - 3cos^2\phi + 1) \\
& - \frac{a_5}{2} sin^2 2\phi sin2\theta \\
A_{17} = \; & 2a_1 sin2\phi sin^2\phi cos\theta - 2a_2 sin2\phi cos\theta(5cos^2\phi - 2) \\
& + \frac{a_5}{2} sin4\phi cos\theta \\
A_{18} = \; & 2a_1 sin2\phi sin^2\phi sin\theta - 2a_2 sin2\phi sin\theta(5cos^2\phi - 2) \\
& + \frac{a_5}{2} sin4\phi sin\theta \\
A_{19} = \; & -2a_1 sin2\phi(1 + sin^2\phi) sin2\theta cos\theta + 2a_2 sin2\theta cos\theta sin2\phi(5cos^2\phi - 1) \\
& + a_4 sin2\phi cos2\theta sin\theta - a_5 sin2\phi sin\theta(cos2\theta + 2cos^2\theta cos2\phi) \\
A_{20} = \; & -2a_1 sin2\phi(1 + sin^2\phi) sin2\theta sin\theta + 2a_2 sin2\theta sin\theta sin2\phi(5cos^2\phi - 1) \\
& - a_4 sin2\phi cos2\theta cos\theta + a_5 sin2\phi cos\theta(cos2\theta - 2sin^2\theta cos2\phi) \\
A_{21} = \; & a_1 sin2\theta sin^2 2\phi + 5a_2 sin^2 2\phi sin2\theta - a_4 sin2\theta cos^2\phi \\
& + a_5 sin2\theta(cos^2 2\phi - sin^2\phi)
\end{aligned}
$$

Appendix B

Steady state solution

To verify the implementation of the generalized Sinha's model into finite element program, an analytical solution with the model is required. It is difficult to find an analytical solution with the model. However, a steady state solution is found with the model without cracking. The steady state is defined as a state where the stress does not change with time any more.

The analytical solution is obtained for a very long thick cylinder subjected to internal pressure. The material of the cylinder is assumed to be a viscoelastic material represented by the generalized Sinha's model without cracking.

A coordinate system (r, θ, z) is established with z in the direction of the length of the cylinder. It is a plane strain problem. Therefore, ϵ_z is equal to zero. When the steady state is reached, the stress rate is zero. From the generalized Sinha's model, a zero stress rate means that the volumetric strain is zero. Therefore, the following equation can be obtained.

$$\dot{\epsilon}_r + \dot{\epsilon}_\theta = 0 \tag{B.1}$$

With the strain displacement relation, the following equation can be obtained.

$$\frac{d\dot{\epsilon}_\theta}{dr} = \frac{\dot{\epsilon}_r - \dot{\epsilon}_\theta}{r} \tag{B.2}$$

With Eqs. B.1 and B.2, the rate of strain can be obtained as below.

$$\dot{\epsilon}_r = -\dot{\epsilon}_\theta = \frac{C}{r^2} \tag{B.3}$$

where C is a constant.

From the generalized Sinha's model, the following equation for strain rate can be obtained.

$$\begin{aligned}
\dot{\epsilon}_r &= \frac{1}{E}\{\sigma_r - \mu(\sigma_\theta + \sigma_z)\} + \frac{\partial f(S_{rr}, T, t)}{\partial t} + K J_2^{\frac{n-1}{2}} S_{rr} \\
\dot{\epsilon}_\theta &= \frac{1}{E}\{\sigma_\theta - \mu(\sigma_r + \sigma_z)\} + \frac{\partial f(S_{\theta\theta}, T, t)}{\partial t} + K J_2^{\frac{n-1}{2}} S_{\theta\theta} \\
\dot{\epsilon}_z &= \frac{1}{E}\{\sigma_z - \mu(\sigma_\theta + \sigma_r)\} + \frac{\partial f(S_{zz}, T, t)}{\partial t} + K J_2^{\frac{n-1}{2}} S_{zz}
\end{aligned} \tag{B.4}$$

where J_2 is the second stress invariant of deviatoric stress tensor; S_{rr}, $S_{\theta\theta}$, and S_{zz} are deviatoric stresses; K and n are constants.

In Eq. B.4, $\frac{\partial f(s,T,t)}{\partial t}$ can be expressed as below.

$$\frac{\partial f(s,T,t)}{\partial t} = C_1 a_T^b \frac{3d_1}{2dE}\{s(0)t^{b-1}exp(-(a_T t)^b) - \int_0^t \frac{\partial s}{\partial t} dexp(-(a_T(t-\tau))^b)\}$$

When time t approaches a very large value, it is clearly shows that the first term in the above equation is going to be zero. The second term will be zero too. This can be proved as below.

$$\begin{aligned}
&The\ second\ term = \int_0^t \frac{\partial s}{\partial t} dexp(-(a_T(t-\tau))^b) \\
&= \int_0^{\frac{t}{2}} \frac{\partial s}{\partial t} dexp(-(a_T(t-\tau))^b) + \int_{\frac{t}{2}}^t \frac{\partial s}{\partial t} dexp(-(a_T(t-\tau))^b) \\
&< Mexp(-(a_T(t-\tau))^b)|_0^{\frac{t}{2}} + \delta exp(-(a_T(t-\tau))^b)|_{\frac{t}{2}}^t \\
&= M\{exp(-(0.5a_T t)^b) - exp(-(a_T t)^b)\} + \delta\{1 - exp(-(05a_T t)^b)\}
\end{aligned} \tag{B.5}$$

where M is the maximum value of $\frac{\partial s}{\partial t}$ between 0 and 0.5t, δ is the maximum value

of $\frac{\partial s}{\partial t}$ between 0.5t and t. If a steady state solution can be achieved, it is always possible to find a time t to satisfy $|\frac{\partial s}{\partial t}| < \delta$ for any small value of δ. Therefore, it is always possible to choose a time t value to make the value for Eq. B.5 as smaller as possible. Therefore, Eq. B.4 can be written as follows when the steady state is reached.

$$\begin{aligned} \dot{\epsilon}_r &= K J_2^{\frac{n-1}{2}} S_{rr} \\ \dot{\epsilon}_\theta &= K J_2^{\frac{n-1}{2}} S_{\theta\theta} \\ \dot{\epsilon}_z &= K J_2^{\frac{n-1}{2}} S_{zz} \end{aligned} \tag{B.6}$$

It is known that $\dot{\epsilon}_z$ is zero. With Eq. B.6, the following equation can be obtained.

$$\sigma_z = \frac{\sigma_r + \sigma_\theta}{2} \tag{B.7}$$

Substituting Eqs. B.6 and B.7 into Eq. B.3, the following equation can be obtained.

$$(\frac{\sigma_r - \sigma_\theta}{2})^n = \frac{C}{Kr^2} \tag{B.8}$$

The equilibrium equation and the boundary condition for the problem is can be given as

$$\begin{aligned} &\frac{d\sigma_r}{dr} + \frac{\sigma_r - \sigma_\theta}{r} = 0 \\ &\sigma_r|_{r=a} = p \\ &\sigma_r|_{r=b} = 0 \end{aligned} \tag{B.9}$$

With Eqs. B.8 and B.9, the stresses can be obtained as below.

$$\begin{aligned} \sigma_r &= \frac{p}{(\frac{b}{a})^{\frac{2}{n}} - 1}\{(\frac{b}{r})^{\frac{2}{n}} - 1\} \\ \sigma_\theta &= \frac{p}{(\frac{b}{a})^{\frac{2}{n}} - 1}\{\frac{n-2}{n}(\frac{b}{r})^{\frac{2}{n}} - 1\} \\ \sigma_z &= \frac{p}{(\frac{b}{a})^{\frac{2}{n}} - 1}\{\frac{n-1}{n}(\frac{b}{r})^{\frac{2}{n}} - 1\} \end{aligned} \tag{B.10}$$

The solution for rate of radial displacement can be obtained by the following equation at steady state.

$$\dot{u}_r = K b^2 \left(\frac{p}{\left(\frac{b}{a}\right)^{\frac{2}{n}} - 1} \frac{1}{n}\right)^n \frac{1}{r} \tag{B.11}$$